PhD Thesis

Numerical Modelling of the Sorting and Transport of Non-uniform Sediments in the Swash Zone

Thesis submitted to The University of Nottingham

for the degree of Doctor of Philosophy

Diego Pedrozo-Acuña

December 2012

Abstract

The sorting and transport of different sediment fractions and the resulting beachface evolution over the swash zone of a beach, is numerically investigated within the framework of the shallow water theory and the active layer theory. The shallow water and Exner equations, along with the volume fraction (sorting) equation given by the active layer theory compose the system which is numerically solved using an uncoupled approach, i.e., the model assumes that changes in bed level (and volume fraction) do not have an effect on the flow. Two different numerical methods are applied to solve the system depending on the type of flow tested (constant current or swash flow); a classic Finite Differences Method and a hybrid Finite Difference-Method of Characteristics (FD-MOC) are then used respectively. The numerical model is first tested for the case of a sand dune composed of two different sediment fractions subjected to a constant current. Comparison between simulations from the model and results given by Hudson (2001) solution (which only considers one sediment fraction) showed that the composition of the bed is crucial for the subsequent bed evolution. This case served to verify that the equations were solved correctly and some interesting features of the kinematics of the system were observed. The model is then applied to the case in which a single Shen and Meyer (1963b) swash event acts over a plane sloping beach composed of two

different sediment fractions in the same proportion. Different values of the A (sediment mobility parameter) are investigated taking as a base point the value calculated by Kelly (2009). The results show that the behaviour in time of P_{fa} (fine volume fraction in the active layer) directly depends on the difference between sediment mobility parameters (A_f and A_c) for the fine and coarse fractions; and this in turn results in an effect on the beachface evolution. The finer the mixture of sediments involved the bigger the bed change. Similar behaviour is obtained when the model is tested for the case in which a non-breaking wave swash is acting over the beach profile, although some interesting differences are noted mainly due to the different driving hydrodynamics. Finally, realistic A parameters for the fine and coarse fraction are defined linking grain diameters that can be found on real beaches to the sediment parameters used in the model. Numerical tests for both type of swash flows (breaking and non-breaking wave) are implemented, in which different initial P_{fa} distributions are considered. The results from these simulations confirmed the crucial role played by the initial distribution of sediments on the beach evolution; it was observed that a kink in the bed (a sort of swash bar/trough) formed around the middle part of the swash zone for the cases in which the initial distribution of sediments showed a maximum or minimum in that area. Comparing the results given by the model when two sediment fractions are considered, with those when a mean value ($\bar{A} = \frac{A_f + A_c}{2}$) which is a common practice in coastal engineering models) showed that the inclusion of the two sediment fractions is crucial in order to get better predictions.

Acknowledgements

I am very grateful to my supervisor Prof. Nicholas Dodd for the patience and the guidance throughout all these years of work. I wish to thank him for all what I have learnt from him, his suggestions, his help and his dedicated support over the past years. I would also like to thank my supervisor Matthew Scase for the friendly chats and kind advise. I wish to acknowledge the National Council of Science and Technology of Mexico (CONACyT), for providing the funding for my PhD. I would also wish to thank my friends and colleagues in C-11, past and present: Meinard, Anurak, Julia, Bruce, Fangfang, Paloma, Karwan, Riccardo, Jeff, Nick, Evgenia, Andy, Ben and Hannah for making the office a nice place to spend the whole day. Special thanks to Fangfang and Paloma for being such a big support both academically and personally. I wish to thank my parents for their endless support, love and encouragement to achieve this goal. Thanks to my dear brother Adrian and my lovely sister Ursula, for all the support that each in their own way has given me. And lastly, thanks to my girlfriend Carmen for the love and support throughout all these years and for her help to create a comfortable life and home in the UK.

Index

List of Figures

List of Tables

Nomenclature

[*] Denotes units of the parameter or variable

A [s^2 m^{-1}]	Sediment mobility parameter for bedload ($q = u^3$)
$\mathbf{A}$ [-]	Coefficient matrix
A_f [s^2 m^{-1}]	Sediment mobility parameter for the fine fraction
A_c [s^2 m^{-1}]	Sediment mobility parameter for the coarse fraction
B [m]	Bed elevation
B_s [m]	Substrate layer upper boundary elevation
B_{max} [m]	Sand dune maximum height
C_D [-]	Drag coefficient
D_{50} [m]	Median grain diameter
d [m]	Grain diameter
Δx [m]	Space interval in x direction
Δt [s]	Time interval
η [m]	Free surface elevation
G [-]	Discriminant of cubic polynomial
g [m s^{-2}]	Acceleration due to gravity

H [m]	Wave height
H_0 [m]	Deep water wave height
H_b [m]	Wave height at the breaking point
h [m]	Water depth
h_0 [m]	Initial bore height
L_a [m]	Thickness of the active layer
Λ [-]	Roots of cubic polynomial
$\lambda_{1,2}$ [m s^{-1}]	Wave speeds
P_{fa} [-]	Fine volume fraction in the active layer
P_{ca} [-]	Coarse volume fraction in the active layer
P_{fs} [-]	Fine volume fraction in the substrate layer
P_{cs} [-]	Coarse volume fraction in the substrate layer
p [N m^{-2}]	Pressure
p_0 [-]	Bed porosity
Q [m^2]	Net sediment flux
q [m^2 s^{-1}]	Instantaneous sediment flux
q_f [m^2 s^{-1}]	Fine fraction sediment flux
q_c [m^2 s^{-1}]	Coarse fraction sediment flux
R [-]	Quantity in the solution of cubic polynomial
s [-]	Ratio of densities if sediment and water
ρ [kg m^{-3}]	Water density
ρ_s [kg m^{-3}]	Sediment density
T [s]	Wave period
T [-]	Quantity in the solution of cubic polynomial

t [s]	Time
t_{in} [s]	Inundation time
t_{in} [s]	Denudation time
τ_0 [N m^2]	Bed shear stress
τ_{cr} [N m^2]	Threshold bed shear stress
$\tan\theta$ [-]	Beach slope
Θ [-]	Shields parameter
Θ_{cr} [-]	Threshold Shields parameter
U [m s^{-1}]	Depth-averaged water velocity in x-direction
U_b [m s^{-1}]	Bore velocity at the shoreline
U_s [m s^{-1}]	Shoreline velocity
U_{cr} [m s^{-1}]	Threshold velocity
u [m s^{-1}]	Water velocity in x-direction
x [m]	Cross-shore position
x_s [m]	Shoreline position
x_{sw} [m]	Seaward point position
x_λ [m]	point over characteristic λ
ξ_b [-]	Surf similarity parameter
ξ [-]	Bed porosity parameter
Φ [-]	Dimensionless bedload transport rate
w [m s^{-1}]	Water velocity in z-direction
z [m]	Vertical abscissa
z_0 [m]	Roughness length

Subscripts:

i	Number of grid point in the x-direction
f	Fine fraction
c	Coarse fraction
a	Active layer
s	Substrate layer

Superscripts:

n	Time level

Abbreviations:

MOC	Method of characteristics
FD	Finite differences
SWE	Shallow water equations

Chapter 1

Introduction

Coastal zones have always been a natural environment of great importance to the development of human civilisations. The nearshore region, which includes the surf and swash zones, is a region where very intense flow/sediment interactions occur, generated by the interaction of waves, currents and sediments (see Figure 1.1). This, in turn, produces intense sediment transport, generating the deposition and erosion of sediments which yield a considarable variation of the beachface. Waves propagating on-shore may undergo a number of wave processes (e.g. refraction, shoaling) before reaching the surf zone which extends from the breaking point to the run-down limit of the shoreline; this point defines the boundary with the swash zone. The swash zone is the area of a beach that is successively covered (run-up) and uncovered (backwash) by the flow. Fluid motion in the swash zone can be mainly due to incident bores (i.e. breaking waves) or infra-gravity waves (i.e. non-breaking waves) but predominance of one of them depends on the inci-

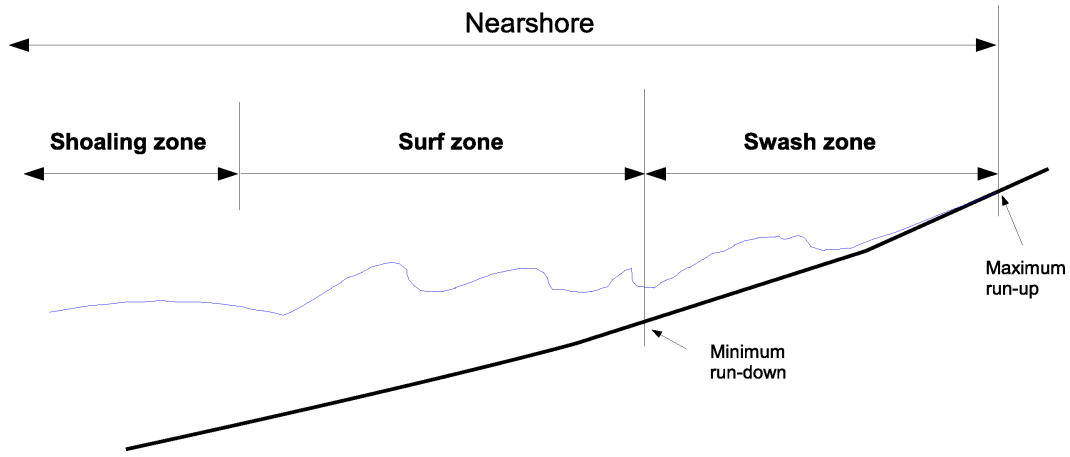

Figure 1.1: Schematic of the nearshore

dent wave form and the beach slope (Erikson et al., 2005). In storm conditions swash flows due to wave breaking is expected to dominate even for beaches with mild slopes; in calm conditions infra-gravity (low-frequency) non-breaking waves are dominant on very shallow beaches (Brocchini and Baldock, 2008). On steep beaches, which will be the ones studied in this research, bore-driven swash flows typically dominate, although if the slope of the beach is sufficiently steep the wave does not break and just surges up and down the beach. The well-known surf similarity parameter (see Battjes (1974)), often also called Iribarren number (see Iribarren and Nogales (1949)), provides a means to know how a wave will break depending on its height and period and the beach slope. The surf similarity parameter defines four types of wave breaking: spilling, plunging, collapsing and surging (see Figure 1.2). Therefore, it is clear that the swash zone is an area where very complex fluid motion and energy dissipation can occur yielding great sediment transport as bed or suspended load, or even the combination of the two.

Sediment transport is usually divided into two transport modes: bed- and suspended load (Masselink and Hughes, 2003). Bedload is defined as that part of the sediment

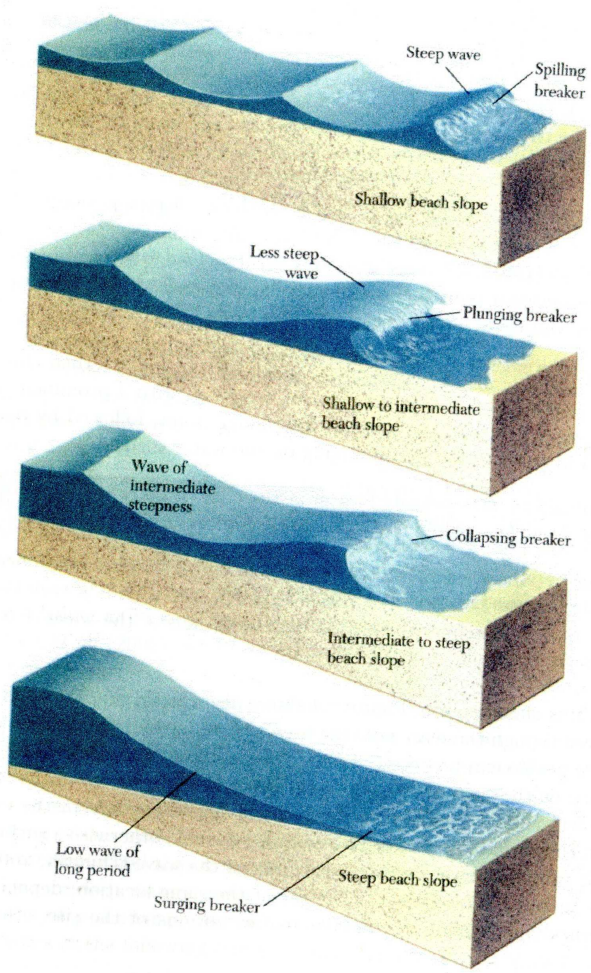

Figure 1.2: Wave breaking types (from Davis (1997))

transport that maintains continuous or intermittent contact with the bed (rolling, hopping and sliding) and reacts instantaneously to changes in the flow, which therefore gives instantaneous bed changes.This type of sediment transport is thought to be dominant for slow flows and/or large grain sizes. When the flow is strong enough (and the grains sufficiently fine) then sediment is put into suspension in the water column; this mode is called, suspended load. Changes in sediment concentration in the water column and changes in bed due to suspended load cannot happen instantaneously because the entrainment of sediment into the water column and settling down on the bed take a certain amount of time and do not take place immediately like with bedload (Soulsby, 1997). Bed level behaviour is then strongly related to both sediment transport modes and this in turn depends on the flow conditions and the sediment size.

When developing numerical models to predict the bed change in beaches, it is common practice in coastal engineering research to represent the grain size of a beach, usually a mix of grain sizes, by one representative grain size (e.g. the median grain size D_{50}). This might work well if the beach is composed of relatively similar grain sizes, but for the case in which the difference between sediments (e.g. mixed sediment beaches) is considerable, predictions made using a single grain size could then give very inaccurate results. In the UK mixed beaches (sand-gravel, sand-shingles, gravel-mud) and gravel beaches are a very common and extremely important to the coastline. For sand-gravel and gravel beaches, which are the main subject of this research, the range of beach slope steepnesses is about 1:10 to 1:2 and typical grain sizes vary between 0.5 mm to 64 mm. However, understanding of processes on these kinds of beaches is less compared with sand beaches (Horn and Walton, 2007) and their importance to the UK environment

makes them a crucial topic for study. Similarly for this kind of beaches, the distribution of different grain sizes across the beach is important, and the sorting and transport of sediments (and the resulting bed change) has to be modeled taking into account at least two fractions. One of the most, simple and widely-known theories to model the transport of sediment mixtures and the resulting bed level change is the active layer theory (also known as the one layer theory). This theory has been applied with success in rivers (see e.g. Ribberink (1987), Tritthart et al. (2011)), and in some coastal environments (see e.g. Walgreen et al. (2003), De Swart et al. (2008)) but its application in the swash zone has not yet been attempted.

Therefore, the motivation of this research is, to numerically model for the first time, the transport and sorting of different sediment sizes in the swash zone of a beach, and thereby to gain considerable physical insight into the process. This will provide us with a better understanding of the dynamics of the so-called mixed beaches, as well as a better modelling of their behaviour under a given swash flow. In the next Chapter a thorough literature review of the numerical modelling of the transport of sediments in the swash zone is detailed, as well as relevant work carried out using the one layer theory (active layer theory) in both, coastal and river environments. In Chapter 3, the derivation of the equations governing the flow, bed level change and volume fraction evolution (sorting equation) is presented. The model is tested for the case in which a sand dune composed by two different sediment fractions is subjected to a constant current in Chapter 4. In Chapter 5 the model is tested for one of the type of swash flow: the swash event caused by a breaking wave (collapsing bore) with the aid of the solution derived by Shen and Meyer (1963a). Chapter 6 presents the application of the

model to simulate the transport and sorting of sediments due to a very different swash event: the non-breaking wave swash event. In Chapter 7 an attempt to obtain realistic values for the most crucial parameters in the model, and its implementation into the model to both of the swash event types is detailed there. Finally, conclusions derived from this work together with some future lines of investigation that could improve the modelling of different sediment fractions in the swash zone are presented in Chapter 8.

Chapter 2

Literature Review

2.1 Sediment transport in the Swash Zone

2.1.1 Forcing Conditions

There have been two major reviews in the field of sediment transport in the swash zone (Bakhtyar et al., 2009; Masselink and Puleo, 2006), and both agreed on the crucial importance of the definition of the forcing mechanisms responsible of the transport of sediments in the swash zone. It was pointed out that the hydrodynamic conditions in the inner surf zone are the most important influence determining forcing conditions in the swash zone.

Elfrink and Baldock (2002) and Masselink and Puleo (2006) identified, according to several theoretical, field and laboratory investigations reviewed, that there are two main

types of swash oscillations: high- and low-frequency swash motions, the first one being produced by the collapse of high-frequency bores (breaking waves) on the beachface and the second produced by low-frequency motions like non-breaking waves. It has been well established that the type of swash motion depends on the incident wave conditions and the beach morphology (Masselink and Puleo, 2006; Elfrink and Baldock, 2002), and that it can be calculated by the surf similarity parameter ξ_b (see eq.(6.1)) or Iribarren number (Iribarren and Nogales, 1949; Battjes, 1974; Guza and Inman, 1975). For natural beaches values of $\xi_b > 2.0$ indicate that the swash is characterised by low-frequency non-breaking wave motion and for values of $\xi_b < 2.0$ indicates swash dominated by incident breaking waves. In this research we are interested mainly in relatively steep beaches, on which wind waves either do not break or collapse just before they reach the shore.

For the case where the waves do not break (standing wave) Carrier and Greenspan (1958) developed an analytical solution to describe the smooth water motion on a plane sloping beach. Some authors have applied this solution to describe the run-up of a solitary wave or standing long waves like the surf beat forced by the breaking of groups of waves (e.g. Baldock and Huntley (2002)). Another application of the standing wave solution is to non-breaking tsunami waves reaching the shore (Carrier et al., 2003), and the run-up caused by non-breaking solitary waves (Synolakis, 1987; Jensen et al., 2003).

When the waves do break, the swash motion is very different in terms of flow depth and velocity. For this case Shen and Meyer (1963b) derived an analytical solution for the swash motion produced by the action of a single bore on a plane beach. Several

investigations have applied this solution resulting in overall good modelling of shoreline motion (Hughes, 1992; Baldock and Holmes, 1999), overtopping flows (Peregrine and Williams, 2001), sediment transport and morphodynamics (Pritchard and Hogg, 2005; Kelly and Dodd, 2010; Zhu et al., 2012); and it is still used as a standard description of the breaking wave swash event.

2.1.2 Field evidence, laboratory experiments and modelling

Horn and Mason (1994) performed field experiments on four beaches (with beach slopes around $0.06^o - 6^o$) in the UK using sediment traps to measure both suspended and bedload ($D_{50} = 0.0002 - 0.0005$ m) during the uprush and backwash of waves ($H = 0.2 - 1.12$ m and $T = 3 - 6$ s). It was concluded from their results that generally the transport of sediments during the uprush phase of the swash was a mixture of bedload and suspended load, and during the backwash phase bedload was found to be the dominant transport mode.

Motivated by the need for information to develop numerical morphodynamical models Hughes et al. (1997) carried out field experiments to obtain measurements of flow velocity and and total sediment load in the swash zone of a steep beach ($\tan\theta = 0.14$) composed of medium-coarse sand ($D_{50} = 0.0005$ m), over which swell waves ($H = 0.4 - 0.5$ m and $T = 10 - 12$ s) were acting. Their results showed that the total load rate in the uprush of the swash displayed a strong correlation with flow velocity cubed; and that in their case sediment transport occurred under sheet flow conditions.

Masselink and Hughes (1998) obtained concurrent measurements of swash flow and sediment transport on a natural beach in order to develop the means to predict sediment transport in the swash zone. The sediment load showed a strong relationship with the time-averaged velocity cubed, consistent with equations for bedload and total load transport under sheet flow, which is in correspondace with Hughes et al. (1997).

With the objective of identifying the processes responsible for onshore transport associated with changes in the velocity (from offshore to onshore) and the offshore transport associated with large, low-frequency backwashes, Butt and Russell (1999) performed field measurements of suspended sediment concentration, velocity and sediment fluxes over the swash zone of a high-energy macrotidal beach. Their results showed that the mechanism responsible for the onshore transport was sediment brought into suspension by the interaction between the uprush and backwash; and that the mechanism responsible for offshore transport was the fast moving backwash.

A numerical model based on the depth-integrated sediment continuity equation including sediment suspension generated by the turbulence caused by wave breaking, sediment storage in the water column, advection of sediment by waves and currents, and settling of sediment on a mobile bed was developed by Kobayashi and Johnson (2001). They used an uncoupled approach in which the changes in bed level do not influence the hydrodynamics. Comparing their results with three large-scale laboratory experiments (accretional, erosional and neutral beach profile changes); they predicted an intense suspension of sediment under the steep front of breaking waves and less but persistent suspension in the rest of the swash. They found difficulty in predicting accurately the

net cross-shore sediment transport because it is a small difference between the onshore and off-shore transport rates. The predicted profile changes agreed with the measured ones although details of the beach profile could not be predicted.

Masselink et al. (2005) reported field measurements of water depth, flow velocity and suspended sediment concentration across the swash and inner surf zones of a dissipative beach. The main conclusions reached after the analysis of their results were: 1) suspended sediment concentrations and transport rates in the swash zone were greater than in the inner surf zone; 2) bed friction during uprush was significantly bigger than that in the backwash; 3) suspended sediment concentrations measured at the beginning and end of the backwash were around 100 kg/m^3 (i.e. a volumetric concentration of ≈ 0.04); and 4) the uprush phase induced a larger suspended sediment transport rate than the backwash.

In order to investigate the relative relevance of bore collapse at the base of the swash zone and the shear stress during the uprush on sediment transport, Jackson et al. (2004) used field data (uprush sediment load and properties of sediment in transport, i.e. settling velocity and grain size) measured on the uprush of several swash events over the steep beachface of a dissipative beach. From the analysis of the spatial variation in sediment load and grain size they concluded that there are two principal mechanisms responsible for the entrainment and transport of sediments in the uprush: the entrainment of sediment by the collapse of a bore seaward of the base of the swash zone and the subsequent transport of this sediment by the uprush; and the entrainment and transport of sediment by the local shear stress during the uprush of the wave. They found as well that at the

first stages of the swash event, when sediment is being transported mainly as suspension, the first mechanism will be more significant; whereas at later stages the second mechanism will tend to dominate because sediment is being transported mainly as sheet flow.

Motivated by the numerical study of Kobayashi and Johnson (2001) and the experimental findings of Jackson et al. (2004), Pritchard and Hogg (2005) carried out an analytical study of the suspended sediment under a swash event considering separately the effects of sediment entrainment by the bore collapse and the lag effects, using a decoupled approach. They used the model of Shen and Meyer (1963b) to solve the hydrodynamics of the swash and a depth-integrated transport equation for suspended sediment to test two different scenarios. The two cases were: steady state transport in which the bore entrained and advected sediment when the lag effects are not considered and a total load description is assumed; and a non-steady state where both bore-entrained sediment and lag effects are considered. They provided an easily reproduced prediction of suspended sediment transport and showed that the swash event may lead to net onshore sediment transport likely to be dominated by the onshore transport of pre-suspended sediment by the bore collapse. It was concluded from their results that the fine sediment load is significantly different from the one predicted by the quasi-steady (total load) approach because of the lag effect, while for coarser sediments this effect was less apparent. They found as well that for coarse sediment the onshore transport of presuspended sediment and the offshore transport by the backwash are more effective than that for the fine sediment. One of the most applicable outcomes of this model is that it could provide an estimate of how erosion or deposition are related to the amount of sediment initially entrained by the bore collapse.

More recently Alsina et al. (2009) performed laboratory experiments to quantify the pre-suspended sediment during wave breaking and the subsequent transport to the swash zone, and to measure how sediment is distributed within the beachface after a swash event caused by a solitary wave. They developed as well a Eulerian-Lagrangian numerical model, based on Alsina et al. (2005), to simulate the bore turbulence, entrainment and transport of sediment. Their results showed that the majority of the sediment entrained by the collapse of the bore is picked up from an area near the the shoreline and is advected to the swash zone. Their model predicted with reasonable accuracy the amount of sediment entrained by the bore collpase and the cross-shore distribution of the sediment load resulting from the advection and settling.

Kelly and Dodd (2010) developed a fully coupled morphodynamic model in which only bedload is considered. The model uses the specified time interval (STI) method of characteristics (MOC) and is used to simulate a single swash event due to a collapsing bore and the resulting bed evolution. Net erosion was observed over the whole swash zone, in agreement with simulations done by Pritchard and Hogg (2005); although net erosion and maximum run-up were considerable reduced in the coupled model.

We can see that sediment transport and beachface evolution using bed- or total load and suspended load has been examined by many authors although there is still some uncertainty of the predominance of bed- or suspended load, and sometimes, even the possibility that both have great importance for simulations in the swash zone. As mentioned before, this research is mainly focused on steep beaches which are generally

composed of mixed coarse sediments, so it seems reasonable to use a bed- or total load sediment transport formula. It is also clear that no one has looked at the sorting of sediments in the swash zone, so a review of the numerical modelling of sorting in other coastal environments is done in the following section.

2.2 Numerical Modelling of Sorting in Coastal Environments

The first two attempts to explain the relationship between the morphology and the hydrodynamics of a beach including sediment variation, sediment sorting processes and the resulting shore-normal distribution of sediments were the null-point hypothesis and the asymmetrical threshold hypothesis.

The null-point hypothesis proposed by Cornaglia (1889) states that for every grain size there is a point (depth) at which the onshore flows induced by waves and the offshore force caused by the downslope component of gravity perfectly balanced each other. This theory was mathematically developed and tested with laboratory and field experiments by Ippen and Eaglenson (1955), Eaglenson and Dean (1959), Eaglenson and Dean (1961), Eaglenson et al. (1961), Eaglenson et al. (1963), Miller and Zeigler (1958) and Miller and Zeigler (1964). This theory suggested that in a given sediment sample with a wide distribution of grain sizes there will be just one grain size at the predicted point (null-point) and all finer grains will move onshore while the coarser grains will move offshore. Laboratory and field experiments carried out later showed the null-point

hypothesis predictions were incorrect (Johnson, 1919; Bagnold, 1940; Zenkovitch, 1946 and Murray, 1967).

The other early theory was based on observations of the orbital motion of waves and its asymmetrical nature. It is called the asymmetrical threshold hypothesis and was first proposed by Cornish (1898) and further developed by Bagnold (1940), Inman (1949), King (1972) and Carter (1988). This asymmetry consists of having high velocity and short duration of the onshore motion and low velocity and longer duration of the offshore motion. The theory states that the higher velocities in the onshore direction are capable of initiating motion of both small and large sediments, and that the lower velocities in the offshore motion will only be capable of moving the smaller particles, favouring the onshore transport of large grains and the relative offshore motion of small sediments.

Horn (1992a) and Horn (1992b) developed a numerical model to simulate the shore-normal sediment size variation in the nearshore, testing the asymmetrical-threshold-under waves hypothesis. The model makes a number of assumptions: the main sediment transport mode is bedload, the driving hydrodynamics are monochromatic waves approaching the beach normally, it assumes an almost horizontal plane bed so it does not take into account bedforms (e.g. ripples) and the along-shore sediment transport is neglected so the beach profile changes just in the shore-normal direction. The model starts from deep water conditions (wave period T, wave height H_0) and calculates the local wavelength and wave celerity for each depth using linear theory. Then the local wave parameters are calculated using the solution of Nielsen (1982) for wave height attenuation due to bed friction, the empirical equation of Madsen (1976) for the breaking wave

height and after breaking the saturation model of Thornton and Guza (1982) for local wave height. Using this local parameters, then the peak nearbed offshore and onshore velocities are calculated with Stokes' second order wave theory. Then the threshold grain size for offshore and onshore peak flows is calculated using the Komar and Miller (1975) equation. The model assumes that the sediment size on the beach profile is in equilibrium and that grain size is the one just at the threshold of movement for the flow velocity due to waves at that location; so a spatial variation of these thresholds grain sizes is predicted by the model as a final result. The predictions of the model were compared with samples taken along the beach profile of 5 different beaches and the agreement found was not good. The difference between the predicted and measured sediment sizes varied over several orders of magnitude, particularly in shallow water; and it was pointed out by Horn (1992a) that a model based on swash/backwash processes was needed in order to improve the simulation of grain size variation. It was finally concluded by Horn (1992b) that even improving the predictability of the model it would not explain sediment sorting on a real beach because the assumption made in the asymmetrical threshold hypothesis, that only one grain size could be in equilibrium at each position of the profile, means that the model does not allow the slope and forces therein to change and affect the grain motion. So it was noted that a better approach for modelling size variation would be one with a dynamic sediment transport model rather that an equilibrium model.

Motivated by the field measurements presented by Liu and Zarillo (1989) of the grain size distributions across the shoreface of a beach; Liu and Zarillo (1993) developed a model to simulate the presented grain size distributions assuming that they are the product of

the differential response of the sediments on the surface to the agitation and transport by wave hydrodynamics. Using a nearshore wave and circulation model based on linear wave theory for shoaling waves and wave-induced currents (Ebersole and Dalrymple, 1979;Kirby and Dalrymple, 1982), three monochromatic wave climates were calculated: average condition, ocean swell and wind storm. The sediment transport is calculated using an empirical formulation based on flume experiments by Sunamura et al. (1978) indicating that the sediment movement under the action of waves is a function of the hydraulic properties of the sediment and the shoaling wave field. Then these sediment transport calculations are converted to probability parameters since the distribution of grain sizes is a probability parameter. The introduced parameters are: the entrainment index, which is related to the probability of movement of each grain size; and the retention index, which is related to the probability of retention of each grain size on the shoreface. Their results comparing the observed cross-shore patterns of size variation over the shoreface and the simulated by their model showed very little agreement. The reason attributed to the poor agreement was that although shoaling waves are the principal process affecting the movement of sediments on the upper shoreface, ignoring the effect of secondary or even tertiary processes (e.g. wave groups, long period oscillations) would definitely lead to inaccuracies of the simulated distribution patterns.

Foti and Blondeaux (1995) carried out flume experiments with mixtures of sands and developed a theoretical analysis in order to investigate the formation of sea ripples under oscillatory flow when the bed is composed of a mixture of sands. The principle objective of this research was to get quantitative data about the influence of graded sediments on the formation of the ripples and to gain more insight into the sorting process taking

place over the bedform under sea waves. The model used a modified Grass type formula taking into account the 'hiding' effect, by which the smaller sediment grains are protected by larger ones from the flow, to calculate the sediment transport. It seems that this research was the first one to apply the model described by Hirano (1971) (to calculate the variation of volume fraction per sediment class) in sea-beach problems. The theoretical analysis ends up with two analytical expressions to calculate the time development of the ripple amplitude and the distribution of grain sizes. From the experiments it was concluded that when a mixture of sediments is present this tends to stabilise the bed and delay the appearance of the ripples, and that the bedforms that are present are characterised by a longer wavelength than those in the uniform case. It was also quantified that due to the grain sorting process coarse sediments accumulate along the crest of the ripples and fine grains in the troughs. The comparison between the theoretical analysis and the experiments showed good qualitave agreement although some quantitative discrepancy was present. The reason for this discrepancy could be attributed to errors in the experimental data, the usage of a simple turbulence closure model and the lack of detailed knowledge of the sediment motion.

To study the effects of the selective sediment transport on the cross-shore bed composition and bed level changes Van Rijn (1997) developed a numerical model. The model takes into account wave propagation and longshore currents. Waves propagate till the breaking point and then wave decay is modelled by an energy dissipation method. Wave-induced set-up and set-down are modelled as well as the longshore currents associated with wave breaking. The sediment transport rate is obtained by summing the bedload and suspended load components. The bedload component is calculated by a formula-

type approach whereas the suspended load component is divided into current-related (time-averaged current velocities) and wave-related (cross-shore orbital motion) components. In order to investigate the effects of the bed composition in the cross-shore transport the bed is divided into a number of size fractions for which the sand transport rate is computed, with a correction factor to account for the effects of the non-uniformity. The bed level changes per fraction are obtained using the one-layer approach given by Hirano (1971). Sensitivity computations were performed to analyse the behaviour of the model, one looking for the effect on the sediment transport in constant depth using a single and a multi-wave approach; another comparing the calculated sediment transport in constant taking into account both, a single fraction and a multiple fraction. Another set of computations were made in order to compare the sand transport rates across the surf zone using the single/multi-wave and the single/multi-sand fraction approaches. One final computation was performed to investigate the effect of the selective transport of grain sizes on the cross-shore bed composition and bed level changes. Van Rijn (1998) compared the results given by this model with flume and field data. The model was used to simulate the behaviour of a nearshore bar at Egmond, The Netherlands and it was applied to the cross-shore profile data measured at the Duck Beach, USA. In the laboratory the model was used to compute the cross-shore distribution of the longshore transport rate in a sand-gravel bed; and finally it was applied to evaluate the behaviour of a shoreface nourishment on a sloping profile. The general conclusions of this work were that most important parameters were the undertow velocity, bed roughness, wave-related suspended transport and sand composition. Wider and flatter bars were obtained when a graded sediment was present. Coarser grains were transported shorewards as bedload and finer sediments were carried seawards as suspended load, being deposited

at the bar troughs and coarse sediment eroded from outer bars is transported landwards to the swash zone during storms.

Based on the model introduced by Calvete et al. (2001) and motivated by field measurements, Walgreen et al. (2003) developed a model to study the mechanisms that could cause the observed pattern of sediment distribution and the influence of grain sorting on temporal and spatial characteristics of shoreface-connected ridges. The water motion in the model is calculated by the 2D shallow water equations and the quasi-steady approximation is used because the hydrodynamic timescale is much smaller than the timescale of the bed evolution. The sediment mixture is split into grain classes and the sediment transport and volume fraction evolution are calculated for each of the grain sizes. Sediment transport rate is considered to be the sum of the bedload and the suspended load components, each affected by a 'hiding' function to take into account non-uniformity of the sediment. The grain size distribution evolution is modeled using the one layer theory (Hirano, 1971; Ribberink, 1987). A linear stability method is applied in order to simulate the evolution of a shoreface-connected ridge driven by a storm and it was concluded from the results that, as observed in many flume experiments, sediment sorting has a stabilising effect on the growth of bedforms; the model appears to be in good agreement with observed grain size distributions over shoreface-connected ridges which showed that finer sediments are located on the downcurrent flank of the ridges and coarser grains on the upcurrent flank; and finally the observed sorting patterns over the ridges were reasonably well reproduced by the model.

Walgreen et al. (2004) modified the model by Walgreen et al. (2003) in order to inves-

tigate and quantify the effect of graded sediment on the formation of tidal sand waves. The modifications made to Walgreen et al. (2003) model are that the dominant forcing is by tides and that in this case suspended load is neglected. The two main objectives of their investigation were to gain knowledge of the physical mechanisms driving the observed grain size distributions over tidal sand waves; and to study how sorting of sediments affects the temporal and spatial characteristics of the sand waves. A sensitivity analysis was performed to investigate the role of grain size distribution (uniform sediment and different bimodal mixtures) and the hiding coefficient in the sediment transport capacity. Simulations driven by symmetric and asymmetric tides were performed and a comparison with field measurements was presented. The results revealed that the forcing conditions are of great importance; when a symmetric tide is used the grain size distribution is in phase with the sand wave topography and the coarser grains where located at the crest; whereas when an asymmetric tide is considered (or a current is added) a shift between the topography of the sand wave and the grain size pattern is introduced, leaving the coarse sand in the onshore flank. The model results are in reasonable good agreement with field data of offshore tidal sand waves. A similar work was performed by Roos et al. (2007) based on the work by Van den Berg and Van Damme (2005) arriving to very close conclusions.

In order to simulate the cross-shore sediment transport and bed topography changes in a beach composed of fine and coarse sand, Arimitsu and Deguchi (2007) extended the SBEACH model by Larson and Krauss (1989) to take into account the different sediment sizes. Sediment transport rates for each grain size are calculated based on the assumption that the beach is uniformly composed of that grain size and bed changes

are obtained using the concept that the total sediment transport rate is the weighted sum of the product of the transport rate and the volume fraction available for each grain size. The volume fraction is calculated by conservation of mass of bed material of each grain size (one layer theory, Hirano (1971)). Flume experiments and simulations were compared in which several combination of proportions of fine and coarse sediments were used, including the cases with uniform fine and uniform coarse sediment. Simulations showed same tendency as measurements in the experiment regarding the type of beach profile, it was noted that the beach profile depends on the initial proportion of coarse sand; an erosive profile was formed when a small proportion of coarse sand was present whereas an accretionary profile formed when having a large proportion of coarse grains. The model was unable to reproduce a bar formed in the experiments just after the breaking point. The volume fraction measured in the experiments showed that the coarse sediment gathered near the shoreline and finer sediment accumulated in the offshore region, this was roughly reproduced by the model. The measured volume fraction of coarse grains fluctuated significantly in the cross-shore direction while the simulated coarse volume fraction of the model was smooth. It was noted in their conclusions that an improvement in the simulation of the swash zone processes would lead to a better agreement between experiments and simulations.

De Swart et al. (2008) developed a model combining those of Calvete et al. (2001) and Walgreen et al. (2003) with two principle objectives: to study the effect of grain sorting on the evolution of shoreface-connected ridges and to demonstrate how shoreface-connected ridges respond to large-scale interventions (e.g. coastal defence structures, dredging channels). This approach differs from Walgreen et al. (2003) in that, along

with the linear stability analysis, a nonlinear analysis (Walgreen, 2003; Calvete and Swart, 2003) is introduced to solve the system. In general the results given by this model showed that the long-term evolution of shoreface-connected ridges and the variation of grain size can be simulated adequately with a nonlinear process-based model. The nonlinear effects caused a reduction in the growth of the height of the ridges which tended to a constant value; the same behaviour was present in the maximum variation of mean grain size; these findings are in agreement with other studies (e.g. Roos et al. (2004), Garnier et al. (2006)). The results were extrapolated to realistic values in order to compare with field data from the inner shelf of Long Island; the values were in good agreement. The model was also used to study the impact of large-scale interventions on shoreface-connected ridges and it was found that the system adjusts to the original equilibrium state. Some discrepancy is found with field data in the sense that including the nonlinear evolution provoked that the finer sediment was located almost at the crest of the ridges.

It can be concluded form this review that the active layer theory has been used successfully to study the influence of different grain sizes on the morphodynamics of some coastal environments, therefore it seems reasonable to consider it a good option to being applied on the study of sorting of sediments in the swash zone.

2.3 Active Layer

2.3.1 Concept

The active layer model was initially developed by Hirano (1970), Hirano (1971) and Hirano (1972) to study the process of armouring in river beds, i.e., the coarsening of sediments on the bed. As the concept of the active layer theory was thought to perform morphological simulations with non-uniform sediments, this theory divides the sediment mixture into different size fractions to which the sediment conservation equation is applied taking into account that each sediment fraction is present in the mixture in a certain percentage (i.e. volume fraction). It is therefore necessary, to characterise the mixture available for transportation, to divide the sediment column into two different layers: the active layer of thickness L_a in which each fraction has its own volume fration P_{ia} and, underneath, a substrate layer with upper boundary B_s and where, like in the active layer, each sediment fraction has a certain volume fraction P_{is}. Two important assumptions made by the active layer theory are: it is considered that no sediment transport occurs between the active layer and the substrate layer; and the sediment fractions in the active layer are available to be transported in the same extent.

2.3.2 Applications

Based on the active layer concept, Armanini and Di Silvio (1988) developed a one-dimensional numerical model to investigate the sediment transport of mixtures in non-equilibrium conditions. They took into account the suspended and bedload components of sediment transport and tested their model for short- (e.g. flood carrying a large

amount of suspended load conveyed to the stream by landslides) and long term simulations (e.g. prediction of the effects of a construction over the period of many years). The model managed to explain the difference between the results given when the bed is considered being composed by two fractions and those given when combined fractions were used in equilibrium conditions. It was noted that for this model there was no need to distinguish between bedload and suspended load since theory provided simplified equation including both.

Hsu and Holly (1992) used the active layer concept to propose a model to simulate the transport of sediment mixtures in which the transported gradation (transport of different sediment sizes) is calculated using the concept of joint probability. In their approach they used the relative mobility of each particular grain size and the availability of them on the bed surface instead of using a hiding or exposure factor correction. They used a set of flume experiments to validate the model, measuring water surface, bed level changes, total bedload output, composition of the bedload and the spatial variation of bed surface material. It was found that the proposed method successfully simulates the experiments with non-uniform sediment in non-equilibrium conditions.

In order to investigate the effect of size gradation in the sediment on the development of alternate river bars, Lanzoni and Tubino (1999) proposed a two-dimensional model. The model uses the active layer concept and the bedload relation proposed by Parker (1990) within the framework of linear stability analysis. The principle output of this approach is that an analytical solution is given for the equations governing the growth of perturbations of the bottom and the grain size distribution. The theoretical results

suggested a significant reduction of bar instability (growth rate and migration speed of bars) is due to heterogeneity of the sediment mixture, while the wavelength of the bar is shortened compared to the uniform sediment case.

Hunzinker and Jaeggi (2002) used the active layer concept to develop a fractionwise sediment transport calculation procedure to describe the dominant processes of grain sorting in armouring rivers. The method was tested against several semi-mobile armour (flow conditions just above the threshold of motion) tests reported in the literature and the results showed that given the simulated conditions (flow range) a inevitably fining of the moving sediment compared with the bed material is found; showing good agreement with experimental results.

More recently Tritthart et al. (2011) developed a numerical sediment transport model, based on the active layer concept, capable of solving the grain size distribution of uniform and non-uniform sediments in a river flow. The model uses the three-dimensional Reynolds-averaged Navier-Stokes equations to simulate the hydrodynamics, and takes into account just the bedload component of the sediment with the effect of bed slope. The flume experiments used to validate the model were: a) unsteady flow in a channel bend and b) steady flow in a flume with lateral contraction. The model was successfully validated with data from the two laboratory tests and it was found generally capable of computing bed and size changes in good agreement with measurements in the experiments.

Just a handful of the research in river contexts have been reviewed in this section, but

it was found that the active layer has been successfully used in many other river applications like evolution of river bed armouring (Parker and Sutherland, 1990), sediment sorting in bends (Parker and Andrews, 1985); gravel sheets (Seminara et al., 1996), roughness streaks (Colombini and Parker, 1995) and longitudinal sorting (Cui et al., 1996).

In beaches, as we already mentioned, it has been applied to look at the formation of ripples (Foti and Blondeaux, 1995), evolution of shoreface-connected ridges (Walgreen et al., 2003; De Swart et al., 2008; Van Oyen et al., 2011) and in the formation tidal sand waves (Walgreen et al., 2004; Van Oyen and Blondeaux, 2009).

As it can be seen from this review a remarkable amount of work has been done in the last decades using the active layer concept in river contexts whereas in beaches very little research has been performed. The active layer theory has been successfully applied in river and some coastal environments giving reasonably good results. Since this research attempts to investigate and simulate the sorting of sediments in the swash zone for the first time, the simplycity of the active layer theory makes it a reasonably good approach to take, without bearing in mind that the swash is a highly unsteady region compared to those river and coastal environments.

Chapter 3

Mathematical Model

As already mentioned, the principal aim of this research is to develop a numerical model in order to simulate the transport and sorting of different sediment fractions in the swash zone of a beach, and with this gain physical insight into the process leading to a better prediction of beach behaviour.

In this chapter the description and derivation of the equations, the assumptions made and the formulae used in this research to develop the numerical model are presented.

The model consists of hydrodynamic and morphodynamic modules. The hydrodynamic part, as this work is focused in the swash zone, is governed by the so-called (depth averaged) shallow water equations and the morphodynamics are based on the equations of conservation of sediment (for the whole mixture) or Exner equation, along with con-

servation of sediment for each sediment fraction present in the mixture hereafter the sorting equation.

3.1 Governing equations

3.1.1 Shallow Water Equations

It has been shown by many researchers worldwide that water motion in the swash zone can be accurately reproduced using the so-called long-wave or shallow-water equations (SWE). The SWE can be derived from the mass conservation equation and the Euler equations only using some simplifying assumptions (see e.g. Toro (2001), Mei (1990)). The assumptions are that the fluid is considered incompressible, which means that there is no variation in the density of the fluid; the fluid is irrotational (no vorticity) and vertical accelerations in the fluid are negligible (i.e. the pressure gradient is hydrostatic).

The assumption of negligible vertical accelerations in the fluid implies that

$$\frac{\partial p}{\partial z} = -\rho g \tag{3.1}$$

where p is the pressure, z is the vertical coordinate (see Figure 3.1), ρ is the fluid density and g is the acceleration of gravity. Assuming that $p(x, z, t)|_{z=\eta(x)}$ = atmospheric pressure = 0 and integrating (3.1)

$$p = \rho g(\eta - z) \tag{3.2}$$

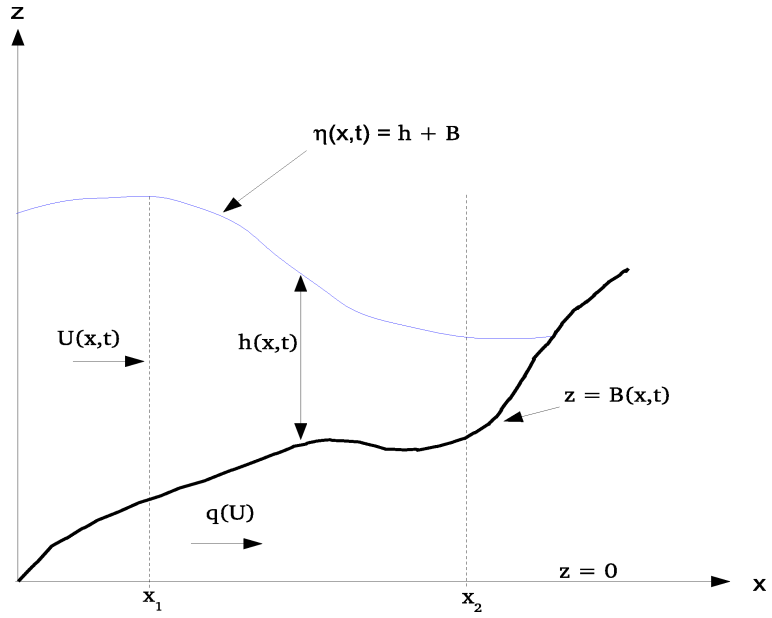

Figure 3.1: Definition sketch for the swash zone

and differentiating (3.2) with respect to x

$$\frac{\partial p}{\partial x} = \rho g \frac{\partial \eta}{\partial x}. \tag{3.3}$$

From this it is concluded that $\frac{\partial p}{\partial x}$ is independent of z and thus the x component of the acceleration $\frac{du}{dt}$ is independent of z. Hence, the x velocity component u is also independent of z, which means that $\frac{\partial u}{\partial z} = 0$.

Now, based on Figure 3.1 and on the assumptions made above, the derivation of the SWE is as follows.

To derive the continuity equation we start from the mass conservation equation, taking

into account that the fluid is incompressible and that the derivation is made over the $x - z$ plane, the equation can be written as

$$\frac{\partial u}{\partial x} + \frac{\partial w}{\partial z} = 0. \tag{3.4}$$

Integrating (3.4) with respect to z, between $z = B(x,t)$ (bottom) and $z = \eta(x,t)$ (free surface)

$$\int_B^\eta \frac{\partial u}{\partial x} dz + \int_B^\eta \frac{\partial w}{\partial z} dz = 0 \qquad \Rightarrow \qquad \int_B^\eta \frac{\partial u}{\partial x} dz + w|_{z=\eta} - w|_{z=B} = 0. \tag{3.5}$$

Defining the bed and the free surface functions respectively as

$$z = B(x,t) \tag{3.6}$$

and

$$z = \eta(x,t) \equiv B(x,t) + h(x,t) \tag{3.7}$$

then, using (3.6) we obtain

$$w|_{z=B} = \frac{dz}{dt}|_{z=B} = \frac{\partial B}{\partial t} + \frac{\partial x}{\partial t}\frac{\partial B}{\partial x}|_{z=B} \Rightarrow w|_{z=B} = \frac{\partial B}{\partial t} + u\frac{\partial B}{\partial x}|_{z=B} \tag{3.8}$$

and using (3.7)

$$w|_{z=\eta} = \frac{dz}{dt}|_{z=\eta} = \frac{\partial \eta}{\partial t} + \frac{\partial x}{\partial t}\frac{\partial \eta}{\partial x}|_{z=\eta} \Rightarrow w|_{z=\eta} = \frac{\partial \eta}{\partial t} + u\frac{\partial \eta}{\partial x}|_{z=\eta}. \tag{3.9}$$

Substituting (3.9) and (3.8) into (3.5)

$$(\frac{\partial \eta}{\partial t} + u\frac{\partial \eta}{\partial x})|_{z=\eta} - \frac{\partial B}{\partial t} - u\frac{\partial B}{\partial x}|_{z=B} + \int_B^\eta \frac{\partial u}{\partial x}dz = 0 \tag{3.10}$$

and using Leibniz rule the last term can be simplified to

$$\int_B^\eta \frac{\partial u}{\partial x}dz = \frac{\partial}{\partial x}\int_B^\eta u dz - u|_{z=\eta}\frac{\partial \eta}{\partial x} + u|_{z=B}\frac{\partial B}{\partial x}. \tag{3.11}$$

Substituting (3.11) into (3.10) and recalling that $\eta = B + h$ gives

$$\frac{\partial h}{\partial t} + \frac{\partial}{\partial x}\int_B^\eta u dz = 0. \tag{3.12}$$

Defining a depth averaged velocity as $U = \frac{1}{h}\int_B^\eta u dz$

$$\frac{\partial h}{\partial t} + \frac{\partial (Uh)}{\partial x} = 0. \tag{3.13}$$

Now the derivation of the momentum equation is done by depth-integrating the x-momentum equation

$$\frac{Du}{Dt} = -\frac{1}{\rho}\frac{\partial p}{\partial x}. \tag{3.14}$$

In order to do so we first multiply the mass conservation equation (3.4) by u and add it to the momentum equation (3.14) to get

$$\frac{\partial u}{\partial t} + \frac{\partial u^2}{\partial x} + \frac{\partial (uw)}{\partial z} = -\frac{1}{\rho}\frac{\partial p}{\partial x} \tag{3.15}$$

integrating over the depth

$$\int_B^\eta \Big(\frac{\partial u}{\partial t} + \frac{\partial u^2}{\partial x} + \frac{\partial (uw)}{\partial z}\Big) dz = -\frac{1}{\rho}\int_B^\eta \frac{\partial p}{\partial x} dz. \tag{3.16}$$

Solving the first three terms with the help of Leibniz formula

$$\int_B^\eta \frac{\partial u}{\partial t} dz = \frac{\partial}{\partial t}\int_B^\eta u dz - u|_{z=\eta}\frac{\partial \eta}{\partial t} + u|_{z=B}\frac{\partial B}{\partial t} \tag{3.17}$$

$$\int_B^\eta \frac{\partial u^2}{\partial x} dz = \frac{\partial}{\partial x}\int_B^\eta u^2 dz - u^2|_{z=\eta}\frac{\partial \eta}{\partial x} + u^2|_{z=B}\frac{\partial B}{\partial x} \tag{3.18}$$

$$\int_B^\eta \frac{\partial (uw)}{\partial z} dz = u|_{z=\eta} w|_{z=\eta} - u|_{z=B} w|_{z=B} \tag{3.19}$$

and for the term on the right hand-side, using (3.3),

$$\int_B^\eta \frac{\partial p}{\partial x} dz = \rho g \frac{\partial \eta}{\partial x} \int_B^\eta dz = \rho g h \frac{\partial \eta}{\partial x}. \tag{3.20}$$

Substituting (3.17), (3.18), (3.19) and (3.20) into (3.16) and recalling (3.8) and (3.9) gives

$$\frac{\partial}{\partial t} \int_B^\eta u dz + \frac{\partial}{\partial x} \int_B^\eta u^2 dz = -gh \frac{\partial \eta}{\partial x}. \tag{3.21}$$

Now, in this case to derive the depth averaged equation defining again the depth averaged velocity as $U = \frac{1}{h} \int_B^\eta u dz$,we have to treat carefully the term $\int_B^\eta u^2 dz$.

The rate of mass transfer through an infinitesimal area dA is $\rho dQ = \rho u dA$, and therefore the momentum transfer rate is $\rho u^2 dA$ (c.f. Akan (2006)). Integrating this over the area A, we obtain the momentum transfer rate through the section as

$$\text{rate of momentum transfer} = \rho \int_A u^2 dA. \tag{3.22}$$

The momentum transfer is often express in terms of the average cross-sectional velocity U as

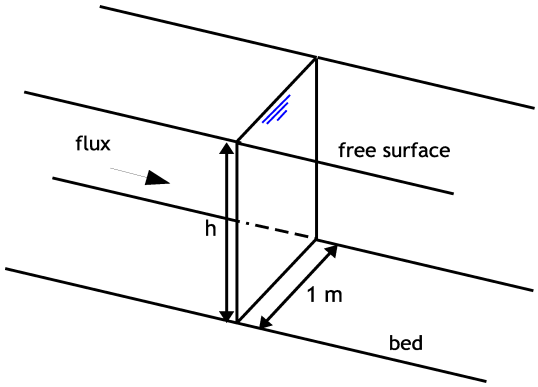

Figure 3.2: Definition in our case of the area (A)

$$\text{rate of momentum transfer} = \beta\rho U^2 A = \beta\rho QU \tag{3.23}$$

where β = momentum coefficient (or momentum correction coefficient) introduced to account for the non-uniform velocity distribution.

Then equating (3.22) and (3.23),

$$\beta = \frac{\int_A u^2 dA}{U^2 A}, \tag{3.24}$$

where, in our case,$A = h \times 1m$ width nominally (see figure 3.2) and $dA = dz$, substituting this into (3.24),

$$\beta U^2 h = \int_B^\eta u^2 dz. \tag{3.25}$$

Substituting (3.25) into (3.21) we obtain

$$\frac{\partial(Uh)}{\partial t} + \frac{\partial(\beta U^2 h)}{\partial x} = -gh\frac{\partial h}{\partial x} - gh\frac{\partial B}{\partial x} \tag{3.26}$$

for regular channels β is often set equal to 1.0, so finally

$$\frac{\partial(Uh)}{\partial t} + \frac{\partial(U^2 h)}{\partial x} = -gh\frac{\partial h}{\partial x} - gh\frac{\partial B}{\partial x}. \tag{3.27}$$

Applying the chain rule and using continuity equation (3.13), rearranging terms finally we get

$$\frac{\partial U}{\partial t} + U\frac{\partial U}{\partial x} + g\frac{\partial h}{\partial x} + g\frac{\partial B}{\partial x} = 0. \tag{3.28}$$

3.1.2 Sediment Conservation (Exner) Equation

To derive the Exner equation, a region x_1 to x_2 in our domain depicted in Figure 3.1 is to be defined, where $x_1 < x_2$ and state that the net sediment flux into the region must be equal to the rate of change of total mass in the region (mass conservation principle).

The total volume of sediment in the region is

$$\int_{x_1}^{x_2}\int_{0}^{B} dzdx = \int_{x_1}^{x_2} Bdx \tag{3.29}$$

so the rate of change of total mass in the region x_1 to x_2

$$\frac{d}{dt}\int_{x_1}^{x_2} B dx. \tag{3.30}$$

On the other hand, the total volume of sediment going into the region at x_1 is $\xi q|_{x_1}$ and the one going out of the region at x_2 is $\xi q|_{x_2}$ in which $\xi = \dfrac{1}{1-p_o}$, p_o is the porosity of the bed material and q is the volumetric sediment transport rate in the x, direction which is proportional to velocity of the fluid. So the net sediment flux into the region would be

$$\xi q|_{x_1} - \xi q|_{x_2}. \tag{3.31}$$

Using, as mentioned above the principle of mass conservation, combining (3.30) and (3.31) to get

$$\frac{d}{dt}\int_{x_1}^{x_2} B dx = \xi q|_{x_1} - \xi q|_{x_2} \tag{3.32}$$

$$\frac{d}{dt}\int_{x_1}^{x_2} B dx + \xi [q]_{x_1}^{x_2} = 0 \tag{3.33}$$

which is the integral form of the sediment conservation equation.

Integrating (3.33) with respect to time t over an interval $[t_1, t_2]$ in which $t_1 < t_2$ in order to obtain the differential form of the equation, we get

$$\int_{x_1}^{x_2} B(x, t_2)dx - \int_{x_1}^{x_2} B(x, t_1)dx + \xi \int_{t_1}^{t_2} [q]_{x_1}^{x_2} dt = 0. \tag{3.34}$$

and then using

$$B(x, t_2) - B(x, t_1) = \int_{t_1}^{t_2} \frac{\partial B}{\partial t} dt \qquad \text{and} \qquad [q]_{x_1}^{x_2} = \int_{x_1}^{x_2} \frac{\partial q}{\partial x} dx \tag{3.35}$$

we get

$$\int_{t_1}^{t_2} \int_{x_1}^{x_2} \left[\frac{\partial B}{\partial t} + \xi \frac{\partial q}{\partial x} \right] dx dt = 0. \tag{3.36}$$

Because x_1, x_2 and t_1, t_2 were defined arbitrarily the differential form of the sediment conservation equation can be written as

$$\frac{\partial B}{\partial t} + \xi \frac{\partial q}{\partial x} = 0. \tag{3.37}$$

3.1.3 Sorting Equation

The derivation of the sorting equation is based on the pioneering work by Ribberink (1987) and is as follows.

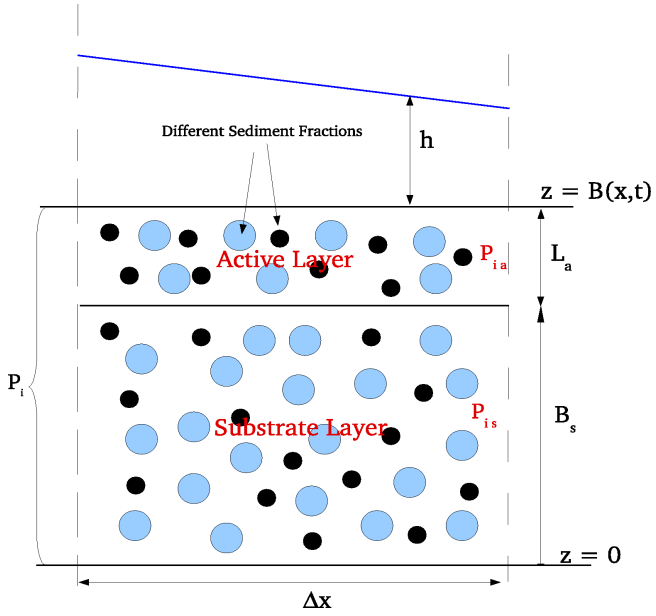

Figure 3.3: Sketch for the sediment column

Starting from the sediment conservation equation for the whole sediment mixture (3.37), suppose now that there are N sediment classes, corresponding to different grain sizes. If (3.37) is applied to each sediment class size becomes

$$\xi \frac{\partial q_i}{\partial x} + \frac{\partial (P_i B)}{\partial t} = 0 \tag{3.38}$$

where q_i is the sediment flux for i^{th} class, P_i is the average volume fraction of the i^{th} sediment class in the total sediment column. Thus

$$\sum_{i=1}^{N} P_i B = B \tag{3.39}$$

which implies that $\sum_{i=1}^{N} P_i = 1$ (where as before, N is the total number of sediment class sizes in the mixture).

In order to derive the sorting equation and adequately characterise the sediment being transported it is useful to split up the bed level into an active layer and a substrate layer based on the so-called one layer theory (see Hirano (1971)). Taking a sufficiently small element with size Δx from the domain depicted in Figure (3.1) and performing the aforementioned splitting of the bed level into: an active layer of thickness L_a, and a substrate layer with upper boundary level at $B_s(x,t)$, we arrive at the situation depicted in Figure (3.3) from which it can be stated that

$$B(x,t) = L_a(x,t) + B_s(x,t). \tag{3.40}$$

In general the two layers will have different compositions and they are related as (see Figure (3.3))

$$P_i B(x,t) = L_a(x,t) P_{ia} + B_s(x,t) P_{is} \tag{3.41}$$

where P_{ia} is the fraction of the i^{th} sediment class in the active layer and P_{is} is the fraction of the i^{th} sediment class in the substrate layer.

So, substituting (3.41) into (3.38)

$$\xi \frac{\partial q_i}{\partial x} + \frac{\partial (P_{ia} L_a)}{\partial t} + \frac{\partial (P_{is} B_s)}{\partial t} = 0 \tag{3.42}$$

and using the assumption that L_a is constant (see e.g. Walgreen et al. (2003), De Swart et al. (2008), Van Oyen et al. (2011)); considering that there is no exchange of sediment

between the active and the substrate layers (i.e. P_{is} is constant) and noting that $B_s = B - L_a$ we finally get

$$\xi \frac{\partial q_i}{\partial x} + L_a \frac{\partial P_{ia}}{\partial t} + P_{is} \frac{\partial B}{\partial t} = 0. \tag{3.43}$$

3.2 Sediment Transport Formula

Sediment transport in the swash zone has been an important research topic in recent decades but to date there is no agreement within the coastal engineering community on which is the dominant sediment motion mode (i.e. the way the sediment is transported) in the swash zone (Masselink and Puleo, 2006; Bakhtyar et al., 2009).

In the first attempts to study the sediment transport in the swash zone, either numerically or in the field, researchers showed that the main sediment transport mode could be either bedload or total load, specially during the backwash (see e.g. Horn and Mason (1994), Hughes et al. (1997), Masselink and Hughes (1998)), although they pointed out that suspendend sediment could play an important role at the first stages of the swash event.

On the other hand, more recently, researchers have shown that suspended sediment can also be the dominant sediment motion mode in the swash zone, especially during the uprush of the swash, due to the suspension of a considerable amount of sediment by the

collapse of the bore (wave breaking) (see e.g. Butt et al. (2004), Pritchard and Hogg (2005), Alsina et al. (2009)).

Butt and Russell (2000) stated that because of the nature of the swash zone the common practice of separating the sediment transport into bedload and suspended load is not applicable in this region.

From all the arguments expressed before it is clear that due to the highly variable nature of the swash (having bedload and suspended load even in the same swash event) the decision of what type of sediment motion is the appropriate to use in the swash zone is difficult. It seems to depend on specific characteristics of the site under study, mainly the type of flow and sediment characteristics. Therefore during this research a total load sediment motion was used for the transport in the swash.

It has been shown that a simple cubic velocity power-law formula based on the work of Grass (1981) for a total load sediment transport formulation is a reasonable approach to use within the swash context (see e.g. Masselink and Hughes (1998), Hsu and Raubenheimer (2006), Kelly and Dodd (2010)). For this reason during this research a total load approximation of this form is used following the work of Hudson and Sweby (2003) and Kelly (2009), which can be written as

$$q = Au^3 \tag{3.44}$$

in which A is a constant with dimensions $\frac{s^2}{m}$ and depends on the bed material and the

type of flow. Its value can be determined either empirically through field data available or numerically through the simplification of Van Rijn formula (see Hudson (2001)).

In this reseach, as it is focused on the transport of different sediment sizes, equation (3.44) has to be modified accordingly. Therefore

$$q = q_1 + q_2 + ... + q_N \tag{3.45}$$

and

$$q_i = P_{ia} A_i u^3 \tag{3.46}$$

in which the sediment mixture has been divided into N different sediment classes, each with a corresponding A_i value and P_{ia} volume fraction within the mixture.

3.3 Morphodynamic Module

The final form of the equations governing the morphodynamics (changes in bed and volume fraction) of the model is obtained as follows. First, it must be mentioned here that since the principal objective of this research is to develop a numerical model for studying the sediment transport of non-uniform sediment mixtures, it was decided for simplicity to take into account a sediment mixture composed by two different sediment classes (i.e. $N = 2$), with different diameter d_i and therefore different value of parameter A_i ($A_1 \neq A_2$). It was considered adequate, for the sake of clarity, to define $A_1 = A_f$ as

the fine sediment and $A_2 = A_c$ as the coarse. Using these assumptions (3.45) changes to

$$q = q_f + q_c \tag{3.47}$$

and (3.46) to

$$q_f = P_{fa} A_f U^3 \tag{3.48}$$

$$q_c = P_{ca} A_c U^3 \tag{3.49}$$

in which we have changed the instantaneous u for the depth-averaged U used in this research and where P_{fa} and P_{ca} are the volume fractions of the corresponding sediment (A_f, A_c) in the active layer, in which the condition $P_{fa} + P_{ca} = 1$ must be met.

Now substituting (3.47), (3.48) and (3.49) into (3.37) we get

$$\frac{\partial B}{\partial t} = -\xi(A_f - A_c)U^3 \frac{\partial P_{fa}}{\partial x} - \xi 3U^2(A_f P_{fa} - A_c P_{fa} + A_c)\frac{\partial U}{\partial x} \tag{3.50}$$

and using again (3.48) in (3.43)

$$\frac{\partial P_{fa}}{\partial t} = -\frac{\xi}{L_a}\left(A_f U^3 \frac{\partial P_{fa}}{\partial x} + A_f P_{fa} 3U^2 \frac{\partial U}{\partial x}\right) - \frac{P_{fs}}{L_a}\frac{\partial B}{\partial t} \tag{3.51}$$

and finally substituting (3.50) in (3.51) we get

$$\begin{aligned}\frac{\partial P_{fa}}{\partial t} &= \frac{\xi}{L_a}U^3(A_f P_{fs} - A_c P_{fs} - A_f)\frac{\partial P_{fa}}{\partial x} \\ &+ \frac{\xi}{L_a}3U^2(-A_f P_{fa} + A_f P_{fs} P_{fa} + A_c P_{fs} - A_c P_{fs} P_{fa})\frac{\partial U}{\partial x}. \qquad (3.52)\end{aligned}$$

Equations (3.50) and (3.52) are the governing equations of the morphodynamic module of the model.

Chapter 4

Sorting and Transport of a Non-uniform Sediment Sand Dune under a constant current

4.1 Introduction

As a first step in the development of the numerical model to simulate the transport of non-uniform sediments it was decided to test the model with a well-known morphodynamic case. The case consists of a sand dune (small perturbation of the bed) under the action of a uniform current, the dune is located in the middle of a channel and has an initial bathymetry given by

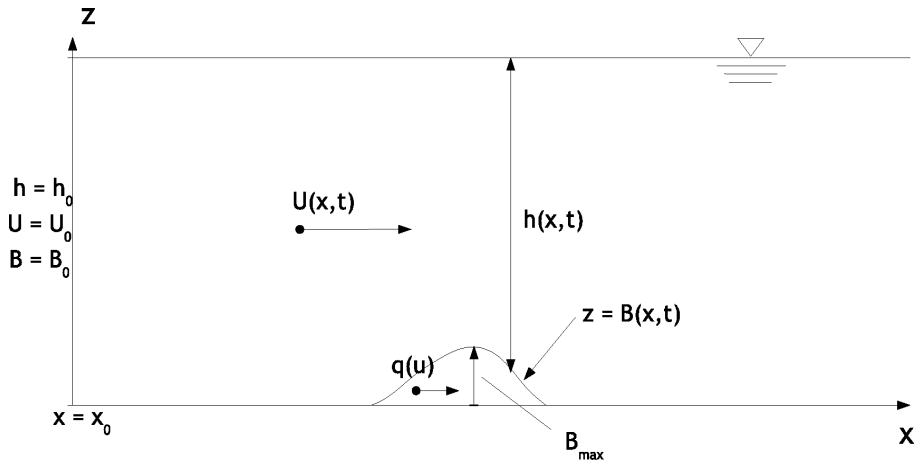

Figure 4.1: Sand dune in a channel

$$B(x,0) = \begin{cases} B_{max} \sin^2 \left\{ \frac{\pi(x-300)}{200} \right\} & \text{if } 300 \leq x \leq 500 \\ 0 & \text{otherwise} \end{cases} \tag{4.1}$$

where $B_{max} = 1$ m is the maximum height of the sand dune. The constant current is given by the upstream boundary conditions $Q_c = U_0 h_0$ in which $U_0 = 1$ m/s and $h_0 = 10$ m (see Figure 4.1). This conditions were chosen in order to compare the results given by our model with the solution given by Hudson (2001). The case is a generic one in coastal engineering modelling and, physically, it can be regarded as a sand wave under a tidal flow or a cross section through a shoreface nourishment under a tidal flow. This morphodynamic test case is very useful because, besides being simple, it has been used before by other authors to evaluate the behaviour of many numerical schemes because an approximate analytical solution exists (see e.g. Hudson and Sweby (2003), Hudson et al. (2005), Kelly and Dodd (2009), Briganti et al. (2011)).

4.2 Assumptions and corresponding Model Equations

In morphodynamics there are two different formulations that can be used for solving the governing equations of sediment transport: the quasi-steady and the unsteady approach. The basic difference between these two approaches is that the quasi-steady approach assumes that the flow is in an equilibrium state, which adjusts as the bed changes; in other words, the bed change happens very slowly compared with the changes in flow (e.g. surface waves), so that, viewed on the bed change timescale the flow has always already adjusted to the bed change and is in equilibrium (i.e. the wave speed of the sand dune is considerable smaller than the wave speed of the water flow). On the other hand in the unsteady approach there are no assumptions and the flow can be quasi-steady or unsteady, meaning that in this case the wave speed of the bed updating equation can be of similar magnitude than that in the water flow.

Cunge et al. (1980) discussed several research works based on the quasi-steady approach and they stated that for most of the cases, in fact, the bed moves with a much smaller wave speed than the water flow. Given the conditions of the problem taken into account in this morphodynamic case it seems reasonable to assume the quasi-steady approach.

Due to the difference in timescales of changes in the flow and bed we can assume the quasi-steady approach, this means that we can rewrite equation (3.13) as

$$\frac{\partial(hU)}{\partial x} = 0 \qquad \Rightarrow \qquad U(x,t)h(x,t) = Q_c \tag{4.2}$$

and (3.28) as

$$U\frac{\partial U}{\partial x} + g\frac{\partial(B+h)}{\partial x} = 0 \tag{4.3}$$

integrating over the whole domain (from x_0 to x) we get

$$\frac{1}{2}U(x,t)^2 + g[B(x,t) + h(x,t)] = \frac{1}{2}U_0^2 + g(B_0 + h_0) \tag{4.4}$$

combining (4.2) and (4.4)

$$U(x,t)^3 + 2[gB(x,t) - K]U(x,t) + 2gQ_c = 0 \tag{4.5}$$

in which $K = \frac{1}{2}U_0^2 + g(B_0 + h_0)$ where the subscript '0' indicates upstream boundary conditions denoted in Figure 4.1.

We can solve (4.5) either numerically or analytically; numerically we used the bisection method and analytically used a formula for the roots of a cubic equation (see e.g.Abramowitz and Stegun (1965)), which is stated here. Given a cubic equation,

$$\Lambda^3 + a_1\Lambda^2 + a_2\Lambda + a_3 = 0$$

setting

$$T = \frac{1}{9}(3a_2 - a_1^2) \qquad \text{and} \qquad R = \frac{1}{54}(9a_1a_2 - 27a_3 - 2a_1^3)$$

the discriminant of which is

$$G = T^3 + R^2.$$

Then the three possible options are:

1. $G > 0$ then one root is real and two are complex.

2. $G = 0$ then all roots are real and two are equal.

3. $G < 0$ then all roots are real and unequal.

If $G < 0$ then the roots can be determined by

$$\Lambda_1 = 2\sqrt{-T}\cos\left(\frac{1}{3}\Gamma\right) - \frac{1}{3}a_1 \tag{4.6}$$

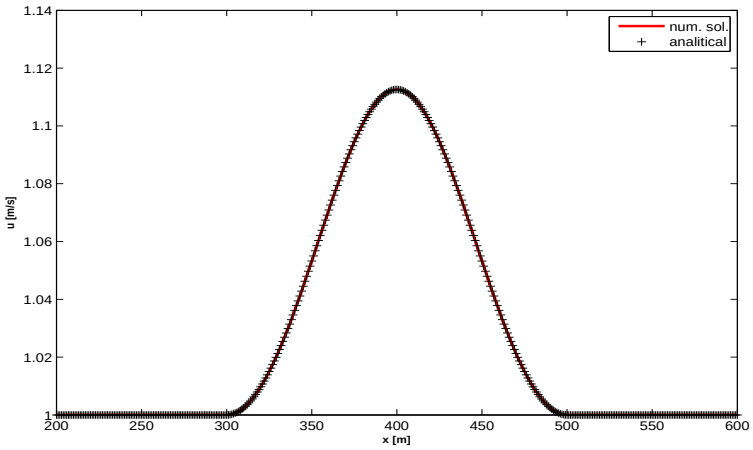

Figure 4.2: Solution of the cubic polynomial taking λ_3 for $t = 0s$

$$\Lambda_2 = 2\sqrt{-T}\cos\left(\frac{1}{3}(\Gamma + 2\pi)\right) - \frac{1}{3}a_1 \tag{4.7}$$

$$\Lambda_3 = 2\sqrt{-T}\cos\left(\frac{1}{3}(\Gamma + 4\pi)\right) - \frac{1}{3}a_1 \tag{4.8}$$

where $\Gamma = \cos^{-1}\left(\frac{R}{\sqrt{-T^3}}\right)$.

In order to be able to use this formula it has to be proved that $G < 0$. In our case $G = \frac{8}{27}[gB(x,t) - K]^3 + g^2Q_c^2$, and substituting the corresponding values it can be shown that the condition is always met.

From (4.6), (4.7) and (4.8) we get one negative and two positive roots. From the positive roots just one is physically correct regarding the problem under study. To find out which root is the correct one, we simply solve the cubic polynomial equation (4.5) for $t = 0$ (initial time) and then compare the obtained roots with the initial velocity (at the upstream boundary $x = x_0$); in this case Λ_3 was the correct one. In Figure 4.2 a comparison between the numerical and analytical solution of (4.5) is shown.

Using (4.8) we can get an expression for U just in terms of the bed level $B(x,t)$ as,

$$U(B) = 2\sqrt{\frac{2}{3}}\cos(\Pi)\sqrt{K - gB(x,t)} \tag{4.9}$$

in which

$$\Pi = \frac{1}{3}\left[\cos^{-1}\left(\frac{-gQ_c}{\sqrt{\frac{-8}{27}(gB(x,t)-K)^3}}\right) + 4\pi\right].$$

For the morphodynamics we use the morphodynamic module of the model, equations (3.50) and (3.52). Analysing these equations one can see that applying the chain rule gives:

$$\frac{\partial B}{\partial t} = -\xi(A_f - A_c)U^3\frac{\partial P_{fa}}{\partial x} - \xi 3U^2(A_f P_{fa} - A_c P_{fa} + A_c)\frac{\partial U}{\partial B}\frac{\partial B}{\partial x} \tag{4.10}$$

$$\frac{\partial P_{fa}}{\partial t} = \frac{\xi}{L_a}U^3(A_f P_{fs} - A_c P_{fs} - A_f)\frac{\partial P_{fa}}{\partial x} + \frac{\xi}{L_a}3U^2(-A_f P_{fa} + A_f P_{fs}P_{fa} + A_c P_{fs} - A_c P_{fs}P_{fa})\frac{\partial U}{\partial B}\frac{\partial B}{\partial x}. \tag{4.11}$$

So if we are able to obtain an expression for $\frac{\partial U}{\partial B}$ it would be possible to couple the equations and solve them simultaneously. In fact, from equation (4.9), the expression needed can be derived as

$$\frac{\partial U}{\partial B} = 2\sqrt{\frac{2}{3}}\left[\frac{-g}{2\sqrt{K - gB(x,t)}}\cos(\Pi) - \frac{1}{3}\sin(\Pi)\frac{\Omega}{\Upsilon}\sqrt{K - gB(x,t)}\right] \tag{4.12}$$

where

$$\Omega = \frac{4g^2Q_c(gB(x,t)-K)^2}{9\sqrt{\frac{-512}{19683}(gB(x,t)-K)^9}} \qquad \text{and} \qquad \Upsilon = \sqrt{1 + \frac{g^2Q_c^2}{\frac{8}{27}(gB(x,t)-K)^3}}.$$

4.3 Numerical Solution

4.3.1 Scheme

The system of equations (4.10) and (4.11) can be expressed as

$$\frac{\partial B}{\partial t} = \alpha\frac{\partial P_{fa}}{\partial x} + \beta\frac{\partial B}{\partial x} \tag{4.13}$$

$$\frac{\partial P_{fa}}{\partial t} = \delta\frac{\partial P_{fa}}{\partial x} + \gamma\frac{\partial B}{\partial x} \tag{4.14}$$

where

$$\begin{aligned}
\alpha &= -\xi(A_f - A_c)U^3 \qquad \beta = -3\xi U^2\frac{\partial U}{\partial B}(A_f P_{fa} - A_c P_{fa} + A_c)\\
\delta &= \frac{\xi}{L_a}U^3(A_f P_{fs} - A_c P_{fs} - A_f)\\
\gamma &= \frac{\xi}{L_a}3U^2\frac{\partial U}{\partial B}(-A_f P_{fa} + A_f P_{fs} P_{fa} + A_c P_{fs} - A_c P_{fs} P_{fa}).
\end{aligned}$$

A Crank-Nicholson type scheme (similar to that described in appendix A) is used to discretise the partial derivatives and solve the system. Using central difference in space and time, evaluating at a point $(j, n+\frac{1}{2})$ and writing the spatial differences in terms of average properties between n and $n+1$ as

$$\begin{aligned}
\frac{\partial B}{\partial t}\Big|_j^{n+\frac{1}{2}} &= \frac{B_j^{n+1} - B_j^n}{\Delta t}; \qquad \frac{\partial P_{fa}}{\partial t}\Big|_j^{n+\frac{1}{2}} = \frac{P_{fa_j}^{n+1} - P_{fa_j}^n}{\Delta t}\\
\frac{\partial B}{\partial x}\Big|_j^{n+\frac{1}{2}} &= \frac{B_{j+1}^{n+1} + B_{j+1}^n - B_{j-1}^{n+1} - B_{j-1}^n}{4\Delta x}\\
\frac{\partial P_{fa}}{\partial x}\Big|_j^{n+\frac{1}{2}} &= \frac{P_{fa_{j+1}}^{n+1} + P_{fa_{j+1}}^n - P_{fa_{j-1}}^{n+1} - P_{fa_{j-1}}^n}{4\Delta x}
\end{aligned}$$

and approximating U, P_{fa} and $\frac{\partial U}{\partial B}$ in α, β, δ and γ at the old time level (i.e U_j^n, $P_{fa_j}^n$

and $\frac{\partial U}{\partial B}\big|_j^n$) the system of equations (4.13) and (4.14) finally becomes

$$\begin{aligned} & CB_{j-1}^{n+1} + B_j^{n+1} - CB_{j+1}^{n+1} + FP_{fa_{j-1}}^{n+1} - FP_{fa_{j+1}}^{n+1} = \\ - \quad & CB_{j-1}^{n} + B_j^{n} + CB_{j+1}^{n} - FP_{fa_{j-1}}^{n} + FP_{fa_{j+1}}^{n} \end{aligned} \tag{4.15}$$

$$\begin{aligned} & EB_{j-1}^{n+1} - EB_{j+1}^{n+1} + DP_{fa_{j-1}}^{n+1} + P_{fa_j}^{n+1} - DP_{fa_{j+1}}^{n+1} = \\ - \quad & EB_{j-1}^{n} + EB_{j+1}^{n} - DP_{fa_{j-1}}^{n} + P_{fa_j}^{n+1} + DP_{fa_{j+1}}^{n} \end{aligned} \tag{4.16}$$

where

$$\begin{aligned} C &= \frac{\beta \Delta t}{4\Delta x} \qquad D = \frac{\gamma \Delta t}{4\Delta x} \\ E &= \frac{\delta \Delta t}{4\Delta x} \qquad F = \frac{\alpha \Delta t}{4\Delta x}. \end{aligned} \tag{4.17}$$

Then the system (4.15) and (4.16) can be solve straightforwardly if proper boundary conditions are given.

4.3.2 Eigenvalues

System (4.13) and (4.14) can also be written in matrix form as

$$\frac{\partial \mathbf{f}}{\partial t} + \mathbf{A}\frac{\partial \mathbf{f}}{\partial x} = 0 \tag{4.18}$$

with

$$\mathbf{f} = \begin{bmatrix} U \\ \\ B \end{bmatrix}, \qquad \mathbf{A} = \begin{bmatrix} -\beta & -\alpha \\ \\ -\delta & -\gamma \end{bmatrix}.$$

The eigenvalues of the matrix $\mathbf{A}$ are the solutions of the characteristic polynomial

$$\det(\mathbf{A} - \lambda \mathrm{I}) = 0$$

$$\lambda^2 + (\beta + \gamma)\lambda + (\gamma\beta - \delta\alpha) = 0$$

from which the roots can be determined by

$$\lambda_{1,2} = \frac{-(\beta+\gamma)}{2} \pm \frac{1}{2}\sqrt{(\beta-\gamma)^2 + 4\delta\alpha}$$

and after some algebraic steps we obtain the expression of the eigenvalues as

$$\begin{aligned}
\lambda_{1,2} = \frac{1}{2}\xi U^2 \Bigg\{ & 3\frac{\partial U}{\partial B}(A_f P_{fa} + A_c - A_c P_{fa}) - \frac{U}{L_a}(A_f P_{fs} - A_c P_{fs} - A_f) \\
& \pm \Bigg(\left(\frac{\partial U}{\partial B}\right)^2 \Big[P_{fa}^2(9A_f^2 - 18A_fA_c + 9A_c^2) + P_{fa}(18A_fA_c - 18A_c^2) + 9A_c^2 \Big] \\
& + \frac{\partial U}{\partial B}\frac{U}{L_a}\Big[P_{fs}P_{fa}(-6A_f^2 + 12A_fA_c - 6A_c^2) + P_{fs}(-6A_fA_c + 6A_c^2) \\
& + P_{fa}(6A_f^2 - 6A_fA_c) - 6A_fA_c \Big] + \frac{U^2}{L_a^2}\Big[P_{fs}^2(A_f^2 - 2A_fA_c + A_c^2) \\
& + P_{fs}(-2A_f^2 + 2A_fA_c) + A_f^2 \Big] \Bigg)^{1/2} \Bigg\}.
\end{aligned} \tag{4.19}$$

In Figure 4.3 the two eigenvalues are plotted as a function of time for different x positons and for a mean value of λ in x. To produce this figure, preliminary values of $A_f = 0.001\frac{s^2}{m}$ for the fine sediment, $A_c = 0.00088\frac{s^2}{m}$ for the coarse were used (chosen to compare later with Hudson solution) and initialising the model with the same amount of fine and coarse sediment as $P_{fa}^0 = P_{ca}^0 = 0.5$. In the figure we can see that for locations outside the sand dune (x = 200, 300 and 700 m) both eigenvalues are constant; for locations on the left side of the sand dune (x = 350 m.) both eigenvalues decrease with time; and for locations on the right side of the dune (x = 450 m.) the eigenvalues increase with time. Note as well that both eigenvalues are bigger for x = 400 m. than

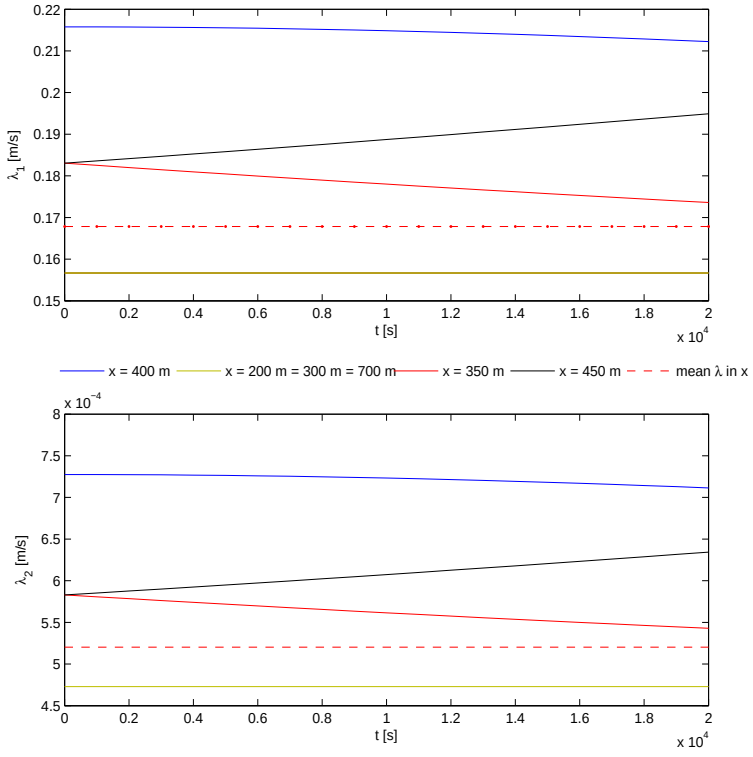

Figure 4.3: Eigenvalues of the sand dune system for different x locations

for the other x locations. Finally, it can be inferred that, due to the big difference in magnitude between λ_1 and λ_2, one eigenvalue (λ_2) corresponds to the velocity of propagation of the sand dune (and therefore the perturbations in P_{fa}) and the other (λ_1) corresponds to the velocity of a transient, more details about this matter are described in the following section.

4.3.3 Initial and Boundary Conditions

The initial and boundary conditions were defined from the analysis of the eigenvalues obtained from (4.19) derived in §4.3.2, and from the preliminary results of first runs. In Figures (4.4) and (4.5) the preliminary result from a test run taking $A_f = 0.001\frac{s^2}{m}$ for the fine sediment, $A_c = 0.00088\frac{s^2}{m}$ for the coarse sediment (which were given in

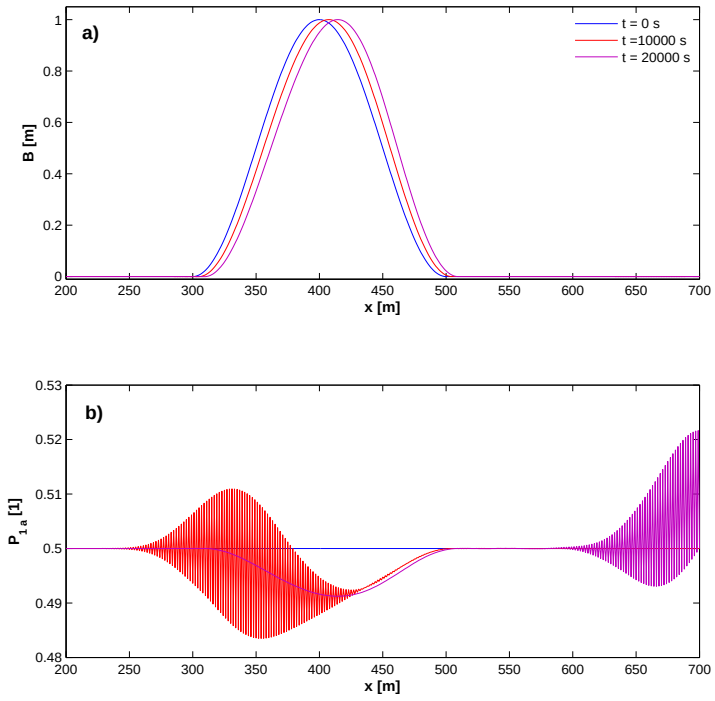

Figure 4.4: **a)**Sand dune evolution; **b)**Volume fraction evolution for the fine sediment (P_{fa})

order to compare with Hudson solution) and initialising with equal amount of fine and coarse sediments as $P^0_{fa} = P^0_{ca} = 0.5$. From Figure (4.4a) it can be seen that the bed level behaviour is correctly simulated by the model, propagating the sand dune in the direction of the flow. However, in Figure (4.4b) big oscillations in the evolution of the volume fraction appear. For that reason a contour plot for the volume fraction variation is shown in Figure(4.5). Note that a feature similar to a transient develops and reflects from the domain boundaries. As expected, the two eigenvalues calculated are the velocity of this transient (see λ_1 blue line) and the velocity of propagation of the sand dune (which is the same for the perturbation in P_{fa}; see λ_2 black line) confirming what was stated in the previous section.

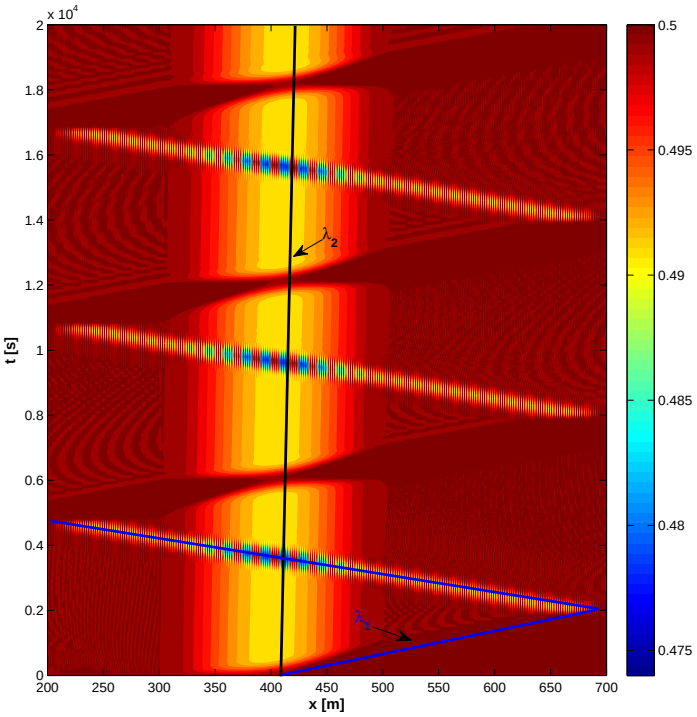

Figure 4.5: Contour plot for P_{fa}

The elimination of this transient was achieved setting appropriate initial conditions. As this transient was appearing in P_{fa} it was thought that the system (and particularly the equation governing P_{fa}) could give us an expression to set appropriate initial conditions in P_{fa} and therefore eliminate the transient. For that reason, from equation (4.11), and stating that at $t = 0$ s $\frac{\partial P_{fa}}{\partial t} = 0$, we obtain

$$\begin{aligned} \frac{\xi}{L_a} U^3 (A_f P_{fs} - A_c P_{fs} - A_f) \frac{\partial P_{fa}}{\partial x} = \\ -\frac{\xi}{L_a} 3U^2 (-A_f P_{fa} + A_f P_{fs} P_{fa} + A_c P_{fs} - A_c P_{fs} P_{fa}) \frac{\partial U}{\partial B} \frac{\partial B}{\partial x}. \end{aligned} \tag{4.20}$$

Approximating with forward differences in space the partial derivatives and using U_j^0, $\frac{\partial U}{\partial B}\Big|_j^0$ and $P_{fa_j}^0$ an expression for the initial condition is obtained from (4.20) as

$$P^0_{fa_{j+1}} = -\frac{3\frac{\partial U}{\partial B}\Big|^0_j}{U^0_j}\frac{(-A_f P^0_{fa_j} + A_f P^0_{fs_j} P^0_{fa_j} + A_c P^0_{fs_j} - A_c P^0_{fs_j} P^0_{fa_j})}{(A_f P^0_{fs_j} - A_c P^0_{fs_j} - A_f)}(B^0_{j+1} - B^0_j) + P^0_{fa_j}. \tag{4.21}$$

From the results given in Figure (4.5) it was evident that to avoid the problem of multiple reflections we must apply transmissive boundary conditions at both, upstream and downstream boundaries. This was done through

$$\begin{aligned} B_j &= B_{j-1} \qquad P_{fa_j} = P_{fa_{j-1}} \qquad \text{on the upstream boundary} \\ B_N &= B_{N+1} \qquad P_{fa_N} = P_{fa_{N+1}} \qquad \text{on the downstream boundary.} \end{aligned}$$

Finally, in Figure 4.6 an equivalent plot to Figure 4.5 but with the new initial and boundary conditions set up in the model is shown; from this figure it can be seen that these conditions are physically reasonable and worked well in the model.

4.4 Results

In order to test the accuracy and reliability of the model and therefore gain some confidence in its application, a set of eight different numerical experiments were performed. The base point of these tests is the original case tested by Hudson (2001) in which the value of A, from now on A_{hud}, was set equal to $0.001 s^2/m$; for which it is shown in ap-

Table 4.1: Sand Dune Tests

Test No.	$A_f[s^2/m]$	$A_c[s^2/m]$	T_{max} **with** A_f **[s]**	T_{max} **with** A_c **[s]**	T_{model} **[s]**	Description
1	0.001	0.00088	238 079	370 544	200 000	$A_f = A_{hud}$; A_c is 12 % coarser than A_{hud}
2	0.001	0.00075	238 079	317 438	200 000	$A_f = A_{hud}$; A_c is 25 % coarser than A_{hud}
3	0.001	0.0005	238 079	476 158	200 000	$A_f = A_{hud}$; A_c is 50 % coarser than A_{hud}
4	0.00112	0.001	212 576	238 079	200 000	$A_c = A_{hud}$; A_f is 12 % finer than A_{hud}
5	0.00125	0.001	190 453	238 079	200 000	$A_c = A_{hud}$; A_f is 25 % finer than A_{hud}
6	0.0015	0.001	158 719	238 079	200 000	$A_c = A_{hud}$; A_f is 50 % finer than A_{hud}
7	0.00112	0.00088	212 570	270 544	200 000	A_f is 12 % finer than A_{hud}; A_c is 12 % coarser than A_{hud}
8	0.00125	0.00075	190 453	314 438	200 000	A_f is 25 % finer than A_{hud}; A_c is 25 % coarser than $Ahud$

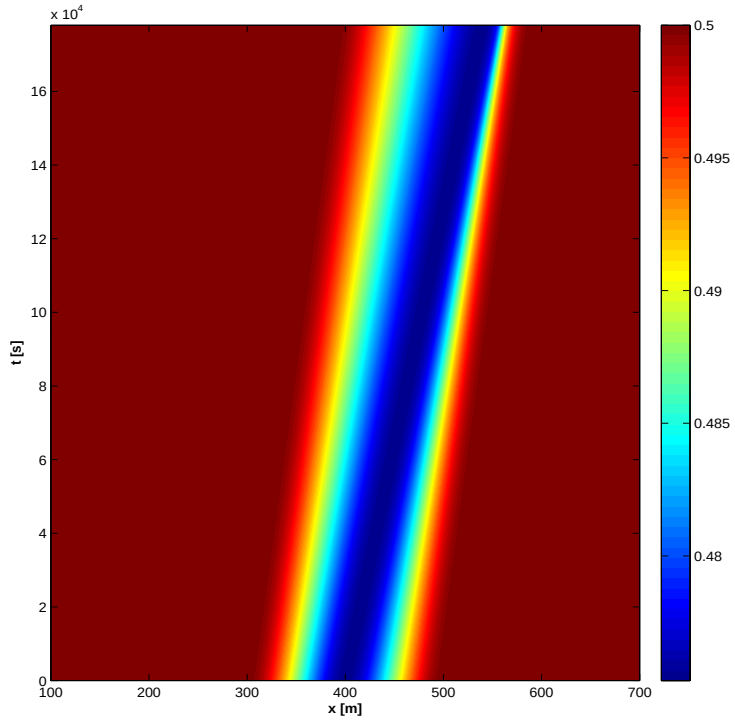

Figure 4.6: Contour plot for P_{fa} with the new initial and boundary conditions

pendix A that the solution for the case with just one grain size is correctly reproduced by the model. Here we examine the model behaviour for different values of A_f and A_c of the two frations considered.

The set of eight tests was divided into three parts (see Table 4.1). In the first three tests A_f was fixed to A_{hud} and A_c was made progressively smaller (meaning that the sediment gets coarser) than A_{hud} by 12 %, 25 % and 50 % respectively. Tests 4, 5 and 6 are similar to those described before, but in this case A_c was fixed to the value of A_{hud} and A_f was progressively bigger (sediment gets finer) by 12 %, 25 % and 50 % respectively. Finally in tests 7 and 8 A_f (A_c) is bigger (smaller) than A_{hud} by 12 % in test 7 and 25 % in test 8.

4.4.1 General Results

In Figure 4.7 the general behaviour of the solution given by the model for Test 1 is presented. From Figure 4.7a) it is seen that the sand dune is well propagated in time without showing any oscillations which gives confidence in the stability of the model (see appendix A for the stability analysis). In Figure 4.7b the variation of the volume fraction is shown, from this figure we can state several conclusions: first, it is interesting to note that the form of the initial condition in P_{fa} determines the behaviour of the volume fraction. For the conditions modeled in Test 1 the initial condition is stating that over the sand dune, the volume fraction for the fine sediment reduces and for the coarse sediment increases; therefore this tendency is just propagated in a similar way than the sand dune on the bed.

Regarding the behaviour of P_{fa} (and therefore P_{ca}) in Figure 4.7b, and to check wether the results obtained are correct the following analysis is presented. Taking (3.47) into (3.37)

$$\frac{\partial B}{\partial t} = -\xi \frac{\partial}{\partial x} \{q_f + q_c\} \tag{4.22}$$

is obtained, substituting (4.22) into (3.43) and taking into account that $P_{fs} + P_{cs} = 1$ (similar to the condition in the active layer) we get

$$\frac{\partial P_{fa}}{\partial t} = -\frac{\xi}{L_a} \left[P_{cs} \frac{\partial q_f}{\partial x} - P_{fs} \frac{\partial q_c}{\partial x} \right]. \tag{4.23}$$

Now it is necessary to know the behaviour of the terms in this equation to find out if the results given by the model are correct. An analysis is performed for equation (4.23)

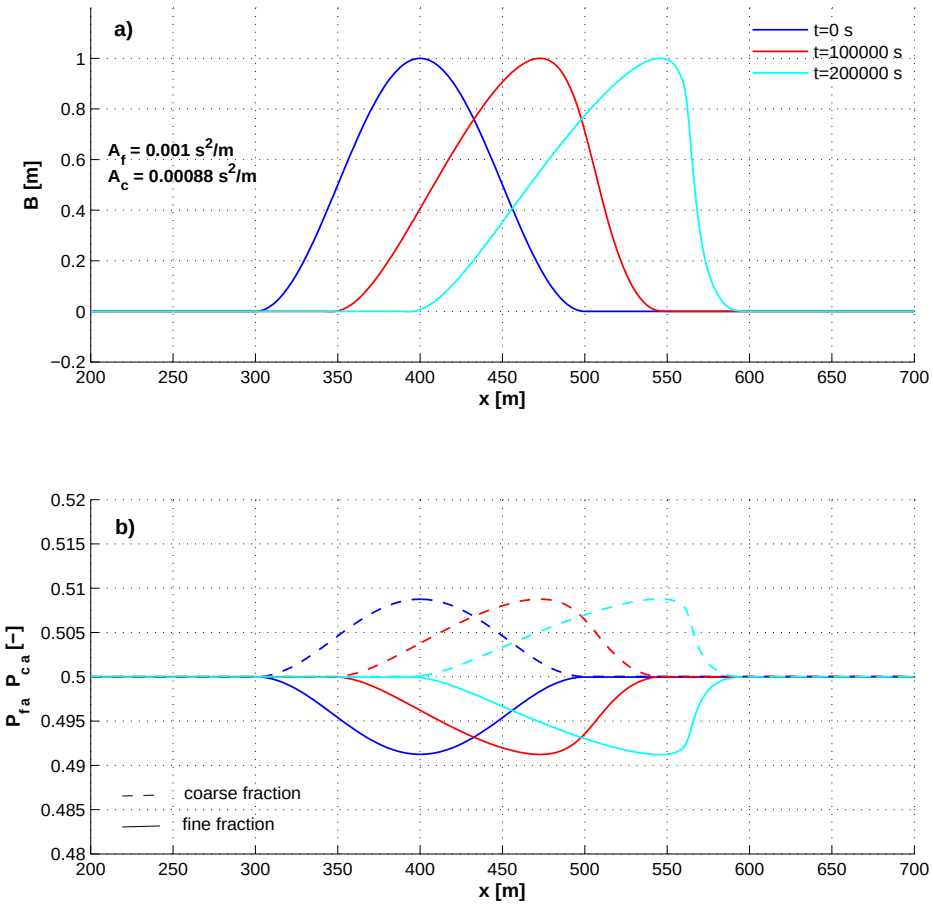

Figure 4.7: Results given by the model for Test 1: **a)** Bed level evolution **b)** Volume fraction evolution. Solid line: Fine fraction; dashed line: coarse fraction

with the aid of Figure 4.8; in this figure the evolution of flow velocity, bed level, fine volume fraction P_{fa}, sediment transport rate and $\frac{\partial q}{\partial x}$ over time is presented.

The analysis is made in four different points over the spatial domain, labeled in Figure 4.8 as points I, II, II and IV; highlighted with a black vertical line. These points are defined based on their location over the sand dune. The points depicted in Figure 4.8 are defined taking the initial bed level condition (blue line) as follows. Point I is located on the upstream side of the sand dune where the bed level is constant and equal to 0. Point IV is an equivalent point to I on the downstream side of the sand dune. Point II is located over the sand dune but on the upstream side of the initial maximum bed level, and finally point III is also located over the dune but this time on the downstream side of the maximum bed level.

Now, regarding these points as cells with a control volume infinitesimally small, it is possible to state that at points I and IV, based on Figure 4.8d) and e)

$$\begin{aligned} q_f^{in} &= q_f^{out}; \qquad \frac{\partial q_f}{\partial x} = 0 \\ q_c^{in} &= q_c^{out}; \qquad \frac{\partial q_c}{\partial x} = 0 \end{aligned}$$

from which it is easily deduced from (4.23) that

$$\frac{\partial P_{fa}}{\partial t} = 0. \tag{4.24}$$

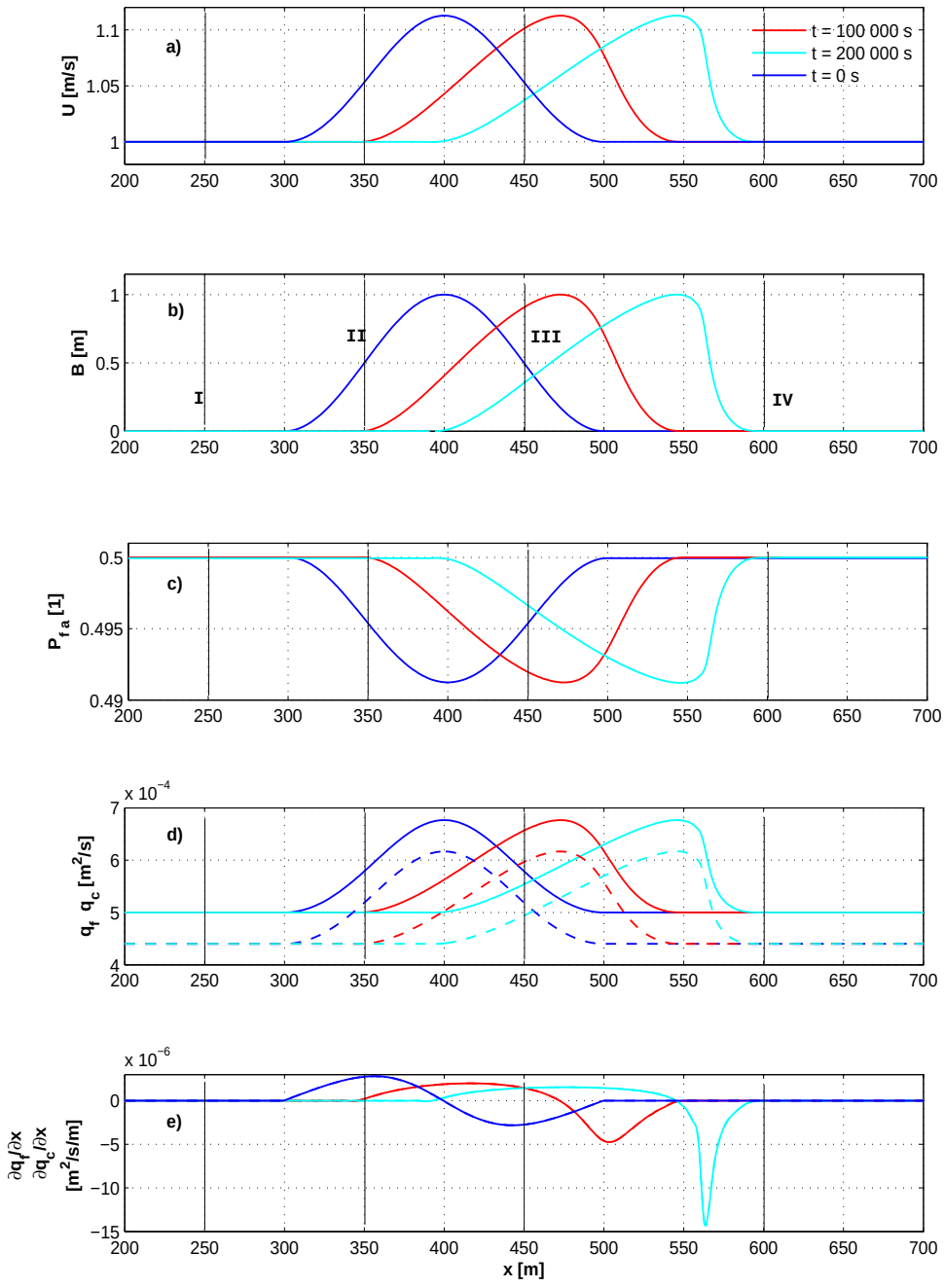

Figure 4.8: **a)**Velocity evolution; **b)**Bed level evolution; **c)**Volume fraction evolution; **d)**Sediment transport rate evolution for each fraction and **e)** $\frac{\partial q}{\partial x}$ for each fraction. Solid line: fine fraction A_f; dashed line: coarse fraction A_c

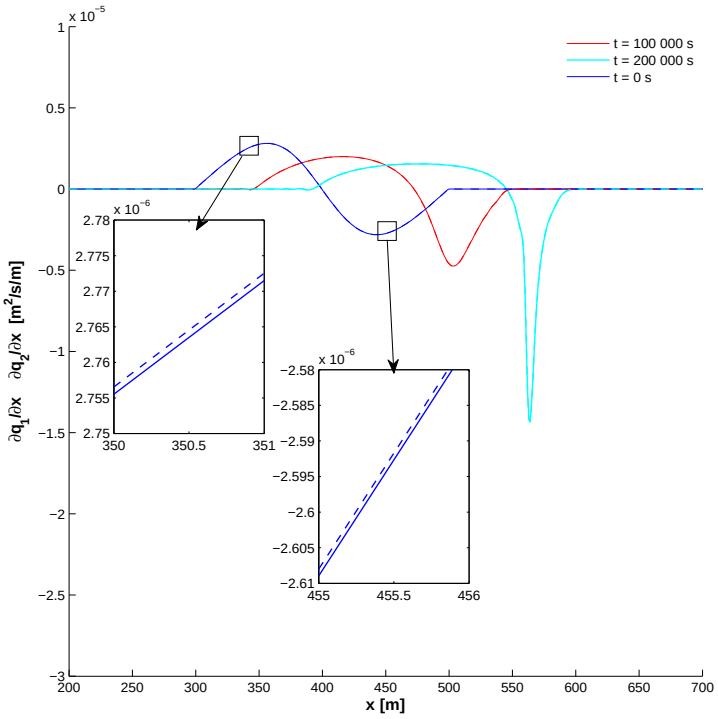

Figure 4.9: $\frac{\partial q}{\partial x}$ evolution. Solid line: fine fraction A_f; dashed line: coarse fraction A_c

In the similar way for point II

$$\begin{aligned} q_f^{in} &< q_f^{out}; \qquad \frac{\partial q_f}{\partial x} > 0 \\ q_c^{in} &< q_c^{out}; \qquad \frac{\partial q_c}{\partial x} > 0 \end{aligned}$$

and for point III

$$\begin{aligned} q_f^{in} &> q_f^{out}; \qquad \frac{\partial q_f}{\partial x} < 0 \\ q_c^{in} &> q_c^{out}; \qquad \frac{\partial q_c}{\partial x} < 0. \end{aligned}$$

In point II and III it is important to know if $\frac{\partial q_f}{\partial x}$ is bigger or smaller than $\frac{\partial q_c}{\partial x}$; in order to find out, a separate graph was plotted for the behaviour of $\frac{\partial q}{\partial x}$ for both fractions (see Figure 4.9).

In this figure a more detailed picture of the behaviour of $\frac{\partial q}{\partial x}$ is presented and a close-up of two points equivalent to points II and III is shown as well. From this figure it is possible to state that at point II

$$\frac{\partial q_f}{\partial x} < \frac{\partial q_c}{\partial x}$$

and that both quantities are positive which yields (observing eq.(4.23)) that for point II

$$\frac{\partial P_{fa}}{\partial t} > 0. \tag{4.25}$$

In a similar way for point III it can be seen that

$$\frac{\partial q_f}{\partial x} > \frac{\partial q_c}{\partial x}$$

but in this case both quantities are negative, which would lead (following eq.(4.23)) to

$$\frac{\partial P_{fa}}{\partial t} < 0. \tag{4.26}$$

Finally comparing these conditions (eqs.(4.24),(4.25) and (4.26)) for the different points defined with the results given in Figure 4.8c), it can be seen that effectively the behaviour of P_{fa} is correctly reproduced: at points I and IV P_{fa} does not change; at point II increases and at point III decreases. This analysis can be applied at any given time (if points I-IV are defined with the same criteria) and successively explain the evolution in time of the volume fraction.

4.4.2 Analysis of Bed Level Results

The bed level results for cases where the coarse sediment (A_c) was made progressively coarser (A_c smaller) while maintaining the fine sediment (A_f) fixed to A_{hud} value are

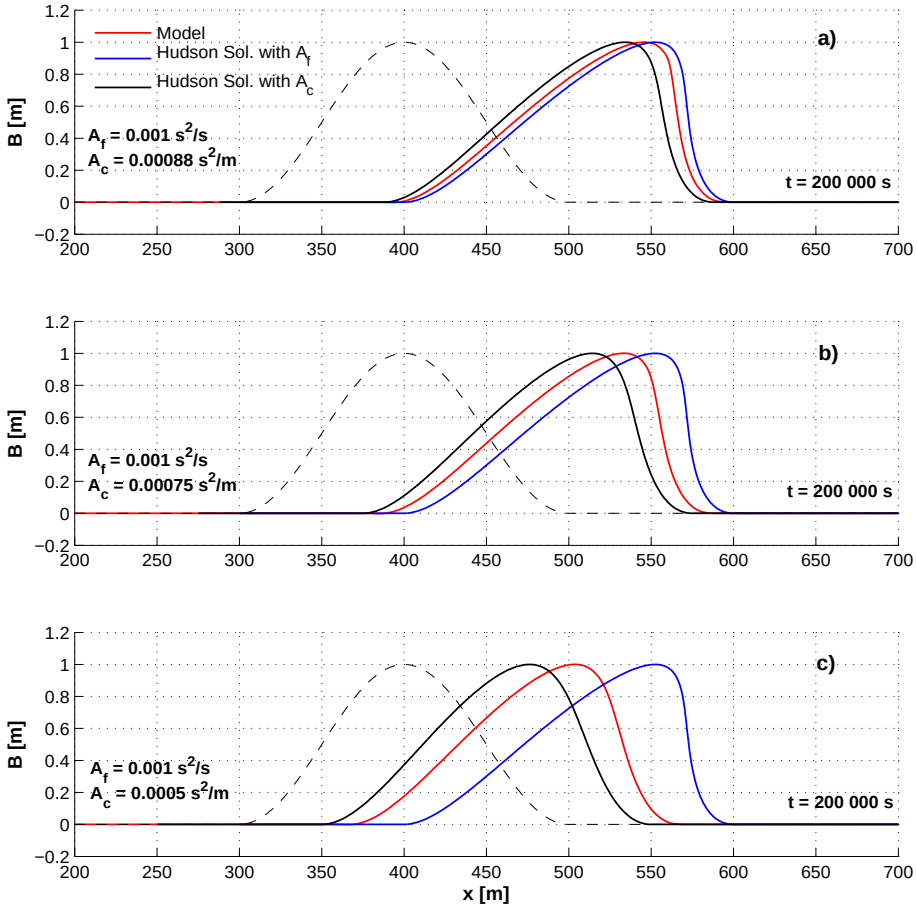

Figure 4.10: Bed level results at t = 200 000 s for a) Test 1, b) Test 2 and c) Test 3. Dashed line: initial condition.

presented in Figure 4.10. In Figure 4.10a) bed level results for the case where A_c is 12% smaller (coarser) than A_{hud} are shown and in Figure 4.10 b) and c) for cases where A_c is 25% smaller (coarser) and 50% smaller (coarser) than A_{hud}. In order to help with the analysis of the results, in these figures the bed level predicted by the Hudson analytical solution taking separately the values of A_f and A_c is also plotted.

From this figure it is concluded that as expected, when the coarse sediment gets progressively coarser, the propagation of the sand dune in the direction of the flow decreases;

this is as expected because physically, the coarser the sediment is the harder it is to transport causing the decrease in the distance propagated by the sand dune. It is also seen that in the three cases the model prediction lies, as might be expected, between the solutions given by Hudson analytical solution taking the fine and coarse sediment separately.

Now, in Figure 4.11 bed level results for cases in which the coarse sediment (A_c) was fixed to A_{hud} and the fine sediment (A_f) was progressively finer (A_f bigger) in 12, 25 and 50 %. In this case, just as in the one described above, the behaviour given by Hudson analytical solution is plotted taking A_f and A_c independently.

The results given in Figure 4.11 are as expected, opposite to those when A_c gets smaller (coarser); i.e., the propagation of the sand dune in the direction of the flow is easier so that the dune reaches greater distances when finer sediments are present in the mixture. This is explained by the same reason as with the coarse case described above: the finer the sediment the easier it is to be transported, thus facilitating the propagation of the sand dune. Here the model solution also lies between the solution given by Hudson for the fine and coarse sediment taken on their own, as expected.

Finally, the bed level predictions given by the model for the cases where both sediments were simultaneously changed are presented in Figure 4.12, for the case when the fine sediment (A_f) was 12% finer (A_f bigger) than A_{hud} and the coarse sediment (A_c) was 12% coarser (A_c smaller) than A_{hud} (Test 7, plot a); and when the fine sediment (A_f) was 25% finer (A_f bigger) than A_{hud} and the coarse (A_c) was 25% coarser (A_c smaller)

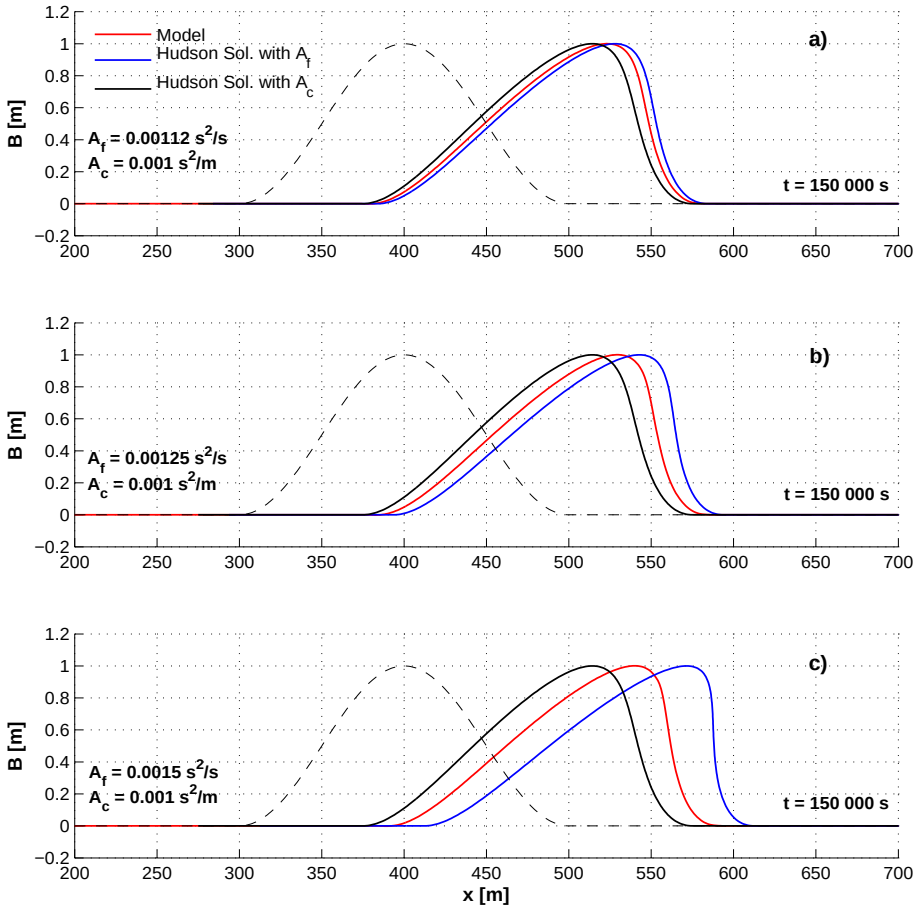

Figure 4.11: Bed level results at t = 150 000 s for a) Test 4, b) Test 5 and c) Test 6. Dashed line: initial condition.

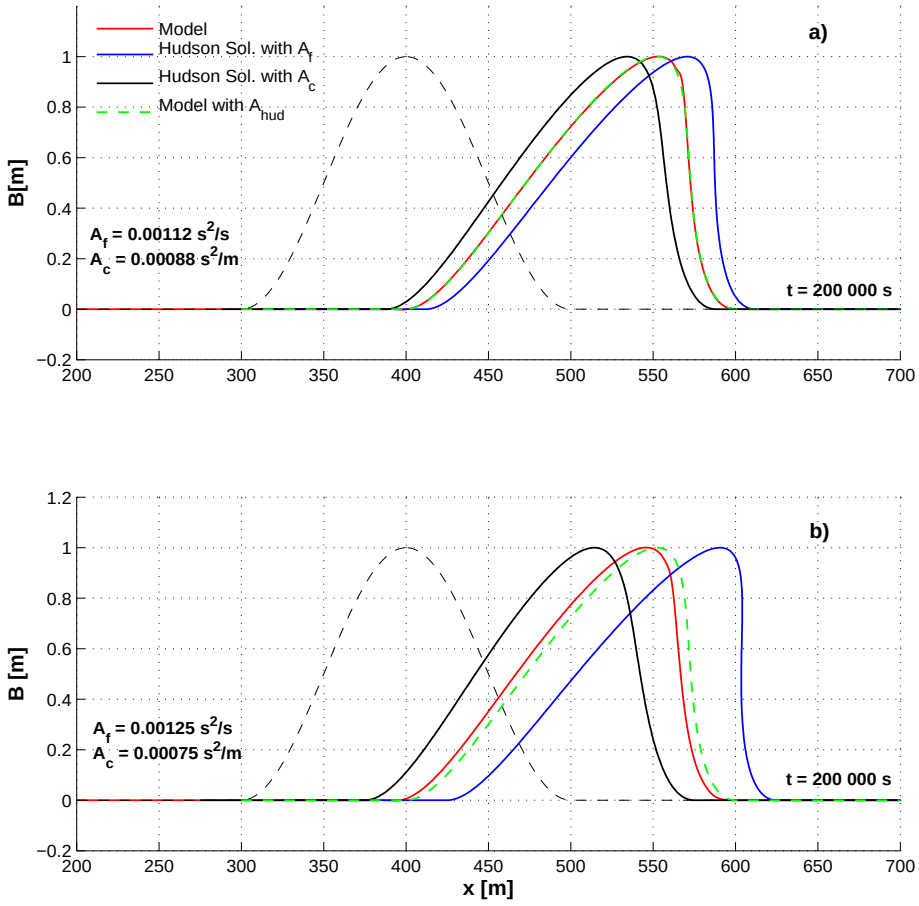

Figure 4.12: Bed level results at t = 200 000 s for a) Test 7 and b) Test 8. - - Initial condition.

than A_{hud} (Test 8, plot b).

Also plotted here is the numerical solution given by the model when both grain fractions are set equal to A_{hud} sediment parameter which here is equivalent to $\bar{A} = \frac{A_f + A_c}{2}$; interestingly this solution is seemingly identical to that when both sediments are changed by 12 % (Figure 4.12 a)). This result can initially yield the conclusion that if both sediments are modified by the same proportion the final result in bed level behaviour is not affected because the sediment fractions counteract each other. This would mean

that a simple mean value between A_f and A_c, which in this case is $0.001 s^2/m$, will yield the same result as that with two different sediment fractions. Now, looking at Figure 4.12b) where the difference between the sediments is greater (A_f 25% finer, and A_c 25% coarser than A_{hud}), it is clear that actually this cannot be done because in this case the bed given by the model taking the two sediment fractions does not correspond with the one taking the mean value $\bar{A}$. This means that the greater the difference between the two sediment fractions present in the mixture the greater is the importance of considering the two sediment sizes separately rather than considering just one sediment size through a rough mean value; which is, actually, common practice in sediment transport models (see e.g. Soulsby (1997), Dean and Dalrymple (2002)).

This result led to Figure 4.13 being produced to compare the bed level results generated by the model using the two sediments, and the ones given by model taking the mean value $\bar{A}$ between them, for the Tests 1-6.

Indeed as expected, Figure 4.13 shows that when the difference between the two sediments is 12 % (Figure 4.13a and d) and 25 % (Figure 4.13b and e) the final bed level prediction using two sediments is seemingly the same as using the mean value; but when the difference between the sediments is bigger (50 %, Figure 4.13c and f) a noticeable difference between the solutions appears. Therefore it could be assumed that if there is a substantial difference between the sediments involved the assumption of working with a mean value between sediments would lead to results that are not accurate.

Now, it is interesting to compare the results for the cases where the difference between

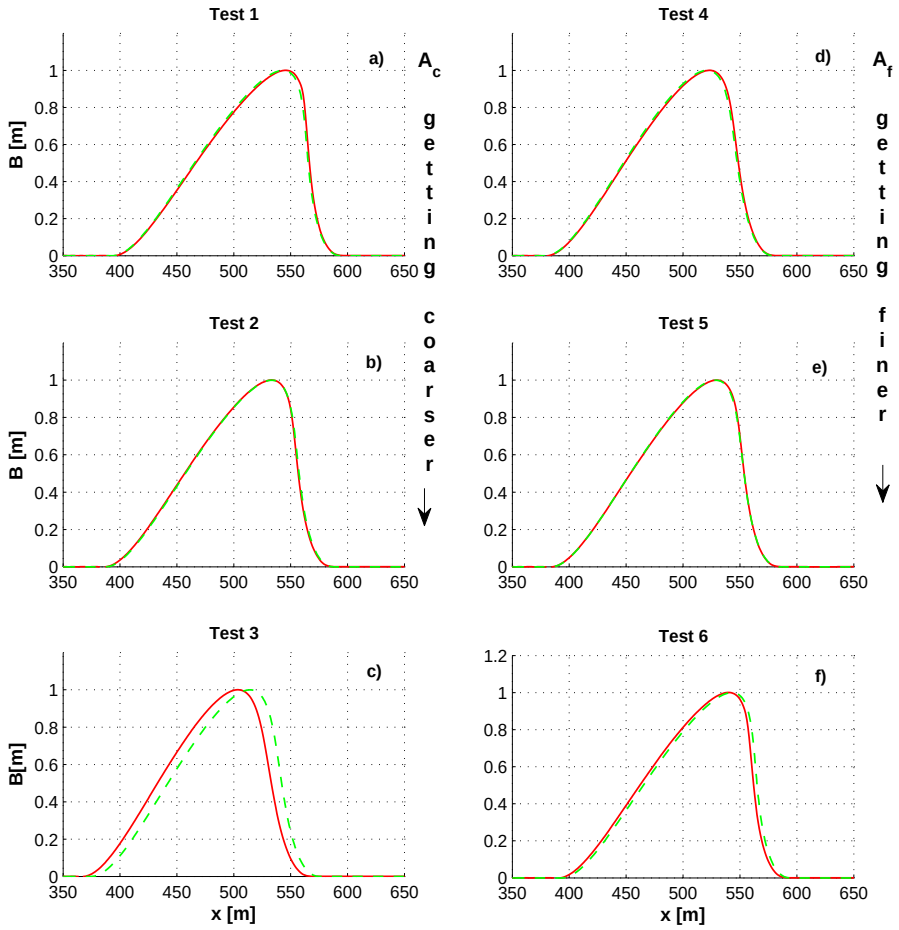

Figure 4.13: Comparison of final bed level results ($t = t_f$) for Test 1 to 6. — Model with A_f and A_c; - - Model with $\bar{A}$

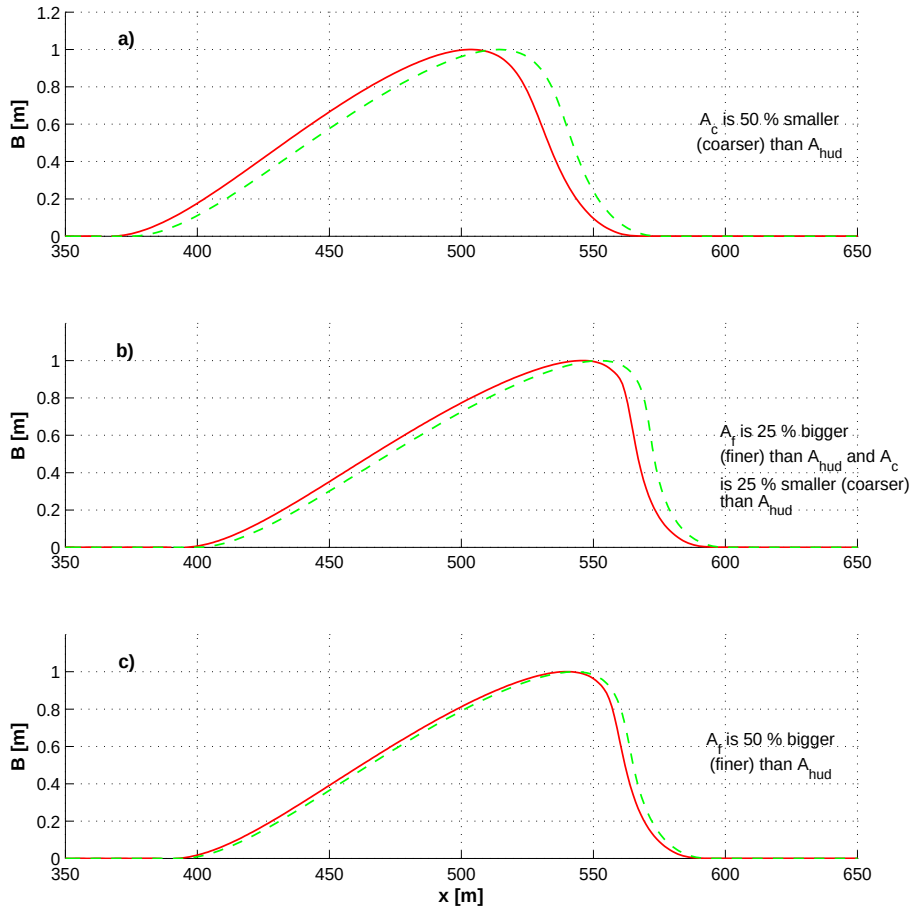

Figure 4.14: Comparison of final bed level results ($t = t_f$) for a) Test 3; b) Test 8 and c)Test 6. — Model with A_f and A_c; - - Model with $\bar{A}$

the sediments is the same in terms of A_f and A_c (Tests 3, 6 and 8). For that purpose, in Figure 4.14 final bed level profiles are shown for the cases where the net difference between A_f and A_c sediment parameters is 50 %. In Figure 4.14a $A_f = A_{hud}$ and A_c is smaller (coarser) than A_{hud}; case where both sediments change by 25 % from A_{hud} is shown in Figure 4.14b and in Figure 4.14c the case in which $A_c = A_{hud}$ and A_f is 50 % bigger (finer) than A_{hud} is presented.

Observing this figure it is evident that although the difference between sediment param-

eters is the same for the three cases shown, the agreement between solutions given by the model when two sediments are taken and that when a mean value is used, is not the same. Moreover, it can be seen that the disagreement is worse when A_c is smaller than A_{hud} (sediment is coarser) than that when the modified sediment is finer than A_{hud}; this means that the disagreement between solutions is bigger when this difference is made towards the coarser sediment and smaller when is made towards the fine sediment. This would mean that taking a coarser sediment into account has more effect in the solution in terms of bed level behaviour but obviously this would depend on the behaviour of the volume fraction P_{fa}, this point will be further discussed in the next section.

4.4.3 Analysis of Volume Fraction Results

For the sake of simplicity and to facilitate the visualisation, results in this section are going to be presented in terms of the fine sediment volume fraction P_{fa} behaviour noting that the evolution of the coarse sediment volume fraction P_{ca} can be inferred from condition $P_{fa} + P_{ca} = 1$ and will have a behaviour similar to that shown in Figure 4.7b (dashed line).

In Figure 4.15 results of the final volume fraction of the fine sediment P_{fa} are presented for the first three tests corresponding to the cases where the fine sediment was fixed to A_{hud} and coarse sediment was made progressively coarser (A_c getting smaller).

Just as seen in Figure 4.7b and as stated in that section, the initial condition determines the distribution of sediments under the dune and the general form of this distribution

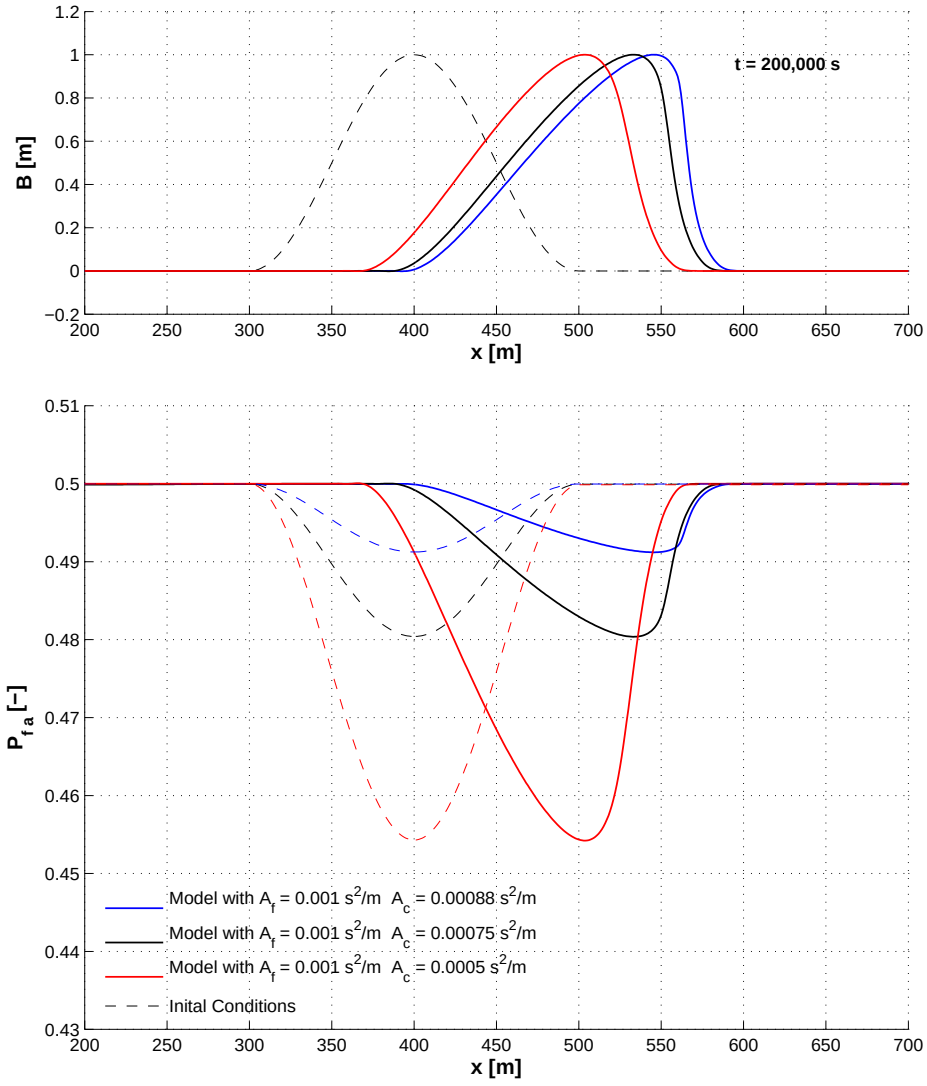

Figure 4.15: Volume fraction results at t = 200 000 s for cases where A_c gets smaller (coarser). — Test 1; — Test 2; — Test 3. On top, the bed Level behaviour for each test is also shown for reference. Dashed lines: initial conditions

is simply propagated along with the sand dune. This wave in P_{fa} is propagated in the direction of the flow and just as seen in the case of the bed level results (Figure 4.10) this propagation reaches smaller distances when the sediment is coarser.

Now, it is seen that as the coarse sediment is made coarser, the proportion of fine sediment in the initial condition, and therefore in the simulation, decreases (and P_{ca} increases). This can be explained analysing the P_{fa} initial condition eq.(4.21). Observing this equation it is seen that, as the hydrodynamic conditions are the same for all tests (i.e. same U and $\frac{\partial U}{\partial B}$), as well as the initial bed slope (i.e. B at t_0), the initial perturbation in P_{fa} is a direct function of $A_f - A_c$ difference because in this case it is being assumed that the initial volume fraction in the active layer is the same as in the substrate (i.e. $P^0_{fa} = P^0_{fs}$). This means that the bigger the difference $A_f - A_c$ is, the bigger the perturbation in the initial shape of P_{fa} is obtained, which agrees with the observed results in the figure.

Results of the fine volume fraction evolution for cases in which the fine sediment was made progressively finer and the coarse sediment was fixed to A_{hud} (Tests 4, 5 and 6) are shown in Figure 4.16.

From this figure, as expected, the propagation of the wave in P_{fa} is done in a similar way as in Figure 4.15; the finer the sediment (A_f) the more distance is reached by the sand dune and therefore by the wave in P_{fa}. The behaviour of P_{fa} in the initial condition and thus in the simulation agrees with what it was described above: the bigger the difference $A_f - A_c$ is, the bigger the perturbation in the initial shape of P_{fa}. Note that

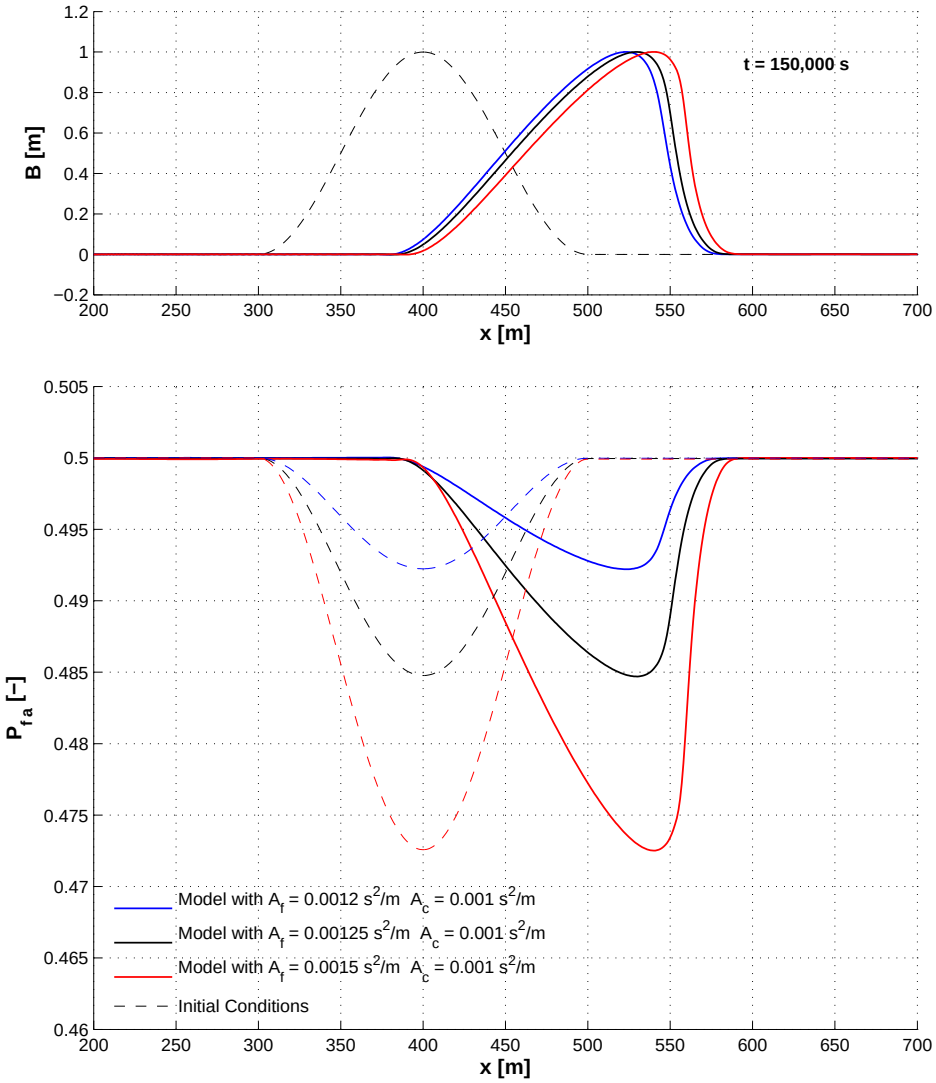

Figure 4.16: Volume fraction results at t = 150 000 s for cases where A_f gets bigger (finer). — Test 4; — Test 5; — Test 6. On top, the bed level behaviour for each test is also shown for reference. Dashed lines: initial conditions

if this is true, the initial perturbation in P_{fa} for tests with the same $A_f - A_c$ difference should be the same. However, note that in the denominator of the second division of eq.(4.21), there is a A_f value that is acting in isolation (i.e. not being multiplied by any other value), making this parameter crucial for the initial form of the fine volume fraction P_{fa} and from which we can conclude that the bigger A_f, the smaller the result of that division will be, giving as a result a smaller initial perturbation for the fine volume fraction P_{fa}. This is why the initial perturbation in P_{fa} in the tests depicted in Figure 4.16 are smaller than that depicted in Figure 4.15.

Now in Figure 4.17 the fine volume fraction results are presented for the cases where both sediments A_f and A_c were modified simultaneously in the same proportion, 12 % and 25 % of A_{hud} (Tests 7 and 8).

For the cases depicted in Figure 4.17 same general conclusions apply as in Figures 4.15 and 4.16, the bigger the difference between the sediments involved the more variation in P_{fa} is obtained.

Now, it is interesting to compare Figures 4.15, 4.16 and 4.17; the following conclusions can be deduced. First, there is more variation in the behaviour of P_{fa} between cases where the coarse sediment was made progressively coarser (Figure 4.15) than that when the fine sediment was progressively finer in the same proportions Figure (4.16). This was already explained by analysing the initial condition eq.(4.21) and concluding that the bigger the difference $A_f - A_c$, the bigger the initial perturbation in P_{fa} is got; and that the bigger A_f, the smaller the initial perturbation.

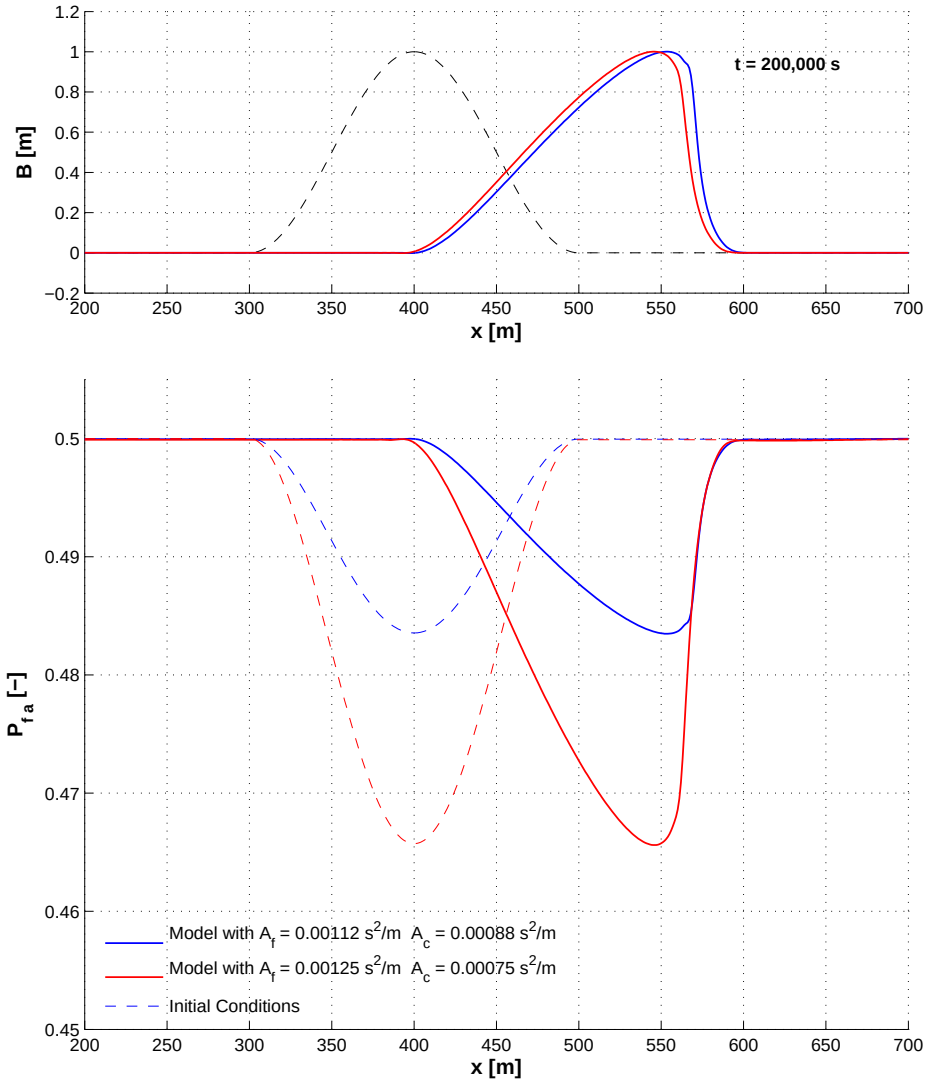

Figure 4.17: Volume fraction results at t = 200 000 s for cases where both fine an coarse sediments were changed simultaneously in 12 % of A_{hud} — Test 7 and in 25 % of A_{hud} — Test 8. On top, the bed level behaviour for each test is also shown for reference. Dashed lines: initial conditions

The second important conclusion is that as mentioned in the previous section, the role of P_{fa} in the behaviour of the bed level B is crucial (see equation 4.10). The disagreement found previously between solutions (with the same difference between sediments) given by the model taking the two sediment fractions, and taking the mean value $\bar{A}$ (see Figure 4.14) was bigger when the coarse sediment was modified than that when altering the fine sediment; this is now completely explain because indeed there is more variation in P_{fa} when the sediment was made coarser (see Figure 4.15) than that when the fine sediment was made finer (see Figure 4.16).

Based on the results presented in this chapter, it can be stated as a general conclusion, with a high degree of confidence, that so far the model is capable to give stable, accurate and physically correct results regarding the sorting and transport of sediments and therefore it is suitable to being applied in other hydrodynamical conditions.

Chapter 5

Sorting and Transport of a non-uniform sediment mixture under a PW01 swash event

5.1 Introduction

In this chapter the model developed in this research is applied to one of the two most general cases of swash motion in order to investigate the transport and sorting of sediment mixtures in this region of a beach. As mentioned before flow in the swash zone on a sloping beach takes two different basic forms, in this case the swash motion when the wave breaks before reaching the shoreline (in this case idealised as a collapsing bore) and then runs up and down over the sloping bed is implemented in the model.

The well-known complexity of the dynamics of the swash zone suggest that if one wants to isolate and study certain phenomena in this region, an appropriate description is to neglect the bottom friction and flow infiltration/exfiltration. The description of a single swash event produced by an incident breaking wave (bore) taking into account these simplifying assumptions is as follows (see Figure 5.1). At initial time $t = t_0$ the bore collapses and its potential energy is abruptly transformed into kinetic energy in a thin layer of water with its tip (shoreline, x_s) moving up the beachface and a block of water with constant depth (h_0), which is located from the x_{sw} point and seawards, begins to run down the slope due to the action of gravity (Figure 5.1 a). Following the bore collapse, the water surface dips seaward and the flow acceleration is directed seawards for almost all the swash event, producing an stretching of the flow at the seaward end (Figure 5.1 b). On the run-down phase (backwash) the flow has started to move completely in the offshore direction and there is no more divergence in the flow (Figure 5.1 c); and finally the backwash flow quickly becomes supercritical until it drains out of the region if swash-swash interactions are not being taken into account (Figure 5.1 d).

For this type of swash event Shen and Meyer (1963b) developed an analytical solution (hereinafter SM63) which was originally proposed for the vicinity of the moving shoreline and later shown as part of a valid solution of the Non-Linear Shallow Water Equations (NLSWE) over the whole swash by Peregrine and Williams (2001) (hereafter PW01). It is important to mention that SM63 solution implies that the swash flow driven by a bore is impinging on a fixed bed and the whole swash flow depends on the conditions at the point of bore collpase (initial conditions). The crucial parameter at that position is

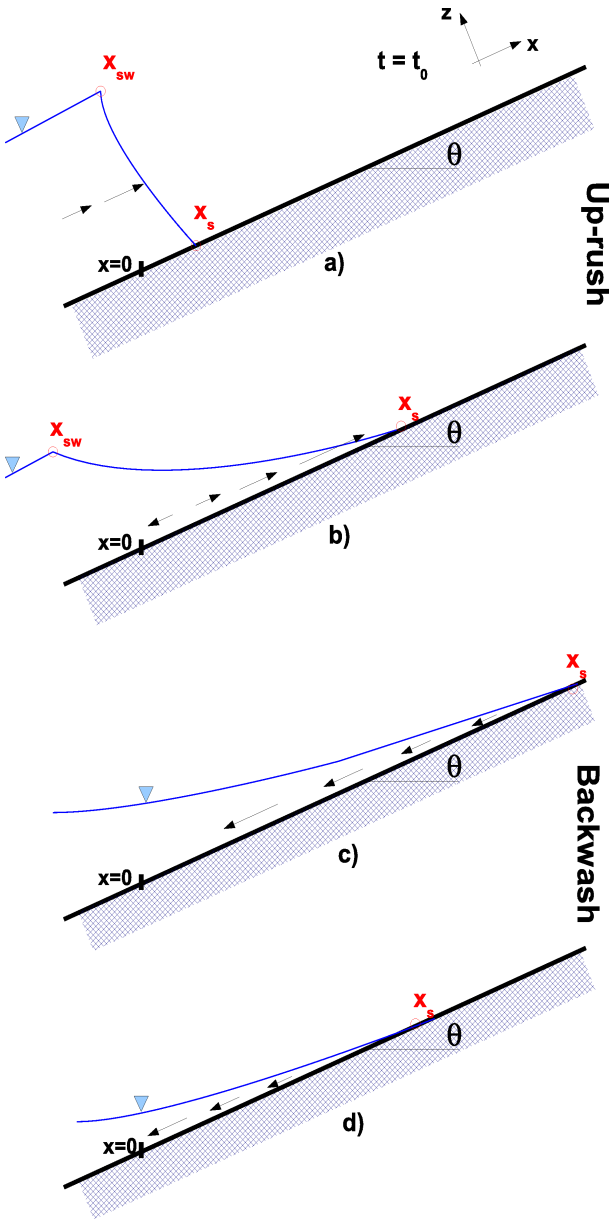

Figure 5.1: Sketch for a PW01 swash flow (the size of the arrows are schematically proportional to the depth-averaged velocity at the point).

the velocity of the bore which determines the maximum run-up length based on ballistic theory.

In the context of the shallow water theory SM63 solution is the only analytical description of a swash event caused by waves that have broken and formed a bore that meets the shoreline. Despite some limitations that have been pointed out like the prediction of unrealistically small depths and the independence of the internal flows of the incident wave conditions; it remains the standard solution for a breaking wave swash event (Guard and Baldock (2007)) and it has been used to study overtopping of structures by swash flows (Peregrine and Williams (2001)) and sediment transport in the swash zone (Pritchard and Hogg (2005)). For this reason it was decided in this research to use it to describe the hydrodynamics of a typical energetic flow (bore collapsing) in the swash zone.

5.2 Model Equations

Initial conditions of the SM63 (or PW01) solution are equivalent of those of the dam-break initial value problem

$$\left.\begin{array}{l} h(x,0) = h_0 \\ U(x,0) = 0 \end{array}\right\} \quad \text{for all} \quad x \leq 0, \tag{5.1}$$

and

$$\left.\begin{array}{l} h(x,0) = 0 \\ U(x,0) = 0 \end{array}\right\} \quad \text{for all} \quad x \geq 0 \tag{5.2}$$

where h_0 is the initial bore height or water depth behind the dam (see Stoker (1957)), which throughout the realisation of this research was set to $h_0 = 1$m.

In dimensional form SM63 solution is expressed as:

$$h(x,t) = \frac{(U_b t - \frac{1}{2} g t^2 \tan\theta - x)^2}{9gt^2} \tag{5.3}$$

for which the maximum extent of the run-up is given by

$$x_{max} = \frac{U_b^2}{2g \tan\theta} \tag{5.4}$$

where U_b is the velocity of the shoreline at the initial time and is equal to $2\sqrt{gh_0}$. Note as well, that as we are interested mostly in steep beaches the slope of the beach in all simulations was set equal to $\tan\theta = 0.1$. In their work Shen and Meyer (1963b) did not give an expression for the velocity of the flow but Peregrine and Williams (2001) derived the expression corresponding to (5.3) which in dimensional form is:

$$U(x,t) = \frac{(U_b t - 2gt^2 \tan\theta + 2x)}{3t}. \tag{5.5}$$

It is possible and useful to derive expressions to calculate the evolution in time of the shoreline (x_s) and seaward (x_{sw}) ponits (see Figure 5.2). Setting (5.3) equal to zero the expression of the shoreline point is derived as

$$x_s(t) = U_b t - \frac{1}{2} g t^2 \tan\theta \tag{5.6}$$

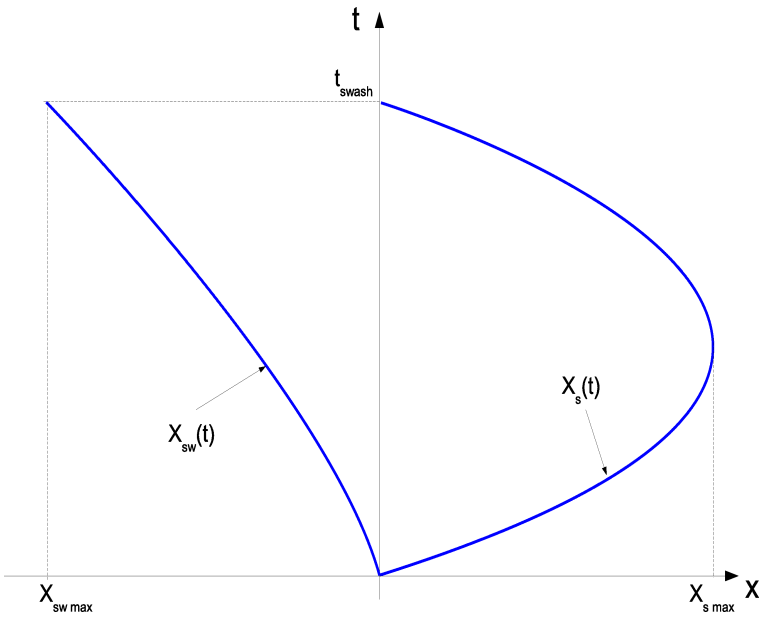

Figure 5.2: Schematical plot of the shoreline x_s and seaward x_{sw} points evolution in time

and again setting (5.3) equal to h_0 (initial constant water depth) the expression for x_{sw} is

$$x_{sw}(t) = -\sqrt{gh_0} - gt\tan\theta. \tag{5.7}$$

Now, for the case under study, it is not possible to get an expression of U in terms of B as done in section 4.2. So a decoupled approach for the morphodynamic module of the model is taken, and equations (3.50) and (3.52) are rewritten here for the sake of clarity

$$\frac{\partial B}{\partial t} = -\xi(A_f - A_c)U^3\frac{\partial P_{fa}}{\partial x} - \xi 3U^2(A_f P_{fa} - A_c P_{fa} + A_c)\frac{\partial U}{\partial x} \tag{5.8}$$

$$\begin{aligned}\frac{\partial P_{fa}}{\partial t} &= \frac{\xi}{L_a}U^3(A_f P_{fs} - A_c P_{fs} - A_f)\frac{\partial P_{fa}}{\partial x} \\ &+ \frac{\xi}{L_a}3U^2(-A_f P_{fa} + A_f P_{fs}P_{fa} + A_c P_{fs} - A_c P_{fs}P_{fa})\frac{\partial U}{\partial x}.\end{aligned} \tag{5.9}$$

It is therefore not necessary to solve these equations simultaneously. Eq. (5.9) can first be solved and the bed calculated via (5.8) as necessary.

From this it is seen that it is useful to derived an expression of $\frac{\partial U}{\partial x}$ from (5.5) as

$$\frac{\partial U}{\partial x} = \frac{2}{3t}. \tag{5.10}$$

5.3 PH05 Analytical Solution

Pritchard and Hogg (2005) studied the effect of sediment advection from the surf zone and the settling lag on the overall sediment transport caused by a PW01 (SM63) swash event. They developed analytical solutions for the net sediment flux based on suspended load for different sediment transport formulae, although the part we use for comparison is that in which it is assumed that there is no settling lag, namely $q = q(u)$. The form used in this research $q \propto u^3$ was not included so that a derivation is detailed in the following.

It is possible to obtain an expression for the instantaneous sediment flux $q(x,t)$ of the form $q = Au^3$ by substituting (5.5) into (3.44) to get

$$q(x,t) = \frac{A}{27}\frac{(U_b t - 2gt^2\tan\theta + 2x)^3}{t^3}. \tag{5.11}$$

In Figure 5.3 instantaneous sediment fluxes are shown for a PW01 (SM63) swash event

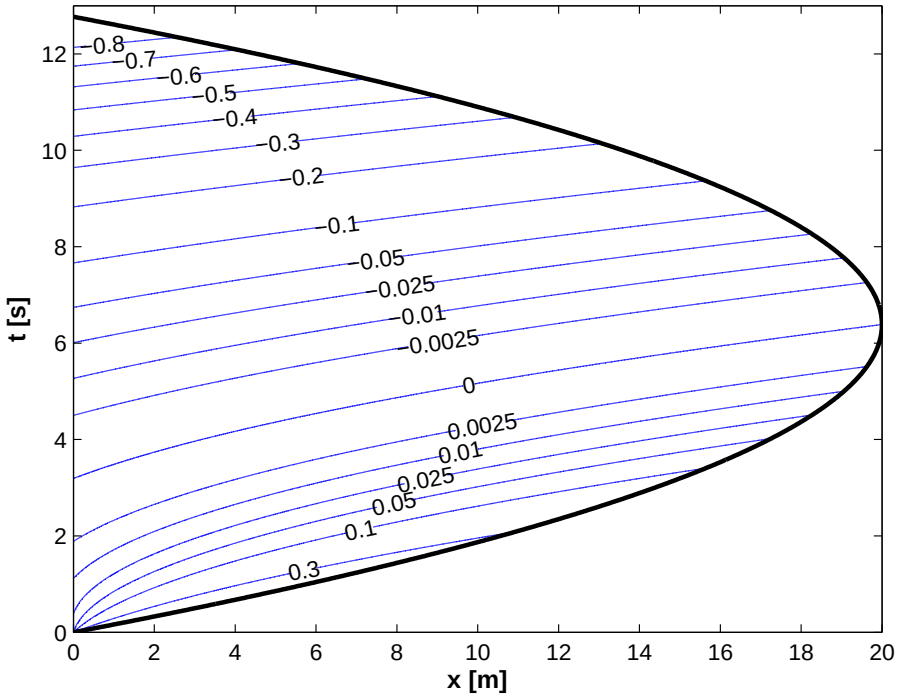

Figure 5.3: Contour plot of instantaneous sediment flux for a PW01 swash event with

$$A = 0.004 s^2/m$$

according to (5.11). In order to generate this graph a representative value of $A = 0.004$ s^2/m for a sediment in the swash zone of a beach is used. This value was used by Kelly (2009) from collected field data in the swash zone of a medium sand beach and it was considered as a characteristic value.

Now, according to Pritchard and Hogg (2005) net sediment fluxes over a swash event can be calculated as

$$Q(x) = \int_{t_{in}(x)}^{t_{de}(x)} q(u)dt = A \int_{t_{in}(x)}^{t_{de}(x)} U^3 dt \tag{5.12}$$

in which $t_{in}(x)$ and $t_{de}(x)$ are the time of inundation and denudation respectively. It is possible to derive expressions for this times of inundation and denudation at a specific location x setting (5.3) equal to zero and solving the resulting second order polynomial:

$$t_{in} = \frac{4\sqrt{gh_0} - \sqrt{16h_0 g - 8gx\tan\theta}}{2g\tan\theta} \tag{5.13}$$

and

$$t_{de} = \frac{4\sqrt{gh_0} + \sqrt{16h_0 g - 8gx\tan\theta}}{2g\tan\theta}. \tag{5.14}$$

Integrating (5.12) net sediment fluxes over a swash event can be obtained analytically according with an specific transport formula, in this case $q = Au^3$. It should be noted that it is possible to obtain net sediment fluxes for a certain period of time (not necessarily the whole swash event) if instead of integrating to t_{de} the integration is made to an specific time t. In Figure 5.4 net sediment fluxes obtained in this manner for different times are shown.

It is possible to obtain as well the bed change at each x position integrating (3.37) with

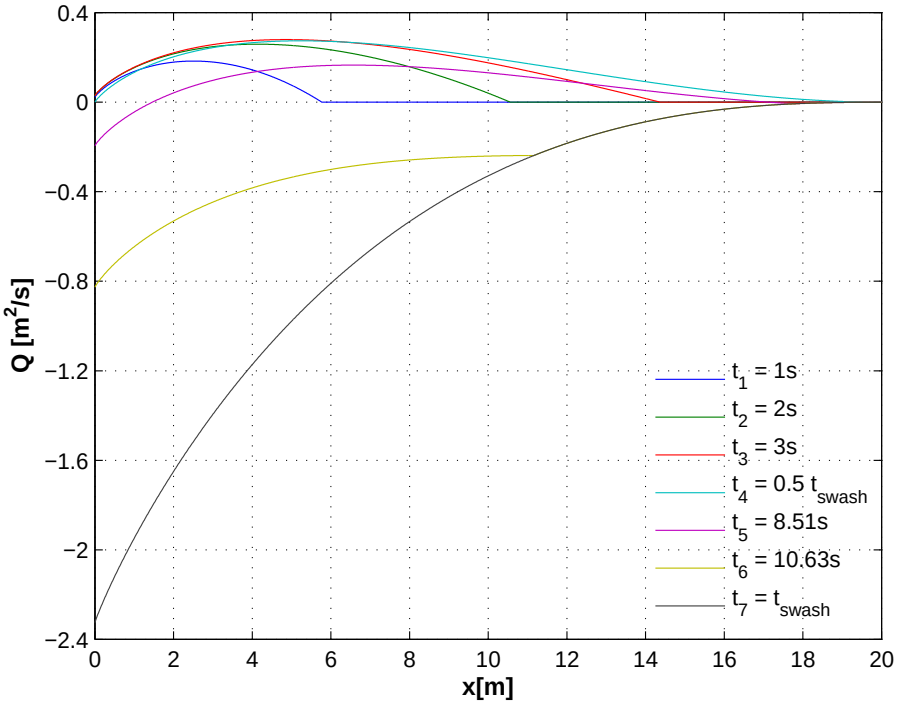

Figure 5.4: Net sediment flux for a PW01 swash event at different times

respect to time to get

$$[B]_{t_{in}}^{t_{de}} = -\xi \int_{t_{in}(x)}^{t_{de}(x)} \frac{\partial q}{\partial x} dt. \tag{5.15}$$

Now for the term the RHS, applying Leibniz rule:

$$\int_{t_{in}(x)}^{t_{de}(x)} \frac{\partial q}{\partial x} dt = \frac{\partial}{\partial x} \int_{t_{in}(x)}^{t_{de}(x)} q(x,t)dt + q(x,t_{in})\frac{\partial t_{in}(x)}{\partial x} - q(x,t_{de})\frac{\partial t_{de}(x)}{\partial x}. \tag{5.16}$$

note here that the term

$$q(x,t_{in})\frac{\partial t_{in}(x)}{\partial x} - q(x,t_{de})\frac{\partial t_{de}(x)}{\partial x} \tag{5.17}$$

represents the change in bed at any x position as the shoreline passes. For a PW01 swash event over a fixed bed this term will be zero due to the symmetry of the tip on

the uprush and the backwash. It was noted by Kelly (2009) that in the case of a mobile bed this might not be exactly zero, however the numerical solution showed that this term was significantly smaller than the main flux divergence term.

So taking this into account and substituting (5.12) into (5.15) we finally get the desired expression to calculate the bed change as

$$[B]_{t_{in}}^{t_{de}} = -\xi \frac{\partial Q}{\partial x}. \tag{5.18}$$

In Figure 5.5 the change in bed relative to the initial bed profile and the evolution of the beach profile are presented for different times during the swash event. It is seen that due to the asymmetry in the velocity caused by the inherent longer duration of the backwash than the uprush, the final beach profile is eroded everywhere.

5.4 Numerical Solution

In this case an uncoupled approximation is used so this allows us to get the numerical solution of the morphodynamic module of the model represented by equations (5.8) and (5.9) using a combination of a MOC based numerical scheme and a finite difference scheme.

Writing (5.8) and (5.9) in their explicit form as

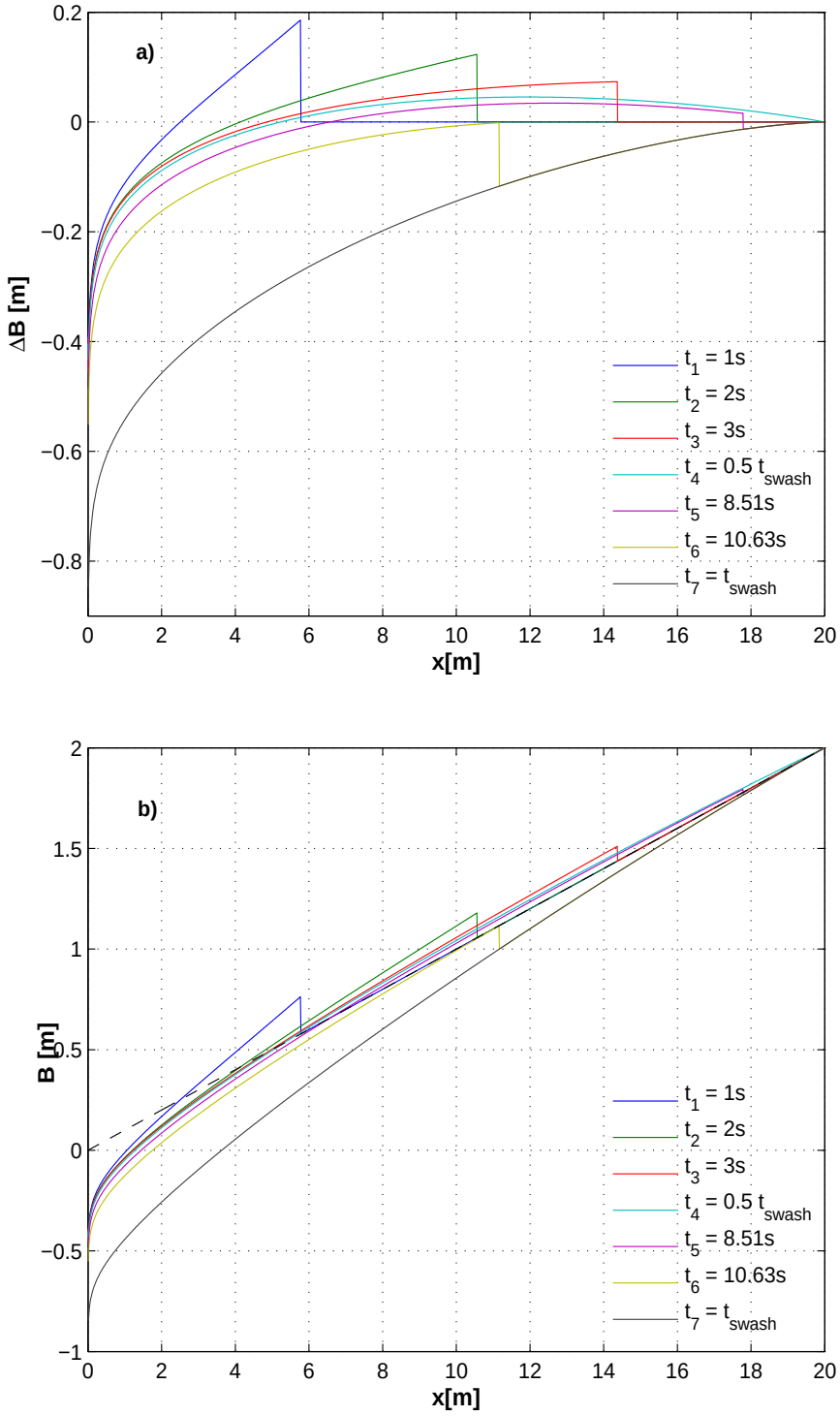

Figure 5.5: a) Change in bed relative to the initial bed profile at different times during a swash event. b) Bed evolution for the same PW01 swash event. Dashed line: initial beach profile.

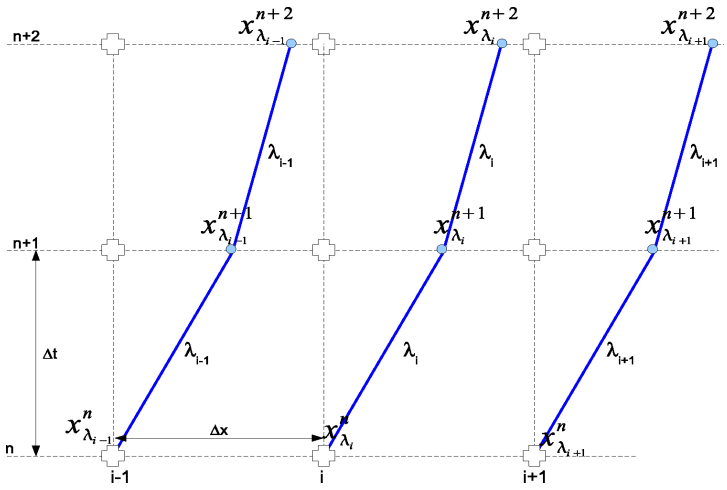

Figure 5.6: Numerical molecule used to solve the morphodynamic module

$$\begin{aligned}\frac{dB}{dt} &= \frac{\partial B}{\partial t} + \frac{dx}{dt}\frac{\partial B}{\partial x} = \\ &- \xi(A_f - A_c)U^3\frac{\partial P_{fa}}{\partial x} - \xi 3U^2(A_f P_{fa} - A_c P_{fa} + A_c)\frac{\partial U}{\partial x} \end{aligned} \tag{5.19}$$

$$\begin{aligned}\frac{dP_{fa}}{dt} &= \frac{\partial P_{fa}}{\partial t} - \frac{\xi}{L_a}U^3(A_f P_{fs} - A_c P_{fs} - A_f)\frac{\partial P_{fa}}{\partial x} = \\ &= \frac{\xi}{L_a}3U^2(-A_f P_{fa} + A_f P_{fs} P_{fa} + A_c P_{fs} - A_c P_{fs} P_{fa})\frac{\partial U}{\partial x} \end{aligned} \tag{5.20}$$

it can be seen that $\frac{dx}{dt} = \lambda = -\frac{\xi}{L_a}U^3(A_f P_{fs} - A_c P_{fs} - A_c)$ is the characteristic associated to P_{fa}.

Now, based on Figure 5.6 the solution procedure in the main body of the flow is as follows:

1. Calculate the slope of the characteristic using data at time level (i,n) with

$$\frac{dx}{dt} = -\frac{\xi}{L_a}(U_i^n)^3(A_f P_{fs_i} - A_c P_{fs_i} - A_f)$$

noting that P_{fs_i} is constant throughout the whole simulation.

2. Calculate the location of point x_λ^{n+1} using

$$x_\lambda^{n+1} = -\frac{\xi}{L_a}(U_i^n)^3(A_f P_{fs_i} - A_c P_{fs_i} - A_f)\Delta t + x_i^n \tag{5.21}$$

3. Solving (5.20) compute at these new locations x_λ^{n+1} the corresponding values of P_{fa} (at time level $n+1$) as

$$P_{fa}^{n+1}(x_\lambda) = \frac{\xi}{L_a} 3(U_{x_\lambda}^{n+1})^2 \Big[- A_f P_{fa}^n(x_\lambda) + A_f P_{fs_i} P_{fa}^n(x_\lambda) + A_c P_{fs_i} - A_c P_{fs_i} P_{fa}^n(x_\lambda) \Big] \frac{\partial U}{\partial x}^{n+1}_{x_\lambda} \Delta t + P_{fa}^n(x_\lambda) \tag{5.22}$$

using P_{fa}^n (the value at the previous time step) for the terms inside the brackets and U and $\frac{\partial U}{\partial x}$ at the new time level $n+1$ at those new locations x_λ^{n+1}

4. Using the P_{fa} values obtained at these new locations x_λ^{n+1} interpolate back onto the original grid points $(i, n+1)$ using linear interpolation. Note that for following time steps the calculation of new P_{fa} are done over the grid of characteristics and then interpolated back onto the original grid.

5. Solve (5.19) over the original grid (Δx,Δt) using central finite differences schemes

$$\frac{\partial B}{\partial t}^{n+\frac{1}{2}}_i = \frac{B_i^{n+1} - B_i^n}{\Delta t} \tag{5.23}$$

$$\frac{\partial P_{fa}}{\partial x}^{n+\frac{1}{2}}_i = \frac{P_{fa_{i+1}}^{n+1} + P_{fa_{i+1}}^n - P_{fa_{i-1}}^{n+1} - P_{fa_{i-1}}^n}{4\Delta x} \tag{5.24}$$

and taking

$$U_i^{n+\frac{1}{2}} = \frac{U_i^{n+1} + U_i^n}{2} \qquad \frac{\partial U}{\partial x}^{n+\frac{1}{2}}_i = \frac{\frac{\partial U}{\partial x}^{n+1}_i + \frac{\partial U}{\partial x}^{n}_i}{2}$$

$$P_{fa_i}^{n+\frac{1}{2}} = \frac{P_{fa_i}^{n+1} + P_{fa_i}^n}{2}$$

to finally get the bed change as

$$B_i^{n+1} = \Phi \Delta t + B_i^n \tag{5.25}$$

in which

$$\begin{aligned}\Phi &= -\xi(A_f - A_c)\left(\frac{U_i^{n+1} + U_i^n}{2}\right)^3 \left[\frac{P_{fa_{i+1}}^{n+1} + P_{fa_{i+1}}^n - P_{fa_{i-1}}^{n+1} - P_{fa_{i-1}}^n}{4\Delta x}\right] \\ &- \xi 3\left(\frac{U_i^{n+1} + U_i^n}{2}\right)^2 \left(A_f\left[\frac{P_{fa_i}^{n+1} + P_{fa_i}^n}{2}\right] - A_c\left[\frac{P_{fa_i}^{n+1} + P_{fa_i}^n}{2}\right] + A_c\right) \\ &\left(\frac{\frac{\partial U}{\partial x}_i^{n+1} + \frac{\partial U}{\partial x}_i^n}{2}\right).\end{aligned}$$

5.5 Initial and Boundary Conditions

5.5.1 Initial Conditions

It was mentioned before that the initial conditions for a PW01 (SM63) swash event are equivalent to a dam-break initial value problem (e.g. equations (5.1) and (5.2)). In this case a singularity exists as the flow variables are multivalued at time $t = 0$. For this reason the numerical solution has to be started at a small time $t = t_0$.

For the flow variables the initial conditions are directly calculated from PW01 solution (5.5) at $t = t_0$.

The bed profile considered at $t = 0$ is a plane sloping bed (see e.g. Figure 5.1). As mentioned before an uncoupled approach is being taken in this research, therefore is assumed that U is unaltered by any bed change. The model was tested using two different initial conditions: one in which it is assumed that the bed profile at $t = t_0$ is the same sloping bed than that at $t = 0$; and another in which the bed profile is calculated at $t = t_0$ using the analytical solution detailed in §5.3. In Figure 5.7 a comparison between the bed change relative to the initial bed profile calculated with the two different initial

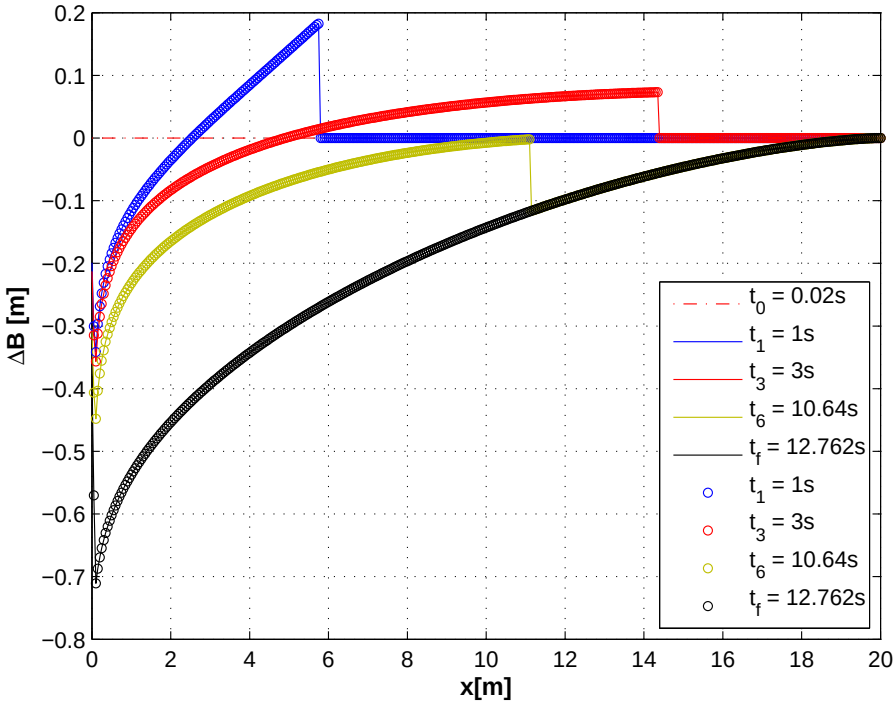

Figure 5.7: Comparison of ΔB at different times of a PW01 swash given by model with different initial conditions in B: a) solid line: plane sloping bed (i.e. same bed profile at $t = 0$ and $t = t_0$); and b) circles: bed profile calculated with the analytical solution at $t = t_0$.

conditions explained above is presented; it is seen that both options produce the same behaviour of the bed change. To be consistent with the uncoupled approach taken it was decided to use the plane sloping bed at $t = 0$ as the initial condition at $t = t_0$.

Based in the same reasoning as the one used for the initial condition in the bed level, the initial condition for the volume fraction P_{fa} at $t = t_0$ is assumed to be the same as that at $t = 0$. The simulations are initialised with a perfectly mixed sediment column, i.e., same proportion of fine and coarse sediment initially over the sloping bed, namely

$$P_{fa}(x, t_0) = P_{ca}(x, t_0) = 0.5. \tag{5.26}$$

This assumption implies as well that the volume fraction in the substrate layer for each sediment is $P_{fs}(x,t) = P_{cs}(x,t_0) = 0.5$, noting that it is always constant in time.

5.5.2 Boundary Conditions

The inherent hydrodynamical nature of a swash event governed by the SM63 solution results in the natural appearance of what might be called "internal" boundary condition at two special points. These two points are the seaward and the shoreline points depicted in Figures 5.1 and 5.2. As can be seen in these figures the seaward point x_{sw} is the point that divides the part of the fluid in which the depth and velocity of the fluid is changing and that in which both variables are constant. The shoreline (wave tip x_s) is that point that defines the natural boundary between the wet and dry beach, sometimes known as the wet-dry boundary. Due to the nature of these points special attention has to be paid to them to carefully solve the governing equations. In this section the treatment of this special points is detailed.

Seaward point and offshore boundary

As the model is a one dimensional one, the treatment of the offshore boundary is done in a simple manner. It is sufficient to ensure that the upstream domain is long enough that it is not necessary to explicitly treat this boundary. This is, we ensure that the x value at the offshore boundary is less than the calculated $x_{sw_{max}}$ (see Figure (5.2)).

At the seaward point a difference in the gradient of the velocity U arises which could be a source of instabilities if the solution is effected through that point without any special handling. Two different cases may possibly appear during the solution of the model, as depicted in Figure 5.8. In this figure the fixed space-time grid is shown with the position of the seaward point at time levels n and $n+1$ and the point at which the calculation is being made is highlighted in black. The location of the characteristic points x_λ at the time levels n and $n+1$ is also shown. As already mentioned the calculation of P_{fa} is done with the method of characteristics (along the characteristic) and the calculation of B is done with a finite differences scheme over the fixed grid. This is why both are depicted in the figure.

For Case A the value of P_{fa} at x_λ^{n+1} is equal to that at x_λ^n due to the fact that at x_λ^{n+1}, $\frac{\partial U}{\partial x} = 0$ so observing eq.(5.22) confirms that $P_{fa}^{n+1} = P_{fa}^n$. To calculate B instead of using the typical finite difference formula over a uniform grid in eq.(5.24) a second order central difference formula over a non-uniform grid is used of the form

$$\frac{\partial f}{\partial x} = \frac{1}{\Delta x_{i+1} + \Delta x_i}\left[\frac{\Delta x_i}{\Delta x_{i+1}}(f_{i+1} - f_i) + \frac{\Delta x_{i+1}}{\Delta x_i}(f_i - f_{i-1})\right] \tag{5.27}$$

in which f is the variable being calculated.

Now, for Case B, the calculation of P_{fa} at x_λ^{n+1} is done using the value of $\frac{\partial U}{\partial x}$ at that time level in eq.(5.22). The value of B is calculated using eq.(5.25) but instead of taking a uniform grid finite difference formula in eq.(5.24), a non-uniform formula eq.(5.27) is used, the Δt in eq.(5.23) is substituted by Δt_r, and the fact that $B_i^n = B_i^{n+1-\Delta t_r}$ and

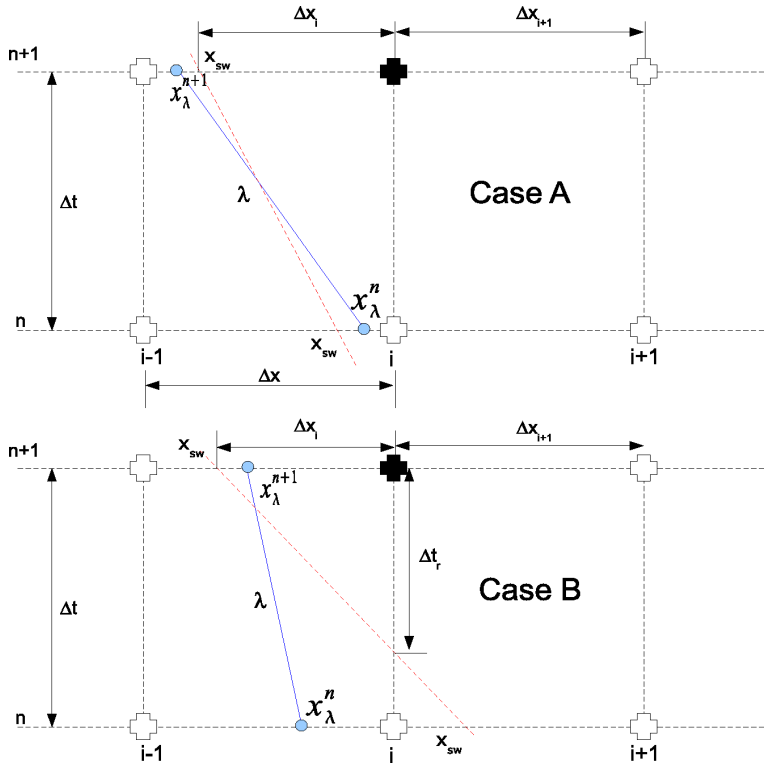

Figure 5.8: Seaward point special cases. — : characteristic λ, — : seaward point x_{sw} path.

$P_{fa_{i-1}}^{n+1} = P_{fa_{x_{sw}}}^{n+1}$ is used.

Shoreline boundary

The downstream boundary (shoreline) is the interface between the fluid and the dry bed and, as such, the boundary is a wet-dry boundary. At this boundary a discontinuity in the dependent variables emerges and causes what it was called a moving boundary condition which is treated explicitly with the help of the shock conditions, which are derived next.

Shock Conditions

The derivation of the shock condition for P_{fa} is as follows. First, it is convenient to derive a conservation form of the governing equation. So, taking eq.(3.47) and substituting into eq.(3.37) we get

$$\frac{\partial B}{\partial t} = -\xi \left(\frac{\partial q_f}{\partial x} + \frac{\partial q_c}{\partial x} \right) \tag{5.28}$$

and substituting this into (3.43)

$$\frac{\partial P_{fa}}{\partial t} = -\frac{\xi}{L_a} \left[P_{cs} \frac{\partial q_f}{\partial x} - P_{fs} \frac{\partial q_c}{\partial x} \right], \tag{5.29}$$

and recalling that $P_{cs} = 1 - P_{fs}$ and arranging terms, we finally get

$$\frac{\partial P_{fa}}{\partial t} = -\frac{\xi}{L_a} \left[\frac{\partial q_f}{\partial x} - P_{fs} \left(\frac{\partial q_f}{\partial x} + \frac{\partial q_c}{\partial x} \right) \right]. \tag{5.30}$$

The shock condition is obtained integrating eq.(5.30) over the discontinuity. Here we do this by integrating between two fixed points x_1 and x_2 (see Figure 5.9). Doing this we

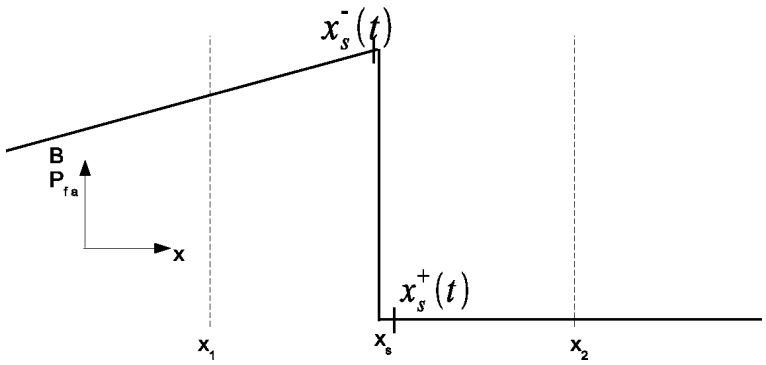

Figure 5.9: Schematical shock

can express

$$\int_{x_1}^{x_2} \frac{\partial P_{fa}}{\partial t} dx = -\frac{\xi}{L_a} \int_{x_1}^{x_2} \frac{\partial q_f}{\partial x} dx + \int_{x_1}^{x_2} P_{fs} \left(\frac{\partial q_f}{\partial x} + \frac{\partial q_c}{\partial x} \right) dx. \tag{5.31}$$

Working with term on the LHS, and applying Leibniz' rule,

$$\int_{x_1}^{x_2} \frac{\partial P_{fa}}{\partial t} dx = \frac{\partial}{\partial t} \int_{x_1}^{x_2} P_{fa} dx + P_{fa}(x_1, t) \frac{\partial x_1}{\partial t} - P_{fa}(x_2, t) \frac{\partial x_2}{\partial t}, \tag{5.32}$$

in which it is seen that as x_1 and x_2 are time independent: $\frac{\partial x_1}{\partial t} = 0$ and $\frac{\partial x_2}{\partial t} = 0$. Splitting the range of integration either side of the shock we obtain

$$\frac{\partial}{\partial t} \int_{x_1}^{x_2} P_{fa} dx = \frac{\partial}{\partial t} \int_{x_1}^{x_s^-(t)} P_{fa} dx + \int_{x_s^+(t)}^{x_2} P_{fa} dx. \tag{5.33}$$

Solving these two terms using once again the Leibniz' theorem

$$\begin{aligned} \frac{\partial}{\partial t} \int_{x_1}^{x_s^-} P_{fa} dx &= \int_{x_1}^{x_s^-} \frac{\partial P_{fa}}{\partial t} dx - P_{fa}(x_1, t) \frac{\partial x_1}{\partial t} + P_{fa}(x_s^-, t) \frac{\partial x_s^-}{\partial t} \\ \frac{\partial}{\partial t} \int_{x_s^+}^{x_2} P_{fa} dx &= \int_{x_s^+}^{x_2} \frac{\partial P_{fa}}{\partial t} dx - P_{fa}(x_s^+, t) \frac{\partial x_s^+}{\partial t} + P_{fa}(x_2, t) \frac{\partial x_2}{\partial t}, \end{aligned} \tag{5.34}$$

and simplifying using relation $\frac{\partial x_{1,2}}{\partial t} = 0$ we get

$$\begin{aligned} \frac{\partial}{\partial t} \int_{x_1}^{x_s^-} P_{fa} dx &= \int_{x_1}^{x_s^-} \frac{\partial P_{fa}}{\partial t} dx + P_{fa}(x_s^-, t) \frac{\partial x_s^-}{\partial t} \\ \frac{\partial}{\partial t} \int_{x_s^+}^{x_2} P_{fa} dx &= \int_{x_s^+}^{x_2} \frac{\partial P_{fa}}{\partial t} dx - P_{fa}(x_s^+, t) \frac{\partial x_s^+}{\partial t}. \end{aligned} \tag{5.35}$$

Now we make the extent of the shock very small (i.e. $x_1 \to x_s^-$ and $x_2 \to x_s^+$), therefore

$$\int_{x_1}^{x_s^-} \frac{\partial P_{fa}}{\partial t} dx \to 0$$
$$\int_{x_s^+}^{x_2} \frac{\partial P_{fa}}{\partial t} dx \to 0 \tag{5.36}$$

as $x_1 \to x_s^-$ and $x_2 \to x_s^+$. Then if we note that $U_s = \frac{\partial x_s}{\partial t} = \frac{\partial x_s^+}{\partial t} = \frac{\partial x_s^-}{\partial t}$, finally (5.32) is reduced to

$$\frac{\partial}{\partial t} \int_{x_1}^{x_2} P_{fa} dx = -U_s \left[P_{fa}(x,t) \right]_{x_1}^{x_2}. \tag{5.37}$$

Now substituting eq.(5.37) into eq.(5.31) we get

$$-U_s \left[P_{fa}(x,t) \right]_{x_1}^{x_2} = -\frac{\xi}{L_a} [q_f]_{x_1}^{x_2} + \frac{\xi}{L_a} P_{fs} [q_f + q_c]_{x_1}^{x_2}. \tag{5.38}$$

Now,recalling that $q_f(x_2,t) = 0$ and $q_c(x_2,t) = 0$, and substituting (3.48) and (3.49) into (5.38), we can finally get the shock condition for P_{fa} as

$$P_{fa}(x_1,t) = \frac{P_{fa}(x_2,t) - \frac{\xi}{L_a} P_{fs} A_c U_s^2}{1 + \frac{\xi}{L_a}(-A_f + A_f P_{fs} - A_c P_{fs}}. \tag{5.39}$$

To derive the shock condition for B we integrate eq.(5.28) from x_1 to x_2

$$\int_{x_1}^{x_2} \frac{\partial B}{\partial t} dx = -\xi \left[\int_{x_1}^{x_2} \frac{\partial q_f}{\partial x} dx + \int_{x_1}^{x_2} \frac{\partial q_c}{\partial x} dx \right]. \tag{5.40}$$

Using the Leibniz theorem to solve the term on the LHS of this equation

$$\int_{x_1}^{x_2} \frac{\partial B}{\partial t} dx = \frac{\partial}{\partial t} \int_{x_1}^{x_2} B dx + B(x_1,t) \frac{\partial x_1}{\partial t} - B(x_2,t) \frac{\partial x_2}{\partial t}. \tag{5.41}$$

Recalling that x_1 and x_2 are time independent and splitting the range of integration in the same way as above, the first term on the RHS is

$$\frac{\partial}{\partial t} \int_{x_1}^{x_2} B dx = \frac{\partial}{\partial t} \int_{x_1}^{x_s^-} B dx + \frac{\partial}{\partial t} \int_{x_s^+}^{x_2} B dx. \tag{5.42}$$

The two terms on the RHS of this equation can be expressed, using the Leibniz theorem, as

$$\begin{aligned}\frac{\partial}{\partial t}\int_{x_1}^{x_s^-} B dx &= \int_{x_1}^{x_s^-} \frac{\partial B}{\partial t} dx - B(x_1,t)\frac{\partial x_1}{\partial t} + B(x_s^-,t)\frac{\partial x_s^-}{\partial t} \\ \frac{\partial}{\partial t}\int_{x_s^+}^{x_2} B dx &= \int_{x_s^+}^{x_2} \frac{\partial B}{\partial t} dx - B(x_s^+,t)\frac{\partial x_s^+}{\partial t} + B(x_2,t)\frac{\partial x_2}{\partial t}\end{aligned} \tag{5.43}$$

and once again compressing the extend of the shock as $x_1 \to x_s^-$ and $x_2 \to x_s^+$ it can be stated that

$$\begin{aligned}\int_{x_1}^{x_s^-} \frac{\partial B}{\partial t} dx &\to 0 \\ \int_{x_s^+}^{x_2} \frac{\partial B}{\partial t} dx &\to 0\end{aligned} \tag{5.44}$$

so substituting this into eq.(5.43) and recalling that $\frac{\partial x_{1,2}}{\partial t} = 0$ and that $U_s = \frac{\partial x_s}{\partial t} = \frac{\partial x_s^+}{\partial t} = \frac{\partial x_s^-}{\partial t}$ we finally get

$$\int_{x_1}^{x_2} \frac{\partial B}{\partial t} dx = \frac{\partial}{\partial t}\int_{x_1}^{x_2} B dx = -U_s [B(x,t)]_{x_1}^{x_2}. \tag{5.45}$$

So, now substituting eq.(5.45) into eq.(5.40) we get

$$-U_s [B(x,t)]_{x_1}^{x_2} = -\xi \left([q_f]_{x_1}^{x_2} + [q_c]_{x_1}^{x_2} \right). \tag{5.46}$$

Recalling once again that $q_f(x_2,t) = 0$ and $q_c(x_2,t) = 0$ and substituting eq.(3.48) and eq.(3.49) into eq.(5.46), we finally get the shock condition for B as

$$B(x_1,t) = B(x_2,t) + \xi[(A_f - A_c)P_{fa}(x_1,t) + A_c]U_s^2. \tag{5.47}$$

Shoreline Special Cases

In Figure 5.10 the three different cases encountered during the solution of the model are shown. In this figure the fixed space-time grid is shown with the position of the

shoreline point at time levels n and $n+1$ and the point at which the calculation of B is being made is highlighted in black. The location of the characteristic ponits x_λ at this times levels n and $n+1$ is also shown due to the fact that the calculation of P_{fa} is done along the characteristics (i.e. over the grid of characteristics), whereas the calculation of B is done with a finite differences scheme over the fixed grid.

Note that Cases A and B correspond to the stage of the swash in which the flow is moving up the slope (i.e uprush stage), and Case C corresponds to that stage at which the fluid is receding back downslope (i.e. backwash), so that the treatment of the cases is slightly different as detailed below.

Case A corresponds to that when a point is added into the domain (i.e. new characteristic) and a value of P_{fa} should be calculated for that point. It is noted here that these new points lie between the last characteristic and the shoreline point. This means that first the shock condition eq.(5.37) is applied to find the value of P_{fa} at the left of the shock, recalling that in the uprush $P_{fa}(x_2,t) = P^0_{fa_{i+1}}$. Then it is possible to obtain the value at point i interpolating between the last characteristic and the shock.

Now, the value of B is calculated as follows. First the shock condition eq.(5.47) is used to find the value of B on the left of the shock knowing that $B(x_2,t)$ in the uprush is $B(x_2,t_0)$, the initial value. Then B_i^{n+1} is calculated interpolating between B_{i-1}^{n+1} and the value at the shoreline calculated with the shock condition.

Case B is similar to Case A, the difference is that the added characteristic point lies

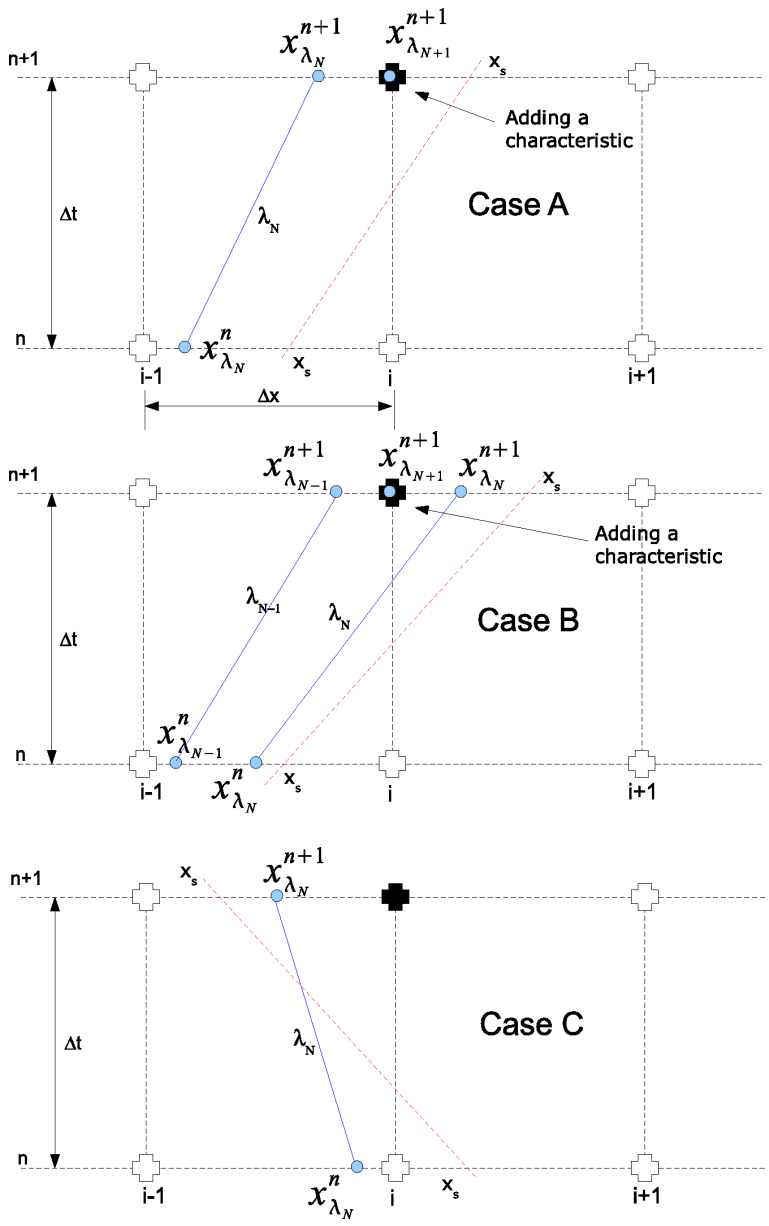

Figure 5.10: Shoreline special cases.— : characteristics λ, — : shoreline point x_s path.

between two already known characteristics, so that in this case there is no need to use the shock condition and the value of P_{fa}^{n+1} at that point is simply interpolated between the values at the sourrounding characteristics. The calculation of B is done in exactly the same way as in case A.

Now, Case C corresponds to that of a swash flow receding downslope and the treatment of the boundary is different. In this case the characteristic is going out of the domain, this means that $U_{x_{\lambda_N}}^{n+1} = 0$ and $\frac{\partial U}{\partial x}{}^{n+1}_{x_{\lambda_N}} = 0$, so in this case we use the shock condition eq.(5.37) to calculate $P_{fa}(x_2)^{n+1}$ using the fact that $P_{fa}(x_1)^{n+1} = P_{fa}(x_{\lambda_{N-1}})^{n+1}$ and assume that $P_{fa}(x_2)^{n+1} = P_{fa}(x_{\lambda_N})^n$. The calculation of B_{i-1}^{n+1} needs particular attention. In this case the shock condition is not used and B on the left of the shock is calculated extrapolating from two previous mesh point (i.e. $(i-2)$ and $(i-3)$) and then the value at '$i-1$' is interpolated.

It is clear that for Cases A and B (uprush cases), there is no need for special treatment of the point on the right of the shock, as in these cases it is evident that $B_{i+1}^{n+1} = B_{i+1}^n$. However, in Case C this is not the case and special treatment of this point should be done. First, the shock condition eq.(5.47) is used to find the value of B on the right of the shock using the interpolated value on the left of the shock and solving for $B(x_2, t)$ at the rigth. Then B_i^{n+1} is calculated interpolating between the value on the right of the shock and the following mesh point '$i+1$'.

5.6 Non-physical Region

Before moving on, it is important to note that during the development of the model a region in the domain where a non-physical behaviour can be observed is sometimes encountered. In this section the description, identification, calculation and supression of this non-physical region is detailed.

5.6.1 Identifying the non-physical region

The 'non-physical' region is that region in which it was seen that the velocity at which P_{fa} was propagating (i.e. λ) was bigger than the velocity of the fluid U which seems physically impossible (see Figure 5.11). To help us understand and identify this region the following procedure was done. We know that at the shoreline the velocity at which P_{fa} is propagating (λ) must be equal to the velocity of the fluid (which is also equal to the shoreline velocity U_s, see Figure 5.11). Then, knowing point (x_r, t_r), it is possible to integrate back along λ to calculate the path of the curve at which the condition $\lambda = U_s$ is met, which is therefore the curve (Γ) bounding the non-physical region ($\lambda > U$).

So, we know that

$$\lambda = \frac{dx}{dt} = -\frac{\xi}{L_a}(A_f P_{fs} - A_c P_{fs} - A_f)U^3 \tag{5.48}$$

and an expression of U_s can be easily obtained taking the derivative of (5.6) with respect to time as

$$\frac{dx_s}{dt} = U_s = U_b - gt\tan\theta. \tag{5.49}$$

So, setting $\lambda = U_s$, and substituting into eq.(5.48) we can finally get the following second

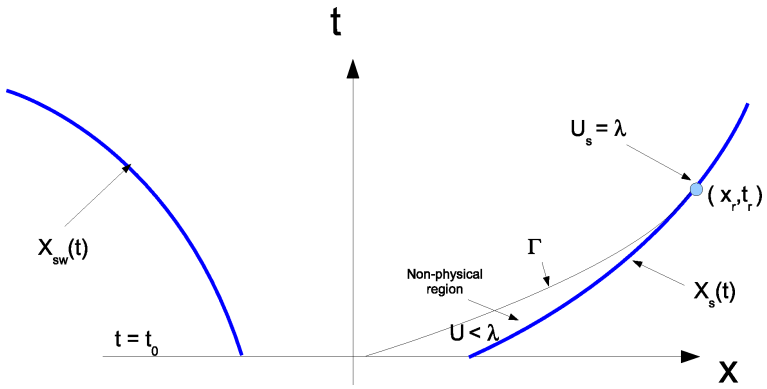

Figure 5.11: Sketch showing the paths followed by the seaward x_{sw} and shoreline x_s points (blue lines) and curve Σ which divides the region in which a physical and a non-physical behaviour was observed.

order polynomial

$$g^2 \tan^2\theta t^2 - 2U_b g \tan\theta t + U_b^2 + \frac{L_a}{\xi(A_f P_{fs} - A_c P_{fs} - A_f)} = 0. \tag{5.50}$$

This can be solved and two real and positive roots are found; one root resulted a time at the early stage of the uprush and the other a time at the latest stage of the backwash. Therefore, taking the root that is physicall meaningful regarding our problem, i.e. the time in the uprush, we have

$$t_r = \frac{U_b - \sqrt{-\dfrac{L_a}{\xi(A_f P_{fs} - A_c P_{fs} - A_f)}}}{g \tan\theta}. \tag{5.51}$$

Once t_r is obtained, x_r can be calculated substituting the t_r into eq.(5.6).

With point (x_r, t_r) known it is possible to know the path of the line depicted in Figure (5.11) integrating back eq.(5.48) form that point to t_0.

5.6.2 Case without non-physical region

The presence of the non-physical region is related with the magnitude of the thickness of the active layer (L_a) and it was found that it is possible to find a condition on L_a at which the absence of this region could be guaranteed. It was noted that it is possible to avoid the precense of the 'non-physical' region by simply ensuring that the condition $\lambda < U$ at the shoreline is met since the initial time t_0. So using eq.(5.48) to express condition $\lambda < U_s$ as

$$-\frac{\xi}{L_a}(A_f P_{fs} - A_c P_{fs} - A_f)U_s^2 < 1 \tag{5.52}$$

and then isolating L_a and using eq.(5.49) valueted at t_0 we finally get the condition that must be met in order to avoid the non-physical region as

$$L_a > -(U_b - g t_0 \tan\theta)^2 \xi (A_f P_{fs} - A_c P_{fs} - A_f). \tag{5.53}$$

5.7 Results

It was already shown in appendix B that the model developed here is capable of reproducing with high accuracy the behaviour of the beach profile driven by a PW01 swash event in which the beach sediment is considered as being composed of just one grain size and the flow is unaffected by the beach change. The model is in good agreement with the solution predicted by PH05.

Now, the principal objective of this research is to gain physical insight into the process

of transport and sorting of different sediment classes (i.e. sediment grain sizes). For this reason numerical tests were designed in which two different sediment sizes are present in the beach. A set of eight different numerical experiments where performed. The base point of these tests is the case examined by Kelly (2009) and Kelly and Dodd (2010) in which the value of A was derived from field measurements over the swash zone of a medium grain size beach. The value was found equal to $0.004s^2/m$ and from now on it is denoted A_K.

The set of eight tests was divided into two parts (see Table 5.1). The two sets of experiments consist of fixing the value of one of the fractions to A_K, and making the other progressively coarser or finer. In the first set, corresponding to the first four tests, the fine fraction was fixed to A_K and A_c was made progressively smaller (i.e. the sediment gets coarser) than A_K by 1%, 10%, 30% and 50% respectively. In the second set (tests 5, 6, 7 and 8), A_c was fixed to A_K and A_f was progressively bigger (i.e. sediment gets finer) in 1%, 10%, 30% and 50% respectively.

It is important to note that the model is initialised with the same amount (volume fraction P_{fa}) of both sediment fractions: $P_{fa} = P_{ca} = 0.5$. The value of the active layer thickness was chosen taking into account the need to avoid the presence of the non-physical region (c.f. §5.6.2).

Table 5.1: SM63 Tests for different A_f and A_c

Test No.	$A_f[s^2/m]$	$A_c[s^2/m]$	**Description**	L_a calculated [m]	L_a used [m]
1	0.004	0.00396	$A_f = A_K$; A_c is 1 % smaller than A_K coarse fraction getting coarser	0.27	0.35
2	0.004	0.0036	$A_f = A_K$; A_c is 10 % smaller than A_K coarse fraction getting coarser	0.25	0.35
3	0.004	0.0028	$A_f = A_K$; A_c is 30 % smaller than A_K coarse fraction getting coarser	0.22	0.35
4	0.004	0.002	$A_f = A_K$; A_c is 50 % smaller than A_K coarse fraction getting coarser	0.19	0.35
5	0.00404	0.004	$A_c = A_K$; A_f is 1 % bigger than A_K fine fraction getting finer	0.26	0.35
6	0.0044	0.004	$A_c = A_K$; A_f is 10 % bigger than A_K fine fraction getting finer	0.27	0.35
7	0.0052	0.004	$A_c = A_K$; A_f is 30 % bigger than A_K fine fraction getting finer	0.3	0.35
8	0.006	0.004	$A_c = A_K$; A_f is 50 % bigger than A_K fine fraction getting finer	0.33	0.35

5.7.1 General Results

It was found that for all the tests the model solution shows similar behaviour. For this reason, an example of the general behaviour is shown in Figures 5.12 and 5.13. In these figures the evolution in time for the fine volume fraction and the bed level for Test 3 are shown and analysed.

Regarding the behaviour of the fine volume fraction (see Figure 5.12) it can be seen that in the uprush phase of the swash the fine sediment is taken by the flow from the lower part of the swash zone and is deposited along the upper zone of the swash zone. Then in the backwash this fine sediment transported up the beach in the uprush is now transported offshore by the backwash, and especially by the tip of the flow, leaving the final bed profile with less fine sediment than that initially in place.

Now from Figure 5.13, it can be seen that similar to what happens with the fine volume fraction, in the uprush the sediment taken from the lower part of the swash zone is transported to the upper zone; and in the backwash the flow and specially the wave tip erodes the sediment offshore.

5.7.2 Comparison for cases in which the coarse sediment is made progressively coarser

In Figures 5.14 and 5.15 a comparison between the results given by the model when the coarse sediment is made progressively coarser is presented.

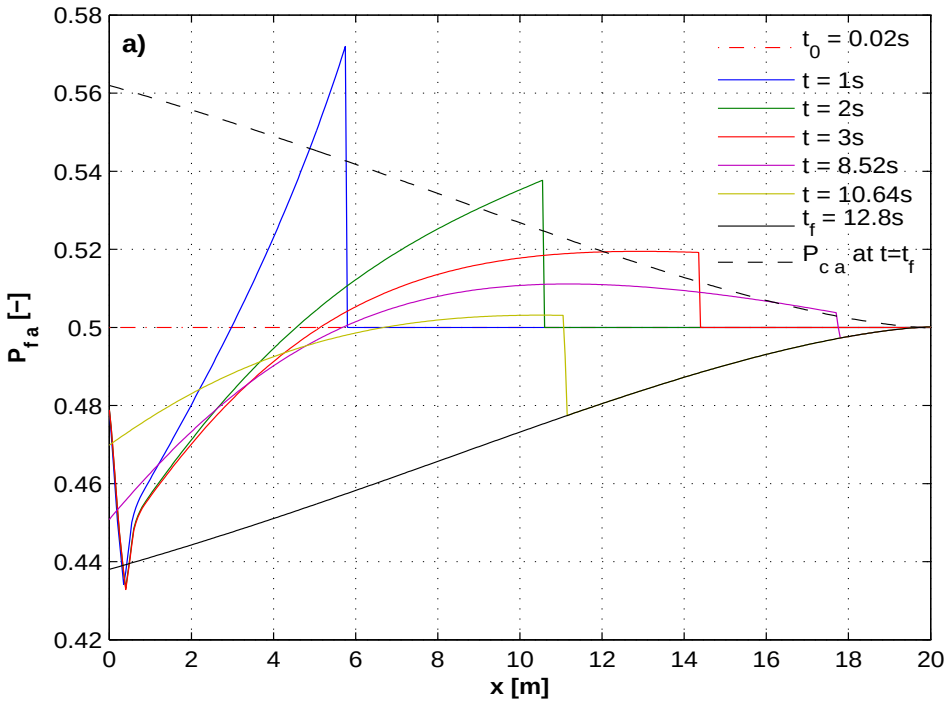

Figure 5.12: Fine volume fraction evolution given by the model for Test 3.

Regarding the fine volume fraction evolution the following conclusion can be stated (see Figure 5.14). When the coarse fraction is made progressively coarser inherently the fine fraction is made finer with respect to the coarse fraction, although is kept fixed. Therefore, the final fine volume fraction decreases accordingly. That is, more coarse fraction and less fine sediment is left over the beach profile. In other words, a progressively coarser coarse fraction makes that fraction more difficult to transport, and therefore the easier it will be to move the fine sediment (relatively to the coarse fraction).

Now looking at Figure 5.15 the results given by the model are physically coherent with what one can expect in a beach where the coarse sediment is made progressively coarser.

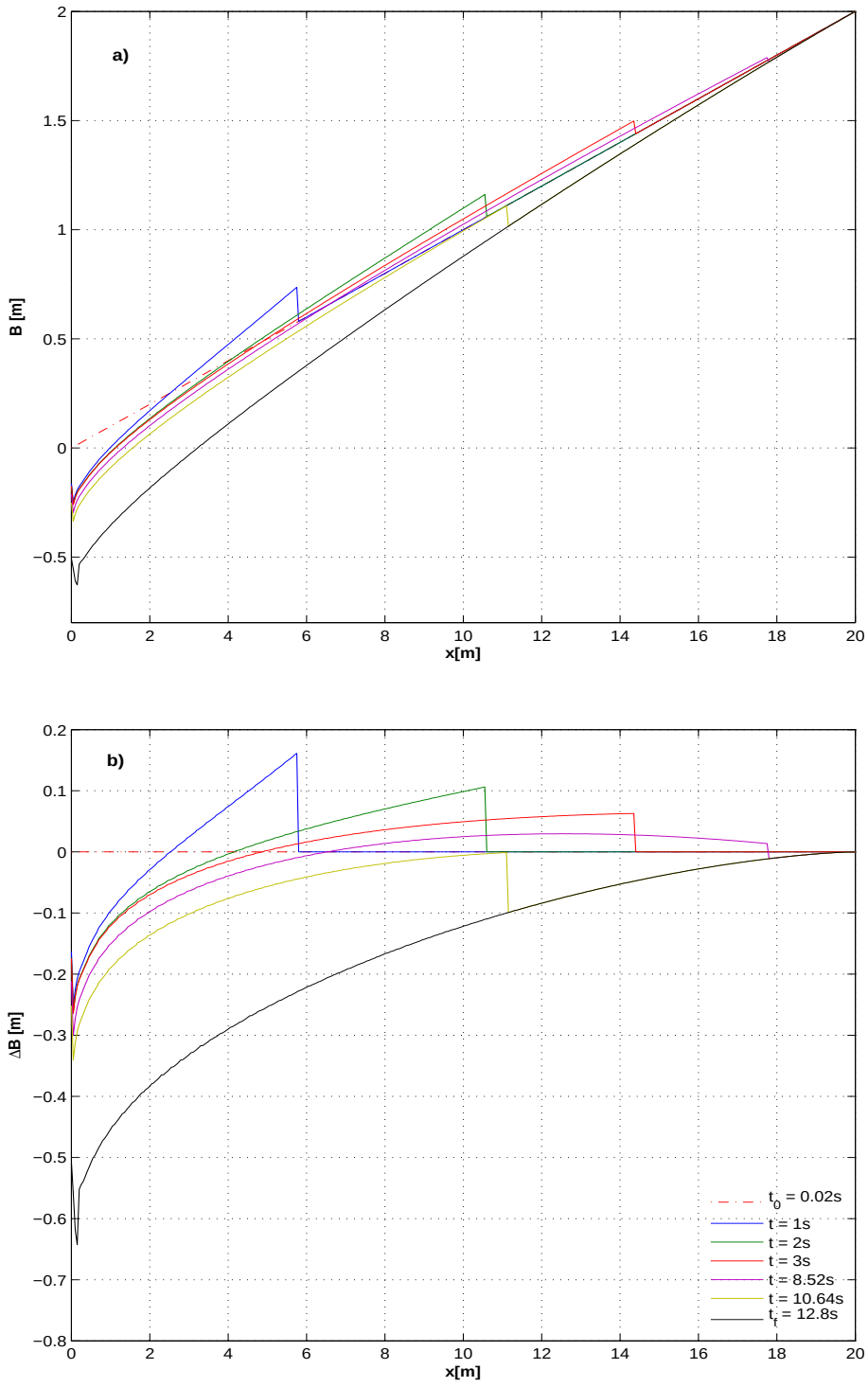

Figure 5.13: Bed level results given by the model for Test 3: a) Bed level evolution; b) Change in bed relative to the initial bed profile.

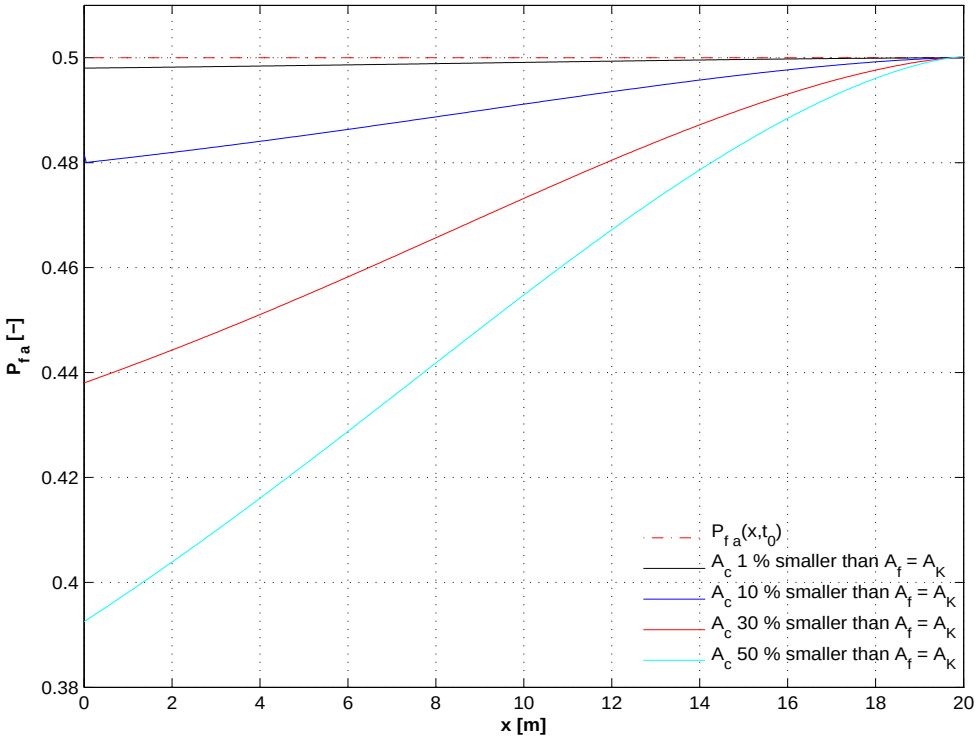

Figure 5.14: Comparison of final fine volume fraction P_{fa} for the cases where the coarse fraction gets coarser.

That is, the coarser the coarse sediment is made, the harder it is to transport, and therefore there is less erosion of the bed profile.

5.7.3 Results for cases in which the fine sediment is made progressively finer

Now the results for the cases when the fine sediment is made progressively finer are compared and analysed with the aid of Figures 5.16 and 5.17.

In Figure 5.16 results regarding the fine volume fraction P_{fa} are shown. The result given by this figure agrees with what one would expect from physical principles: the finer the fine fraction is made, the more that fine sediment will be removed from the bed, and, as a consequence, the less fine volume fraction will be present after the swash event.

In the case of bed level results Figure 5.17 shows that, similar to the case where the coarse fraction is made progressively coarser, in this case when the fine fraction is made progressively finer it is more easily eroded from the bed, therefore more bed change in bed level will result. This shows that the model correctly predicts the physical effect of the sediment mixture being more movable from the bed.

Now, it very intersting to compare Figures 5.14 and 5.16 to analyse the behaviour of the fine volume fraction when the fine and the coarse fraction are changed in the same proportion (i.e. tests where the difference between A_f and A_c is the same). To this end Figure 5.18a is presented. From this comparison it can be seen that when the sediment

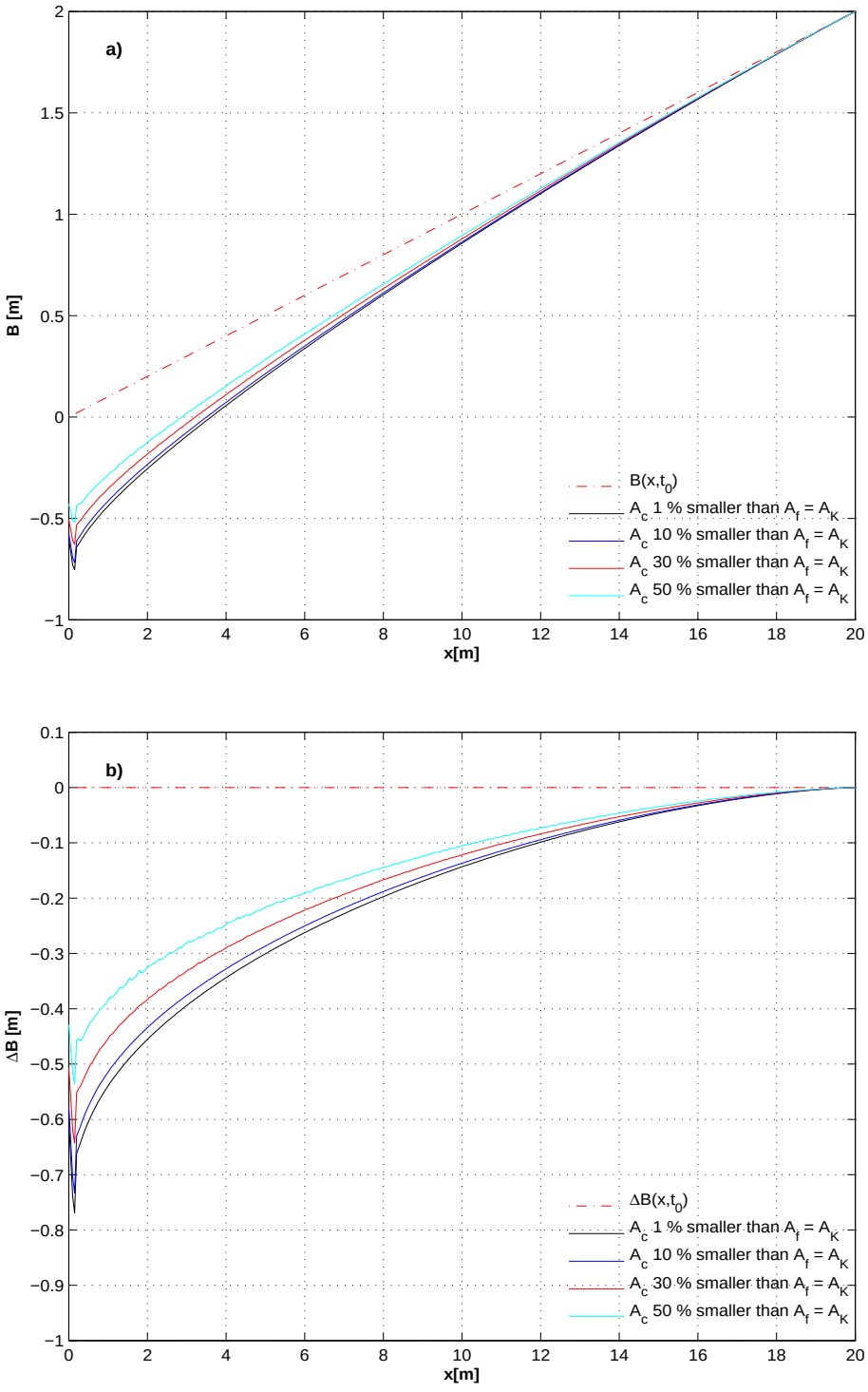

Figure 5.15: Bed profile results when the coarse fraction is made progressively coarser: a) Final bed level. b) Final change in bed relative to the initial bed level.

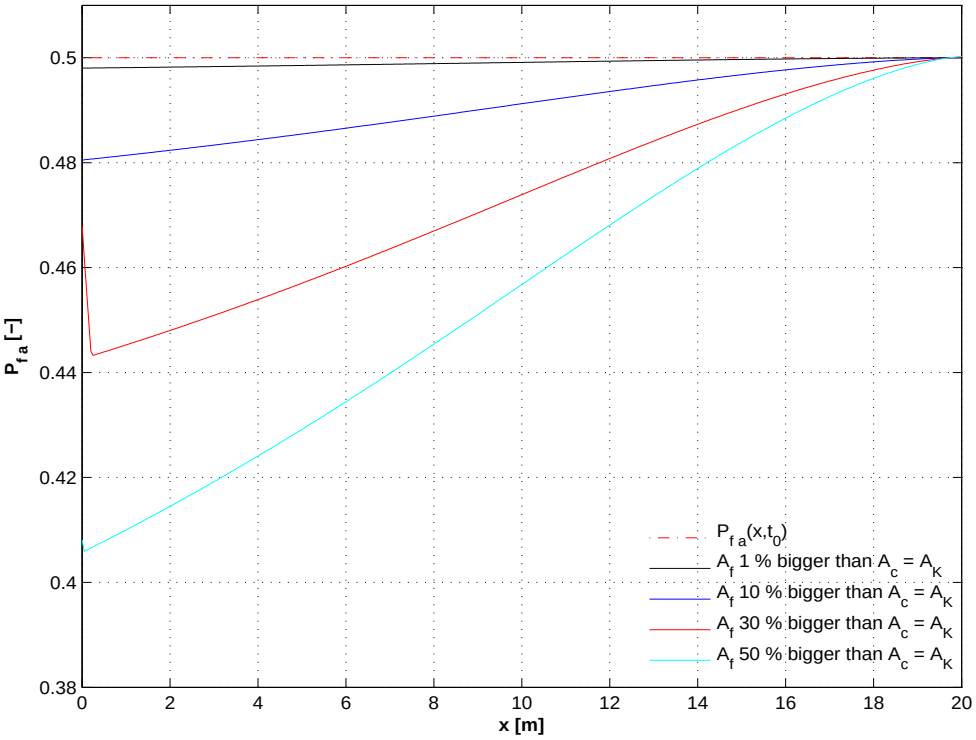

Figure 5.16: Comparison of final fine volume fraction P_{fa} for the cases where the fine fraction gets finer.

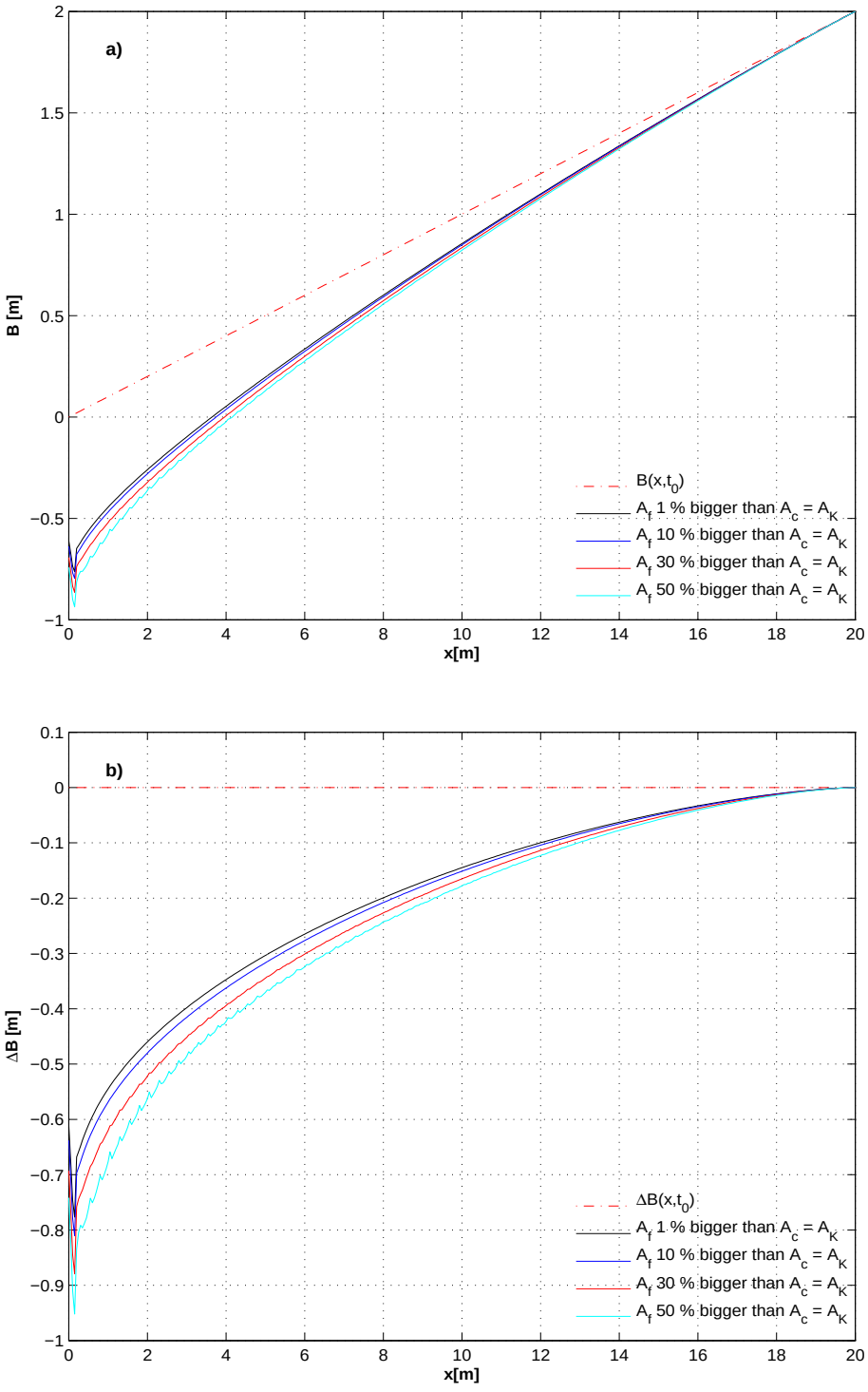

Figure 5.17: Bed profile results when the fine fraction is made progressively finer: a) Final bed level. b) Final change in bed relative to the initial bed level.

is made finer the final fine volume fraction is less than that when the sediment is made coarser in the same proportion; and this difference increases as this difference is made bigger.

This behaviour can be easily explained using the fine volume fraction governing equation (3.52). First doing the case in which A_c is made progressively smaller (i.e. the coarse sediment is made progressively coarser), and expressing this as

$$A_f = A_K \qquad \text{and} \qquad A_c = (1-\epsilon)A_K \tag{5.54}$$

in which ϵ is the proportion of A_k that A_c is being modified (i.e. 1%, 10%, 30% and 50%); and then substituting (5.54) into (3.52), after some algebraic steps we get

$$\begin{aligned}\frac{\partial P_{fa}}{\partial t} = & - \frac{\xi}{L_a}\Big[(A_K - \epsilon A_K P_{fs})U^2\frac{\partial P_{fa}}{\partial x} \\ & + (A_K P_{fa} - A_K P_{fs} + \epsilon A_K P_{fs} - \epsilon A_K P_{fs} P_{fa})3U^2\frac{\partial U}{\partial x}\Big].\end{aligned} \tag{5.55}$$

Now, in a similar way, doing the case in which A_f is made progressively bigger (i.e. the fine sediment is made progressively finer), we can express this as

$$A_f = (1+\epsilon)A_K \qquad \text{and} \qquad A_c = A_K \tag{5.56}$$

and again substituting this into eq. (3.52) we obtain

$$\begin{aligned}\frac{\partial P_{fa}}{\partial t} = & - \frac{\xi}{L_a}\Big[(A_K - \epsilon A_K P_{fs})U^2\frac{\partial P_{fa}}{\partial x} \\ & + (A_K P_{fa} - A_K P_{fs} + \epsilon A_K P_{fa} - \epsilon A_K P_{fs} P_{fa})3U^2\frac{\partial U}{\partial x}\Big].\end{aligned} \tag{5.57}$$

Note that comparing both equations they are almost the same, but actually, there is a small difference in the third term inside the second parentheses. In eq.(5.55) is $\epsilon A_K P_{fs}$ and in eq.(5.57) is $\epsilon A_K P_{fa}$. This explains the difference observed in Figure 5.18a, because while P_{fs} is maintained constant along the whole simulation, P_{fa} is varying and

in fact, getting smaller and smaller throughout the simulation, this results in less change in P_{fa} for the cases in which the fine sediment (i.e A_f) is being modified than those in which the coarse (i.e.A_c) is changed.

In Figure 5.18b a comparison of the bed change given by all tests is presented. It is clear that the behaviour follows what is expected from basic physical principles: the sediment transport, and thereforethe bed change, is bigger for the case in which the sediments in the mixture are finer and viceversa.

This can be explained doing a similar analysis than what was done for P_{fa}. For the case in which the coarse sediment A_c is made smaller; substituting (5.54) into (3.50) we get

$$\frac{\partial B}{\partial t} = -\xi\Big[\epsilon A_K \frac{\partial P_{fa}}{\partial x} U^3 + (\epsilon A_K P_{fa} + A_K - \epsilon A_K) 3U^2 \frac{\partial U}{\partial x}\Big]. \tag{5.58}$$

Then for the case in which the fine sediment is being modified; substituting (5.56) into (3.50) we obtain

$$\frac{\partial B}{\partial t} = -\xi\Big[\epsilon A_K \frac{\partial P_{fa}}{\partial x} U^3 + (\epsilon A_K P_{fa} + A_K) 3U^2 \frac{\partial U}{\partial x}\Big]. \tag{5.59}$$

Now comparing (5.58) and (5.59), it is evident that the less bed change would happen for the case in which the coarse sediment parameter A_c is being changed due to the fact that the extra term $-\epsilon A_K$ in (5.58) (which does not appear in (5.59)) is making the bed change less for those cases.

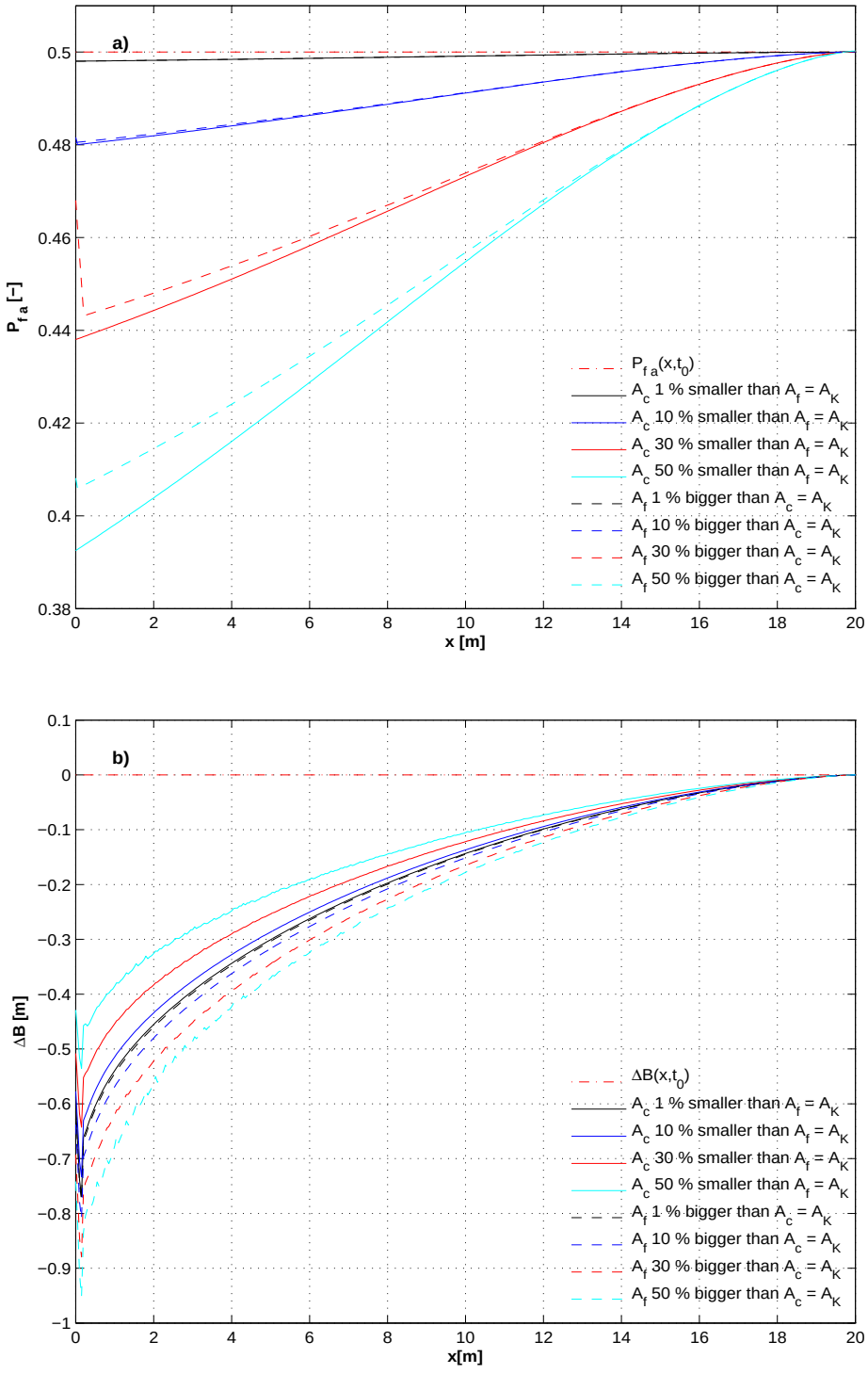

Figure 5.18: a) Comparison of finial P_{fa} for all tests. b) Comparison of final bed change for all tests.

Chapter 6

Sorting and Transport of a non-uniform sediment mixture under swash event caused by a non-breaking wave

6.1 Introduction

As mentioned in chapter 5, there are two basic forms that the flow in the swash zone can take: the swash driven by a breaking wave and the swash driven by a non-breaking wave. Battjes (1974) derived the surf similarity parameter ξ_b (similar to the Iribarren

number, see Iribarren and Nogales (1949))

$$\xi_b = \frac{\tan\theta}{\sqrt{H_b/L_0}} \tag{6.1}$$

where $\tan\theta$ is the beach slope, H_b is the wave height at the breaking point and L_0 is the deep water wave length. The surf similarity parameter has been successfully used to determine whether or not a wave is going to break and which type of wave breaking will be observed. According to Battjes (1974) waves will break when $\xi_b < 2.0$, either as spilling breaker type ($\xi_b < 0.4$) or plunging breaker ($0.4 < \xi_b < 2.0$); and waves will not break when $\xi_b > 2.0$ with a surging or collapsing type of breaking.

The model was already examined for the swash event caused by a breaking wave in chapter 5; in this chapter the model formulated in this research is applied to the swash motion caused by a non-breaking wave that runs up and down the sloping bed.

The kind of waves that we are interested in here, are the non-breaking (refrective) waves, i.e., waves at wind wave periods ($6-20$ s approx.) that are of low steepness. These kind of waves can occur in mild conditions on steep beaches (like the 0.1 beach slope tested here). Beach cusps are thought to form in those kinds of conditions by some authors (see e.g. Dodd et al. (2008)). So waves that might be regarded as a model of the waves taken into account in this chapter are swell waves (generated by winds on long distances offshore) or even, in an extreme event, non-breaking tsunami waves.

A general description of a swash event due to a long non-breaking wave is as follows (see Figure 6.1). The long wave propagates over still water depth and approaches the sloping

bed (Figure 6.1 a). Then the wave reaches the sloping bed and starts running up the bed; at some point the velocity reaches its maximum value (Figure 6.1 b) and begins to decelerate before reaching the maximum run-up. Then the swash reaches the maximum run-up and the flow begins going downslope with increasing velocity in that direction so the backwash starts (Figure 6.1 c). Then the swash reaches its maximum downslope velocity and begins to decelerate (Figure 6.1 d). Finally the flow reaches its maximum downslope point and begins running up the slope again due to the next incoming wave. (Figure 6.1 e).

In this research, in order to get the hydrodynamic behaviour of a long wave approaching a sloping bed, the OTT-2d numerical model is used. This model was developed by Hubbard and Dodd (2002) (see also Hubbard and Dodd (2000)) as part of the ANEMONE (Advanced Non-linear Engineering MOdels for the Nearshore Environment) project.

6.2 OTT-2d Model Overview

The OTT-2d is a validated inner surf zone and swash zone model that simulates the behaviour of water depth and depth-averaged velocity components, cross-shore and alongshore, as well as the movement of the shoreline and run-up.

The governing equations solved by the model are the 2-d non-linear shallow water equations, similar to those deduced in section 3.1, but in this case obviously the equations are 2-d (i.e. two dimensional in plan) and the effects of bottom friction can be taken into

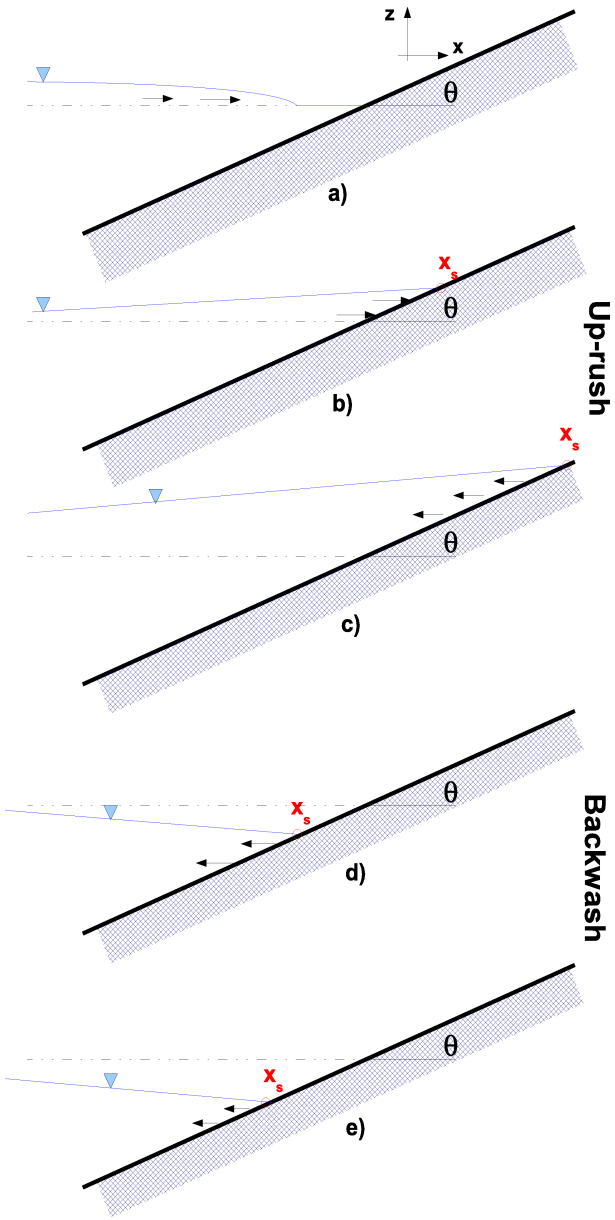

Figure 6.1: Sketch for a swash flow caused by a long (low-frequency) wave (the size of the arrows are schematically proportional to the depth-averaged velocity at the point).

account. The numerical solution is obtained using an upwind finite volume technique that makes use of Roe-type approximations to solve the Riemann problem.

As the model showed good behaviour in all the validation tests it was used in this research with a high degree of certainty.

6.3 Swash Flow of a non-breaking wave

6.3.1 Long wave and swash event selection

The OTT-2d model was run in order to obtain the evolution in time of the depths (h) and corresponding velocities (U) when a long wave reaches a sloping bed and runs up and down a beach.

The bathymetry chosen is similar to that tested in chapter 5, but in this case the wave first propagates over a horizontal bed and then reaches a sloping bed with $\tan\theta = 0.1$ (see Figure 6.2) to facilitate the implementation of the boundary condition (in our model) on that part of the domain and therefore avoid numerical problems that may occur related to this.

Several combinations of wave height (H), wave length (L) and period (T) were tested as input to the OTT-2d model in order to get the hydrodynamic behaviour and corresponding swash event of a long non-breaking wave. In Figure 6.3 the resulting free surface (η) for a number of swash events and the corresponding behaviour of the shoreline for the

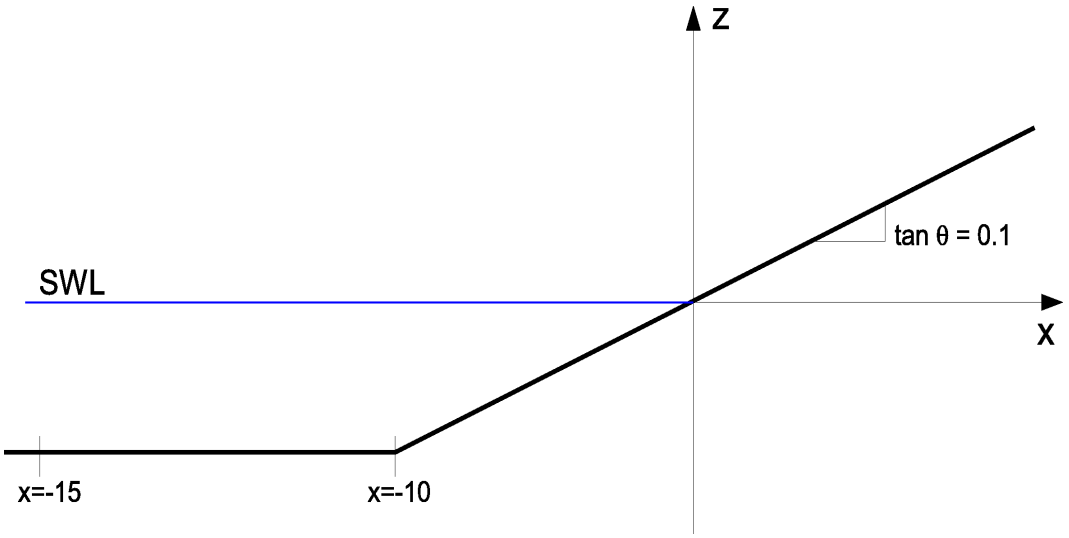

Figure 6.2: Sketch of the bathymetry used in the OTT-2d model.

whole simulation time of three example cases are shown. The three cases are sine waves with same wave height but different wave length and period, namely: 1) $H = 0.3$ m; $T = 6.49$; 2) $H = 0.3$ m; $T = 16$ s; and 3) $H = 0.3$ m; $T = 31.95$ s. All tests were run for about 10 periods to allow initial transients to exit the domain. In Figures 6.3 a) and b) the results for case 1 are shown, in which the presence of bores in the inner surf zone are evident, this means that the wave is actually breaking prior to encountering the shoreline. Note as well that the shoreline behaviour presents a sharp-pointed shape in the transition between waves which indicates that the interaction between them is abrupt and may ultimately induce wave breaking (c.f. e.g. Carrier and Greenspan (1958) and Erikson et al. (2005)). Figures 6.3 c) and d) show the results for a longer wave; the swash flow appears to be more like the one we are interested in, but the wave seems to became almost vertical and about to break. From the shoreline behaviour it can be seen that the sharp-pointed behaviour is still present indicating the presence of interaction between waves and therefore enhancing wave breaking. Note here, that these two cases are more similar to the PW01 swash event taken into account in chapter 5; and that

this illustrates it is a case that can be reproduced by engineering model and not just by the mathematical model used in this research. Finally, in Figures 6.3 e) and f), results of the swash event and shoreline behaviour of a very long wave are presented. From these figures it can be concluded that the swash flow is completely smooth and without breaking. The shoreline behaviour plot confirms that the interaction and transition of waves is smoother and the waves interact in a way they do not promote wave breaking; getting as a result the swash event of a long non-breaking wave. For this reason this case was chosen as the driven hydrodynamics for the study of sorting of sediments by a swash event due to a non-breaking wave.

It is important to note here that due to fact that in this research the principal motivation is to understand the process of sorting driven by a single swash event, therefore the actual OTT-2d driving data used, is that corresponding to a single swash event. The swash event selected in this case was the one between times $t = 124.3$ s and $t = 156$ s. The selection of theses times were carefully done by inspecting Figure 6.3f, identifying the instant where the shoreline starts moving upslope again and checking that the velocity value at that instant and at the last point with water (considered for now the shoreline) is positive, ensuring that the shoreline is actually going upslope and that a new swash event is starting.

6.3.2 Post-processing OTT-2d data

Once the data from the OTT-2d model is obtained a methodology to process the raw data was designed in order to smooth the data corresponding to the swash event selected.

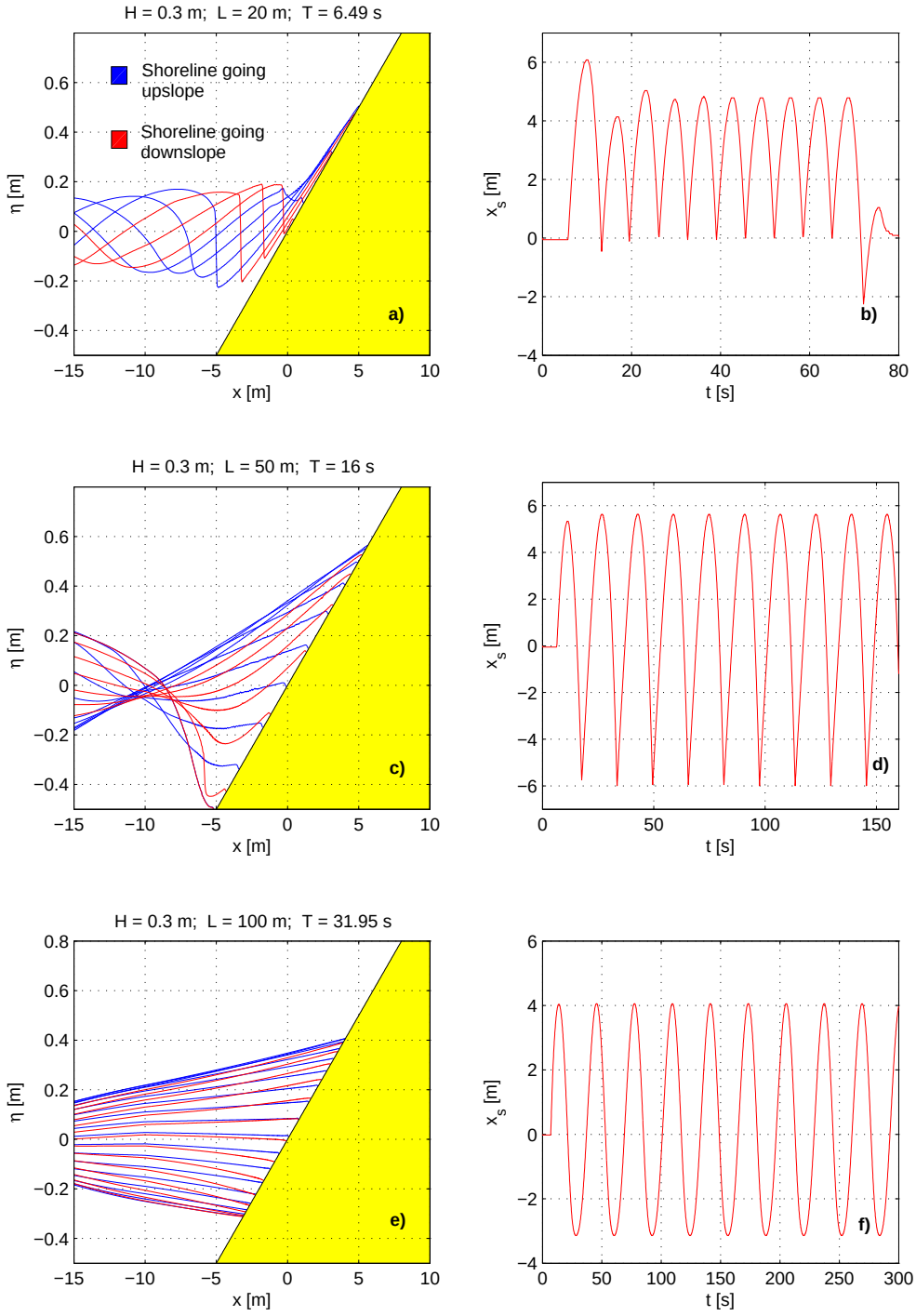

Figure 6.3: Free surface for one swash event and corresponding shoreline behaviour for the whole simulation time (approx. $10 \times T$) for 3 different sine waves as input. a) and b) : $H = 0.3$ m; $T = 6.49$ s; c) and d) : $H = 0.3$ m; $T = 16$ s; e) and f) : $H = 0.3$ m; $T = 31.95$ s.

The methodology consists of the following steps.

First, due to the presence of small oscillations in the raw data from OTT-2d an averaging process was designed (see Figure 6.4).The smoothing is done using a moving average filter which uses a span of five points to calculate the new value. The new data is then calculated as

$$U_{new}(i) = \frac{1}{5}[U_{data}(i-2) + U_{data}(i-1) + U_{data}(i) + U_{data}(i+1) + U_{data}(i+2)] \quad (6.2)$$

at every time step. Note that at the shoreline the filter is applied from that point and backwards taking the same amount of points.

Because of the discrete wetting and drying process and because a smooth shoreline is very important for obtaining accurate results (see e.g. the shock conditions derived in §5.5.2), a recalculation of the shoreline is now implemented. It was mentioned at the end of last section, that the shoreline was considered, until now, to be the last point with water $x_{sh_{data}}$ (see Figure 6.5). So the first step to calculate the definitive shoreline, is to removed from the original shoreline data $x_{sh_{data}}$ positions that are identical to the previous datum; then the definitive shoreline $x_{sh_{def}}$ was calculated by interpolating values between the remaining points.

Once the definitive shoreline is calculated, another step is necessary to get smooth data from OTT-2d. As one may expect the grid (Δt, Δx) used in OTT-2d is not related with the one needed in our model, for this reason we interpolate from the OTT-2d data to the model grid. This interpolation is done using a cubic spline function. Figure 6.4 shows the comparison between the raw data from the OTT-2d model and the post-processed

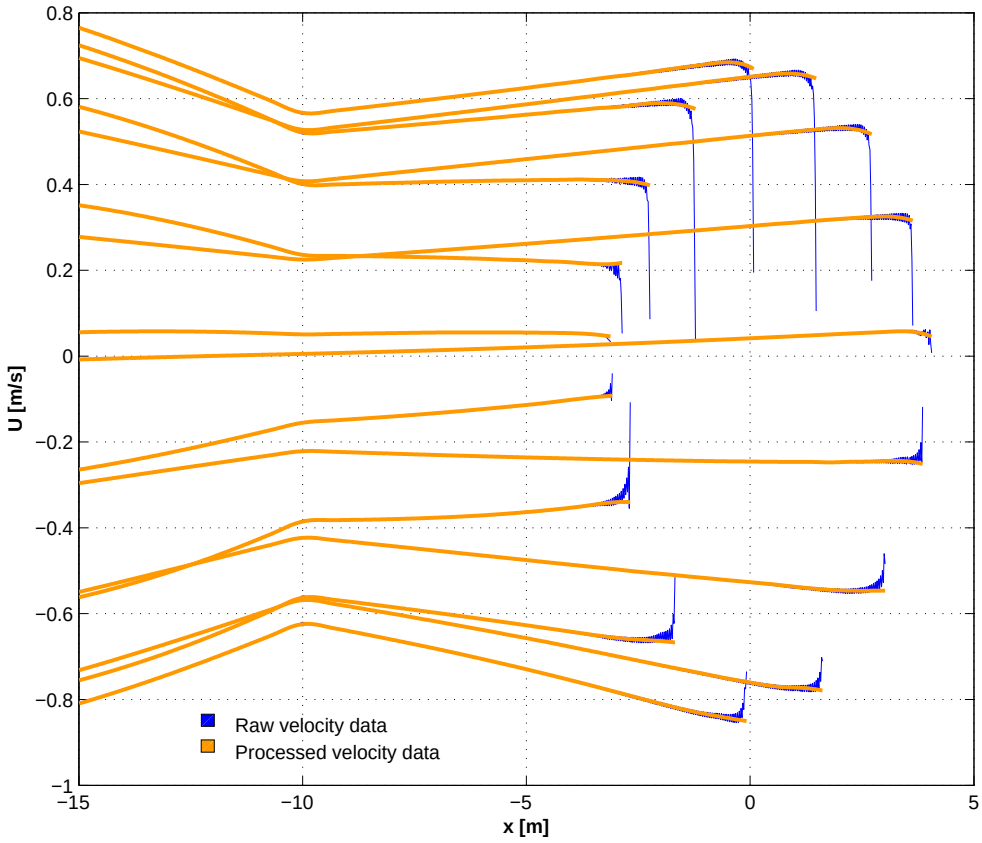

Figure 6.4: Comparison between raw data form OTT-2d and the post-processed data

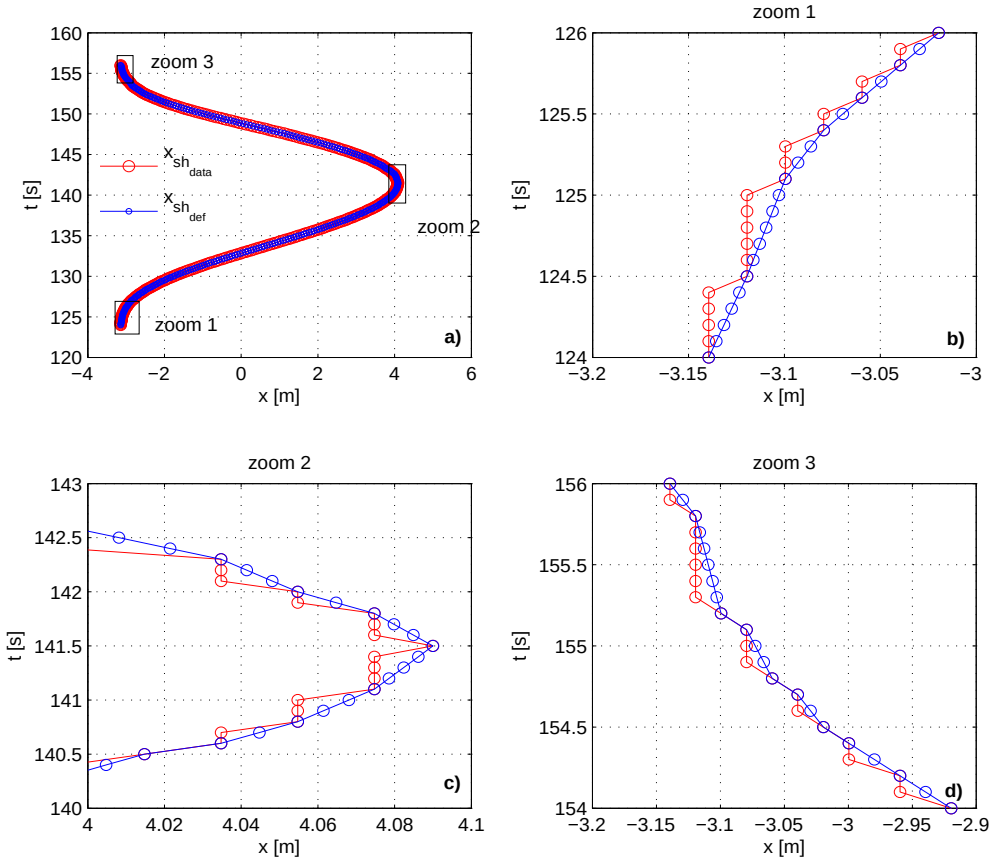

Figure 6.5: Comparison between the original and the recalculated shoreline

data (averaging + interpolation) described above.

As noted before the location of the shoreline is of great importance to the accuracy of the model, but the velocity of the shoreline is also very important. Therefore a last step in this post-processing methodology was necessary: the accurate calculation of this velocity. In the first instance the velocity of the shoreline was calculated using $U_s = \frac{dx_s}{dt} = \frac{x_s(i+1) - x_s(i-1)}{\Delta t}$ but it was found to give results in with big oscillations which definitely could produce problems in our model. For these reason it was decided to calculate this value by extrapolating it from the velocities in the water (the processed velocity data, see Figure 6.4). In Figure 6.6 a comparison between these two ways of calculating the shoreline velocity is shown; from the figure it was noted that the extrapolated velocities were smoother but still suffered from small oscillations, so a moving average filter (similar to that applied to the raw data: eq.(6.2)) was applied to smooth the extrapolated data and finally get the definitive shoreline velocity.

6.4 Numerical Solution

The numerical solution of the morphodynamic module of the model represented by (5.8) and (5.9) is obtained in the same way as detailed in sections 5.4, 5.5 and 5.6, with some small differences. First, the initial conditions are the same as those used in section 5.5.1, but in this case due to the fact that the driving hydrodynamics are directly obtained from the OTT2d model the initial time t_0 will be different from that used for the PW01 swash; as mentioned in §6.3 the selected swash event in this case starts at $t_0 = 124.3$

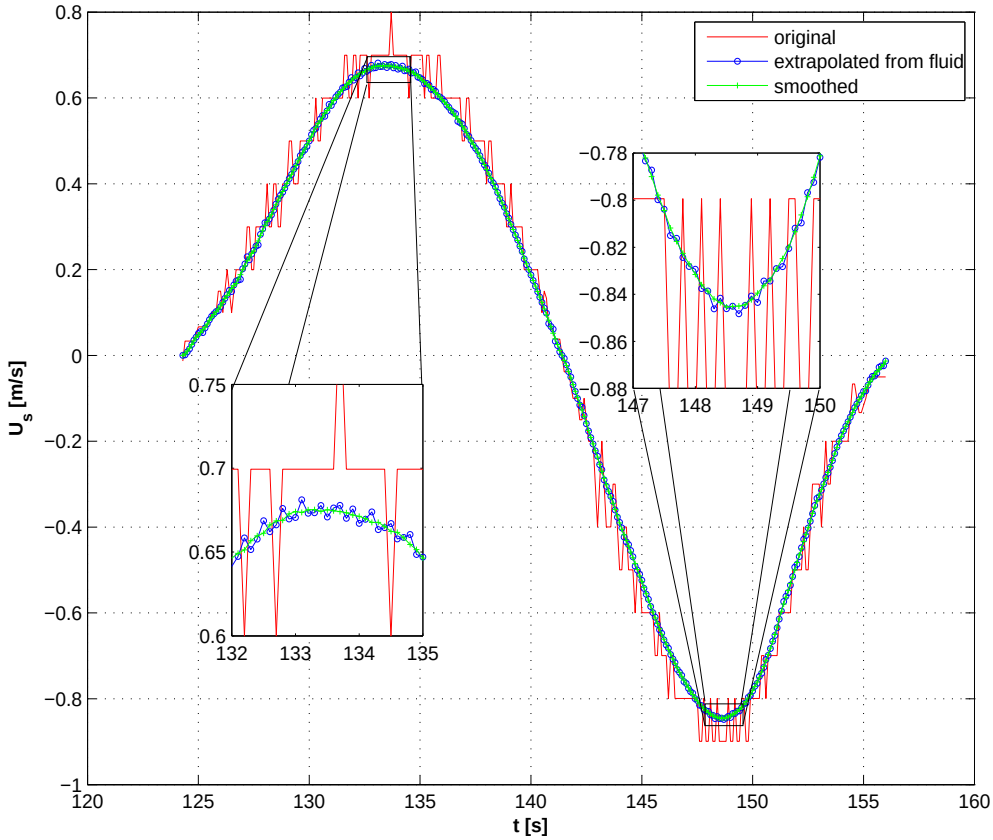

Figure 6.6: Comparison between the original shoreline velocity calculated directly from the raw data; the one calculated extrapolating from the velocities in the fluid and the one smoothed using a moving average filter

s. The other difference is that the initial bed profile is of the form depicted in Figure 6.2. It is important to remember here, that the comparison between the PW01 and the non-breaking will be done focusing on the behaviour of the variables over the sloping part of the beach (and in the region where the swash flow acted); the inclusion of the horizontal bed at the seaward boundary was done to avoid possible problems due to the implementation of boundary conditions.

Now, due to the fact that the hydrodynamics are driven by the OTT-2d model, the form of the swash event is slightly different from that depicted in Figure 5.2 (PW01 swash); the difference is that in this case the seaward point (x_{sw}) does not exist. For this reason the boundary conditions used are the same as those described in §5.5.2 although the special seaward point cases are not used.

6.5 Results

A set of numerical experiments was designed to test the model for a PW01 swash event in §5.7. It seems reasonable to use the same set of experiments to be able to evaluate and compare the sorting for the non-breaking wave too. For this reason, in this chapter the same A_f, A_c values are tested for a long non-breaking wave swash event. The numerical experiments are presented in Table 6.1.

Note that in this case the value of the active layer thickness (L_a) is calculated with the new driving hydrodynamics (i.e. U from OTT-2d model) and it can be observed that

Table 6.1: Non-breaking wave swash tests

Test No.	$A_f[s^2/m]$	$A_c[s^2/m]$	**Description**	L_a calculated [m]	L_a used [m]
1	0.004	0.00396	$A_f = A_K$; A_c is 1 % smaller than A_K	0.0049	0.35
2	0.004	0.0036	$A_f = A_K$; A_c is 10 % smaller than A_K	0.0047	0.35
3	0.004	0.0028	$A_f = A_K$; A_c is 30 % smaller than A_K	0.0042	0.35
4	0.004	0.002	$A_f = A_K$; A_c is 50 % smaller than A_K	0.0037	0.35
5	0.00404	0.004	$A_c = A_K$; A_f is 1 % bigger than A_K	0.0049	0.35
6	0.0044	0.004	$A_c = A_K$; A_f is 10 % bigger than A_K	0.0052	0.35
7	0.0052	0.004	$A_c = A_K$; A_f is 30 % bigger than A_K	0.0057	0.35
8	0.006	0.004	$A_c = A_K$; A_f is 50 % bigger than A_K	0.0061	0.35

this calculated value is several orders of magnitude less than that for the PW01 swash event (see tables 5.1 and 6.1). To be consistent with the experiments for the PW01 swash event, and to be able to compare qualitatively and quantitatively between results from both swash events, it was decided to run the tests with the same value of L_a as that for the PW01 case. Further analysis of the role played by the active layer thickness in the model is performed in chapter 7.

6.5.1 General results

Similar to the PW01 swash event in this case it was found that the solution given by the model shows similar behaviour for all tests. Therefore in Figures 6.8 and 6.9 the behaviour of the fine volume fraction and the change in bed profile for test No. 4 only are shown as examples of the general results given by the model.

Now analysing the behaviour of the fine volume fraction (see Figure 6.8) it can be seen that the accelerating onshore flow in the first half of the uprush the fine sediment is taken from the lower part of the beach towards the middle and upper zones of the bed. Note that at the end of the uprush phase the fine sediment is accumulated in the middle part of the swash excursion. This is because, as it can be seen in Figure 6.7, the maximum onshore velocity takes place in that zone of the bed, moving more fine sediment than in any other part of the slope. Something similar happens in the backwash; the flow accelerates now in the offshore direction (see Figure 6.7) so that the fine sediment is transported in that direction. Just like in the uprush, the fine sediment is more eroded in the middle zone of the swash excursion, due to the fact that in that region the offshore

velocity is bigger, and deposited seaward of the swash zone.

The final distribution of the fine (solid black line) and coarse (dashed black line) sediments are shown as well as the location of the initial, final and maximum position of the shoreline, which delimits the area where the swash has been acting. The final result then, after one swash event of a non-breaking wave, is that the bed is left with less fine sediment (more coarse) especially around the middle part of the swash and more fine sediment (less coarse) around a small region near the initial position of the shoreline as well as in the most shoreward part of the surf zone.

Now from Figure 6.9 it can be seen that something similar to what was described above happens with the bed change. During the first half of the uprush, sediment is transported upslope and accumulated around the middle zone of the swash excursion. Then in the backwash, sediment is re-worked by the offshore flow such that there is a maximum erosion around the middle part of the swash excursion, with accretion in the adjacent surf zone, with some sediment around the initial location of the shoreline point.

6.5.2 Comparison for cases in which the coarse sediment is made progressively coarser

In this section a comparison and analysis between the results given by the model when the coarse sediment in the mixture is made progressively coarser is made with the aid of Figures 6.10 and 6.11.

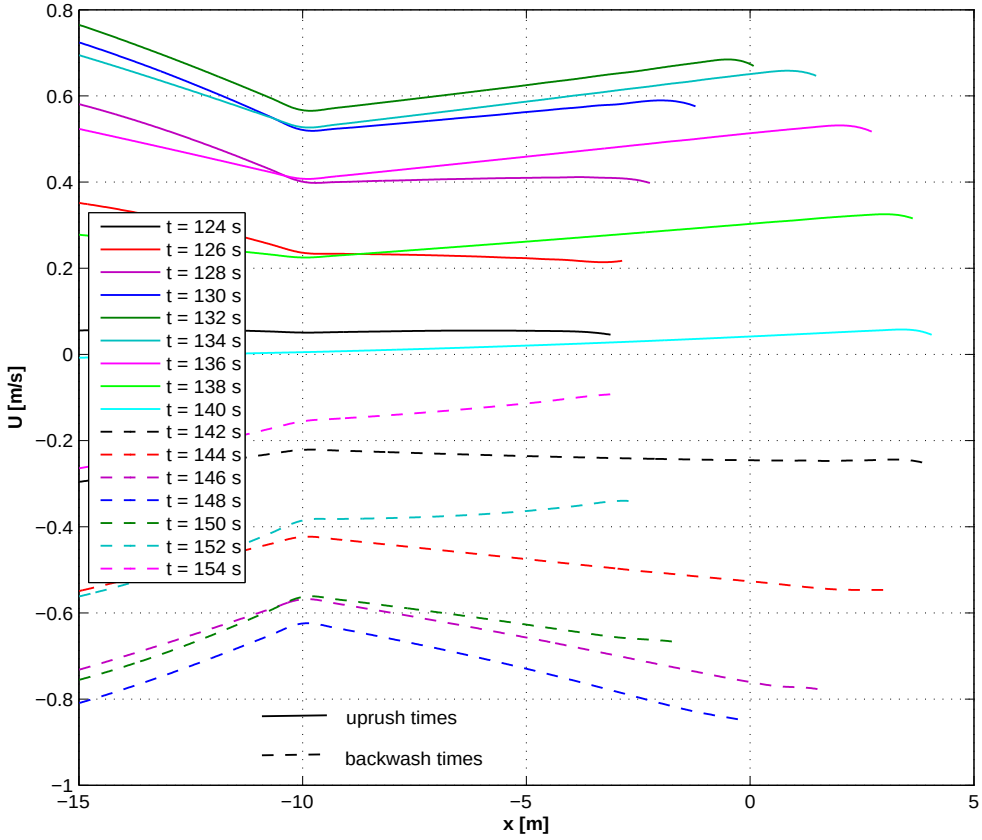

Figure 6.7: Velocity field in the uprush and backwash of the non-breaking wave swash event

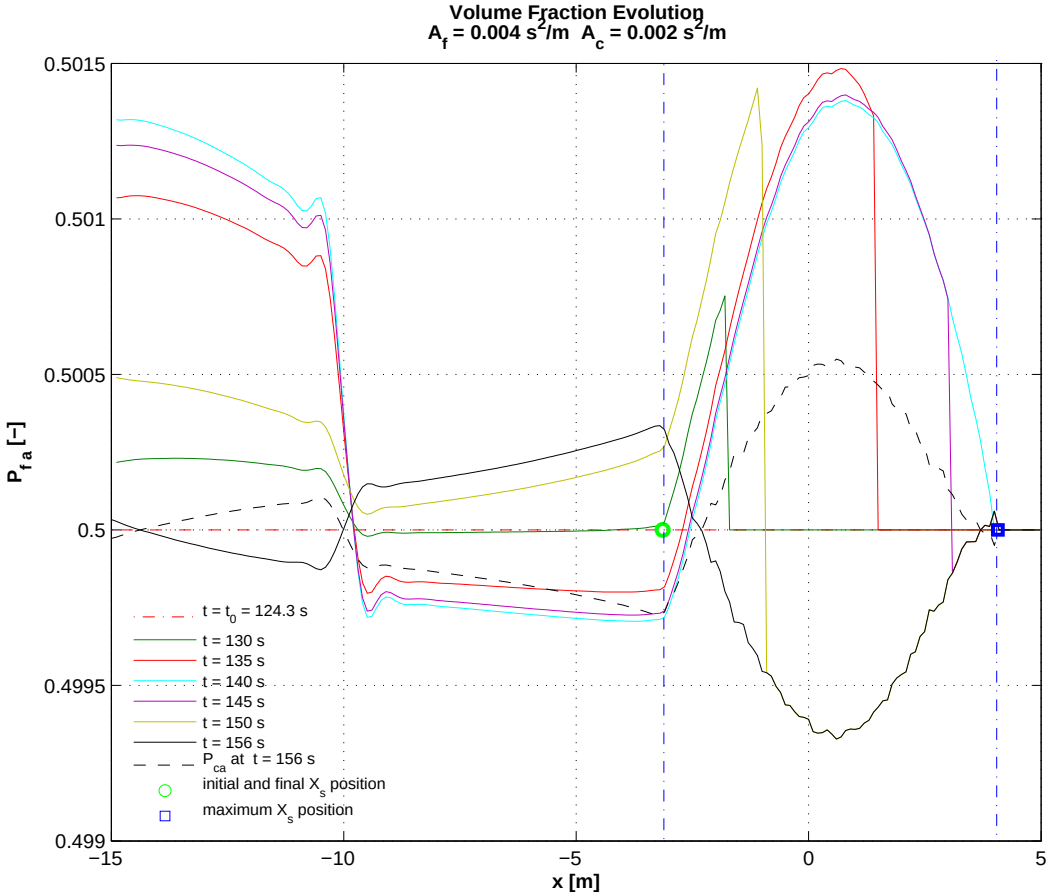

Figure 6.8: Fine volume fraction given by the model for Test No. 4

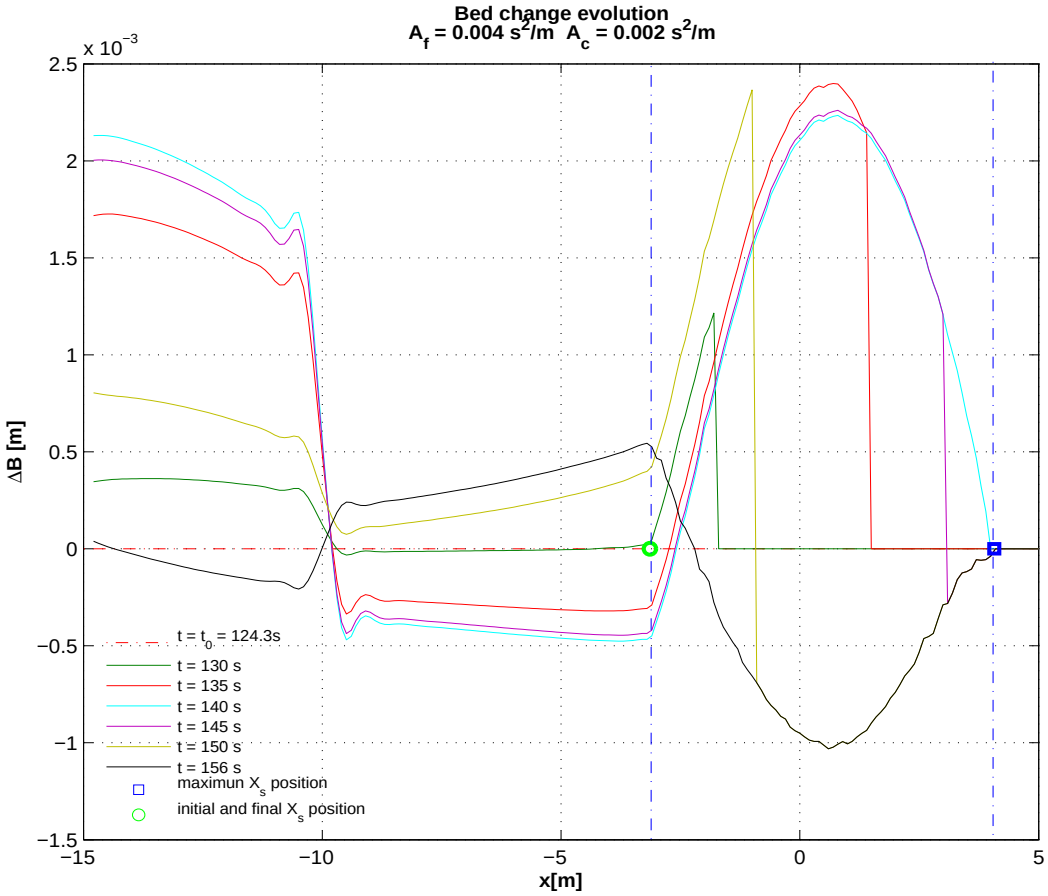

Figure 6.9: Bed change given by the model for Test No. 4

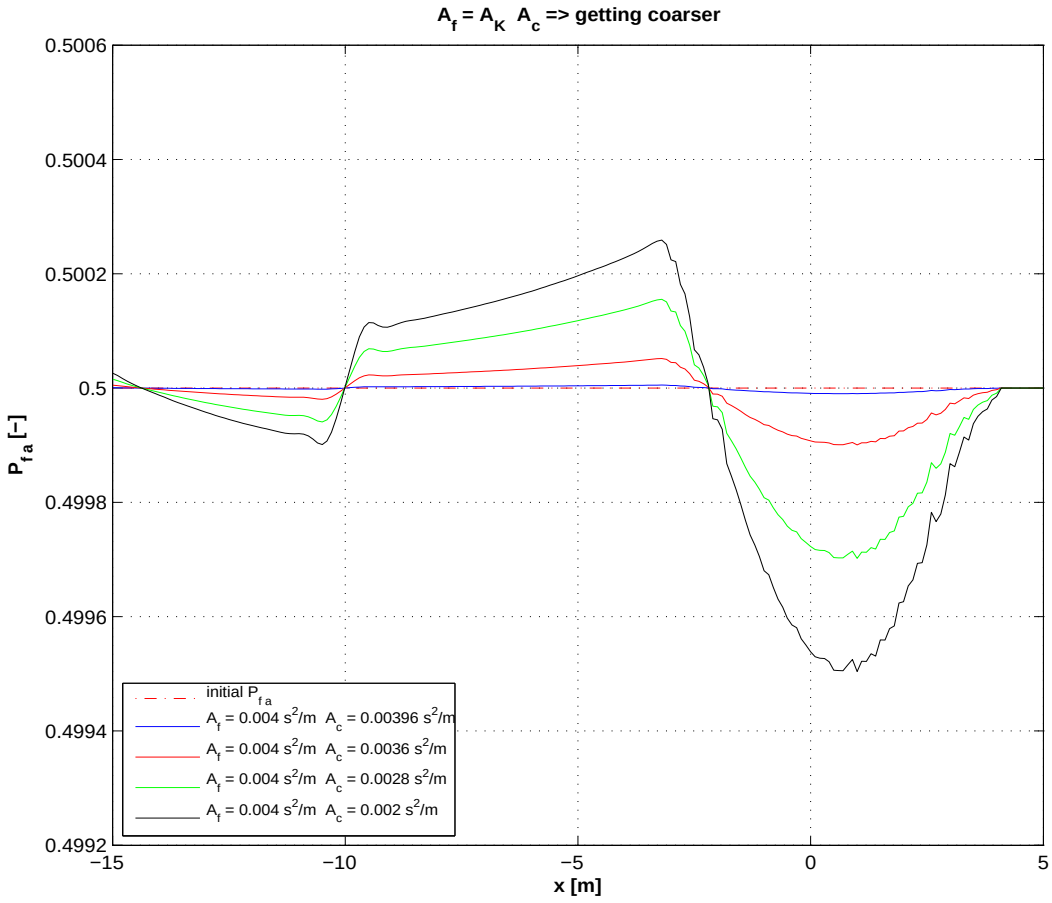

Figure 6.10: Final fine volume fraction given by the model for test where the coarse sediment parameter A_c was made progressively smaller (coarse sediment getting coarser)

From Figure 6.10 it can be seen that making the coarse sediment progressively coarser also implies that the fine sediment is made progressively relatively finer. The final fine volume fraction decreases accordingly: i.e., more coarse sediment remains in the swash zone after the swash event.

From the associated bed change shown in Figure 6.11 it can be seen that when the coarse sediment is made progressively coarser the results are in accordance with the physics: there is less bed change when a coarse sediment is involved. In other words, the coarser

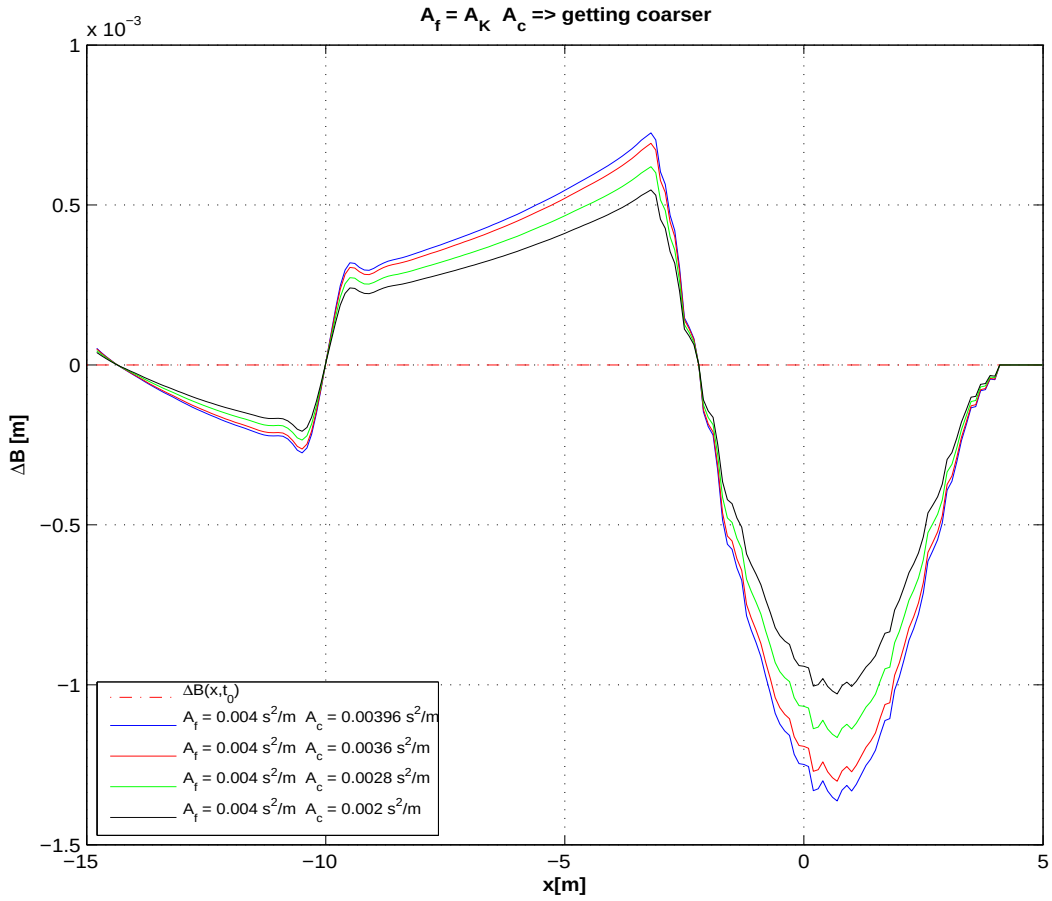

Figure 6.11: Final bed change given by the model for test where the coarse sediment parameter A_c was made progressively smaller (coarse sediment getting coarser)

the sediment is made the harder it is to transport and therefore less erosion of the bed profile will be present.

To summarise: making the coarse sediment coarser makes that sediment fraction less easy to transport and therefore more of what is moved will be fine fraction.

6.5.3 Comparison for cases in which the fine sediment is made progressively finer

Now an analysis and a comparison of the results given by the model is performed for the case where the fine sediment is made progressively finer. This comparison is shown in Figures 6.12 and 6.13 and is analysed in this section.

In Figure 6.12 it is clearly seen that when the fine sediment is made progressively finer, less fine sediment is left on the bed slope in the zone where the swash was acting. The behaviour of the bed change shown in Figure 6.13 is as expected from basic physical principles: the finer the sediment, the more movable is the mixture, therefore the more bed change there is.

Now in Figure 6.14 comparison between the results in terms of P_{fa} and ΔB are shown for all cases tested; when the coarse sediment was made progressively coarser (solid lines) and when the fine sediment was made progressively finer (dashed lines).

In Figure 6.14a the behaviour of the fine volume fraction is almost the same for both cases (when the coarse or the fine fraction is modified in the same proportion). On the other hand in Figure 6.14b the bed change behaviour agrees well with what physically one would expect: when the coarse sediment involved in the mixture is made progressively coarser, the sediment (and therefore the mixture) is more difficult to transport giving as a result less and less bed change; and, conversely, when the fine sediment in the mixture is made finer the mixture is transported more easily and therefore more bed

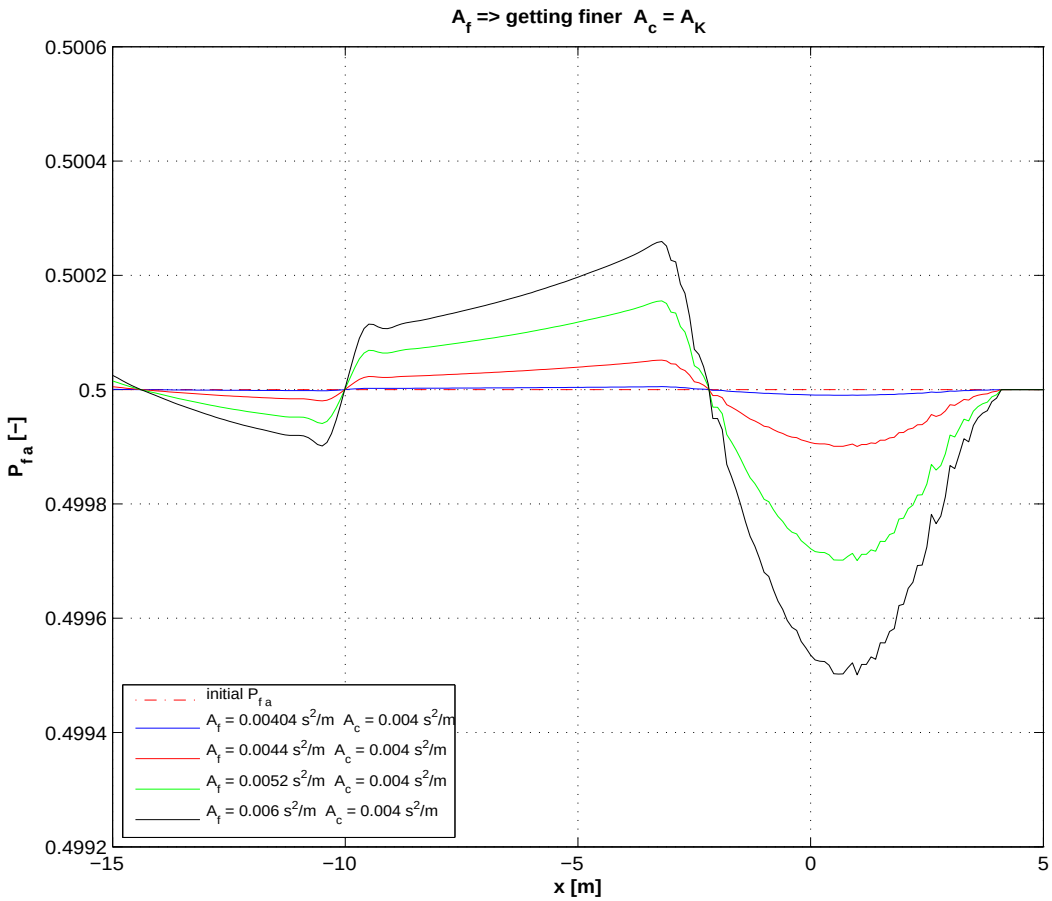

Figure 6.12: Final fine volume fraction given by the model for tests where the fine sediment parameter A_f was made progressively bigger (fine sediment getting finer)

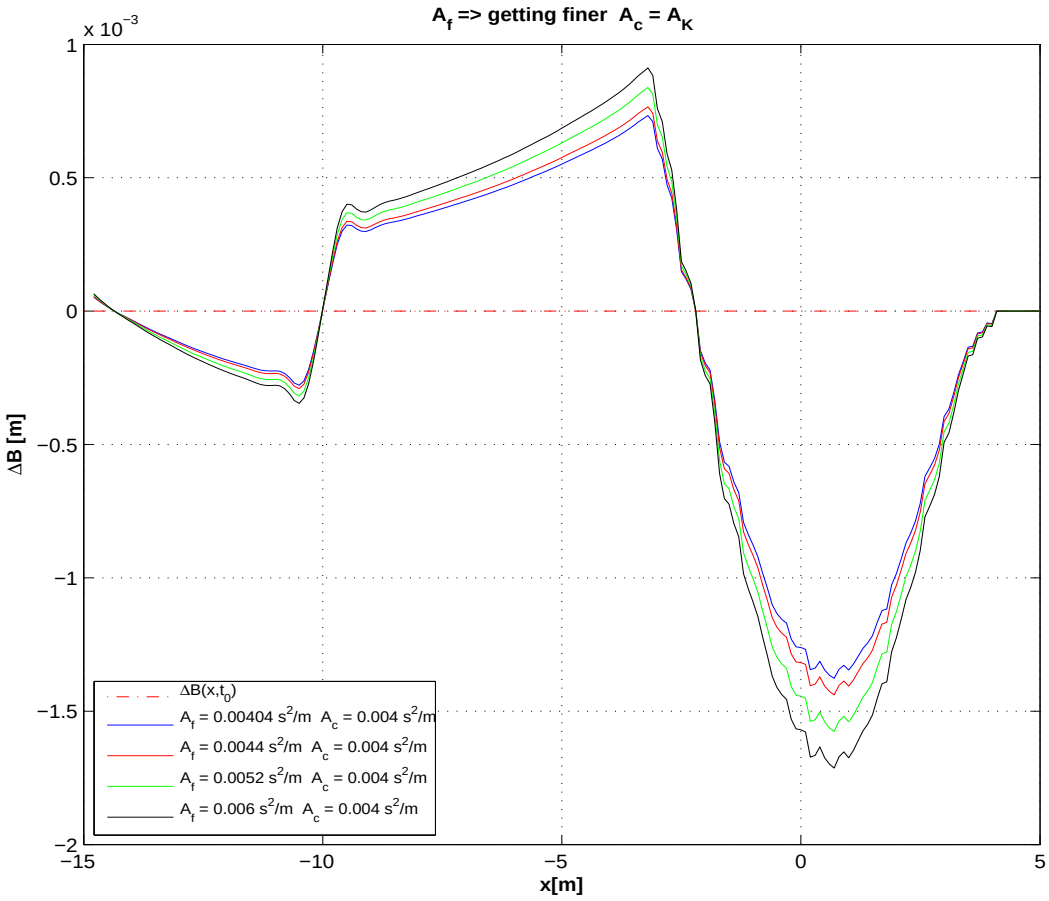

Figure 6.13: Final bed change given by the model for tests where the fine sediment parameter A_f was made progressively bigger (fine sediment getting finer)

change is present.

The behaviour described above is similar than that observed in the PW01 swash event (see §5.7.3). The change in the fine volume fraction when the fine sediment is made finer than A_K is almost the same as that when the coarse fraction is made coarser than A_K (in the same proportion). However, note that in this case the difference between similar tests is barely noticeable. This is because the swash event caused by the non-breaking wave taken into account here is much less energetic (in term of velocities) than the PW01 swash (see Figure 6.15), so that less change in P_{fa} (which implies in our case that P_{fa} is more similar to P_{fs}) is obtained and therefore less difference between tests (c.f. eqs. (5.55), (5.57) and the accompanying explanation).

Now, in the case of the bed change, again, the same thing as in the PW01 case applies: the finer the mixture involved the more bed change is obtained over the profile. This is in agreement with basic physical principles and is corroborated by the analysis of equations (5.58) and (5.59) done in §5.7.3.

6.5.4 Results for test with several swash events

As established before the main objective of this research is to gain physical insight into the processes of transport and sorting of sediments in the swash zone of the beach and to model it for the first time. Until now the model has been tested for two different types of swash event (i.e. PW01 and non-breaking wave swash events), but these numerical experiments were restricted to the transport and sorting of the sediment during

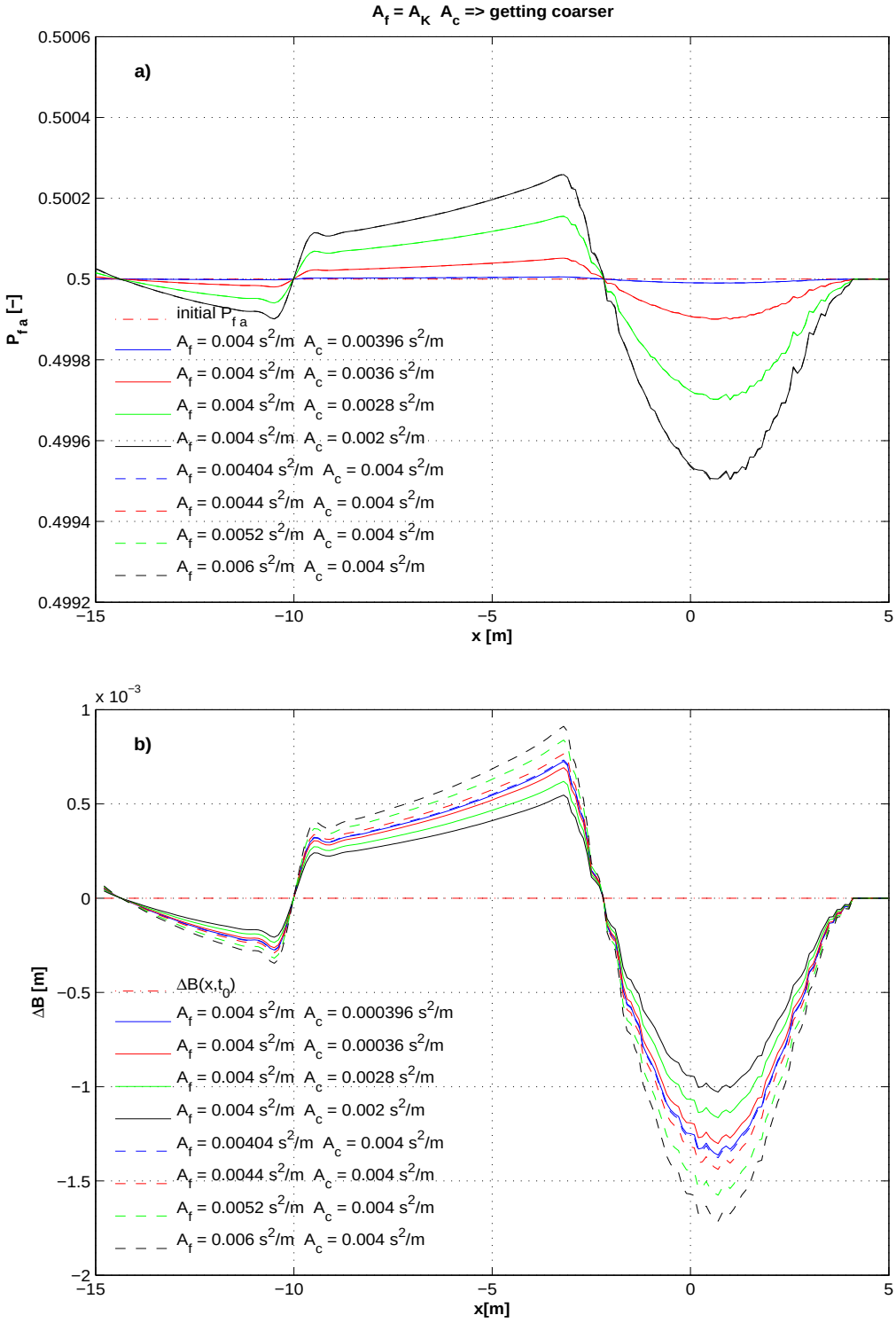

Figure 6.14: Comparison between cases where the coarse fraction was made progressively coarser and when the fine fraction was made progressively finer for a) Fine volume fraction and b) Bed level change

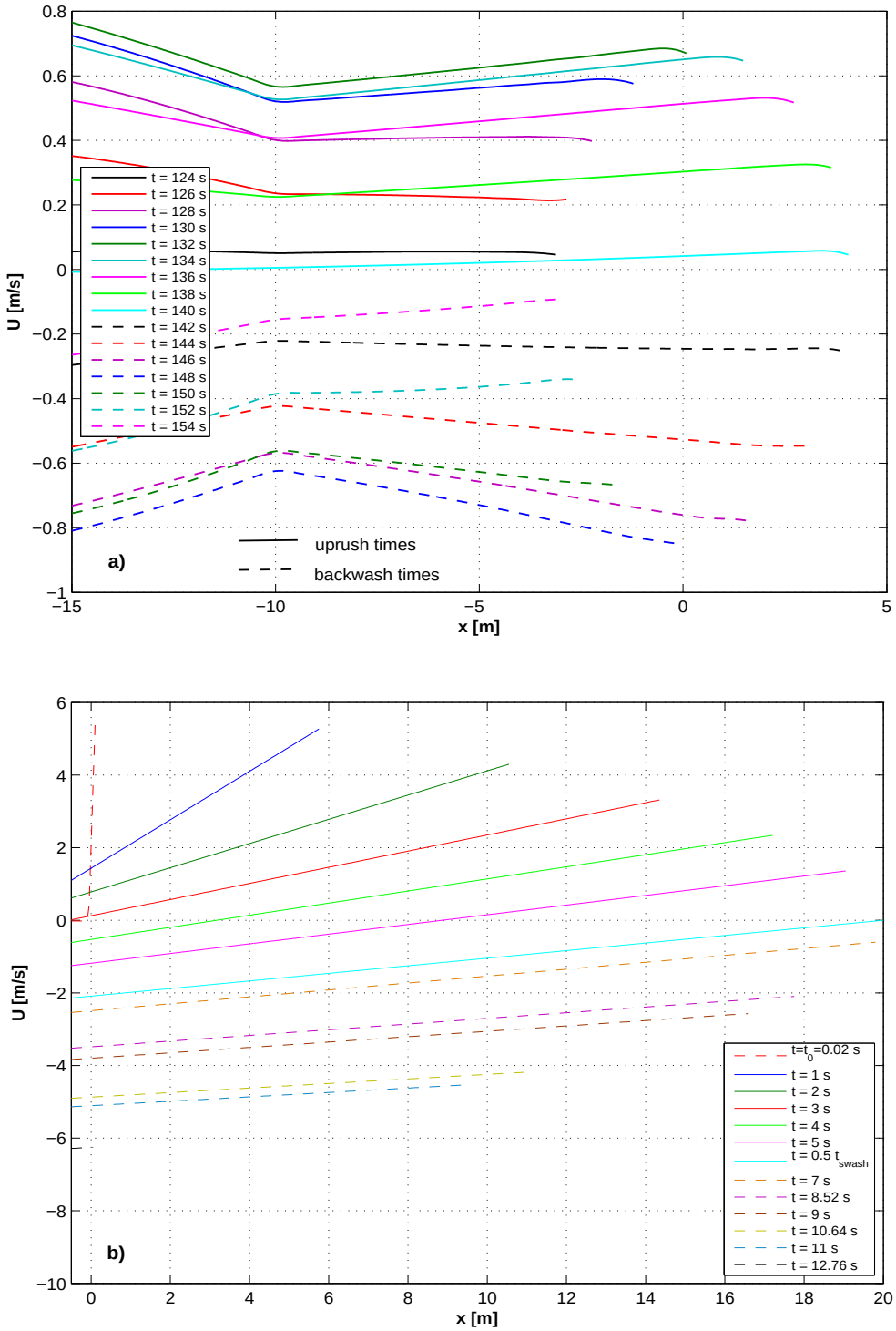

Figure 6.15: Velocity field for a) the non-breaking wave swash; and b) the PW01 swash event

Table 6.2: Cases tested with several swash events acting on the slope

Test No.	$A_f[s^2/m]$	$A_c[s^2/m]$	**Description**	L_a calculated [m]	L_a used [m]
1	0.004	0.002	$A_f = A_K$; A_c is 50 % smaller than A_K	0.0037	0.35
2	0.006	0.004	$A_c = A_K$; A_f is 50 % bigger than A_K	0.0061	0.35
3	0.006	0.002	A_f is 50 % bigger than A_k A_c is 50 % smaller than A_K	0.0049	0.35

one swash event. It is interesting to test the numerical model for more than one non-breaking swash event over the same beach slope in order to investigate if the sediment fraction starts to achieve a settled state on the next swash.

A set of three experiments was performed taking as a base point the ones already carried out in §6.5 (c.f. Table 6.1). These test are summarised and presented in Table 6.2. They are chosen because these tests are the ones with the bigger difference between A_f and A_c, this implies bigger variation in both P_{fa} and the bed change ΔB, which is highly desirable in this case.

To perform the numerical experiments with more than one swash event the model was run for three consecutive identical swash events in which the first event is run as before with $P^0_{fa} = P^0_{ca} = 0.5$ and with the initial flat sloping bed profile; and the consecutive swash events are run with the final P_{fa} and bed profile taken from the previous swash event as initial conditions.

In Figure 6.16 the fine volume fraction and bed change evolution for Test No. 2 is shown. In Figures 6.16 a) and b) the results for the first swash are shown, which are similar to those presented in Figures 6.8 and 6.9. Now, in Figures 6.16 c) and d) the evolution of the P_{fa} and ΔB are shown respectively for the second swash event. From this figures it can be seen that the simulation is successfully ran starting from the bed and fine volume fraction left from the first swash event; by the end of the second swash the fine volume fraction is less than that left by the first swash and the bed is further eroded from the slope. Finally, the results for the third swash event are shown in Figures 6.16 e) and f) from which it can be seen that the uprush is not capable of counteract the reduction that already happened in the fine fraction neither the bed erosion from the bed slope.

Now a comparison of the final fine volume fraction and the change in bed after one, two and three swash events for the three tests performed is shown in Figure 6.17. Regarding P_{fa}, the behaviour of the fine (and therefore coarse) volume fraction depends on the relative difference between fractions, this is the difference between A_f and A_c. As we can see in the figure in the left column, the fine volume fraction behaviour is almost the same for Tests 1 and 2 (figures a and c) which have different A_f and A_c values but the relative difference between them is exactly the same. Note then that for Test 3 in which the difference between A_f and A_c is bigger, more fine sediment is moved by the end of each swash event.

Regarding the bed change, looking at Figure 6.17 b), d) and f) it can be observed that the less bed change happened for Test 1 which is the coarsest mixture tested, and the bigger bed change of all happened for Test 2 (figure d), the finer mixture, agreeing with what one would expect from simple physics: the coarser the mixture, the less bed change

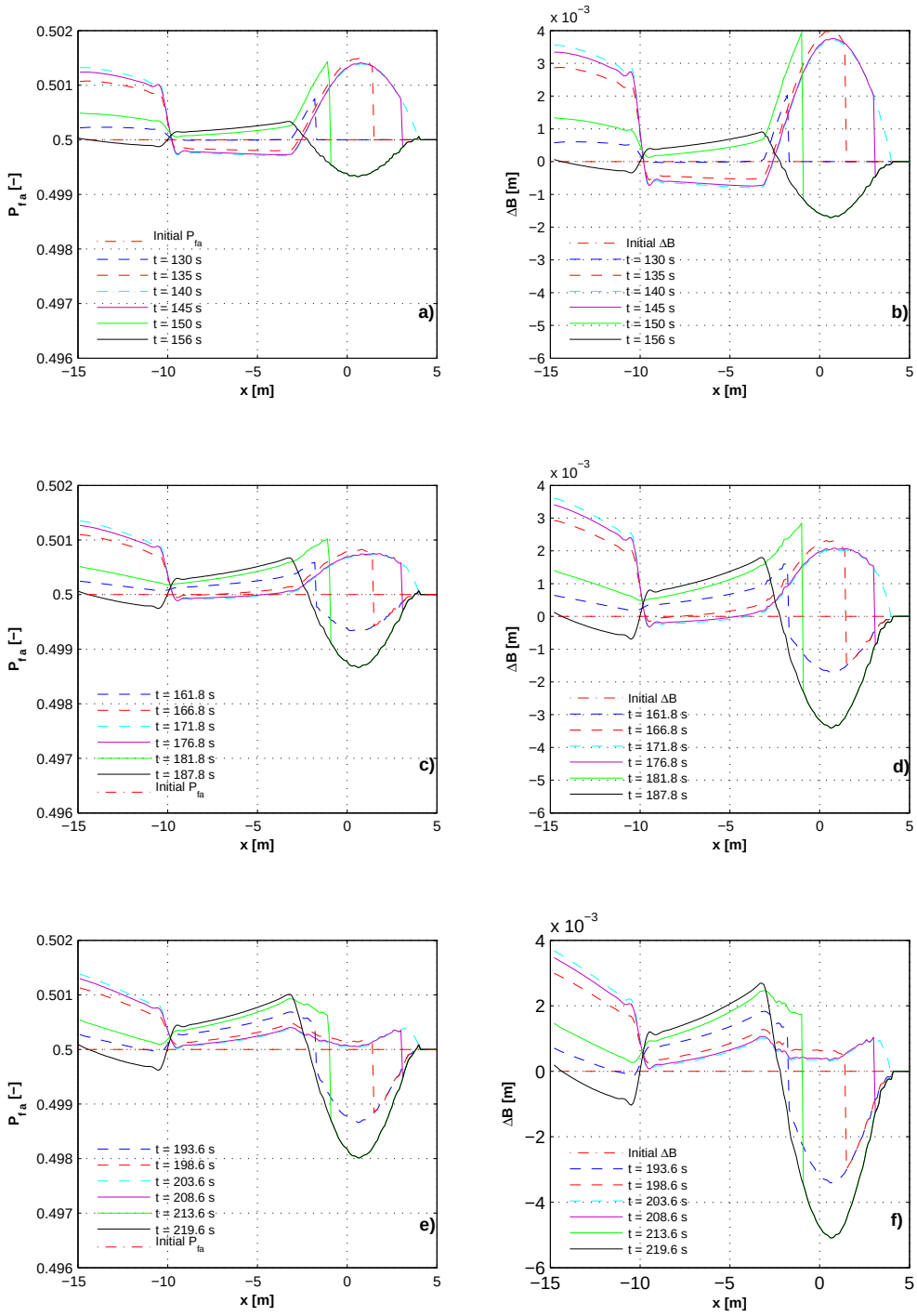

Figure 6.16: Fine volume fraction evolution for the a) first. c) second and c) third swash event; and Bed change evolution for the b) first, d) second and f) third swash event. Dashed lines:uprush Solid lines:backwash

will be obtained.

Note that in none of the cases tested P_{fa} shows any sign of being reaching a steady value as expected, in every swash event P_{fa} keeps decreasing over the swash zone. For this reason, the model was run again for three consecutive swash events leaving $A_c = 0.002s^s/m$ and increasing the value of A_f; what is sought with this is to remove fine sediment more quickly so we could see if P_{fa} starts reaching a steady value. The A_f values tested are $A_f = 0.007s^2/m$, $A_f = 0.008s^2/m$ and $A_f = 0.009s^2/m$.

In Figure 6.18 the behaviour of P_{fa} and the bed change for these tests is presented. It can be seen that not even when A_f is increased a steady value in P_{fa} is reached. Now, another way to try to observed if at some point P_{fa} reaches a steady state behaviour is to run the model for more than three swash events. Therefore the model was ran for ten consecutive swash events acting on the beach, keeping the sediment parameters as $A_f = 0.009s^2/m$ $A_c = 0.002s^2/m$. It was observed that, not even in this case, P_{fa} reaches a steady behaviour and that the results for this case were very similar to those shown in Figures 6.17 e) and f) (therefore results for this case are not shown here).

It is clear that the behaviour of P_{fa} and the bed change is crucially related to the values that A_f, A_c and L_a can take, and therefore the fact that a steady P_{fa} behaviour is not reached is related to this as well. In next chapter this issue is investigated further.

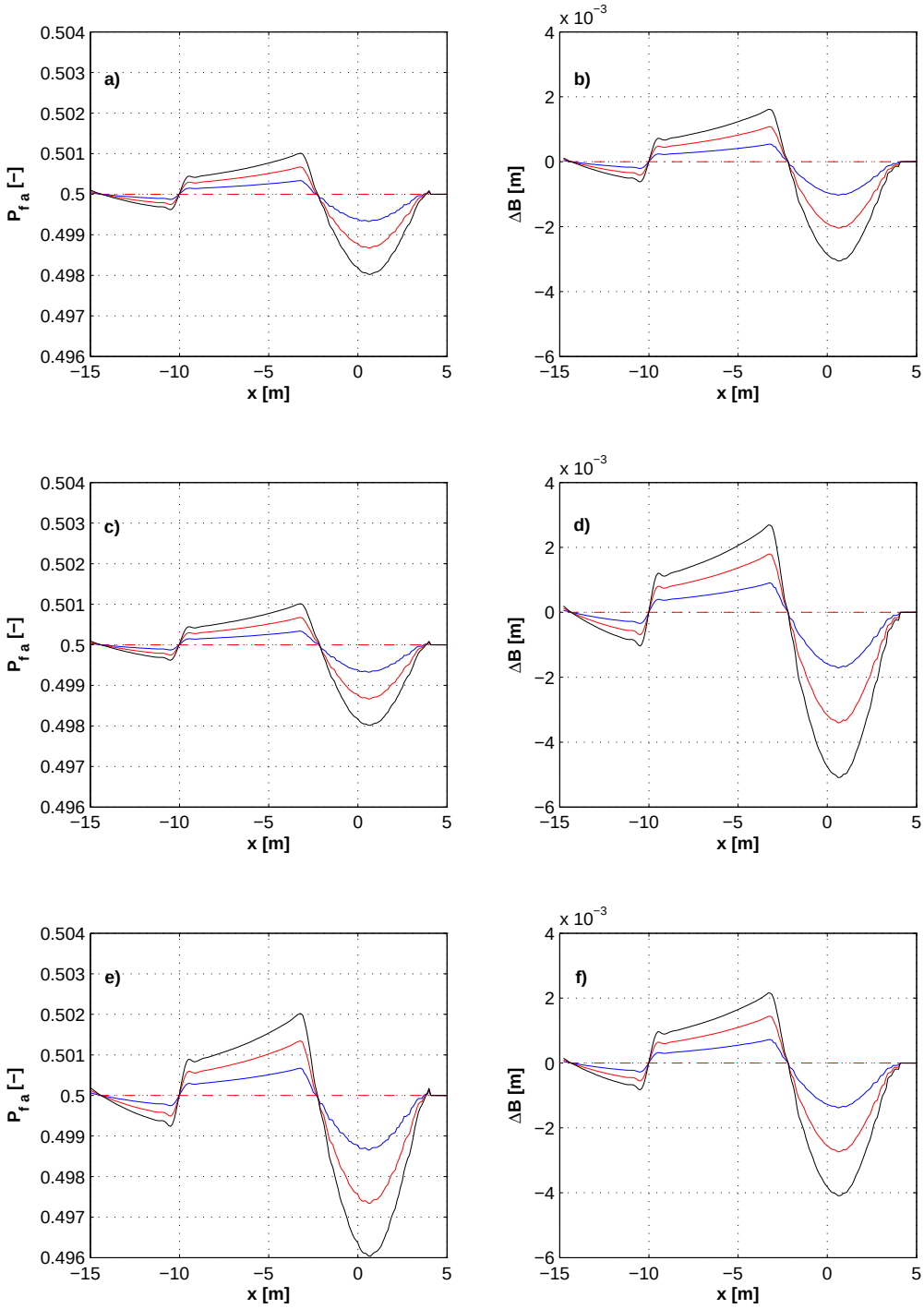

Figure 6.17: Comparison of final fine volume fraction and bed change after one, two and three swash events. a) and b) Test No. 1; c) and d) Test No. 2 and e) and f) Test No.3. — first swash; — second swash; — third swash

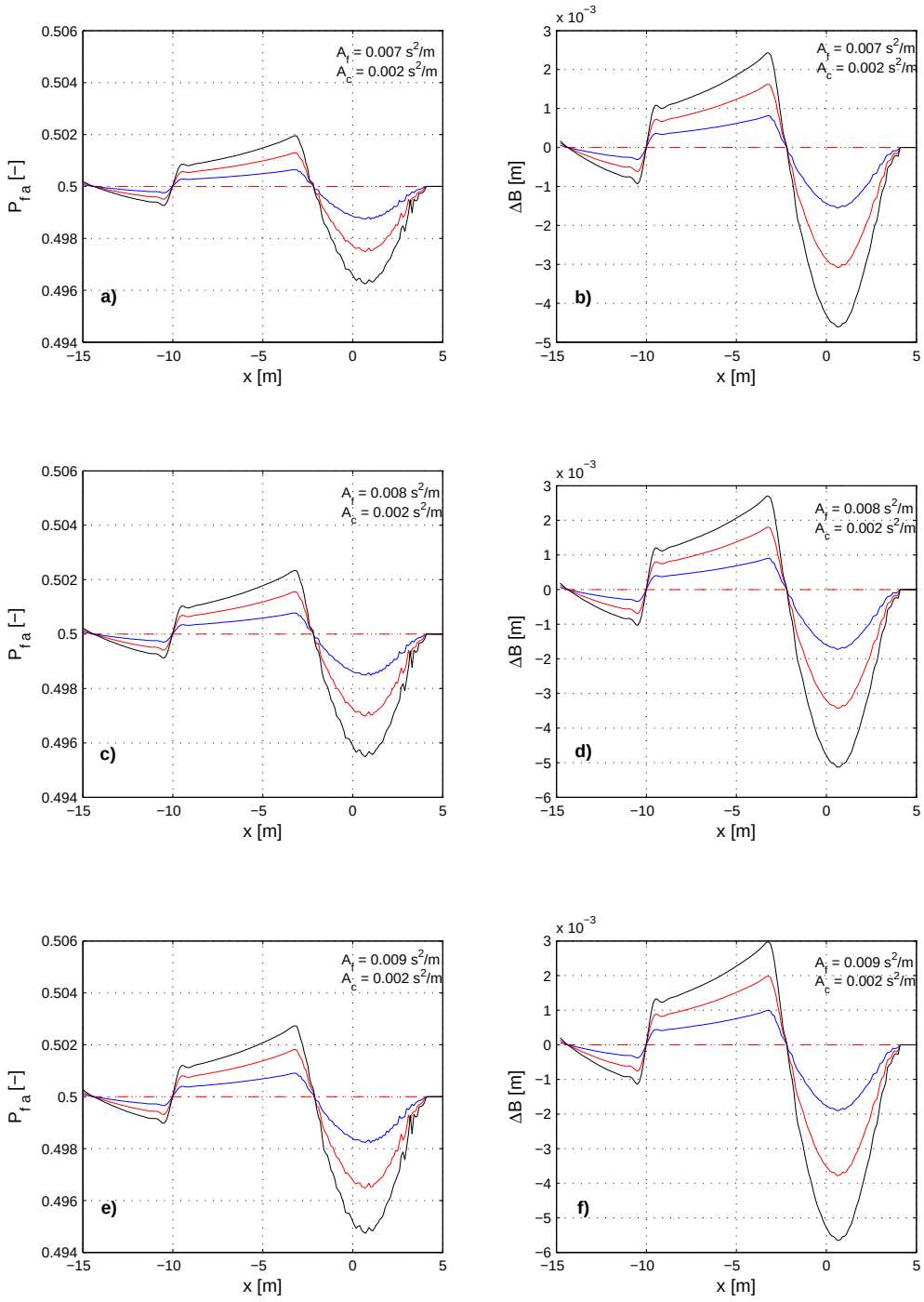

Figure 6.18: Final P_{fa} and bed change after one, two and three swash events. a) and b) $A_f = 0.007 s^2/m$ $A_c = 0.002 s^2/m$; c) and d) $A_f = 0.008 s^2/m$ $A_c = 0.002 s^2/m$; and e) and f) $A_f = 0.009 s^2/m$ $A_c = 0.002 s^2/m$; — 1^{st} swash; — 2^{nd} swash; — 3^{rd} swash

Chapter 7

Parametric analysis of the model for real beaches

7.1 Introduction

During this research it was noted that the most important parameters determining the behaviour of the model were: the sediment parameters A_f and A_c, the thickness of the active layer L_a, and the initial fine volume fraction P_{fa}. Until now, these parameters have been arbitrarily defined, for instance, the values of A_f and A_c where simply set equal (and varied from this base point) to A_K value defined by Kelly (2009), which was based on field measurements of the sediment transport over a medium sand beach.

For this reason, in this chapter an analysis of the values these crucial parameters assume

in more realistic conditions, and the role they could play on model results is presented. First we relate the sediment parameters A_f and A_c to real beach grain diameters. Then, the value of the realistic thickness of the active layer L_a for the two swash events studied is analysed. Finally, as the purpose of this chapter is to test the model for conditions that can be observed in real beaches, other initial configurations of the initial volume fraction (with spatial variation over the bed slope) are defined in order to evaluate the role of this parameter on the results of the model.

7.2 Defining realistic A_f and A_c parameters

As a first attempt to set a more realistic sediment parameter A three commonly used bedload transport formulae were analysed: Meyer-Peter-Müller (MPM), Bagnold (B) and Madsen (M).

MPM formula can be written as

$$\Phi = 8(\Theta - \Theta_{cr})^{3/2} \tag{7.1}$$

with $\Theta_{cr} = 0.047$ being the value of Θ at the threshold of motion, where Θ is the Shields parameter defined as

$$\Theta = \frac{\tau_0}{g\rho(s-1)d} \tag{7.2}$$

in which $\tau_0 = \rho C_D U^2$ is the bed shear stress, C_D is the drag coefficient, g is the acceleration due to gravity, ρ is the water density, $s = \frac{\rho_s}{\rho}$ is the ratio of densities of sediment and water, and d is the grain diameter.

MPM equation (7.1) is written in its dimensionless form in which Φ is equal to

$$\Phi = \frac{q_b}{[g(s-1)d^3]^{1/2}} \tag{7.3}$$

where q_b is the volumetric bedload transport rate per unit width. Substituting (7.2) and (7.3) into (7.1) it is possible to obtain the MPM volumetric bedload transport formula as

$$q_{b_{MPM}} = \frac{8C_D^{3/2}}{g(s-1)}(U^3 - U_{cr}^3) \tag{7.4}$$

from which it is possible to establish that the value of the sediment parameter A_{MPM} for the MPM transport formula is

$$A_{MPM} = \frac{8C_D^{3/2}}{g(s-1)}. \tag{7.5}$$

The B transport formula in its dimensionless form is

$$\Phi = F_B \Theta^{1/2}(\Theta - \Theta_{cr}) \tag{7.6}$$

with

$$F_B = \frac{0.1}{C_D^{1/2}(\tan\phi + \tan\theta)} \tag{7.7}$$

in which $\phi = 32°$ is the angle of repose and θ is the angle of the beach slope. In the same way as with the MPM formula it is possible to obtain the volumetric bedload transport formula as

$$q_{b_B} = \frac{F_B C_D^{3/2}}{g(s-1)} U(U^2 - U_{cr}^2) \tag{7.8}$$

and obtain the sediment parameter value A_B for the Bagnold formula as

$$A_B = \frac{F_B C_D^{3/2}}{g(s-1)}. \tag{7.9}$$

Now, the Madsen dimensionless transport formula is

$$\Phi = F_M(\Theta^{1/2} - 0.7\Theta_{cr}^{1/2})(\Theta - \Theta_{cr}) \tag{7.10}$$

where $F_M = \frac{8}{\tan\phi}$, which again can be re-written to obtain the volumetric bedload formula as

$$q_{b_M} = \frac{F_M C_D^{3/2}}{g(s-1)}(U - 0.7U_{cr})(U^2 - U_{cr}^2) \tag{7.11}$$

and similarly, as in the other cases, the sediment parameter A_M for the Madsen formula can be written as

$$A_M = \frac{F_M C_D^{3/2}}{g(s-1)}. \tag{7.12}$$

Note that in all these equations the drag coefficient C_D is approximated as

$$C_D = \Big[\frac{0.40}{1 + \ln\left(\frac{z_0}{h}\right)}\Big]^2 \tag{7.13}$$

in which the bed roughness length is $z_0 = \frac{d}{12}$ (Soulsby (1997)).

For B and M formulae Θ_{cr} is calculated using the Soulsby-Whitehouse formula

$$\Theta_{cr} = \frac{0.30}{1 + 1.2D_*} + 0.055[1 - e^{-0.02D_*}] \tag{7.14}$$

in which

$$D_* = \Big[\frac{g(s-1)}{\nu^2}\Big]^{1/3} d \tag{7.15}$$

Now, in Table 7.1 the sediment parameter A corresponding to the three bedload transport formulae, equations (7.5), (7.9) and (7.12), for different depths and grain diameters is shown. The grain diameters chosen correspond to fine, medium, coarse and very coarse sand respectively.

Table 7.1: Sediment parameters for the three bedload transport formulae

$\mathbf{h}[\mathbf{m}]$	$\mathbf{d}[\mathbf{m}]$	$\mathbf{C_D}[-]$	$\mathbf{A_{MPM}}[\mathbf{s^2/m}]$	$\mathbf{A_B}[\mathbf{s^2/m}]$	$\mathbf{A_M}[\mathbf{s^2/m}]$
0.1	0.00015	0.0025	6.48×10^{-5}	2.22×10^{-5}	6.615×10^{-5}
	0.0004	0.003	9.6×10^{-5}	2.677×10^{-5}	8.686×10^{-5}
	0.0007	0.0038	1.23×10^{-4}	3.457×10^{-5}	1.258×10^{-4}
	0.0015	0.0050	1.79×10^{-4}	4.407×10^{-5}	1.835×10^{-4}
0.5	0.00015	0.0025	3.74×10^{-5}	1.546×10^{-5}	3.814×10^{-5}
	0.0004	0.003	5.16×10^{-5}	1.796×10^{-5}	4.775×10^{-5}
	0.0007	0.0038	6.72×10^{-5}	2.194×10^{-5}	6.446×10^{-5}
	0.0015	0.0050	8.51×10^{-5}	2.677×10^{-5}	8.685×10^{-5}
1	0.00015	0.0025	3.03×10^{-5}	1.345×10^{-5}	3.094×10^{-5}
	0.0004	0.003	4.1×10^{-5}	1.54×10^{-5}	3.814×10^{-5}
	0.0007	0.0038	4.93×10^{-5}	1.86×10^{-5}	5.032×10^{-4}
	0.0015	0.0050	6.48×10^{-5}	2.232×10^{-5}	3.615×10^{-4}
5	0.00015	0.0025	1.96×10^{-5}	1.006×10^{-5}	2.0×10^{-5}
	0.0004	0.003	2.54×10^{-5}	1.134×10^{-5}	2.395×10^{-5}
	0.0007	0.0038	2.97×10^{-5}	1.327×10^{-5}	3.032×10^{-5}
	0.0015	0.0050	3.78×10^{-5}	1.546×10^{-5}	3.814×10^{-5}
10	0.00015	0.0025	1.65×10^{-5}	8.981×10^{-6}	1.688×10^{-5}
	0.0004	0.003	1.961×10^{-5}	1.006×10^{-5}	2.0×10^{-5}
	0.0007	0.0038	2.447×10^{-5}	1.166×10^{-5}	2.497×10^{-5}
	0.0015	0.0050	3.03×10^{-5}	1.345×10^{-5}	3.094×10^{-5}

Note that for the three bedload formulae the value of the sediment parameter A increases with grain size for all the depths tested; therefore if the threshold of motion is not taken into account in equations (7.4), (7.8) and (7.11), and we end up with a transport formula of the form $q = AU^3$ (as assumed in this research), the sediment transport rate will increase with grain size. This result seems physically unrealistic, i.e. the sediment transport should decrease as the grain diameter increases.

For this reason it was decided to take into account the threshold of motion and calculate the sediment transport using the three bedload formulae to see if in that case the sediment transport behaves as expected. In Table 7.2 these calculations are summarised for the same range of depths and grain sizes as for Table 7.1. It can be noted that the inclusion of the threshold of motion improves the behaviour of the sediment transport just for $h \geq 1$ m and for coarse or very coarse sediments; for smaller depths (like the ones found in the swash zone problems) the behaviour does not improve.

It seems that within the coastal engineering community it is common practice to set a value of $C_D = 0.0025$ (constant and independent of h) if no measurements are available (see Soulsby (1997)). This might be due to the lack of agreement on how to calculate the drag coefficient specially in the swash zone; some researchers have used a Chezy approach (see e.g. Zhu et al. (2012)) and recently other have proposed to use a description of the bottom boundary layer (see e.g.Briganti et al. (2011)). In Table 7.3 the sediment transport rates according to the MPM formula taking into account the threshold of motion for the different grain sizes, and taking a constant value for the drag coefficient are shown. Note that setting C_D constant makes the sediment parameter A constant for all

Table 7.2: Sediment transport rates for the three bedload formulae tested taking into account the threshold of motion

$\mathbf{h[m]}$	$\mathbf{d[m]}$	$\mathbf{C_D}[-]$	$\mathbf{q_{b_{MPM}}[m^2/s]}$	$\mathbf{q_{b_B}[m^2/s]}$	$\mathbf{q_{b_M}[s^2/m]}$
0.1	0.00015	0.0025	6.42×10^{-5}	2.092×10^{-5}	5.112×10^{-5}
	0.0004	0.003	9.35×10^{-5}	2.501×10^{-5}	6.661×10^{-5}
	0.0007	0.0038	1.17×10^{-4}	3.135×10^{-5}	9.157×10^{-5}
	0.0015	0.0050	1.61×10^{-4}	3.722×10^{-5}	1.122×10^{-4}
0.5	0.00015	0.0025	3.68×10^{-5}	1.406×10^{-5}	2.738×10^{-5}
	0.0004	0.003	4.91×10^{-5}	1.621×10^{-5}	3.366×10^{-5}
	0.0007	0.0038	5.72×10^{-5}	1.902×10^{-5}	4.162×10^{-5}
	0.0015	0.0050	6.65×10^{-5}	1.942×10^{-5}	4.176×10^{-5}
1	0.00015	0.0025	2.97×10^{-5}	1.205×10^{-5}	2.145×10^{-5}
	0.0004	0.003	3.84×10^{-5}	1.371×10^{-5}	2.584×10^{-5}
	0.0007	0.0038	4.34×10^{-5}	1.568×10^{-5}	3.066×10^{-5}
	0.0015	0.0050	4.62×10^{-5}	1.548×10^{-5}	2.808×10^{-5}
5	0.00015	0.0025	1.91×10^{-5}	8.657×10^{-6}	1.272×10^{-5}
	0.0004	0.003	2.28×10^{-5}	9.586×10^{-6}	1.467×10^{-5}
	0.0007	0.0038	2.38×10^{-5}	1.035×10^{-5}	1.589×10^{-5}
	0.0015	0.0050	1.87×10^{-5}	8.617×10^{-6}	1.135×10^{-5}
10	0.00015	0.0025	1.59×10^{-5}	7.58×10^{-6}	1.031×10^{-5}
	0.0004	0.003	1.85×10^{-5}	8.303×10^{-6}	1.169×10^{-5}
	0.0007	0.0038	1.83×10^{-5}	8.74×10^{-6}	1.126×10^{-5}
	0.0015	0.0050	1.17×10^{-5}	6.604×10^{-6}	7.604×10^{-6}

grain sizes, but using the threshold of motion the behaviour of the sediment transport rate is as expected: sediment transport decreases when grain size increases. Note as well that if the threshold of motion is not taken into account then as C_D and A are constant the sediment transport rate would be constant for all grain sizes (sediment transport does not change with d) which also seems physically impossible.

From all this analysis it can be concluded that in the case of bedload the sediment parameter A usually does not depend directly on grain size d (see equations (7.5), (7.9) and (7.12)) but in C_D which is dependent on d. However, there is not a well-established way to calculate the value of the drag coefficient in terms of the grain size and, actually, it seems to be common practice to set a constant $C_D = 0.0025$, independent of grain size, when measurements are not available. Doing this implies that A is constant for all grains sizes and therefore this parameter is not the one differentiating the transport of different sediments; it is the inclusion of the threshold of motion (Θ_{cr}, which depends on d) that is responsible for the different transport rates for different grain sizes. For all these reasons it is concluded that it is not possible to use a bedload formula to define the values of the sediment parameters A_f and A_c, and relate them with grain diameter d, therefore it was decided to use a total load approach.

Van Rijn (1985) derived a full theory of sediment transport in rivers and simplified the results in the following total load formula

$$q_t = q_b + q_s \tag{7.16}$$

Table 7.3: Sediment transport rate according with MPM formula taking the threshold of motion into account

$\mathbf{d}[\mathbf{m}]$	$\mathbf{C_D}[-]$	$\mathbf{A_{MPM}}[\mathbf{s^2/m}]$	$\mathbf{U_{cr}}[\mathbf{m/s}]$	$\mathbf{q_{b_{MPM}}}[\mathbf{m^2/s}]$
0.00015	0.0025	6.45×10^{-5}	0.2091	6.39×10^{-5}
0.0004	0.0025	6.45×10^{-5}	0.2957	6.28×10^{-5}
0.0007	0.0025	6.45×10^{-5}	0.4516	5.86×10^{-5}
0.0015	0.0025	6.45×10^{-5}	0.661	4.59×10^{-5}

in which

$$q_b = 0.005\ Uh \left[\frac{U - U_{cr}}{[(s-1)gd]^{1/2}}\right]^{2.4} \left(\frac{d}{h}\right)^{1.2} \tag{7.17}$$

$$q_s = 0.012\ Uh \left[\frac{U - U_{cr}}{[(s-1)gd]^{1/2}}\right]^{2.4} \left(\frac{d}{h}\right) D_*^{-0.6} \tag{7.18}$$

with

$$U_{cr} = 0.19\ d^{0.1} \log_{10}\left(\frac{4h}{d_{90}}\right) \qquad \text{for} \quad 0.1 \leq x \leq 0.5\text{mm}$$

$$U_{cr} = 8.5\ d^{0.6} \log_{10}\left(\frac{4h}{d_{90}}\right) \qquad \text{for} \quad 0.5 \leq x \leq 2\text{mm}$$

Using (7.17) and (7.18) in (7.16) we get

$$q_t = A_{VR}\ U[U - U_{cr}]^{2.4} \tag{7.19}$$

in which $A_{VR} = A_b + A_s$ with

$$A_b = \frac{0.005}{[(s-1)\ g]^{1.2} h^{0.2}} \tag{7.20}$$

$$A_s = \frac{0.012\ D_*^{-0.6}}{[(s-1)\ g]^{1.2} d^{0.2}} \tag{7.21}$$

If the threshold of motion is not taken into account (i.e. $U_{cr} = 0$) in (7.19) then we get

$$q_t = A_{VR}\ U^{3.4} \tag{7.22}$$

Note that although in this case the exponent of U is 3.4 and in our model is 3 (see equation (3.44)), it was considered that the Van Rijn formula could still provide us with a good approximation of the sediment parameters and therefore be able to relate them with the grain diameter in order to give more realistic values to A_f and A_c.

In Table 7.4 values of the sediment parameters A_{VR}, A_b and A_s using (7.20) and (7.21) are shown. Note that as expected A_b only varies with the depth h, this confirms the conclusion stated before; changes in bedload transport rate for different grain sizes are, as with bedload formulae, mainly due to the inclusion of the threshold velocity. In contrast A_s varies only with the grain size d, and as expected, its value decreases as the grain size increases.

From this analysis it can be concluded that A_s is the main responsible for the variation in the transport rate with the grain size. Note as well that generally $A_s > A_b$, but at small depths ($h \leq 0.5$ m) and coarser sediments ($d \geq 0.0015$ m) values of $A_b > A_s$ as expected. All these conclusions allow us to use with some degree of confidence the Van Rijn formula to approximate realistic values for A_f and A_c and relate them to the grain size d. It was decided then to use $d = 0.0004$ m, a typical grain size for medium sand, for the fine fraction, and $d = 0.0015$ m, for the coarse fraction. Therefore the sediment parameters obtained are $A_f = 9.043 \times 10^{-4}\ s^2/m$ for the fine fraction and $A_c = 5.069 \times 10^{-4}\ s^2/m$ for the coarse.

Table 7.4: Sediment parameters A_b, A_s and A_{VR} for different depths and grain sizes

h[m]	**d[m]**	$\mathbf{D_*}[-]$	$\mathbf{A_b}[\mathbf{s^2/m}]$	$\mathbf{A_s}[\mathbf{s^2/m}]$	$\mathbf{A_{VR}}[\mathbf{s^2/m}]$
10	0.00015	3.0468	1.176×10^{-4}	0.0013	0.0015
	0.0004	8.1247	1.176×10^{-4}	6.088×10^{-4}	7.265×10^{-4}
	0.0007	14.2183	1.176×10^{-4}	3.891×10^{-4}	5.068×10^{-4}
	0.0015	30.4678	1.176×10^{-4}	2.115×10^{-4}	3.291×10^{-4}
5	0.00015	3.0468	1.351×10^{-4}	0.0013	0.0015
	0.0004	8.1247	1.351×10^{-4}	6.088×10^{-4}	7.44×10^{-4}
	0.0007	14.2183	1.351×10^{-4}	3.891×10^{-4}	5.242×10^{-4}
	0.0015	30.4678	1.351×10^{-4}	2.115×10^{-4}	3.466×10^{-4}
1	0.00015	3.0468	1.865×10^{-4}	0.0013	0.0015
	0.0004	8.1247	1.865×10^{-4}	6.088×10^{-4}	7.953×10^{-4}
	0.0007	14.2183	1.865×10^{-4}	3.891×10^{-4}	5.756×10^{-4}
	0.0015	30.4678	1.865×10^{-4}	2.115×10^{-4}	3.979×10^{-4}
0.5	0.00015	3.0468	2.142×10^{-4}	0.0013	0.0015
	0.0004	8.1247	2.142×10^{-4}	6.088×10^{-4}	8.23×10^{-4}
	0.0007	14.2183	2.142×10^{-4}	3.891×10^{-4}	6.033×10^{-4}
	0.0015	30.4678	2.142×10^{-4}	2.115×10^{-4}	4.257×10^{-4}
0.1	0.00015	3.0468	2.955×10^{-4}	0.0013	0.0016
	0.0004	8.1247	2.955×10^{-4}	6.088×10^{-4}	9.043×10^{-4}
	0.0007	14.2183	2.955×10^{-4}	3.891×10^{-4}	6.846×10^{-4}
	0.0015	30.4678	2.955×10^{-4}	2.115×10^{-4}	5.069×10^{-4}

7.3 Defining real active layer thickness L_a values

There is a some confusion concerning the definition of the active layer (L_a), because many terminologies have been used to describe the thickness of the layer of sediment that is moved in response to the driving hydrodynamics. These terms are not applied consistently and can be related to different measurement methods or different temporal scales. Sherman et al. (1994) used the term "depth of activity" to refer to the thickness of sediment that is reworked by the flow during a storm. Sunamura and Krauss (1985) and Sherman et al. (1994) both refer to "mixing depth" to the thickness of reworked sediment, but measured over just a few hours. Ferreira et al. (1998) and Ferreira et al. (2000) however, used this same term to describe the thickness of reworked sediment measured during a tidal cycle. In this research the terms adopted by Anfuso (2005) and Miller and Warrick (2012) are used. The active layer term is used to refer to the sediment that is physically reworked by hydrodynamic processes, and the depth of disturbance is the actual vertical measurements of the thickness of reworked sediment at certain x positions over the bed profile carried out by Miller and Warrick (2012), so it seems logical to use this values to approximate the thickness of the active layer (see Figure 7.1).

The concept of a relatively uniform layer of sediment moving as bedload in the direction of the flow and the important task of measuring the thickness of this transported sediment has been a matter of research in the last two decades (see e.g. Madsen (1989) and Van Wellen et al. (2000)). Some field measurements of the active layer on steep, non-dissipative beaches have been made (e.g Ciavola et al. (1997)); fewer have been made on mixed beaches (e.g. Masselink et al. (2010)). Therefore there is little information to

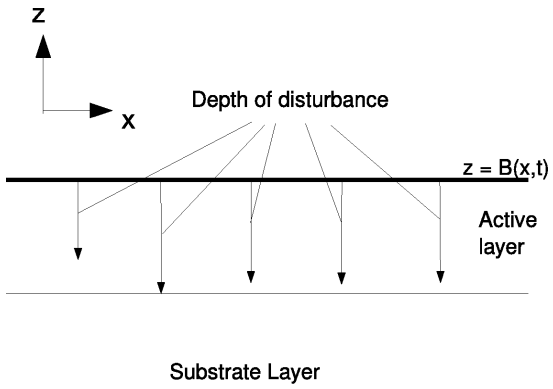

Figure 7.1: Schematic active layer and depth of disturbance

accurately estimate the thickness of the active layer.

Anfuso (2005) analysed available field measurements and concluded that the main factors defining the depth of disturbance (here used as an approximation of the active layer thickness) are breaking wave type and height, and beach characteristics, which together define the morphodynamic beach state. This was later confirmed by Miller and Warrick (2012). It was observed that for low energy wave conditions (dissipative beaches) relatively small depth disturbances were found (10 cm. max. depth of disturbance) and for higher wave energies (reflective beaches associated with plunging breakers) bigger values of disturbance depth were observed (30 cm. max. depth of disturbance).

The findings described above are consistent with those values used in §5.6 using (5.53) for the values of A_f and A_c used there, for the two swash event types used in this research. In tables 5.1 and 6.1 these L_a values are presented, and it can be seen that the maximum L_a value for the PW01 swash event is 0.35 m, while for the non-breaking wave the maximum value is 0.0061 m. Note that the PW01 swash event could corre-

spond to a high energy wave condition in which case the calculated value agrees well with field observations. Similarly, the non-breaking case tested here could correspond to a low energy wave condition; the calculated L_a used here is also consistent with field observations.

Note now, that due to the fact that L_a depends on the values of A_f and A_c, a new active layer thickness for the new realistic A_f and A_c parameters is calculated for both types of swash event. Again using (5.53) and using the respective maximum U_s value for each swash event; and in both cases setting $P_{fs} = 0.2$, which is the smaller volume fraction used in the numerical tests (see §7.4), the calculated active layer thickness for the PW01 swash event is then 0.0536 m., and for the non-breaking wave swash is 0.001 m. Since eq.(5.53) only provides us with a maximum value of L_a at which the non-physical region will be present, it was decided to use $L_a = 0.06$ m for the PW01 event, and $L_a = 0.0015$ m for the non-breaking wave event. Also, bear in mind that we wanted to use the smallest L_a value possible because this would make changes in P_{fa} more evident, so that we are able to analyse them and therefore establish possible relations with the changes in bed level.

7.4 Variations in fine volume fraction P_{fa} initial conditions

For simplicity up to now the initial proportion of fine and coarse sediment was taken constant and equal; i.e. $P_{fa}(x, t_0) = P_{ca}(x, t_0) = 0.5$. Clearly, the initial distribution of sediments on the slope of a beach plays a key role on the evolution in time of the

volume fraction and therefore influences the beachface change. For this reason it was considered important to investigate the effect on the model of different volume fraction initial conditions.

In real beaches one can find a lot of different configurations of the proportion of fine and coarse sediments: one beach can have many grain sizes instead of just one fine and one coarse; $P_{fa} \neq P_{ca}$ in general; and fine and coarse sediment fractions can vary in the cross-shore direction (i.e. $P_{f/ca}(x, t_0)$). Therefore, seven different initial configurations of the volume fraction are considered here. A schematic representation of these seven conditions are presented in Figure 7.2. Note that initial conditions Test 1 to 3 are cases in which volume fraction is constant in the cross-shore direction with different proportions of fine and coarse sediment. Initial conditions Test 4 to 7 were designed to evaluate the effect that a spatial variation in the initial volume fraction can have on the final results given by the model. These initial conditions slightly vary depending on which type of swash event is being tested (i.e. PW01 or non-breaking wave swash) because the values of the maximum and minimum length of the shoreline (x_s^{max} and x_s^{min}) depend on the type of swash. The initial conditions for both types of swash flow are detailed in Table 7.5. Note that for the PW01 swash event $x_s^{min} = 0$, $x_m = 10$ and $x_s^{max} = 20$; and for the non-breaking wave swash event $x_s^{min} = -3.1395$, $x_m = 0.4652$ and $x_s^{max} = 4.07$; and that all $x = \frac{\hat{x}}{\Delta x}$, where $\hat{x}$ is the x-position in meters and $\Delta x = 1$m.

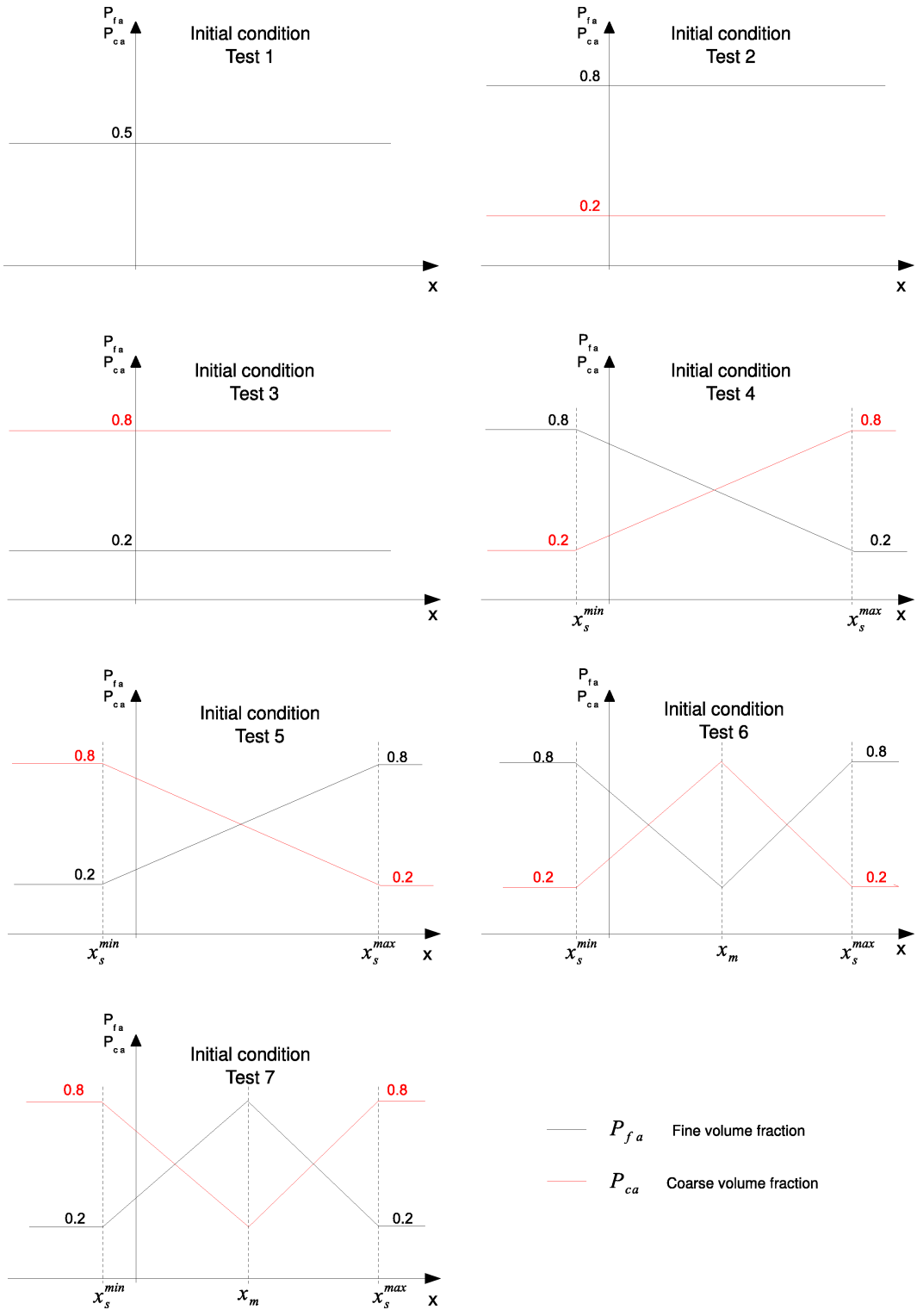

Figure 7.2: Schematic representation of the initial volume fraction configurations tested

Table 7.5: Volume fraction initial conditions for the PW01 and non-breaking wave swash events

Test No.	PW01	Non-breaking wave
1	$P_{fa}(x,t_0) = 0.5$	$P_{fa}(x,t_0) = 0.5$
2	$P_{fa}(x,t_0) = 0.2$	$P_{fa}(x,t_0) = 0.2$
3	$P_{fa}(x,t_0) = 0.8$	$P_{fa}(x,t_0) = 0.8$
4	$P_{fa}(x,t_0) = \begin{cases} 0.8 & x < x_s^{min} \\ -0.03x + 0.8 & x_s^{min} \leq x \leq x_s^{max} \\ 0.2 & x > x_s^{max} \end{cases}$	$P_{fa}(x,t_0) = \begin{cases} 0.8 & x < x_s^{min} \\ -0.0832x + 0.5386 & x_s^{min} \leq x \leq x_s^{max} \\ 0.2 & x > x_s^{max} \end{cases}$
5	$P_{fa}(x,t_0) = \begin{cases} 0.2 & x < x_s^{min} \\ 0.03x + 0.2 & x_s^{min} \leq x \leq x_s^{max} \\ 0.8 & x > x_s^{max} \end{cases}$	$P_{fa}(x,t_0) = \begin{cases} 0.2 & x < x_s^{min} \\ 0.0832x + 0.4614 & x_s^{min} \leq x \leq x_s^{max} \\ 0.8 & x > x_s^{max} \end{cases}$
6	$P_{fa}(x,t_0) = \begin{cases} 0.8 & x < x_s^{min} \\ -0.06x + 0.8 & x_s^{min} \leq x \leq x_m \\ 0.06x - 0.4 & x_m < x \leq x_s^{max} \\ 0.8 & x > x_s^{max} \end{cases}$	$P_{fa}(x,t_0) = \begin{cases} 0.8 & x < x_s^{min} \\ -0.1664x + 0.2774 & x_s^{min} \leq x \leq x_m \\ 0.1664 - 0.1228 & x_m < x \leq x_s^{max} \\ 0.8 & x > x_s^{max} \end{cases}$
7	$P_{fa}(x,t_0) = \begin{cases} 0.2 & x < x_s^{min} \\ 0.06x + 0.2 & x_s^{min} \leq x \leq x_m \\ -0.06x - 1.4 & x_m < x \leq x_s^{max} \\ 0.2 & x > x_s^{max} \end{cases}$	$P_{fa}(x,t_0) = \begin{cases} 0.2 & x < x_s^{min} \\ 0.1664x + 0.7226 & x_s^{min} \leq x \leq x_m \\ -0.1664 - 0.8772 & x_m < x \leq x_s^{max} \\ 0.2 & x > x_s^{max} \end{cases}$

7.5 Results

After defining the realistic values of the most important parameters in the model (A_f, A_c, L_a and $P_{fa}(x, t_0)$), a set of different numerical tests were preformed for both types of swash flow, in order to analyse the results given by the model and also, identify if these more 'realistic' parameters give as a result a more 'realistic' prediction of the volume fraction and bed change in the beach.

7.5.1 PW01 swash event

The seven numerical tests for the PW01 swash event are those corresponding to the initial conditions Test 1-7 in Table 7.5, using the sediment parameters defined before $A_f = 0.0009043 s^2/m$ and $A_c = 0.0005069 s^2/m$ and the corresponding thickness of the active layer $L_a = 0.06$m.

Fine volume fraction

The evolution of P_{fa} for all numerical tests described in Table 7.5 is shown in Figure 7.3. Comparing this figure with the general results in Figure 5.12 it can be seen that the behaviour of P_{fa} is similar in both figures: in the uprush phase the fine sediment is transported upslope so P_{fa} increases; then in the backwash the fine sediment is taken offshore by the flow.

Now, comparing Figures 7.3 (a), (b) and (c) (cases in which the initial P_{fa} is constant

along the cross-shore profile), the behaviour of P_{fa} is very similar: in the three cases fine sediment from the lower part of the beach profile is transported and located in the upper part of the slope during the upslope; and in the backwash this transported fine sediment is then transported downslope by the backwash leaving, in the three cases, less fine sediment than that at the initial condition.

Comparing now the cases in which the initial P_{fa} varies spatially (linearly increasing or decreasing) Figures 7.3 (d) and (e), their behaviour is somewhat different. In the case where the initial P_{fa} linearly decreases in the cross-shore direction (Figure (d)) it can be seen that the fine sediment taken from offshore is transported and distributed onshore in the uprush, leaving more fine sediment than the initial one in almost all the beach profile; whereas in the backwash this fine sediment is transported offshore by the backwash leaving, over the whole beach profile, less sediment than that at the initial time. Meanwhile in the case where the initial P_{fa} linearly increases in the onshore direction (Figure (e)); during the uprush the fine sediment is eroded from the lower and middle part of the swash zone whereas in the upper zone the fine sediment is increased, in the backwash the fine sediment is transported offshore which eventually increases its proportion on the lower part of the swash zone.

From Figures 7.3 (f) and (g) we can compare the cases in which the initial P_{fa} varies spatially but in a different manner than above (see Figure 7.2). In Figure (f) (with a minimum in the middle part) it can be seen that in the uprush (t = 1,2 and 3 s.) the fine sediment fraction is increased except from a small region around the middle part of the swash zone from which the fine sediment is taken to be deposited in the upper

part of the beach. In the backwash, the fine sediment is slightly eroded from the upper part of the profile to be deposited (and accumulated) around the middle zone of the beach and completely eroded offshore in the lower part. Finally, in Figure (g) (with a maximum in the middle part) it is noted that during the uprush phase the fine fraction is decreased for the lower half of the profile and shows a small increment in the upper half, while in the backwash fine sediment is eroded form the upper part and deposited in the lower half of the swash zone causing an accumulation of the fine fraction in the lower part of the beach profile.

Finally, observe that the behaviour of the P_{fa} in the uprush and backwash for the case in which the initial P_{fa} linearly decreases (Figure 7.3 (d)) is very similar to that shown in Figure 7.3 (f) on the part of the slope where the initial P_{fa} linearly decreases (lower part of the profile); and in the same way, the behaviour of P_{fa} when the initial condition states that the initial P_{fa} is linearly increasing (Figure 7.3 (e)) is very similar to that shown in the same Figure 7.3 (f) in the zone of the beach where the initial P_{fa} linearly increases. This analysis can be applied in a similar manner to Figure 7.3 (g) to describe the behaviour of P_{fa}. Therefore it can be concluded that the initial distribution of sediments on the slope is a very important parameter influencing the behaviour in time of the volume fraction.

Now, to see more clearly what is the influence of the initial condition in P_{fa} on the final shape of the volume fraction, in Figure 7.4 the final P_{fa} for the seven numerical tests is plotted. Firstly, when the initial condition in P_{fa} is constant or linearly decreasing in the cross-shore direction (Test 1-4), P_{fa} is reduced (eroded offshore) from the whole

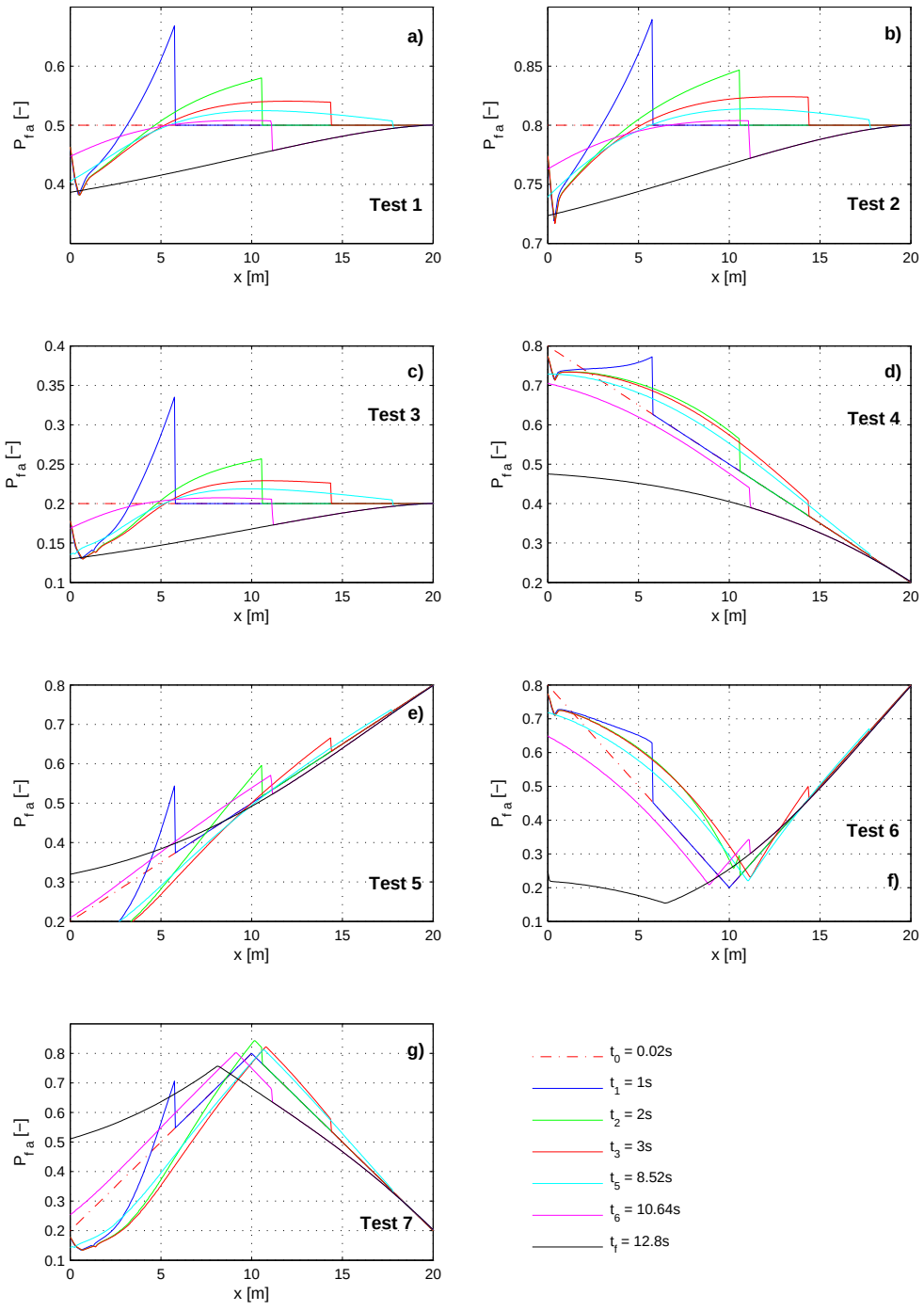

Figure 7.3: Fine volume fraction evolution in time for the PW01 numerical tests

beach profile (Figures 7.4 (a), (b), (c) and (d)). Secondly, it is seen form Figure (e) that when the initial condition in P_{fa} linearly increases (Test 5), P_{fa} shows an accumulation in the lower middle part of the swash zone and a little reduction on the upper part. Note that if we carefully look at figures (f) and (g) a combination of the two conclusions mentioned above applies. For instance, in Figure (f) (/test 6), the area of the beach profile in which the initial condition in P_{fa} is linearly decreasing ($x < 10$m) P_{fa} is reduced, and in the part of the profile in which the initial condition in P_{fa} is linearly increasing ($x > 10$ m), P_{fa} shows an increment at the base (around $x = 10$ m) and a small decrement in the upper part of the swash. The same reasoning can applied to explain the behaviour in Test 7 showed in Figure (g).

In Figure 7.5 the final change in P_{fa} relative to the initial P_{fa} for all the tests is shown. It can be seen that for Tests 1-4 P_{fa} decreases over the whole beach profile, and Test 4 is the one showing greater ΔP_{fa}. Now, Test 5 and 7 show an increment in P_{fa} in the lower part of the swash zone and a decrement in the upper part, with Test 7 giving the bigger changes in both areas of the swash zone. Finally, it can be observed that Test 6 is the only case showing an increment in P_{fa} around the middle part of the swash zone and is the case with bigger reduction of P_{fa} in the lower part.

To analyse and understand the behaviour of P_{fa}, we can re-write eq.(3.43) for the fine fraction as

$$L_a \frac{\partial P_{fa}}{\partial t} = -\xi \left[P_{cs} \frac{\partial q_f}{\partial x} - P_{fs} \frac{\partial q_c}{\partial x} \right] \tag{7.23}$$

from which we can see that it is important to know the behaviour of the terms $P_{cs}\frac{\partial q_f}{\partial x}$ and $P_{fs}\frac{\partial q_c}{\partial x}$. For this reason in Figure 7.6 the behaviour of these two terms, at two

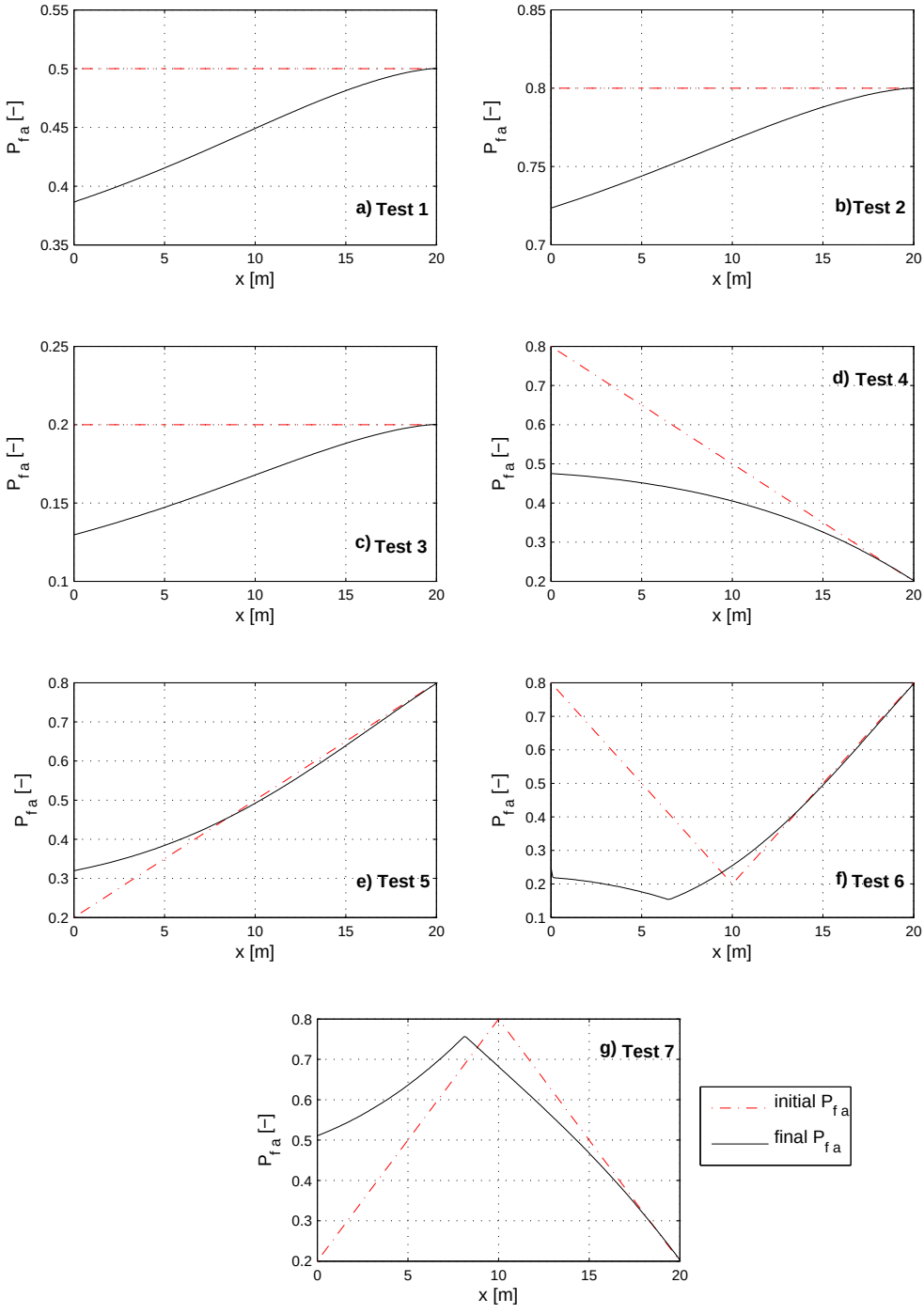

Figure 7.4: Comparison of the final fine volume fraction for all the PW01 numerical tests. Initial P_{fa} -.-, final P_{fa} —

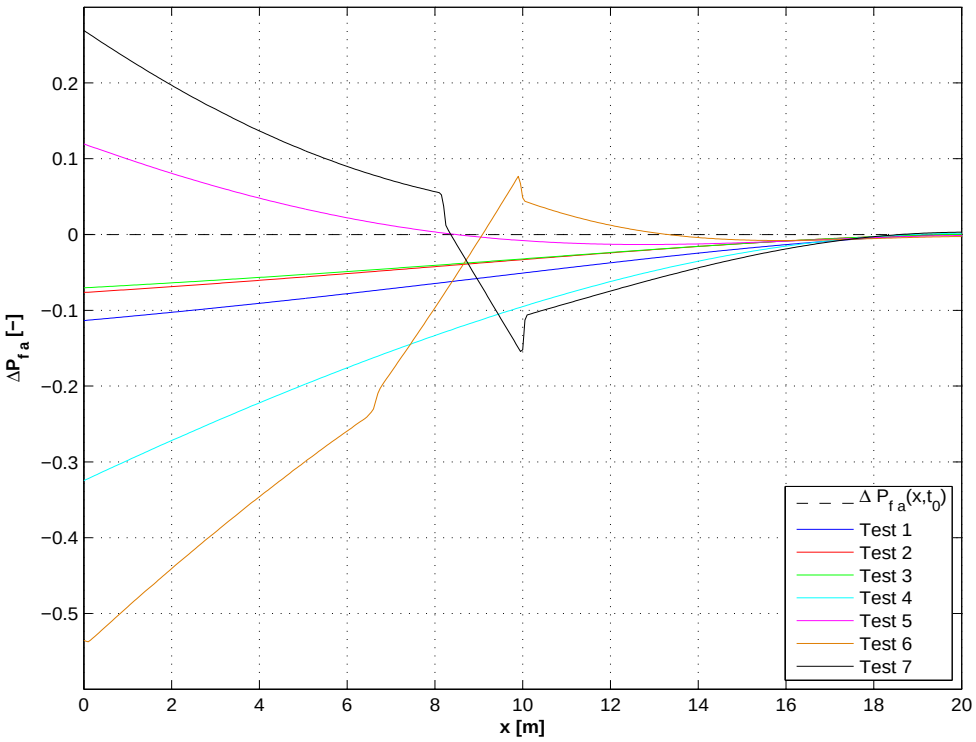

Figure 7.5: Comparison of the final ΔP_{fa} for the PW01 numerical tests

different times in the backwash for all the numerical tests is presented.

It is noted that for Tests 1 to 4, $P_{cs}\frac{\partial q_f}{\partial x} > P_{fs}\frac{\partial q_c}{\partial x}$ and that both are positive over most of the swash zone which yields $\frac{\partial P_{fa}}{\partial t} < 0$ according to (7.23), explaining the reduction of P_{fa} over the whole area (see Figures 7.4 a, b, c and d). Now for Test 5, it can be observed that for $x \leq 5$ m, $P_{fs}\frac{\partial q_c}{\partial x}$ is positive and $P_{cs}\frac{\partial q_f}{\partial x}$ is negative, and also that $|P_{cs}\frac{\partial q_f}{\partial x}| > |P_{fs}\frac{\partial q_c}{\partial x}|$, which according to (7.23) gives the increment in P_{fa} observed in Figure 7.4 (e). For Test 6, it is seen that for $x \leq 8$ m, $P_{cs}\frac{\partial q_f}{\partial x}$ is positive and $P_{fs}\frac{\partial q_c}{\partial x}$ is negative, and that $|P_{cs}\frac{\partial q_f}{\partial x}| > |P_{fs}\frac{\partial q_c}{\partial x}|$, which gives $\frac{\partial P_{fa}}{\partial t} < 0$; note as well that for x around 10 m $P_{fs}\frac{\partial q_c}{\partial x} > 0$ and $P_{cs}\frac{\partial q_f}{\partial x} < 0$, and that $|P_{cs}\frac{\partial q_f}{\partial x}| > |P_{fs}\frac{\partial q_c}{\partial x}|$ resulting in $\frac{\partial P_{fa}}{\partial t} > 0$. These observations explain the behaviour of P_{fa} observed in Figure 7.4 (f). Finally, for Test 7, note that for $x < 8$ m $P_{fs}\frac{\partial q_c}{\partial x} > 0$ and $P_{cs}\frac{\partial q_f}{\partial x} < 0$, and regardless

which is bigger we always get $\frac{\partial P_{fa}}{\partial t} > 0$; in the same way, for $x > 8$ m $P_{cs}\frac{\partial q_f}{\partial x} > 0$ and $P_{fs}\frac{\partial q_c}{\partial x} < 0$ (or nearly zero) and regardless which is bigger we always get $\frac{\partial P_{fa}}{\partial t} < 0$. These observations explain the behaviour of P_{fa} shown in Figure 7.4 (g).

Bed change

The bed change evolution in time for the seven numerical tests is shown in Figure 7.7. Comparing this figure with Figure 5.13 it is evident that the general behaviour of bed change is very similar between figures, but it is important to note that the order of magnitude of the bed change in Figure 7.7 is at least one order of magnitude smaller than that in Figure 5.13. In Figure 5.13 the maximum bed change is around 0.8 m whereas in Figure 5.13 is around 0.1 m. This is due to the fact that in this chapter more realistic parameters are considered and therefore a more realistic bed change (after one swash event) is given as result.

Now we compare bed change results for similar initial P_{fa} conditions. First comparing Figures 7.7 a, b and c (Test 1, 2 and 3) in which the initial P_{fa} condition is constant; it is seen that the general evolution in time of the bed change is very similar between tests but it is noted that the bigger bed change takes place in the case in which there is more fine sediment present in the mixture (Figure 7.7b, Test2), and, conversely, when the amount of fine sediment in the mixture is less than the coarse (Figure 7.7c, Test 3) the bed change is less than for the other cases. Now looking at the tests in which the initial P_{fa} linearly varies in the cross-shore direction, we can observe that again the evolution in time of the bed change is very similar between cases, but that there is a substantial

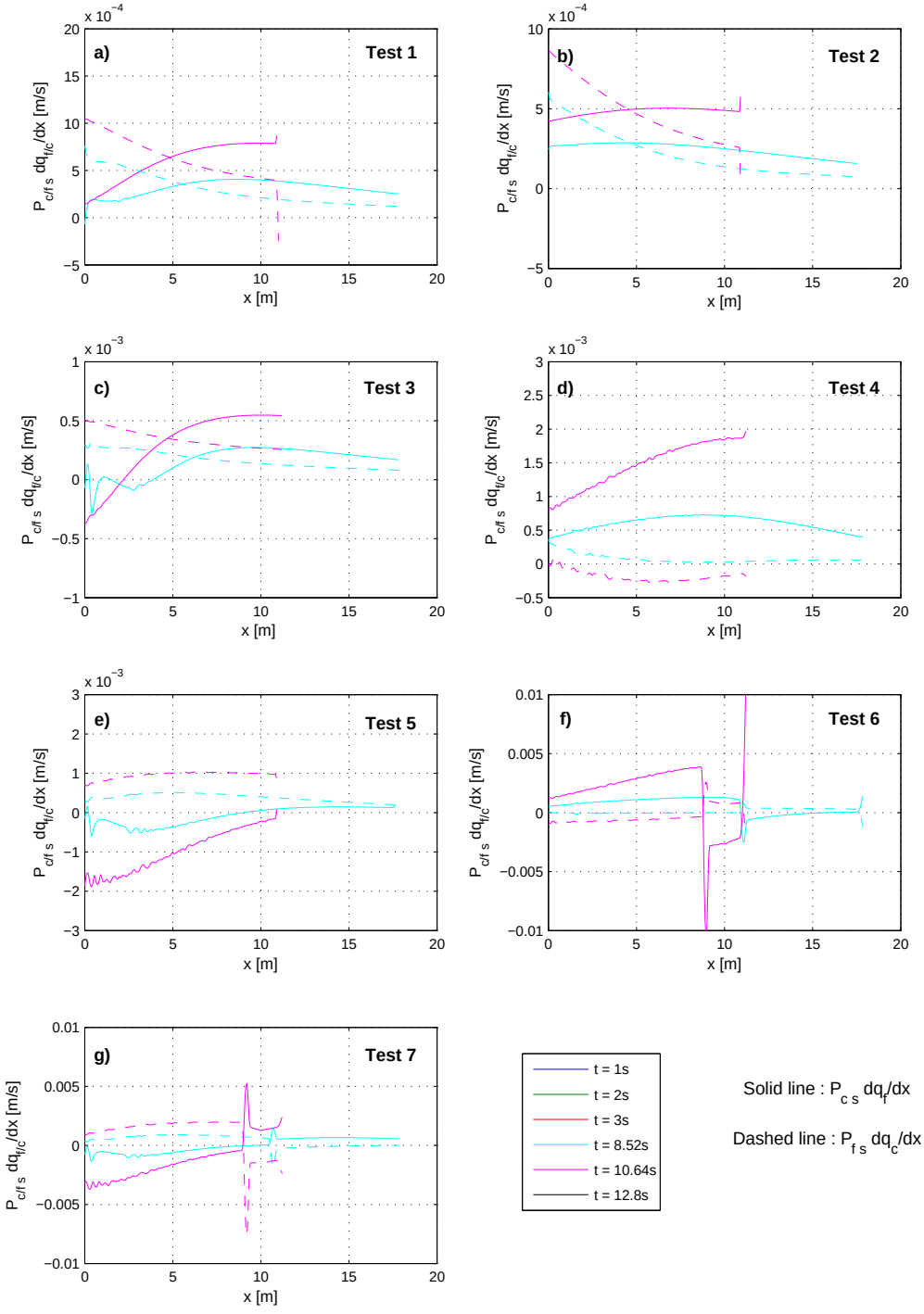

Figure 7.6: Behaviour of the terms $P_{cs}\frac{\partial q_f}{\partial x}$ and $P_{fs}\frac{\partial q_c}{\partial x}$ at two times in the backwash, for the PW01 numerical tests.

difference in the shape of the curves, especially for Tests 6 and 7. It is observed that for Test 6 and 7 a kink appears around $x = 10$ m which does not appear in any other test. This kink is a consequence of the minimum and maximum on the initial P_{fa} condition, which reduces and enhances respectively the sediment transport and therefore the bed change.

In Figure 7.8 a comparison between the final bed change for the seven tests is presented. In this figure it is clear that Test 3 (initial P_{fa} constant and equal to 0.2) is the one with smaller the bed change across the whole beach profile. On the other hand, Test 2 ($P_{fa}(x, t_0) = 0.8$) is the one with greater bed change across the whole profile. Now analysing the figure by regions it is interesting to note the following. In the region close to $x = 0$ the bed change is the same for test 3, 5 and 7 and smaller than that for Tests 2, 4 and 6. Around that area the initial P_{fa} condition is the same for Tests 3, 5 and 7 and has a value around 0.2 (less presence of fine sediment) which produces a smaller bed change than Test 2, 4 and 6 in which the initial amount of fine sediment is bigger ($P_{fa}(x, t_0) = 0.8$). Now in the region around $x = 10$ m the bed change for Test 6 is the smallest of all whereas the biggest is for Test 7, this is because the initial P_{fa} value has a minimum in Test 6 and a maximum in Test 7. Finally, for the region near the maximum run-up ($x = 20$ m) the bed change is almost the same for all the tests although it can be still noted that Test 3 has the smallest bed change and Test 2 the biggest. This is, again, in accordance with the initial amount of fine sediment present in the mixture, and therefore in agreement with one could expect from the physics: the more fine sediment present the more movable the sediment mixture is. So finally, it can be concluded that the importance of the initial fine volume fraction is crutial in the stability (in bed change

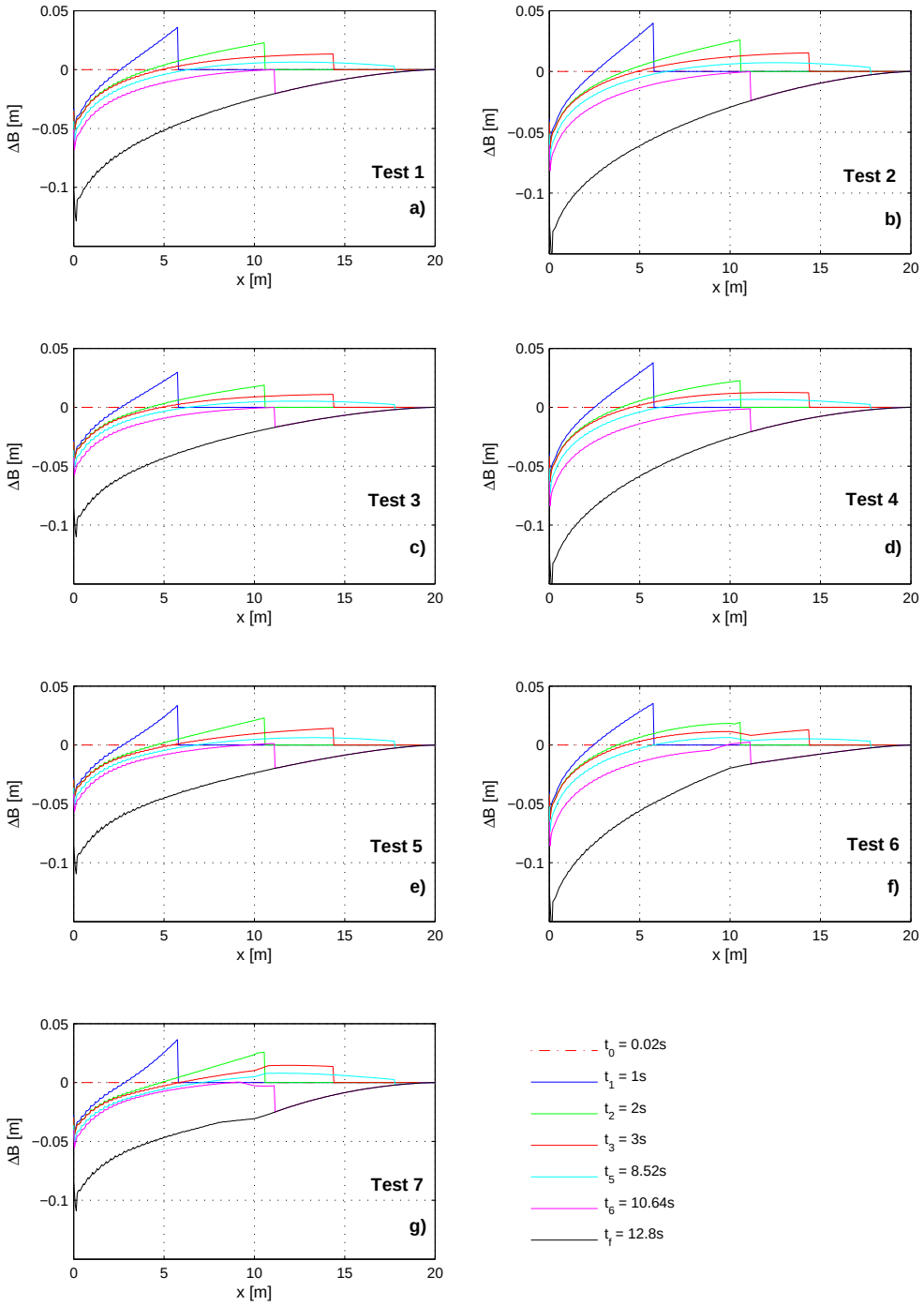

Figure 7.7: Bed change evolution in time for the PW01 numerical tests

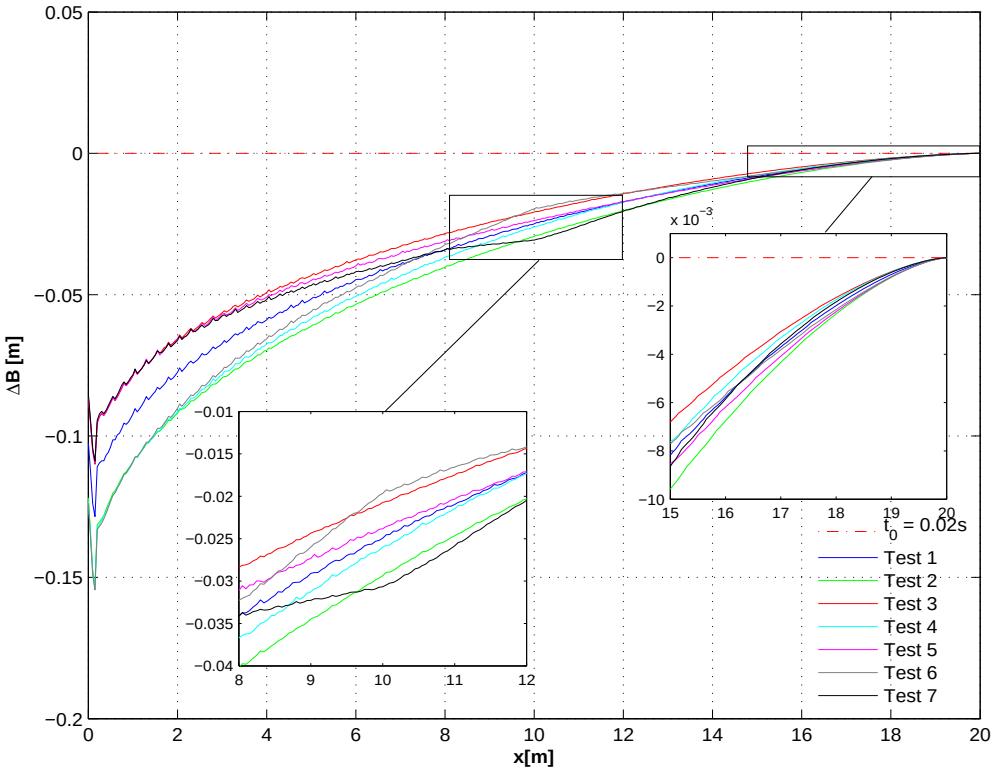

Figure 7.8: Comparison of the final bed change for the PW01 numerical tests

terms) of the beach profile.

7.5.2 Non-breaking wave swash event

The numerical tests for the swash event caused by a non-breaking wave are defined by the initial conditions presented in Table 7.5. These tests are run with the same values of the A_f and A_c parameter than for the PW01 swash event, with the difference that in this case, due to the different hydrodynamics, $L_a = 0.0015$ m.

Fine volume fraction

In Figure 7.9 the evolution in time of the fine volume fraction for all the tests is shown; results are shown just for the region of the slope where the swash event was acting which is denoted in the figure by the blue and green circles. The behaviour depicted in Figures a, b and c is very similar to that given in the general result shown in Figure 6.8 with the only difference being that in this case the variation in P_{fa} is bigger, which is again, thought to be due to the fact that in this case we are using more realistic parameters to run the model. It can be seen that when the initial P_{fa} is constant across the profile (Figures a, b and c, Tests 1-3) the evolution in time of P_{fa} is very similar: P_{fa} increases during the uprush phase leaving a maximum in the middle part of the swash zone; during the backwash P_{fa} is reduced in the upper two thirds of the swash zone with a minimum value around the middle part and an increase around the lower part of the swash zone. Now, comparing Tests 4 and 5, in which the initial condition in P_{fa} is linearly variable in the cross-shore direction, it can be seen that when the initial condition is linearly decreasing P_{fa} is reduced over the whole swash zone, and conversely, when the initial condition is linearly increasing there is an increase in P_{fa} around the lower part of the swash zone and a small decrease on the upper part. Finally, comparing Figures (f) and (g) (Tests 6 and 7), combines the conclusions observed so far: the final P_{fa} shows an increment in those regions where the initial condition is increasing and a substantial decrement in the area where the initial condition is linearly decreasing.

In Figure 7.10 the final change in P_{fa} relative to the initial P_{fa} for all the tests is shown. It can be seen that for Tests 1 to 3 P_{fa} shows similar behaviour, it decreases in the upper half and increases in the lower part (near the boundary with the surf zone), with

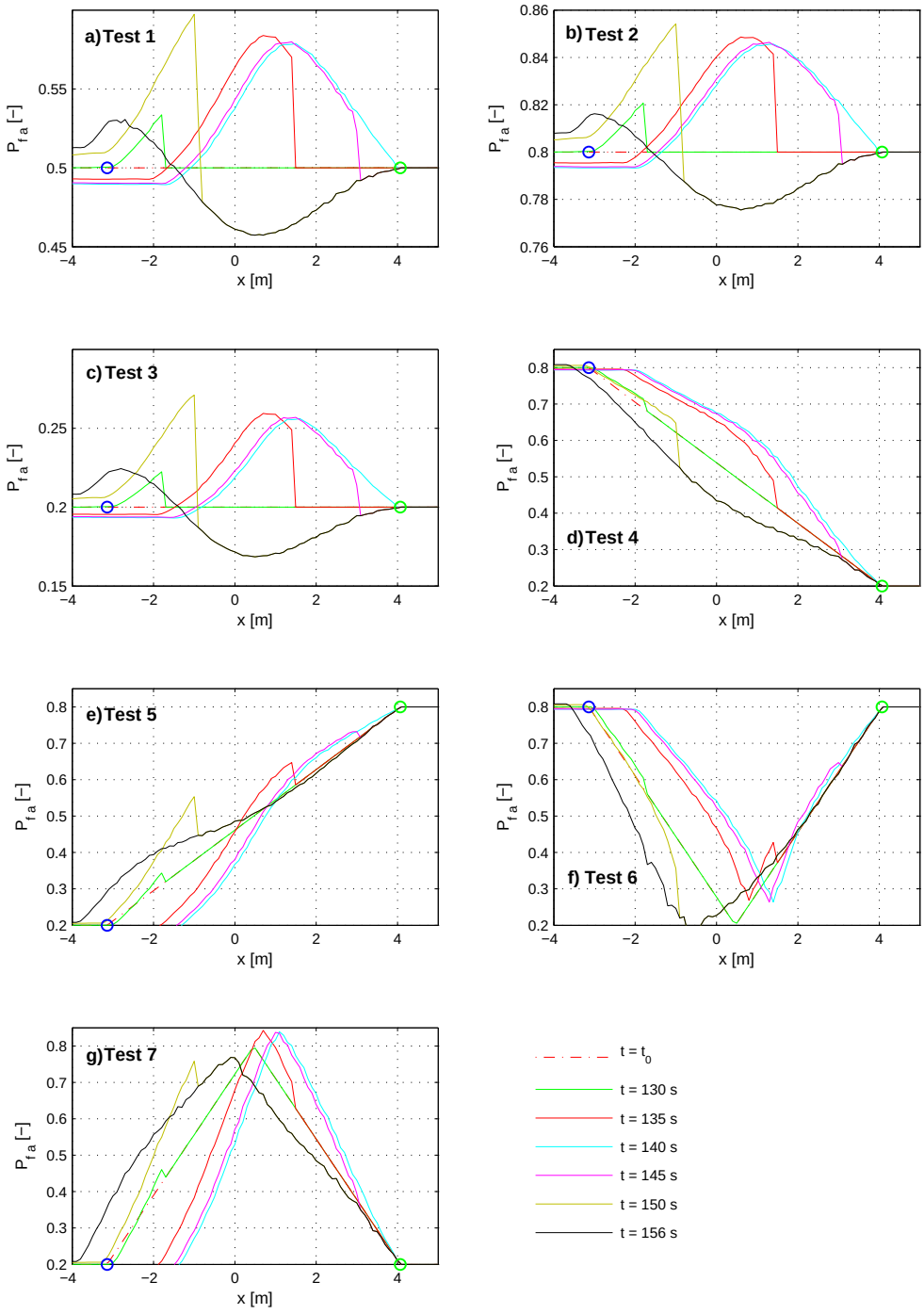

Figure 7.9: Fine volume fraction evolution in time for the non-breaking wave swash tests. (blue circle: initial and final x_s position; green circle: maximum x_s position)

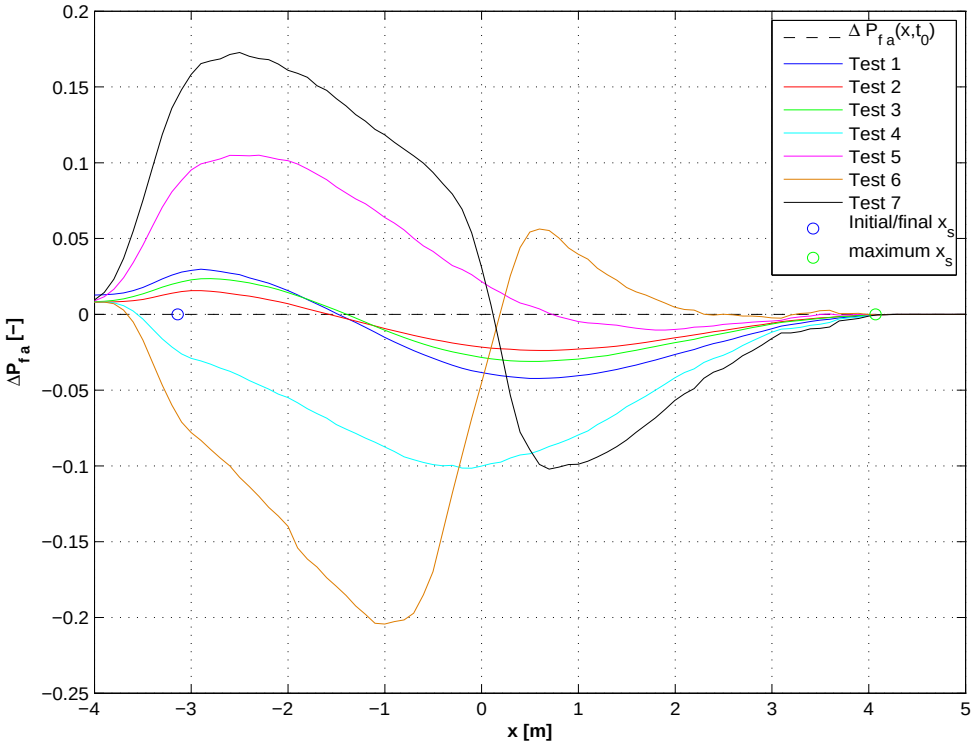

Figure 7.10: Compraison of the final ΔP_{fa} for the non-breaking wave numerical tests

the bigger variation happening for Test 1. It is also observed that Test 4 is the only case in which P_{fa} is reduced over the whole swash zone. Note that Test 5 and 7 show bigger increments of P_{fa} on the lower half of the swash zone, although Test 7 shows the biggest reduction in P_{fa} on the upper part. Finally, Test 6 shows the biggest decrease in P_{fa} in the lower half and is the only case in which P_{fa} increases on the upper half of the swash zone.

Just as in the PW01 case, eq.(7.23) and Figures 7.11 and 7.12 are used to explain and understand the behaviour of the final P_{fa}. In Figure 7.11, for the sake of clarity, the initial and final P_{fa} for all the tests is presented; and in Figure 7.12 the behaviour of the terms $P_{cs}\frac{\partial q_f}{\partial x}$ and $P_{fs}\frac{\partial q_c}{\partial x}$ at two different times in the backwash is shown. Two key features are analysed: the increment in P_{fa} in the lower part of the swash zone in the

tests where the initial P_{fa} condition is constant (Tests 1-3); and the accumulation and reduction of P_{fa} in Tests 4-7 (Figures 7.11 (d)-(g)). First, to explain the increment in P_{fa}, note in Figure 7.12 (a), (b), and (c) (Tests 1, 2, and 3) that throughout the whole backwash $P_{cs}\frac{\partial q_f}{\partial x} > P_{fs}\frac{\partial q_c}{\partial x}$ (and both are negative) around the point $x = -3$m (the point of increment), which in eq.(7.23) results in an increment in P_{fa}. Now, note in Figure 7.12 (d), that for Test 4 $P_{cs}\frac{\partial q_f}{\partial x} > 0$ and $P_{fs}\frac{\partial q_c}{\partial x} < 0$ throughout the whole backwash which in eq.(7.23) gives a reduction in P_{fa}. For Test 5, it can be seen that in the region of the slope where the final P_{fa} shows an increment ($x \leq 0$) $P_{cs}\frac{\partial q_f}{\partial x} < 0$ and $P_{fs}\frac{\partial q_c}{\partial x} > 0$ which causes $\frac{\partial P_{fa}}{\partial t} > 0$ in that region. Now for Test 6, it is observed that in the region $x \leq 0$ the values of $P_{cs}\frac{\partial q_f}{\partial x} > 0$ and for $P_{fs}\frac{\partial q_c}{\partial x} < 0$, then in that area $\frac{\partial P_{fa}}{\partial t} < 0$ according to eq.(7.23). Note as well, that around the point $x = 2$ m the value of $P_{cs}\frac{\partial q_f}{\partial x} < 0$ and $P_{fs}\frac{\partial q_c}{\partial x} > 0$ which explains the increment in the final P_{fa}. Lastly, for Test 7 the increment showed in the final P_{fa} in the region $x \leq 0$ can be explained because there the value for $P_{cs}\frac{\partial q_f}{\partial x} < 0$ and $P_{fs}\frac{\partial q_c}{\partial x} > 0$ which according to eq.(7.23) gives an increment in P_{fa}. Note as well that in the same way the reduction in P_{fa} in the area $x > 0$ is explained because there $P_{cs}\frac{\partial q_f}{\partial x} > 0$ and $P_{fs}\frac{\partial q_c}{\partial x} < 0$ resulting in the corresponding reduction of P_{fa} according to eq.(7.23).

Bed change

Regarding the bed change evolution, in Figure 7.13 the behaviour in time of the bed change for all the tests is presented. From this figure it can be seen that for all tests the bed change evolution is quite similar: in the uprush sediment is transported upslope and deposited over the profile with a maximum around the middle part of the swash zone;

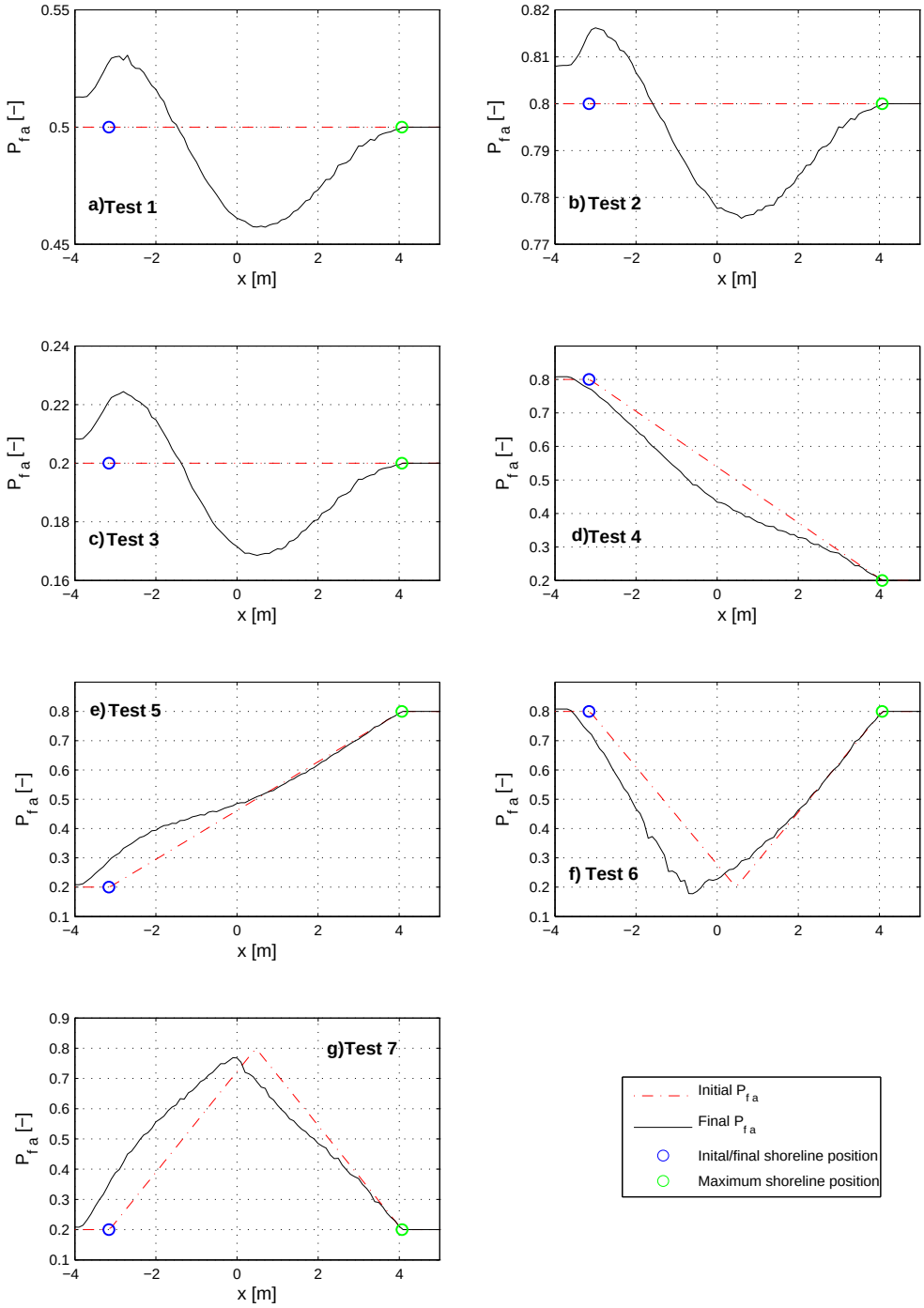

Figure 7.11: Comparison of the final fine volume fraction for the non-breaking wave tests. Initial P_{fa} -.-, final P_{fa} —

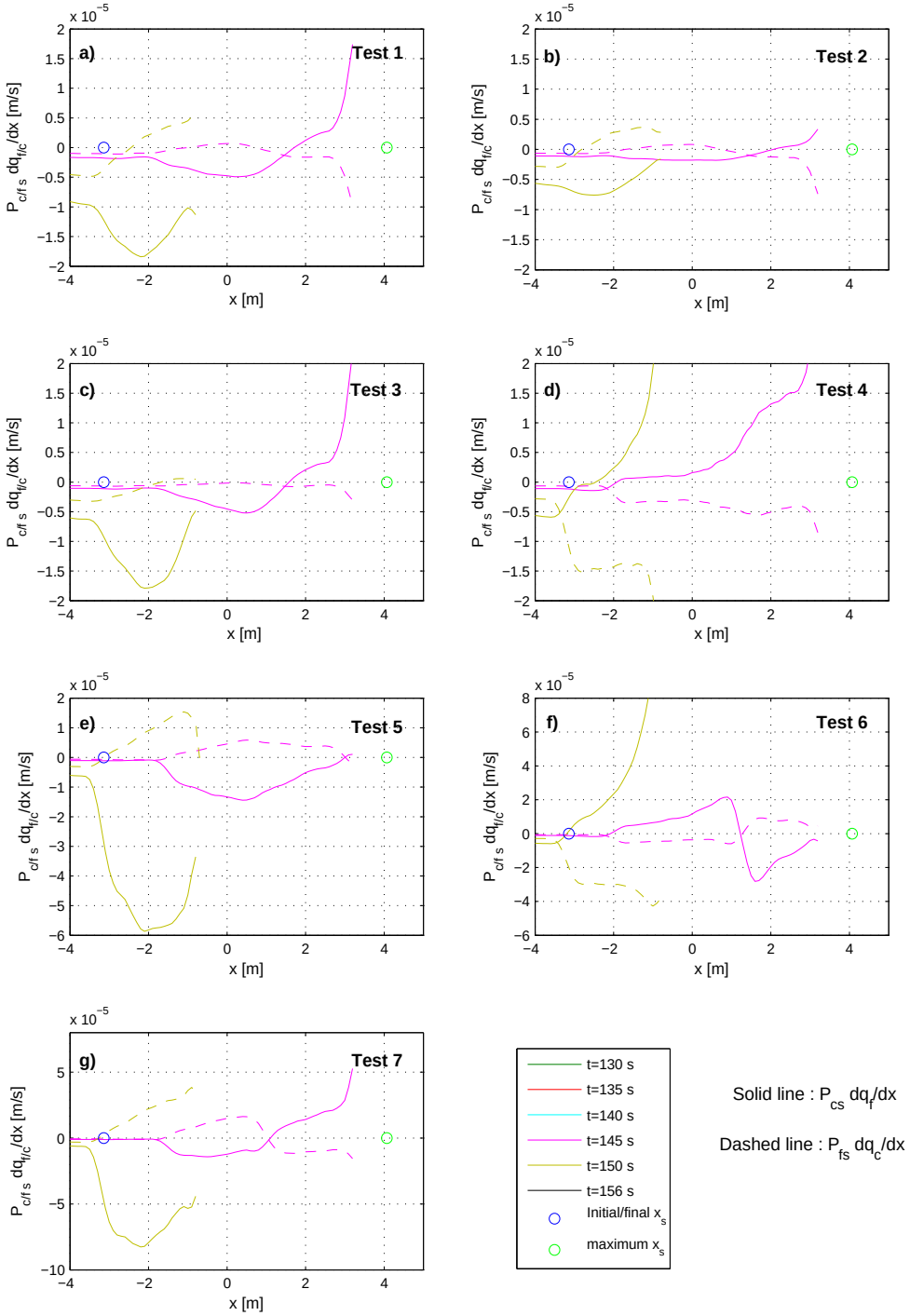

Figure 7.12: Behaviour of the terms $P_{cs}\frac{\partial q_f}{\partial x}$ and $P_{fs}\frac{\partial q_c}{\partial x}$ at two times in the backwash, for the non-breaking wave numerical tests.

during the backwash sediment is eroded and transported offshore leaving the swash zone with less sediment than the initially present on the slope with minimum again in the middle part of the swash zone and as well, showing an increment around the seaward limit of the swash zone. It can be noted as well that the for Tests 1, 2, 3, 4 and 5 the form of the bed change is very similar between these tests, noting that the bigger changes happen for cases in which there is more fine sediment present (Test 2 and 4). This kind of behaviour is understandable for Tests 1, 2 and 3 because the initial amount of fine and coarse sediment present in the mixture is constant along the beach profile, so it is expected that the form of the bed change should be similar between them. In the case of Test 4 it is noted the initial P_{fa} is modified by the flow and is increased during the uprush phase (see Figure 7.9 (d)) promoting the transport of sediments in the uprush. Now, in test 5 it can be observed that the bed change is different, especially in the first half of the uprush, this is due to the the fact that at the initial state there is less presence of fine fraction in the lower part of the swash zone than in the upper part, and this effect is even made larger due to the fact that at the initial stage of the uprush the fine sediment is further reduced in that area (see Figure 7.9 (e)). In Test 6, it is observed that the form of the bed change in the uprush shows a strong change around the middle part of the profile. This feature is the effect that the initial P_{fa} has over the overall sediment transport: the first strong reduction on the bed change is due to the decrement in the initial P_{fa} (reducing the transport of sediments), and the increment in the second half of the slope is due to the fact that in that area the initial P_{fa} is increasing in the cross-shore direction (see Figure 7.9 (f)) enhancing the transport of sediments. Finally, for Test 7 the form of the bed change is due to, again, the initial P_{fa} condition that shows a maximum around the middle part of the swash zone (enhancing

the transport) influencing the overall bed change behaviour.

Now a comparison between the final bed change for all the tests is shown in Figure 7.14. A comparison between the tests in which the initial condition in P_{fa} is constant along the beach profile is show in Figure (a); from this figure it can be observed that, as expected, the biggest bed change present in the swash zone is that when there is more presence of fine sediment at the initial condition (Test 2), and the less bed change happens in Test 3 in which there is less fine sediment in the mixture. This is physically logical because the more fine sediment present in the mixture, the greater sediment transport will take place and therefore more bed change and vice versa. In Figure (b) the bed change for the tests in which the initial condition is linearly varying from a maximum to a minimum is shown; again, more bed change happens in the first half of the swash zone for Test 4 which has more fine sediment in that area of the beach, and conversely, in the second half presents a smaller bed change than Test 5 because there the initial amount of fine sediment in the mixture is less than for Test 5. Lastly, Test 6 and 7 are compared in Figure (c), it can be observed that on the first half of the swash zone the bed change is bigger for Test 6 which has more fine sediment in that part, then, around the middle part of the swash zone (and onshore) there is an abrupt change because now there is much less presence of fine sediment in the mixture in Test 6 (and more for Test 7) whereby the bed change is less than that for Test 7.

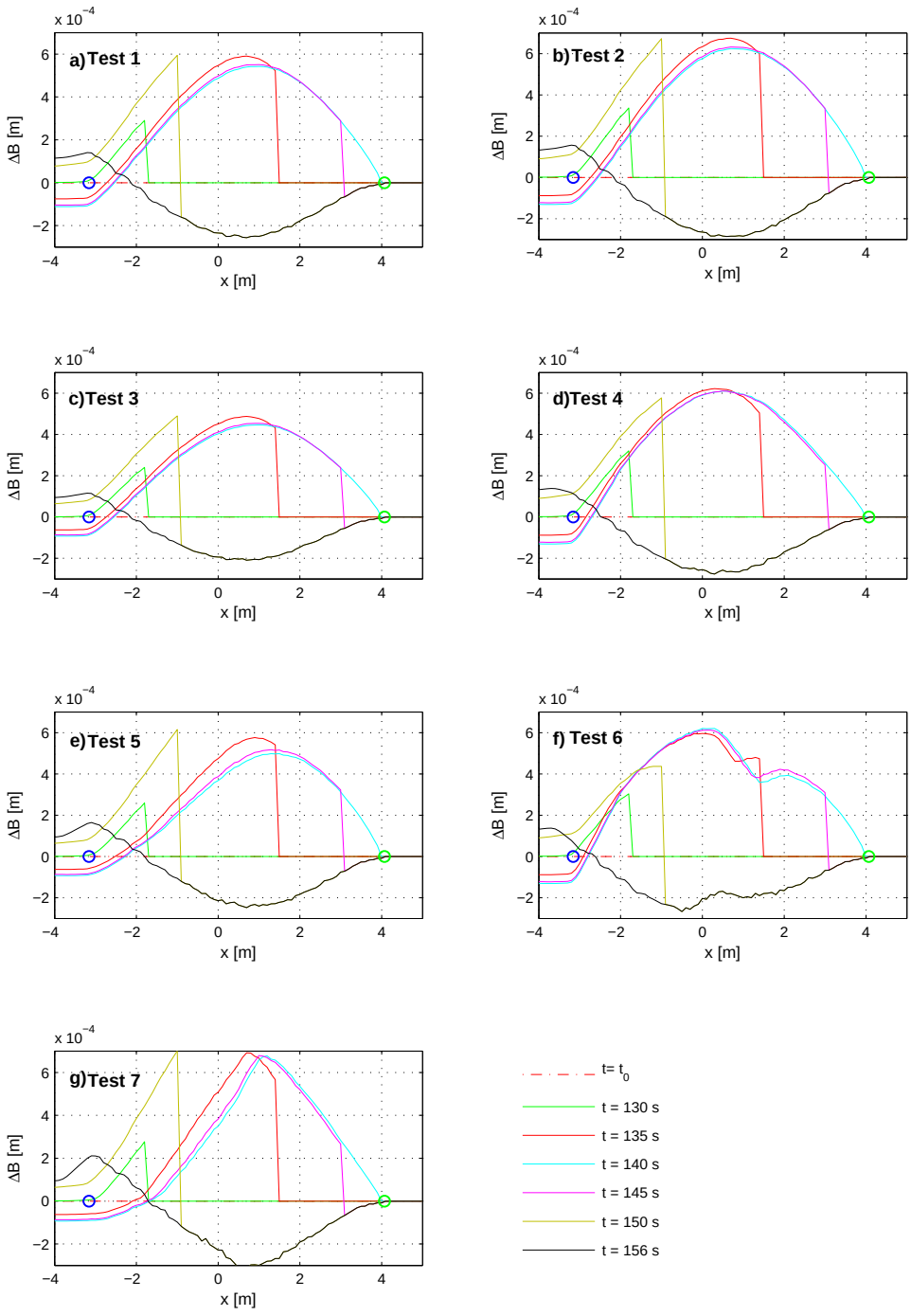

Figure 7.13: Bed change evolution in time for the non-breaking wave tests

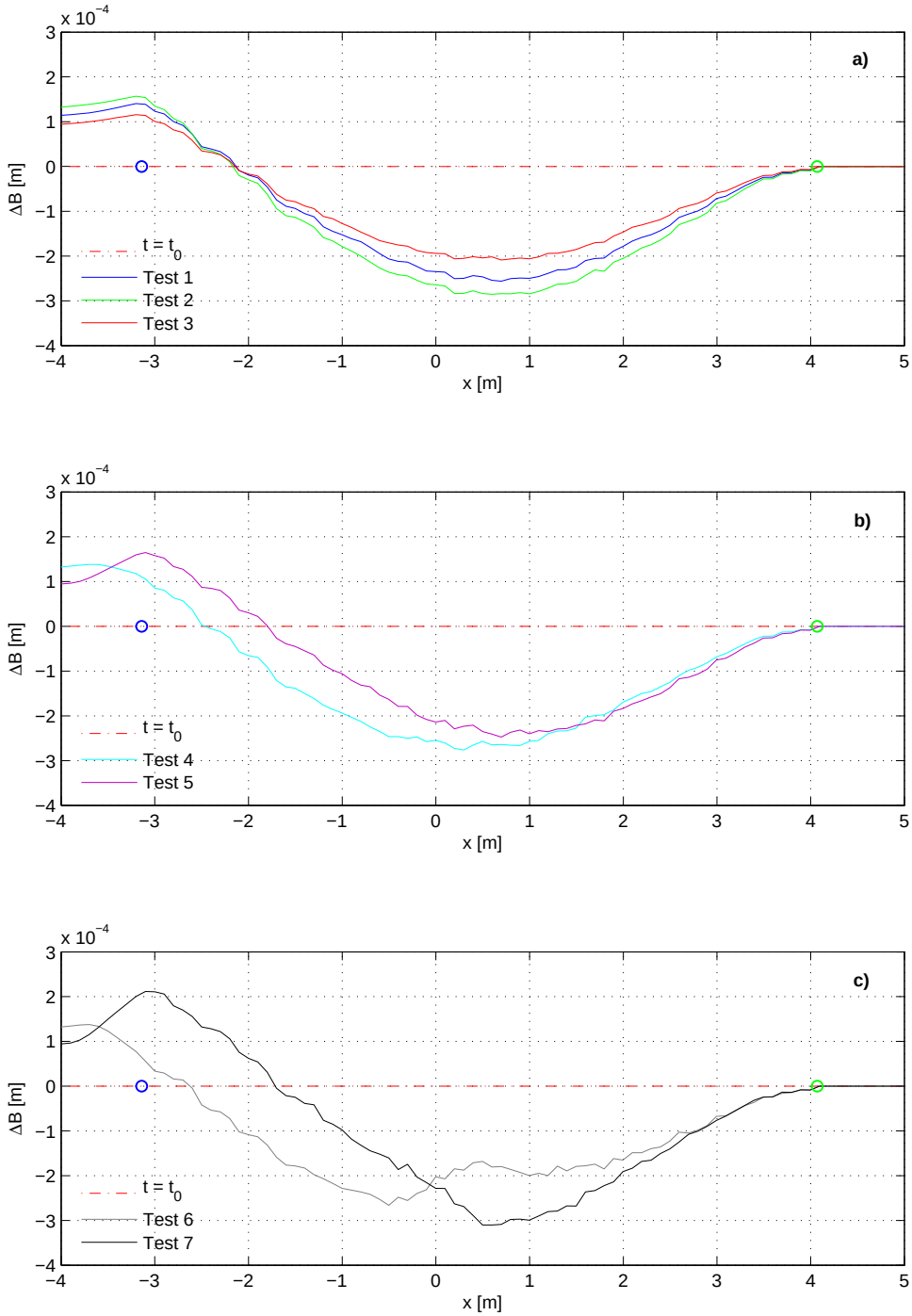

Figure 7.14: Comparison of the final bed change for the non-breaking wave tests

7.5.3 Several non-breaking swash events

It was noted in section 6.5.4 that for the cases tested at that point, the fine volume fraction did not reach a steady value when more than one swash event was acting on the beach profile. This was thought to be related to the values of the parameters A_f, A_c and L_a. For this reason, it was decided to run the model for twenty identical consecutive swash events, using the derived realistic parameters: $A_f = 0.0009043 s^2/m$, $A_c = 0.0005069 s^2/m$, $L_a = 0.0015$m, and starting with the same amount of fine and coarse sediment, i.e., $P_{fa}(x, t_0) = 0.5$.

In Figure 7.15 the final P_{fa} and bed change behaviour, after each swash event, when twenty identical consecutive swash events are acting over the beach profile is presented. From this figure it can be seen that, for these more realistic parameters, although big oscillations appear near the maximum run-up position, P_{fa} reaches a steady value in the swash zone (denoted in the figure by the green and blue circles), while the bed change remains varying with the same pattern. That big oscillations near the maximum run-up position are thought to be related to the way shock conditions are implemented or to the interpolation of P_{fa} values back to the original fixed grid.

7.5.4 Comparison using $\bar{A}$ and using A_f and A_c

It is common practice in coastal engineering models to idealise the beach profile as if it was composed by a single grain size, taking, in most occasions, the mean grain size present in the beach. Just until recent years different grains sizes are starting to being

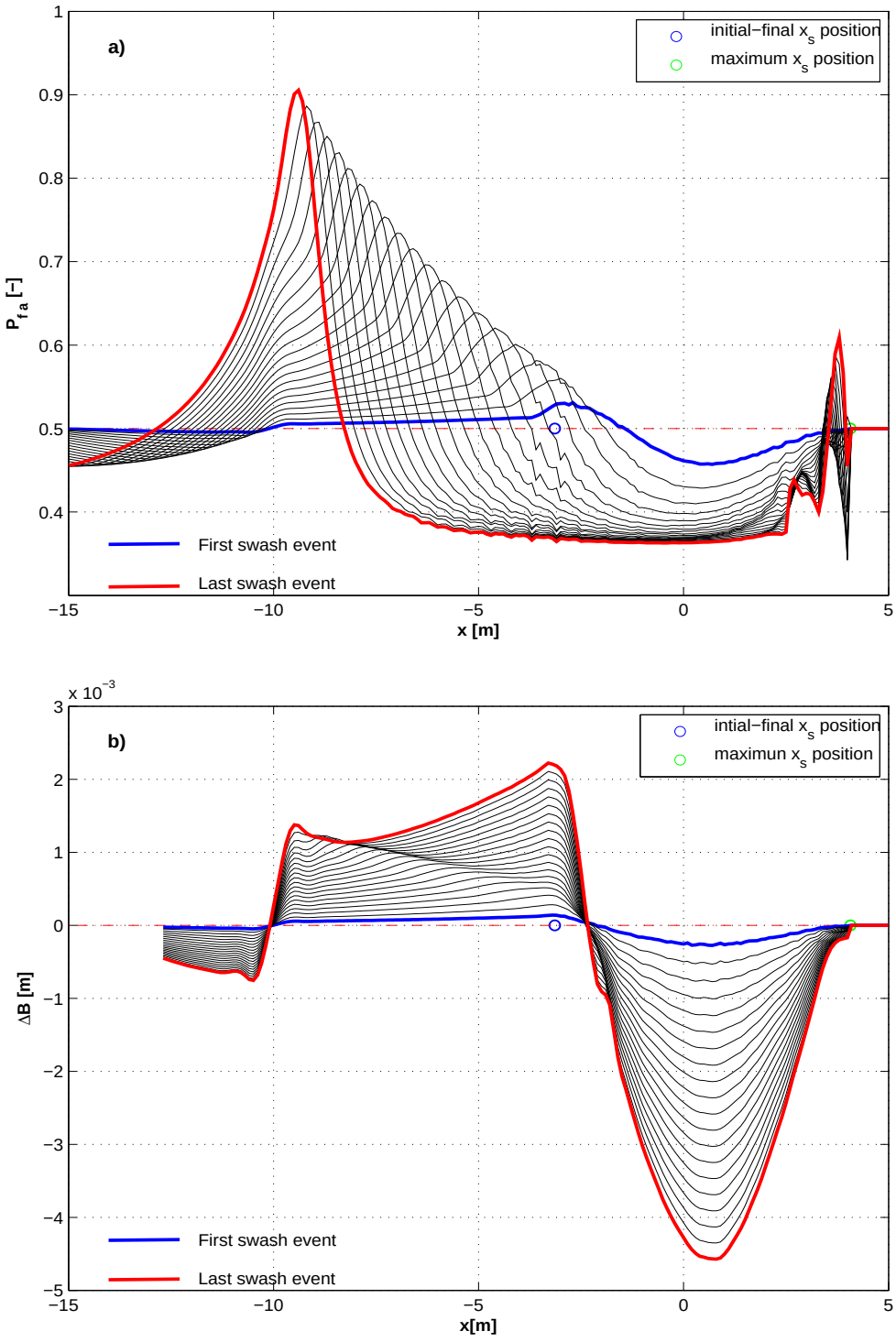

Figure 7.15: a) Final P_{fa} and b) Final bed change for each swash event when 20 consecutive swash events are acting on the swash zone

taken into account when modelling of the morphodynamics of a coastal environment is done (see e.g. Van Oyen et al. (2011) and De Swart et al. (2008)). To the knowledge of the author, there is not yet a model of the morphodynamics of the swash zone that takes into account the role of different sediment sizes in the sorting and transport of sediments. For this reason it was considered important to compare the predictions given by our model using our values A_f and A_c, with those using a mean between them as $\bar{A} = \frac{A_f + A_c}{2}$ and thereby effectively determine if there is a difference between the resulting bed level predictions.

To this end, the model was run again for the seven tests (described in Table 7.5) for both type of swash events (the PW01 and the non-breaking wave), taking the mean value $\bar{A}$ so that in the model $A_f = A_c = \bar{A}$.

In Figures 7.16 and 7.17, the comparison between the final bed change using A_f and A_c and using the mean value $\bar{A}$ for the PW01 and the non-breaking wave swash is presented. It can be clearly seen that only for the case in which the sediments are considered to be initially in the same amount and uniformly distributed over the swash zone (Test 1), the predicted bed change is seemingly the same. For all other cases, a substantial difference between bed level predictions is observed. An important thing to note here is that the kink that forms for Tests 6 and 7 when two fractions ara taken into account, is not reproduced by the model when the mean is used. This result confirms that it is of great importance to consider the different type of sediments that compose a beach, because different sediments and different initial P_{fa} conditions play a key role on the morphodynamics of the swash zone of a beach.

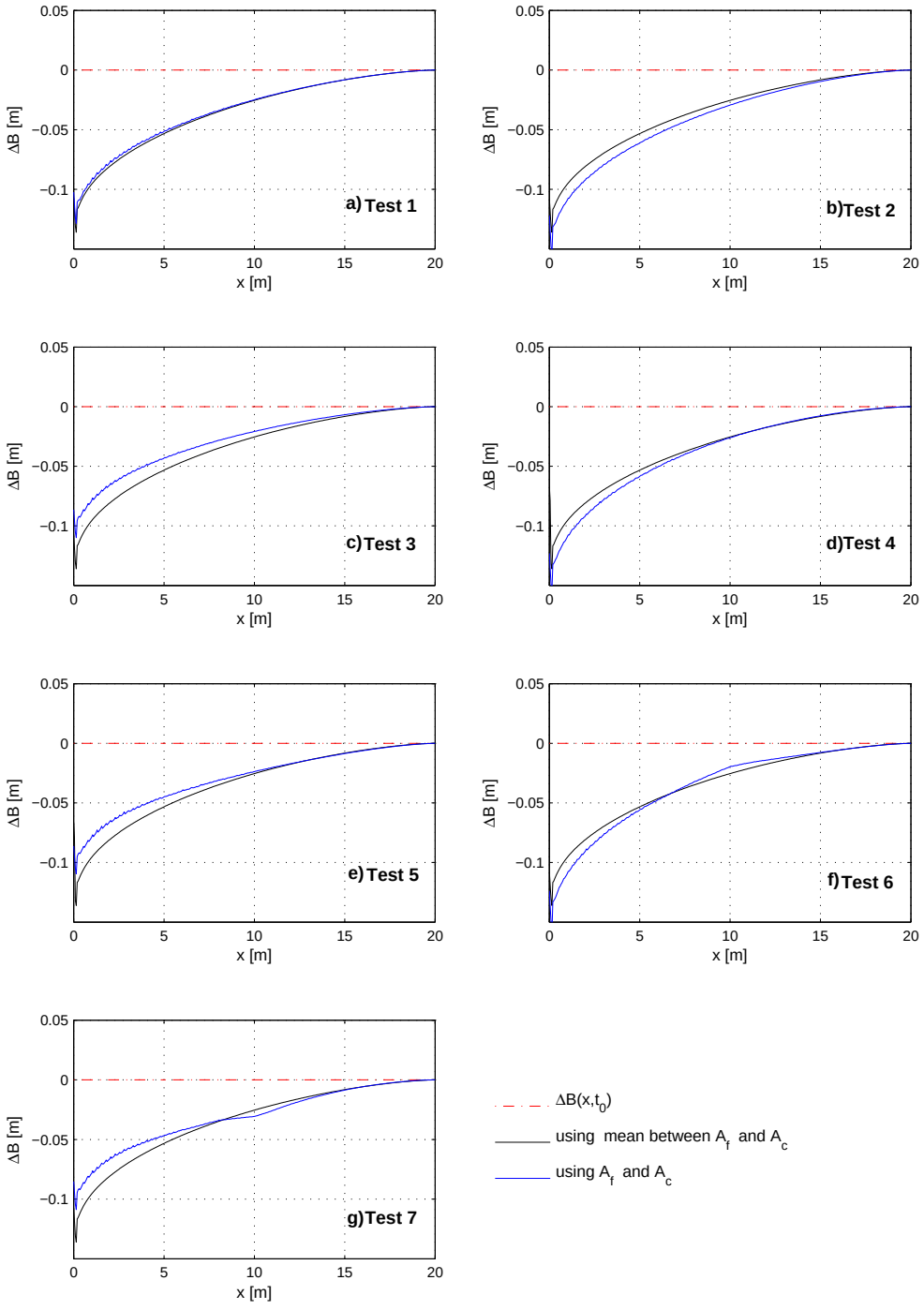

Figure 7.16: Comparison of the final bed change for the PW01 swash tests using A_f and A_c and using the mean value $\bar{A}$

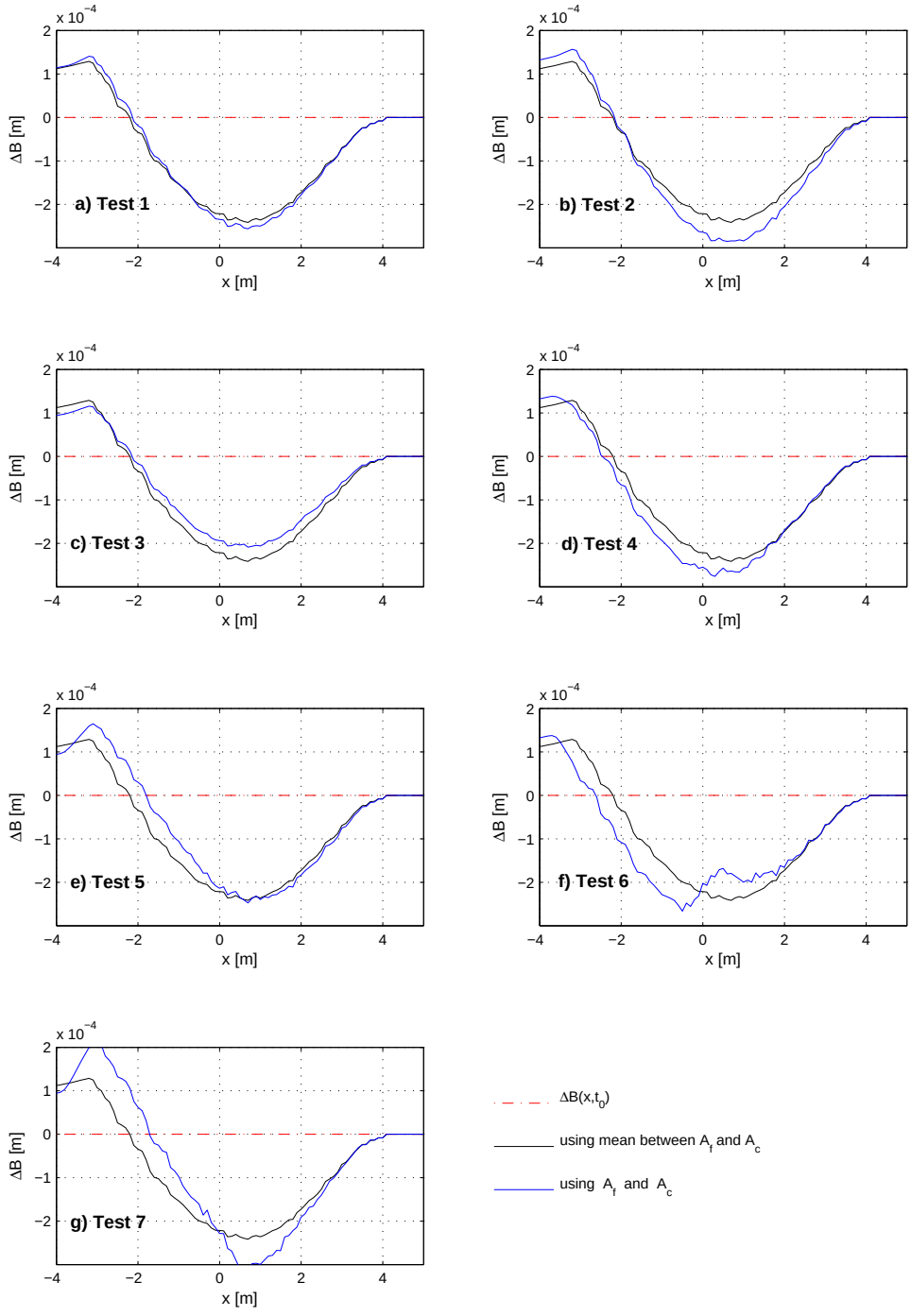

Figure 7.17: Comparison of the final bed change for the non-breaking wave swash tests using A_f and A_c and using the mean value $\bar{A}$

Chapter 8

Conclusions and Recommendations

8.1 Review and conclusions

The principal objective of this research is to understand and model for the first time the sorting of sediments and the resulting beachface evolution in the swash zone forced by a single swash event. In order to do this, a one-dimensional numerical model based on the NLSWE, the Exner equation and the one layer theory has been developed and tested. Similar models have been used in coastal environments to look at the formation of tidal sand waves (see e.g. Van Oyen and Blondeaux (2009)) or the evolution of shoreface connected ridges (see e.g. De Swart et al. (2008)), but its application in the swash zone has not been done until now.

The evolution of a sand dune composed by two different grain sizes under a constant current is examined using the developed model. It is seen that the initial condition in P_{fa} (the fine volume fraction in the active layer) is the key factor determining the behaviour of P_{fa} and the resulting propagation of the sand dune. It was observed that P_{fa} is propagated along with the sand dune according with the driving hydrodynamics. It was shown that the initial perturbation in P_{fa} (the initial shape) directly depends on the difference between the sediment parameters $A_f - A_c$: the bigger this difference, the bigger the initial perturbation. It was also noted that for the same $A_f - A_c$, different behaviour of P_{fa} (and therefore in B) is obtained; this difference was found to be due to the role that A_f plays in the definition of the initial perturbation in P_{fa}: the bigger A_f the smaller the initial perturbation. Regarding the propagation of the sand dune, it was seen that, according to basic physical principles, the coarser the mixture involved the smaller the distance traveled by the sand dune and vice versa. It was also shown that it is important to use two fractions to properly simulate the transport and propagation of the sand dune; it is not enough to use a mean value of the sediment parameters $\bar{A}$, especially if the difference between them is big, because the simulations differ substantially when a mean is taken and when two fractions are involved. This sand dune test case was useful to verify that the equations were solved correctly and to observed if the dynamics of the system were reproduced correctly. From the analysis of this case it was noted that two different wave speeds appeared; one of which resulted to be the speed of propagation of the sand dune and P_{fa} variations, and the other being a transient inherent to the system.

Beachface and P_{fa} evolution during a single PW01 swash event, which is an idealised

way to model an energetic swash event (or a swash driven by breaking wave), are investigated using the sediment parameter A_K calculated by Kelly (2009) as a base point, and considering initially the same amount of fine and coarse sediment over the bed profile. In all tests P_{fa} decreases over the whole swash zone and it is at the offshore boundary where this decrement is biggest; this implies that more fine sediment is always eroded offshore from the bed than coarse sediment. Just like in the sand dune case, it was found that the bigger the difference between A_f and A_c the bigger the change in P_{fa}. When one fraction is fixed to A_K and the other is changed by some proportion of this value, the final P_{fa} is slightly bigger for the cases in which the coarse fraction was modified. It was shown that this difference is due to the P_{fs} value in the P_{fa} governing equation (which in turn comes from the one layer theory); there is no agreement on which value P_{fs} must take so $P_{fs} = P_{fa}(x, t_0)$ is used in this research. Note that if $P_{fs} = P_{fa}$ had been used, then the behaviour of P_{fa} would have been the same for cases where either fraction is modified in the same proportion (i.e. equal $A_f - A_c$). However, note that if $P_{fs} = P_{fa}$ then it would not have been possible to derive the shock conditions in P_{fa} (see §5.5.2). Regarding the bed change, the model satisfactorily simulates the behaviour and the role that different grain sizes play on it. The results are as expected, the finer the mixture of sediments involved the bigger the bed change. It is important to note here that the work done in this research is the first application of this system to an unsteady regime. From the analysis of the kinematics of the system (wave speeds) the appearance of a 'non-physical' region was observed; in this region the wave speed of P_{fa} was found to be bigger than the velocity of the fluid which seemed physically impossible. Therefore, a condition was successfully derived to avoid the presence of the 'non-physical' region. The numerical method used to solve the equation was changed

from the Finite Difference (FD) method used in the sand dune test, to a hybrid Finite Differences-Method of Characteristics (FD-MOC). This was mainly due to problems encountered when the FD method was used to deal with the moving shoreline in the PW01 test case; the treatment of these kinds of boundaries was found simpler using the hybrid FD-MOC method which gave better results.

When a non-breaking wave swash event is tested in the model, the following conclusions can be drawn. It is observed that in all tests P_{fa} decreases in the upper three-quarters of the beach profile and increases in the lower part near the boundary with the surf zone. It is seen that the resulting P_{fa} profile possesses a minimum around the middle part of the swash zone; this is because the driving hydrodynamics have a maximum velocity in that area (in the uprush and in the backwash). Just like in the the other cases tested (the sand dune and the PW01 event) it is observed that bigger bed change is obtained when finer sediments are involved in the mixture. However, the form of the bed change is different to that in the PW01 swash event, in this case the greater erosion of sediments is observed around the middle part of the swash zone, and accretion is obtained in the lower part near the boundary with surf zone. This behaviour and difference from the PW01 event is due fundamentally to the different driving hydrodynamics. Then when the model was tested for more than one swash event, although the model appears numerically robust (in terms of appearance of spurious oscillations), it is observed that for the A_f and A_c values used, P_{fa} does not reach a steady-state (i.e. a state where the P_{fa} values at the end of the swash event are almost the same than that at the beginning) and further decreasing of P_{fa} and bed level were obtained.

Realistic A_f and A_c parameters were then successfully calculated and linked with grain sizes that can be found in real beaches using the total load formula given by Van Rijn (1985). Agreement was found between the calculations of the active layer thickness done in this research and what has been measured in the field for two different types of swash flow. New values of L_a were calculated using the more realistic sediment paremeters for the two types of swash flow and the following conclusion can generally be drawn when both types of swash flows are tested. The model satisfactorily simulates the behaviour of P_{fa} and bed change with the more realistic parameters; this in turn yields a more realistic prediction of the magnitude of the change in bed than that given with the previous parameters. It was shown that the initial distribution of sediment influences the evolution of P_{fa}: if the initial P_{fa} is linearly decreasing (in the onshore direction), a reduction in P_{fa} is observed over the whole swash zone; and if the initial P_{fa} is linearly increasing an increment in P_{fa} is expected at the lower part of the swash zone. In a similar manner, it is also observed that when the initial P_{fa} linearly decreases (in the onshore direction), the change in bed is bigger than that when P_{fa} is linearly increasing. Moreover, the appearance of a kink around the middle part of the swash zone in the bed change behaviour, when the initial P_{fa} condition has a maximum (or minimum) in that area, confirms the importance of the initial P_{fa} condition and its role in the beachface evolution. It was mentioned before that the L_a value was chosen in order to allow us to see noticeable changes in P_{fa} and B, and thus be able to analyse the results given by the model. By doing so, we could consider that the changes in P_{fa} and B are perhaps representative of what it could happen after many swash events have acted over the bed. Bearing this in mind, it is perhaps possible to say that the kink that appears on the bed profile (for the cases in which the initial P_{fa} shows a maximum or minimum around the

middle part of the swash zone), could be a sort of swash zone bar/trough that would developed in the long term.

When the several non-breaking wave swash events are tested with the realistic parameters, it was found that the P_{fa} value starts to reach a steady-state although big numerical oscillations appear near the maximum run-up position. These oscillations are thought to be due to the way shock conditions are implemented or the way the interpolation of P_{fa} back onto the original grid is done. It was also shown that the inclusion of different sediment sizes is very important in order to get more accurate predictions, the common practice of idealising the beach as if it was composed of a single grain size is not a very good option especially if there is a big difference in grain sizes and if the initial P_{fa} varies spatially over the bed.

Finally, although it was stated that there are a lot of similarities between the PW01 and the non-breaking swash events, there is a fundamental difference between them; this is, the different driving hydrodynamics. This fundamental difference is responsible of the different form in which changes in P_{fa} and bed level take place in both cases. The different hydrodynamics are also responsible for the difference in the magnitude of the change in bed for the PW01 swash event (which is an example of an energetic swash); the magnitude of the change in bed level is several orders of magnitude bigger than that for the non-breaking wave swash event (which is a low-energy swash). Also, the non-breaking wave swash event is less likely to suspend sediment, so the predictions in that case are more likely to be correct.

8.2 Recommendations

The numerical model presented in this work is, to the knowledge of the author, the first attempt to study and simulate the sorting and transport of different grain sizes in the swash zone. As such, in its derivation, a number of physical processes were left out, and assumptions were made in order to make it simple but accurate at the same time. For this reason the following suggestions for future research are given.

The model uses a simple power-law-based formula which has a great effect on the beachface and P_{fa} evolution. It has already been pointed out by some authors (see e.g. Pritchard and Hogg (2005), Kelly (2009), Zhu (2012)) that these kind of formulae have deficiencies and encourage bigger offshore sediment transport. Therefore, numerical experiments using different sediment transport formulae can be done to further analyse the effect on the behaviour of P_{fa} and bed level variation. Moreover, the sediment transport formula used here considers that all grains are availabe for transportation in the same extent, i.e., coarse and fine grains are equally available for transportation. It is thought that the 'hiding' of fine sediments under the coarser ones might have an effect on the evolution of P_{fa} and the beachface, so the inclusion of this effect is advised.

Although the predominance of bed- or suspended load in the swash zone is directly dependent on the wave and beach conditions, it was pointed out by Pritchard and Hogg (2005) that the inclusion of suspended load is crucial to accurately simulate beachface behaviour, specially when the surf zone dynamics encourage the pre-suspension of sediments. For this reason, it is considered important to develop a combined load version

of the model where suspended load is taken into account.

For simplicity an uncoupled approach was taken into account in this work, i.e., the morphodynamic variables P_{fa} and bed level do not have an effect on the flow variables. Kelly and Dodd (2010) and Zhu et al. (2012) showed that the coupling of the flow variables with the morphodynamics can be important to predict sediment transport in the swash zone, because it can dramatically alter the way beachface evolution results. Therefore, the fully coupling of the model is thought to be the next step to better understand and model the sorting of sediments in the swash zone.

The model presented intentionally left out a number of physical processes that could play an important role in the final results; two of the most important are infiltration/exfiltration and bed shear stress. Infiltration might reduce the sediment transport while exfiltration is thought to encourage it, helping the setting in motion of sediments. It is suggested to include infiltration using a simple Darcy's law following the work by Dodd et al. (2008). Infiltration and exfiltration might also be included using the piston-like movement model derived by Steenhauer et al. (2012).

Bed shear stress is also important in swash flows due to the very small depths found, especially near the shoreline, which reduces the amount of sediment transport. Therefore, it is considered a potential addition to the model. Bed shear stress can be included using a Chezy approach to examine the effect of bed shear stress on the swash flow and morphodynamics (including P_{fa}). Another interesting option to take into account bed shear stress in a more realistic way is using the boundary layer approach (Barnes and Baldock

(2010) and Briganti et al. (2011)), which, it is thought, could give more accurate results.

A very crude attempt to examine the effect of several swash event was done in this work running the same swash event for several times. Although an interesting result was given by the model, it has been pointed out by Kelly (2009) and Zhu (2012) that swash interactions might be very important in the evolution in the beachface although it was stated that the modelling of swash interactions can be very complex. Despite this, it is considered very interesting to take swash interaction into account in the model to see its influence in P_{fa} form and evolution.

Finally, it is considered of great importance to obtain precise field measurements of the grain size distribution in the swash zone (which are rare), and data from laboratory experiments to compare with the results given by our model and verify the findings achieved in this research.

Appendix A

Sand Dune Case for Uniform Sediment

A.1 Hudson Approximate Solution

Hudson (2001) determined an approximate solution for the propagation of a sand dune in which it is assumed that the free surface elevation η_c and discharge Q_c are constants during the whole simulation time, i.e.,

$$\eta = \eta_c = h(x,t) + B(x,t) \qquad \text{and} \qquad u(x,t)h(x,t) \approx Q_c. \tag{A.1}$$

This allow us to write the velocity in terms of the bed level as

$$u(x,t) \approx \frac{Q_c}{\eta_c - B(x,t)}. \tag{A.2}$$

The Exner equation (3.37) can be written in quasi-linear form as

$$\frac{\partial B}{\partial t} + \lambda \frac{\partial B}{\partial x} = 0$$

where the wave speed is $\lambda = \xi \dfrac{\partial q}{\partial B}$.

Using eq.(A.2) in eq.(3.44) we can re-write the sediment transport flux formula in terms of the bed level as,

$$q(B) = AQ_c^3[\eta_c - B(x,t)]^{-3}$$

and differentiate this equation with respect to B in order to get the wave speed

$$\lambda = 3A\xi Q_c^3[\eta_c - B(x,t)]^{-4}.$$

Then we can state that the characteristics are given by

$$\frac{dx}{dt} = 3A\xi Q_c^3[\eta_c - B(x_0,0)]^{-4}.$$

where $(x_0, 0)$ is on a characteristic line; and assuming an initial bathymetry of the form eq.(4.1), we get

$$\frac{dx}{dt} = 3A\xi Q_c^3 \begin{cases} \left(\eta_c - B_{max}\sin^2\left\{\frac{\pi(x_0-300)}{200}\right\}\right)^{-4} & \text{if } 300 \le x_0 \le 500 \\ \eta_c^{-4} & \text{otherwise.} \end{cases}$$

Integrating we get

$$x = x_0 + 3A\xi Q_c|Q_c|^2 t \begin{cases} \left(\eta_c - B_{max}\sin^2\left\{\frac{\pi(x_0-300)}{200}\right\}\right)^{-4} & \text{if } 300 \le x_0 \le 500 \\ \eta_c^{-4} & \text{otherwise} \end{cases} \tag{A.3}$$

from which we cannot get x_0 in terms of x; but we know that along a charracteristic $\frac{dB}{dt} = 0$ therefore B is constant, hence the approximate solution is

$$B(x,t) = \begin{cases} B_{max}\sin^2\left\{\frac{\pi(x_0-300)}{200}\right\} & \text{if } 300 \le x_0 \le 500 \\ 0 & \text{otherwise} \end{cases} \tag{A.4}$$

for which at any given time t we find the x values substituting values of x_0 and t into eq.(A.3).

This solution is only valid until a certain time when the characteristics cross (i.e. the wave 'breaks'), which Hudson identifies as

$$t_{max} = \frac{-200\left[\eta_c - \sin^2\left(\frac{\pi(x_0-300)}{200}\right)\right]^5}{12A\xi Q_c|Q_c|^2\pi\sin\left(\frac{\pi(x_0-300)}{200}\right)} \tag{A.5}$$

in the region $300 \le x_0 \le 500$. It is important to know this time because it is the maximum time at which the model can be run; thereafter the solution is no longer valid.

A.2 The Model for the Uniform Sediment Case

Using the morphodynamic module developed in this research to simulate the evolution of the transport of a sand dune composed of uniform sediment, implies that $A_f = A_c = A$

and $P_{fs} = P_{fa} = P_{cs} = P_{ca}$. Substituting this into eq.(4.11) we get that $\frac{\partial P_{fa}}{\partial t} = 0$ as expected, and doing the same with eq.(4.10) we get

$$\frac{\partial B}{\partial t} = -\xi F(B) \frac{\partial B}{\partial x} \tag{A.6}$$

in which $F(B) = 3AU^2 \frac{\partial U}{\partial B}$.

In order to numerically solve this differential equation a finite difference schemes is used (see e.g. Smith (1978)). Two different finite difference schemes where applied and are detailed below.

A.2.1 Schemes

For the first scheme a forward difference in t and central difference in x is used, so that eq.(A.6) becomes

$$B_j^{n+1} - B_j^n = -\xi F(B) \frac{\Delta t}{2\Delta x} [B_{j+1}^{n+1} - B_{j-1}^{n+1}] \tag{A.7}$$

where $F(B)$ is approximated by $F(B)|_j^n$, and $B_j^n(j\Delta x, n\Delta t)$.

The second scheme is a Crank-Nicholson type scheme based on central differences in both time t and space x, for which eq.(A.6) can be written as

$$B_j^{n+1} - B_j^n = -\xi F(B) \frac{\Delta t}{4\Delta x} [B_{j+1}^{n+1} + B_{j-1}^n - B_{j-1}^{n+1} - B_{j-1}^n] \tag{A.8}$$

in which

$$B_{j+1}^{n+\frac{1}{2}} = \frac{B_{j+1}^{n+1} + B_{j+1}^n}{2} \qquad \text{and} \qquad B_{j-1}^{n+\frac{1}{2}} = \frac{B_{j-1}^{n+1} + B_{j-1}^n}{2}$$

and here $F(B) \approx F(B)|_j^n$ has been used.

A.2.2 Von Neumann Stability Analysis and Phase Velocity

In order to be confident using the schemes described above, it is useful to perform a Von Neumann stability analysis for both finite difference schemes. This analysis is based on the expansion of the finite difference equation in a Fourier series, allowing us to evaluate the decay or growth of an amplification factor which indicates whether or not the numerical algorithm is stable (see e.g. Smith (1978), Chung (2002)).

Assuming that the computed solution B_j^n is the sum of the exact solution $\bar{B}_j^n$ and the error ε_j^n, we know that $\bar{B}_j^n$ satisfies exactly the discretized equation, so the error ε_j^n must also satisfy it. So using eq.(A.7) we can state

$$\varepsilon_j^{n+1} - \varepsilon_j^n = -\alpha_p \frac{\Delta t}{2\Delta x}[\varepsilon_{j+1}^{n+1} - \varepsilon_{j-1}^{n+1}] \tag{A.9}$$

where $\alpha_p = \xi F(B)$.

For linear differential equations the spatial variation or the error may be expanded in a finite Fourier series. Assuming that the amplitude of the error (A_0^n) at a certain time level n is an exponential function of time, we can write the error function as

$$\varepsilon_j^n = \sum_{j=1}^{N} A_0^n e^{ikjx}$$

where $i = \sqrt{-1}$. Since the difference equation for the error is linear (the behaviour of each term of the series is the same as the series itself), it is enough to consider the growth of the error of a typical term:

$$\varepsilon_j^n = A_0^n e^{ikjx}. \tag{A.10}$$

Substituting eq.(A.10) into eq.(A.9)

$$A_0^{n+1}e^{ikjx} - A_0^n e^{ikjx} = -\frac{\alpha_p \Delta t}{2\Delta x}[A_0^{n+1}e^{ik(j+1)x} - A_0^{n+1}e^{ik(j-1)x}]$$

and after some algebraic manipulations we get

$$\frac{A_0^{n+1}}{A_0^n} = \frac{1}{1 + \frac{\alpha_p \Delta t i}{\Delta x}\sin(kx)}.$$

Defining the amplification factor as $g \equiv \frac{A_0^{n+1}}{A_0^n}$, the necessary and sufficient condition for the error to remain bounded is that $|g| \leq 1$, this means that

$$\left| \frac{1}{1 + \frac{\alpha_p \Delta t i}{\Delta x}\sin(k\Delta x)} \right| \leq 1$$

which implies that the first scheme (A.7) is unconditionally stable.

Following a similar procedure with the second scheme eq.(A.8) we obtain

$$g \equiv \left| \frac{A_0^{n+1}}{A_0^n} \right| = \left| \frac{1 - \frac{\alpha_p \Delta t i}{2\Delta x}\sin(kx)}{1 + \frac{\alpha_p \Delta t i}{2\Delta x}\sin(kx)} \right| \leq 1$$

which clearly states that the second scheme is unconditionally stable as well.

As a first attempt, in order to evaluate if the chosen schemes are going to give an accurate solution, it is useful to examine if they are able to accurately reproduce the phase velocity at which the propagation is going to take place. From eq.(A.6) we can straightforwardly get an analytical expression for the phase velocity, α_p, if we assume

that a simple solution of the equation is

$$B(x,t) = A_m e^{i(kx-\omega t)}$$

so that

$$\frac{\omega}{k} = \xi \bar{F} = \alpha_p \tag{A.11}$$

where $\bar{F}$ is a mean value of $F(B)$.

In a similar way it is possible to get the expression for the numerical phase velocity for the schemes used. For scheme 1, (A.7):

$$\alpha_{p_{sch1}} = \frac{1}{k\Delta t}\tan^{-1}\left(\frac{\alpha_p \Delta t}{\Delta x}\sin(k\Delta x)\right), \tag{A.12}$$

and for scheme 2, (A.8), we get:

$$\alpha_{p_{sch2}} = \frac{2}{k\Delta t}\tan^{-1}\left(\frac{\alpha_p \Delta t}{2\Delta x}\sin(k\Delta x)\right). \tag{A.13}$$

In Figure A.1 the relative percentage error between the analytical eq.(A.11) and the numerical phase velocities eqs.(A.12) and (A.13) is presented. Noting first that both schemes accurately approximate the phase velocity in a very similar way, means that both schemes would give a similarly accurate numerical solution for the propagation of the sand dune. Second, for a given value of Δx and Δt scheme 2 eq.(A.8) incurred in less error than scheme 1 eq.(A.7) in the approximation of the phase velocity, which is explained by the fact that scheme 2 is second order in both, space and time, while scheme 1 is first order in time and second order in space. This may suggest that scheme

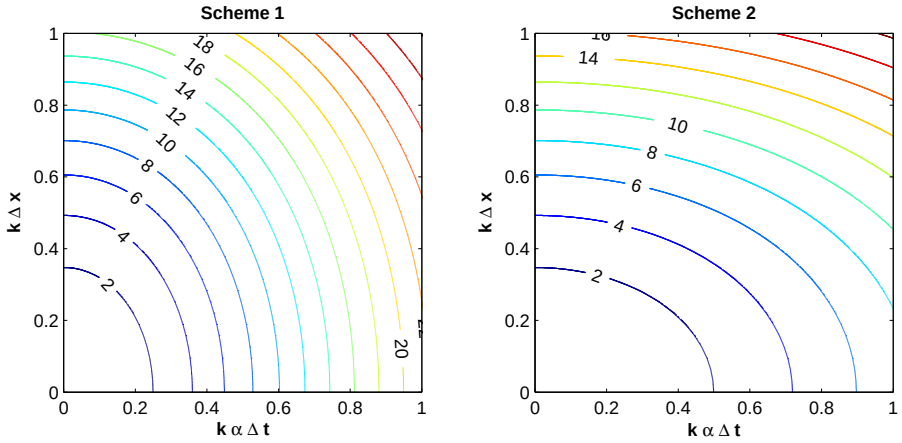

Figure A.1: Contours of percentage error in modelling the phase velocity with schemes eq.(A.12) and eq.(A.13)

2 would be more accurate in the numerical solution of the problem.

Finally, it is important to note that the previous analysis is only rigorous for a linear equation. In fact, eq.(A.6) is nonlinear and it has been assumed that $F(B) = \bar{F}(B)$, where $\bar{F}(B)$ is an 'average' value. Nevertheless, the analysis made here gives us, to some extent, a good idea of the stability and precision of the suggested model.

A.3 Comparison of Model with Hudson

To be able to compare and validate the model derived in this research with the test described by Hudson (2001) the conditions of the case simulated are $B_{max} = 1$ m with $A = 0.001\frac{s^2}{m}$. In Figure A.2 the evolution in time of the sand dune using scheme 2 (A.8) is shown, compared with the approximate solution of Hudson eqs.(A.3)-(A.5). The model is stopped at a time just before the sand dune front becomes vertical (time given by

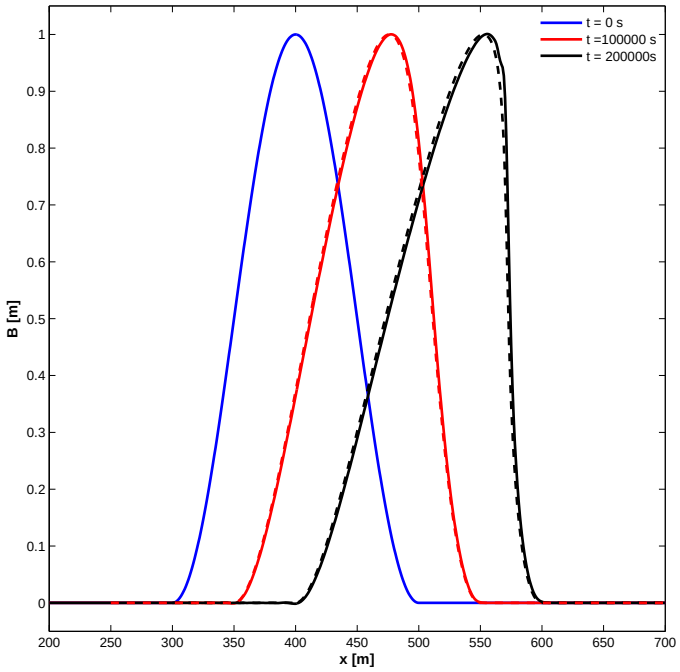

Figure A.2: Behaviour of the sand dune propagation using the model derived in this work (solid line) compared with Hudson approximation (dashed line)

eq.(A.5) $t = 238079$ s). It is concluded that the model accurately solves the propagation of the sand dune for the case when it is composed for a single sediment and that the results given by the model are in very good agreement with Hudson solution. This result gives us some degree of confidence in the model and to apply it to non-uniform cases.

A.4 Convergence

One of the most important features to test the model accuracy is the convergence of the solution. To investigate this feature in the model several combinations of Δt and Δx were tested calculating the relative error between them and looking for the one in which the relative error is sufficiently small, but at the same time not taking too much

computational time.

In Figure (A.3) the behaviour of the relative error for the different combinations of Δx and Δt (comparisons A, B, C and D) are shown. From the figure it is seen that for smaller Δx and Δt less error is got. In the same figure, a close up of the region where the relative error has the best behaviour is shown, from this it is seen that comparisons C and D are the best ones, and furhermore, we can say that it is enough to take $\Delta x = 0.005L$ $\Delta t = 3.75 \times 10^{-5}T$ (approach (4) in the figure) because the value of the error is small enough. $\Delta x = 0.005L$ $\Delta t = 3.75 \times 10^{-5}T$ was chosen over $\Delta x = 0.005L$ $\Delta t = 3.75 \times 10^{-6}T$ because the difference in Δt makes a big difference in the time taken for the model to run.

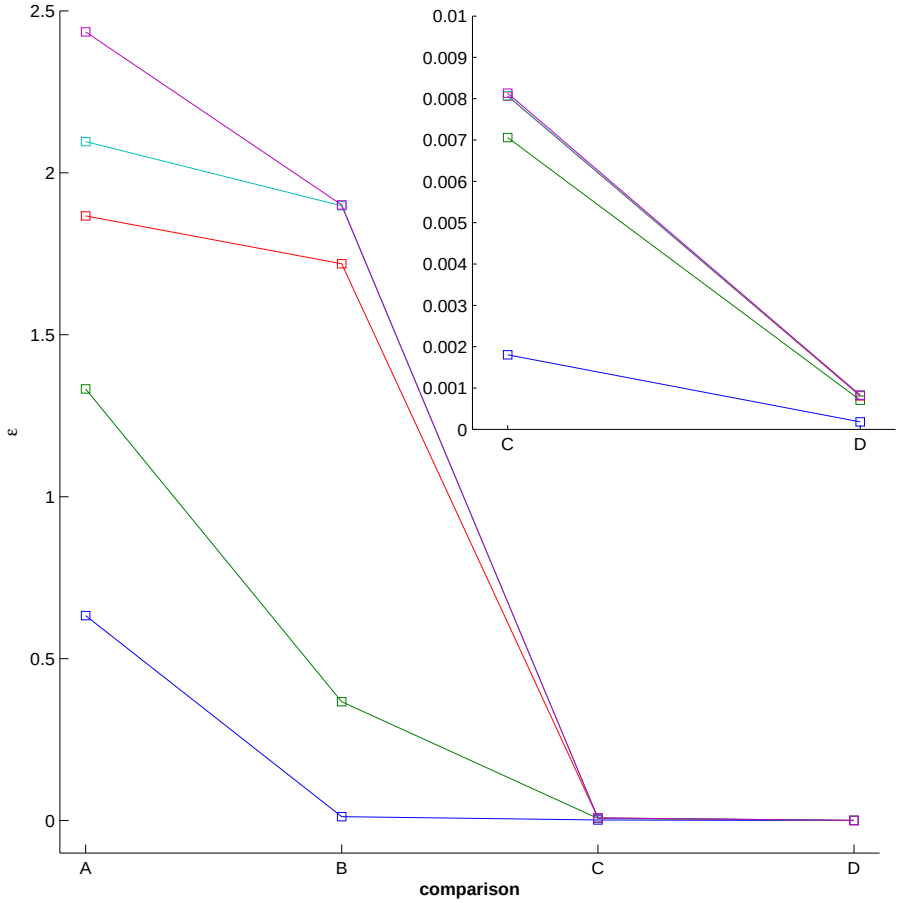

Figure A.3: Relative error (ε) in the solution given by the model calculated using different combinations of Δx and Δt. A: using (1)-(2); B: using (2)-(3); C: using (3)-(4); and D: using (4)-(5). (1) $\Delta x = 0.05L$, $\Delta t = 0.0375T$; (2) $\Delta x = 0.025L$, $\Delta t = 0.00375T$; (3) $\Delta x = 0.005L$, $\Delta t = 0.000375T$; (4) $\Delta x = 0.005L$, $\Delta t = 3.75 \times 10^{-5}T$; and (5) $\Delta x = 0.005L$, $\Delta t = 3.75 \times 10^{-6}T$; ($B_{max} = 1\text{m}$; $L = 200m$ is length of the sand dune; $T \approx 266,666s$ period of the sand dune); (—:$t \approx 0$s, —:$t = \frac{t_f}{4}$s, —:$t = \frac{t_f}{2}$s, —:$t = \frac{3t_f}{4}$s, —:$t = t_f$s).

Appendix B

Model verification, convergence and mass conservation for the PW01 case

B.1 Model Verification

It is of crucial importance to check that the numerical solution derived in this research and used in chapter 5 is capable of reproducing an already known analytical solution. For this reason the solution (Pritchard and Hogg (2005)) derived in section 5.3 as eq.(5.18) is used to verify the numerical solution. As stated before, PH05 solution was derived for the case in which a single sediment particle is considered; for this reason the morphodynamic module equations (3.50) and (3.52) are applied taking $A_f = A_c = 0.004 s^2/m$

and $P_{fa} = P_{ca} = 0.5$, which ensures that the beach is composed of one sediment.

This value of parameter A was chosen according to Kelly (2009) who calculated this value from field measurements in the swash zone of a medium sand beach. This value was successfully used by Zhu et al. (2012) to verify and test their derived morphodynamic numerical, model which gives us some degree of certainty in its use. So, although as noticed by both Kelly (2009) and Zhu et al. (2012), the procedure to get this value of A is crude, it can perhaps be assumed as a characteristic value found in some beaches.

The comparison between PH05 analytical solution and the numerical model is shown in Figure B.1. The model results presented in this figure were obtained using a grid definition: $\Delta x = 0.02$ m and $\Delta t = 0.001$ s. The solution given by the model compares very well with PH05 analytical solution although small discrepancies are found when the shoreline has retreated back. From this comparison it can be concluded that the model successfully recreates a well-known morphodynamic problem so it can be use with reasonable confidence to simulate other related cases.

B.2 Convergence

In order to check the validity of the approach taken in the model and to define the magnitude of the spatial and time increment (i.e. grid resolution), convergence tests were carried out. Thats is, as the grid resolution is made finer, the solution given by the model should converge to the same value. Three different pairs of Δx and Δt were

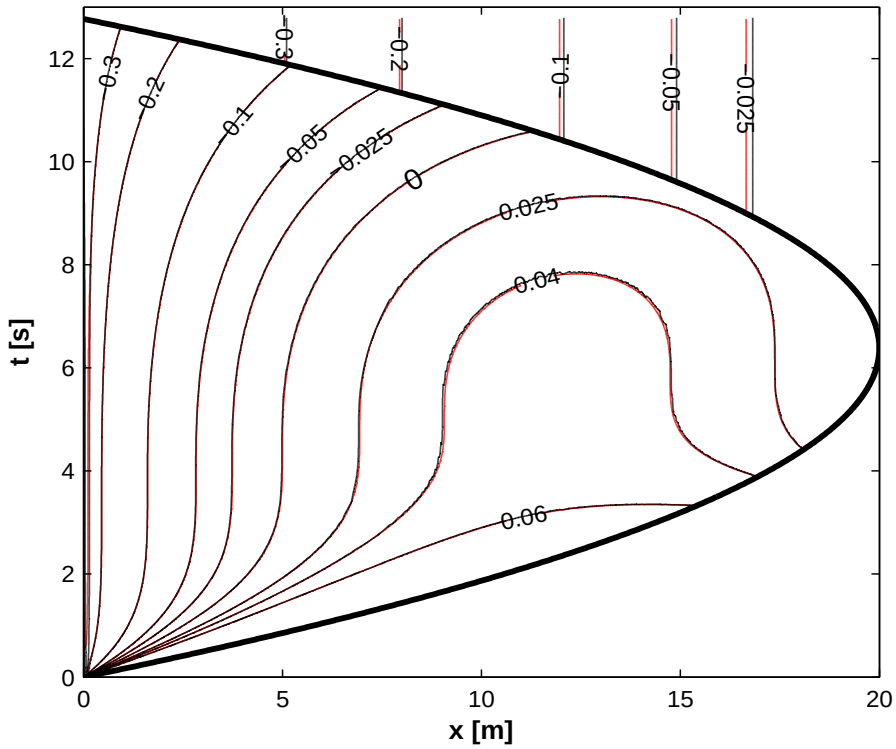

Figure B.1: Contour plots for ΔB given by — present model and — PH05 solution.

tested and compared with each other for the case where a single sediment is present (i.e.$A_f = A_c = 0.004 s^2/m$).

Figure B.2 (top) shows the convergence of ΔB, at the final time step, as the grid resolution is increased. From this figure it can bee seen that the solution indeed convergences as the grid resolution becomes finer. In this figure a close-up of a region between $x = 0 - 0.4$ is shown, in which PH05 is plotted as a red dashed line, where we can see that there is a small discrepancy between the solution given by the model and PH05 solution. This could be attributed to the interpolation method used in the model in the vicinity of a gradient discontinuity.

Convergence was checked for the whole simulation time and in Figure B.2 (bottom) contour plot for ΔB given by the model using the three grid resolutions mentioned above are presented. From this figure we can confirm that indeed, the solution given by the model convergences as the grid resolution is increased.

B.3 Mass Conservation

As a final step to check the accuracy and certainty of the numerical model derived in this research, it was considered appropriate to do a mass balance (mass conservation) check.

It is possible to evaluate if the mass is being conserved in the model using eq.(3.38), in which we can state that $i = f$ (i.e. taking the fine fraction) to get

$$\xi \frac{\partial q_f}{\partial x} + \frac{\partial (P_f B)}{\partial t} = 0. \tag{B.1}$$

Integrating eq.(B.1) over the whole spatial domain, this is from x_1 to x_2, in which x_1 is the offshore boundary of the domain and x_2 is the onshore boundary of the domain, we obtain

$$\frac{\partial}{\partial t} \int_{x_1}^{x_2} P_f B dx = -\xi [q_f]_{x_1}^{x_2}. \tag{B.2}$$

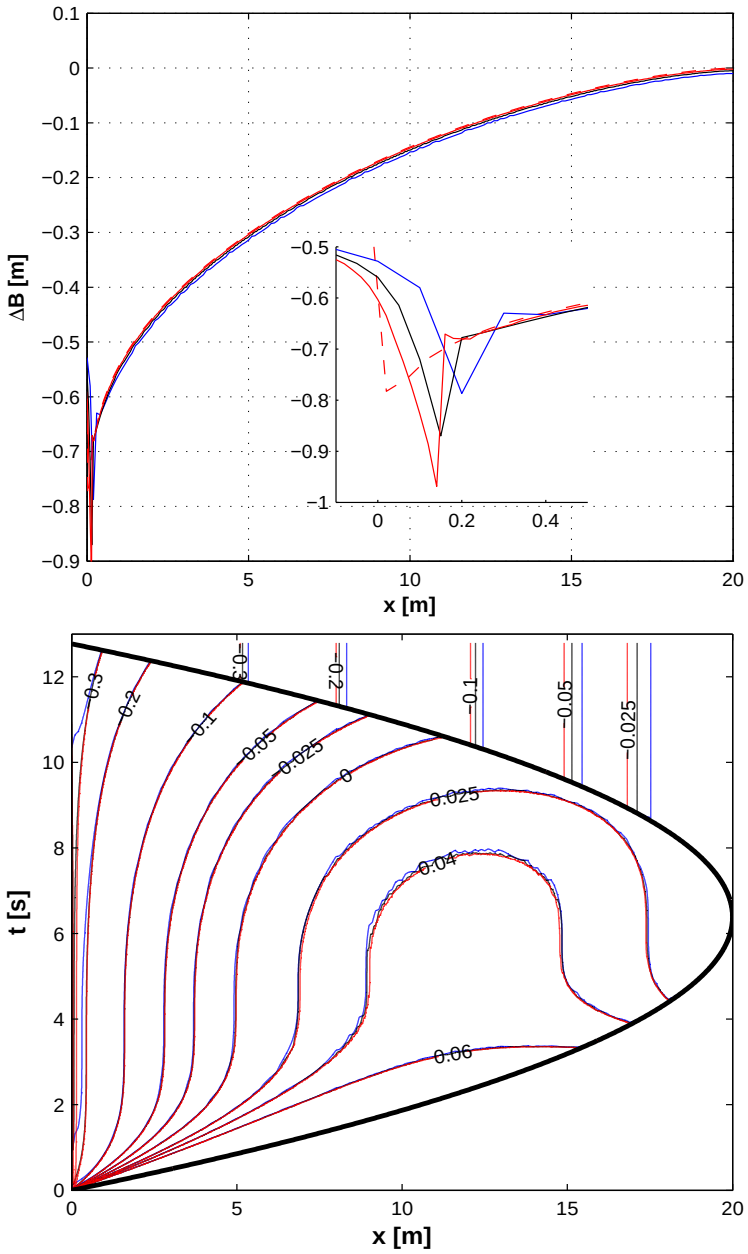

Figure B.2: Top: Convergence in change in bed ΔB relative to the initial bed profile at the end of the simulation; — — PH05 solution. Bottom: Convergence of contours for ΔB. For both graphs: — $\Delta x = 0.1$m and $\Delta t = 0.004$ s; — $\Delta x = 0.05$m and $\Delta t = 0.002$ s; — $\Delta x = 0.02$m and $\Delta t = 0.001$ s.

Now, integrating in time eq.(B.2) from $t = 0$ to an arbitrary t_n and recalling that $q_f(x_2, t)$ is always equal to zero we get

$$\Big[\int_{x_1}^{x_2} P_f B dx\Big]_0^{t_n} = \xi \int_0^{t_n} q_f(x_1, t) dt. \tag{B.3}$$

It is important to note that in order to avoid the inclusion of errors in the calculation, it is better to use ΔB instead of B (see Figure B.3), where ΔB is defined as the change in bed relative to the initial bed profile at $t = t_0$ (i.e. $\Delta B(x,t) = B(x,t) - B(x,t_0)$); so eq.(B.3) can be expressed as

$$\Big[\int_{x_1}^{x_2} P_f \Delta B dx\Big]_{t_n} - \Big[\int_{x_1}^{x_2} P_f \Delta B dx\Big]_0 = \xi Q(x_0, t_n) \tag{B.4}$$

and it is clear that the second term at the left hand side is equal to zero, so finally the expression to check if the mass is being conserved is

$$\Big[\int_{x_1}^{x_2} P_f \Delta B dx\Big]_{t_n} = \xi Q(x_0, t_n). \tag{B.5}$$

In Figure B.4 two graphs are presented to illustrate how the mass is being conserved in the model. In the top figure values of the two terms of eq.(B.5) are shown. It can be seen that the disagreement between the two curves is negligible, which means that indeed the model is conserving mass. In the botton figure the relative error between the two terms of the mass balance equation (B.5) are shown. From this figure we can see that the relative error at early stages of the simulation is quite big, but this can be attributed to the fact that the values of the terms in the mass balance equation are very

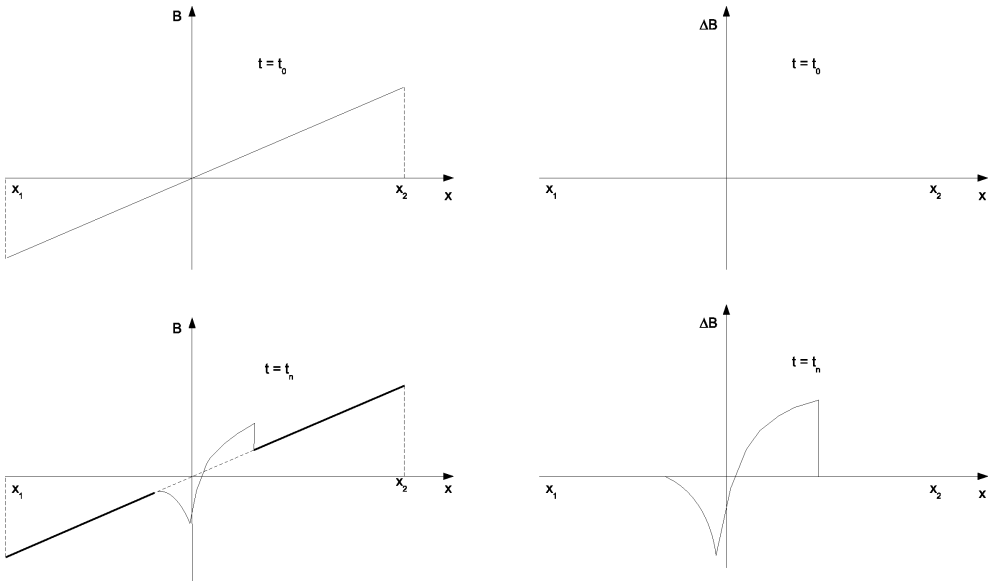

Figure B.3: Schematic difference between B and ΔB for the mass balance check.

small, so even though the relative error might seem big, the actual agreement between the values is good as confirmed by the top figure. For the rest of the figure the relative error tends to zero so we can state that indeed the model is conserving mass, giving us further confidence in the model.

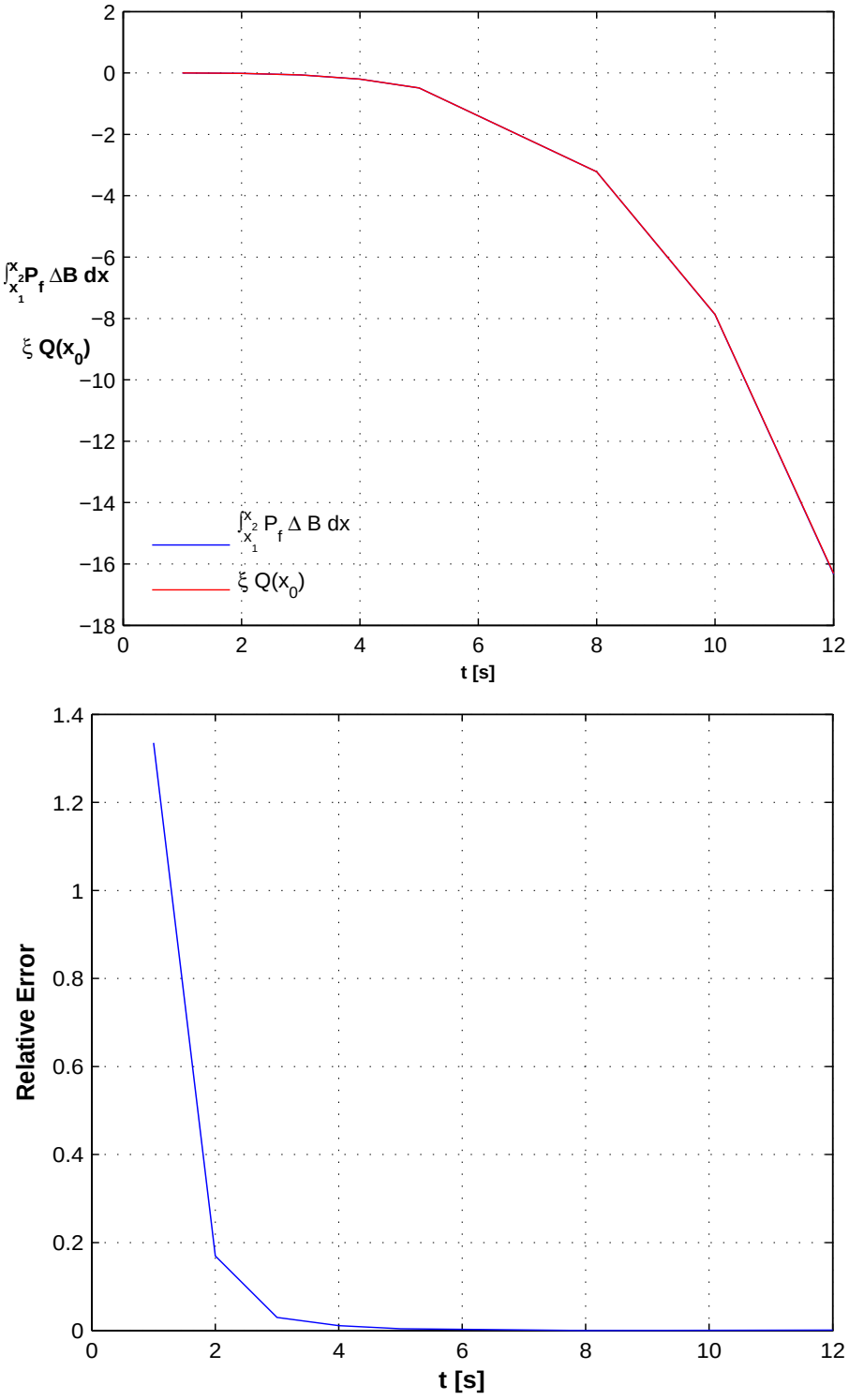

Figure B.4: Top: Comparison between the two terms in equation (B.5). Bottom: Relative error between the two terms of equation (B.5).

References

Abramowitz, M. and Stegun, I. A., editors (1965). *Handbook of Mathematical Functions with Formulas, Graphs, and Mathematical Tables*. Dover.

Akan, A. (2006). *Open Channel Hydraulics*. Butterworth-Heinemann.

Alsina, J., Baldock, T., Hughes, M., Weir, F., and Sierra, J. (2005). Sediment trasnport numerical modelling at the swash zone. In *Proceedings of Coastal Dynamics ASCE*, Barcelona, Spain.

Alsina, J., Falchetti, S., and Baldock, T. (2009). Measerements and modelling of the advection of suspended sediment in the swash zone by solitary waves. *Coastal Engineering*, 56:621–631.

Anfuso, G. (2005). Sediment-activation depth values for gentle and steep beaches. *Marine Geology*, 220:101–112.

Arimitsu, T. and Deguchi, I. (2007). Simulation of sorting in the crossshore direction and topography change of beach composed of fine and coarse sands. In *Proc. of the 17th International Offshore and Polar Engineering Conference*, pages 2454–2460, Lisbon, Portugal.

Armanini, A. and Di Silvio, G. (1988). A one-dimensional model for the transport of

a sediment mixture in non-equilibrium conditions. *Journal of Hydraulic Research*, 26:275–292.

Bagnold, R. (1940). Beach formation by waves: Some experiments in a wave tank. *J. Inst. Civ. Eng. Pap.*, 5237:27–53.

Bakhtyar, R., Barry, D. A., Li, L., Jeng, D. S., and Yeganeh-Bakhtiary, A. (2009). Modeling sediment transport in the swash zone: A review. *Ocean Engineering*, 36:767–783.

Baldock, T. E. and Holmes, P. (1999). Simulation and prediction of swash oscillations on a steep beach. *Coastal Eng.*, 36:219–242.

Baldock, T. E. and Huntley, D. A. (2002). Long-wave forcing by the breaking of random waves on a beach. *Proc. Roy. Soc. London A.*, 458:2177–2201.

Barnes, M. and Baldock, T. (2010). A lagrangian model for boundary layer growth and bed shear stress in the swash zone. *Coastal Eng.*, 57:385–396.

Battjes, J. (1974). Surf similarity. In *Proc. 14th Int. Conf. Coast. Eng.*, pages 466–479, Copenhagen. A.S.C.E.

Briganti, R., Dodd, N., Pokrajac, D., and O'Donoghue, T. (2011). Non linear shallow water modelling of bore-driven swash: Description of the bottom boundary layer. *Coastal Eng.*, 58:463–477.

Brocchini, M. and Baldock, T. (2008). Recent advances in modelling swash zone dynamics: The influence of suf-swash interaction on nearshore hydrodynamics and morphodynamics. *Rev. Geophys.*, 46:21 p.p.

Butt, T. and Russell, P. (1999). Suspended sediment transport mechanisms in high-energy swash. *Mar. Geol.*, 161:361–375.

Butt, T. and Russell, P. (2000). Hydrodynamics and cross-shore sediment transport in the swash zone of natural beaches: a review. *J. Coastal Res.*, 16:255–268.

Butt, T., Russell, P., Puleo, J., Miles, J., and Masselink, G. (2004). The influence of bore turbulence on sediment transport in swash and inner surf zones. *Cont. Shelf Res.*, 24:757–771.

Calvete, D., Falqués, A., and De Swart, H. E. (2001). Modelling the formation of shoreface-connected sand ridges on storm-dominated shelves. *J. Fluid Mech.*, 441:169–193.

Calvete, D. and Swart, H. E. (2003). A nonlinear model study on the long-term behavior of shoreface-connected ridges. *J. Geophys. Res.*, 108.

Carrier, G. F. and Greenspan, H. P. (1958). Water waves of finite amplitude on a sloping beach. *J. Fluid Mech.*, 4:97–109.

Carrier, G. F., Wu, T. T., and Yeh, H. (2003). Tsunami run-up and draw-down on a plane beach. *J. Fluid Mech.*, 475:79–99.

Carter, R. (1988). *Coastal Environments*. Academic Press, London.

Chung, T. (2002). *Computational Fluid Dynamics*. Cambridge University Press, Cambridge.

Ciavola, P., Taborda, R., Ferreira, O., and Dias, J. (1997). Field observations of sand-mixing depths on steep beaches. *Marine Geology*, 141:147–156.

Colombini, M. and Parker, G. (1995). Longitudinal streaks. *J. Fluid Mech.*, 304:161–183.

Cornaglia, P. (1889). On beaches. *Accademia Nazionale dei Lincei, Atti. Classe di Scienze, Matematiche e Naturali*, Mem 5 ser. 4:284–304.

Cornish, V. (1898). On sea beaches and sand banks. *Geogr. J.*, 11:528–559, 628–647.

Cui, Y., Parker, G., and Paola, C. (1996). Numerical simulation of agradation and downstream fining. *Journal of Hydraulic Research*, 34:185–204.

Cunge, J. A., Holly, F. M., and Verway, A., editors (1980). *Practical aspects of computational river hydraulics*. Pitman.

Davis, R. A. (1997). *The evolving coast*. Scientific American Library.

De Swart, H. E., Walgreen, M., and Calvete, D. (2008). Nonlinear modelling of shoreface-connected ridges: impact of grain sorting and interventions. *Coastal Eng.*, 55:642–656.

Dean, R. G. and Dalrymple, R. A. (2002). *Coastal Processes with Engineering Applications*. Cambridge University Press, Cambridge,UK, first edition.

Dodd, N., Stoker, A., Calvete, D., and Sriariyawat, A. (2008). On the evolution of beach cusps. *J. Fluid Mech.*, 597:145–169.

Eaglenson, P. and Dean, R. (1959). Wave-induced motion of bottom sediment particles. *Journal of Hydraul. Div.*, HY10:53–79.

Eaglenson, P. and Dean, R. (1961). Wave-induced motion of bottom sediment particles. *Trans. Am. Soc. Civil Eng.*, 126 (1):1162–1189.

Eaglenson, P., Glenne, B., and Dracup, J. (1961). Equilibrium characteristics of sand

beaches in the offshore zone. *U.S. Army Corps Eng. Beach Erosion Board Tech.*, Memo 126.

Eaglenson, P., Glenne, B., and Dracup, J. (1963). Equilibrium characteristics of sand beaches. *Proc. Am. Soc. Civ. Eng. J. Hydraul. Div.*, 89 HY1:35–57.

Ebersole, B. and Dalrymple, R. (1979). Numerical modeling of the nearshore circulation including convective acceleration and lateral mixing. Tech. Report 4, Dep. Civ. Eng. Univ. Delaware, Newark, Delaware.

Elfrink, B. and Baldock, T. (2002). Hydrodynamics and sediment transport in the swash zone: a review and perspectives. *Coastal Eng.*, 45:149–167.

Erikson, L., Larson, M., and Hanson, H. (2005). Prediction of swash motion and run-up including the effects of swash interaction. *Coastal Eng.*, 52:285–302.

Ferreira, O., Barrios, M., Pereira, H., Ciavola, P., and Dias, J. (1998). Mixing depth levels and distribution on steep foreshores. *Journal of Coastal Research*, 26:292–296.

Ferreira, O., Ciavola, P., Taborda, R., Barrios, M., and Dias, J. (2000). Sediment mixing depth determination for a steep and gentle foreshores. *Journal of Coastal Research*, 16(3):830–839.

Foti, E. and Blondeaux, P. (1995). Sea ripple formation: The heterogeneous case. *Coastal Engineering*, 25:237–253.

Garnier, R., Calvete, D., Falqués, A., and Caballeria, M. (2006). Generation and nonlinear evolution of shore-oblique / transverse bars. *J. Fluid Mech.*, 567(doi:10.1017/S0022112006002126):327–360.

Grass, A. (1981). Sediment transport by waves and currents. Report FL29, Ma. Tecnol., SERC London Cent.

Guard, P. A. and Baldock, T. E. (2007). The influence of seaward boundary conditions on swash zone hyrdodynamics. *Coastal Eng.*, 54:321–331.

Guza, R. T. and Inman, D. L. (1975). Edge waves and beach cusps. *J Geophys. Res*, 80:2997–3012.

Hirano, M. (1970). On phenomena of river-bed lowering and armouring below reservoirs. In Comm., C. E. A. H., editor, *14th Hydraulics Lecture Meeting*, Tokyo.

Hirano, M. (1971). River bed degradation with armouring. *Trans. JSCE*, 195:55–65.

Hirano, M. (1972). Studies on variation and equilibrium state of river bed composed of non-uniform material. *Trans. JSCE*, 4:128–129.

Horn, D. (1992a). A numerical model for shore-normal sediment size variation on a macrotidal beach. *Earth Surface Processes and Landforms*, 17:755–773.

Horn, D. (1992b). A review and experimental assessment of equilibrium grain size and the ideal wave-graded profile. *Marine Geology*, 108:161–174.

Horn, D. and Walton, S. (2007). Spatial and temp[oral variations of sediment size on a mixed sand and gravel beach. *Sedimentary Geology*, 202:509–528.

Horn, D. P. and Mason, T. (1994). Swash zone sediment transport modes. *Mar. Geol.*, 120:309–325.

Hsu, S. and Holly, F. (1992). Conceptual bed-load transport model and verification for sediment mixtures. *Journal of Hydraulic Engineering*, 118:1135–1152.

Hsu, T. and Raubenheimer, B. (2006). A numerical and field study on inner-surf and swash sediment transport. *Cont. Shelf Res.*, 26:589–598.

Hubbard, M. E. and Dodd, N. (2000). ANEMONE: OTT-2d a user manual (first version). TR 65, Hydraulics Research Wallingford.

Hubbard, M. E. and Dodd, N. (2002). A 2-d numerical model of wave run-up and overtopping. *Coastal Eng.*, 47(1):1–26.

Hudson, J. (2001). *Numerical Techniques for Morphodynamic Modelling*. Ph.d. thesis, University of Reading, Department of Mathematics.

Hudson, J., Damgaard, J. S., Dodd, N., Cooper, A. J., and Chesher, T. J. (2005). Numerical approaches for 1d morphodynamical modelling. *Coastal Eng.*, 52(8):691–707.

Hudson, J. and Sweby, P. K. (2003). Formulations for numerically approximating hyperbolic systems governing sediment transport. *J. Sci. Comp.*, 19:225–252.

Hughes, M. (1992). Application of a nonlinear shallow water theory to swash following bore collapse on a sandy beach. *J. Coastal Res.*, 8(3):562–578.

Hughes, M. G., Masselink, G., and Brander, R. W. (1997). Flow velocity and sediment transport in the swash zone of a steep beach. *Mar. Geol.*, 138:91–103.

Hunzinker, R. and Jaeggi, M. (2002). Grain sortin processes. *Journal of Hydraulic Engineering*, 128:1060–1068.

Inman, D. (1949). Sorting of sediments in the ligth of fluid mechanics. *J. Sediment. Petrol.*, 19:51–70.

Ippen, A. and Eaglenson, P. (1955). A study of sediment sorting by waves shoaling on a beach. *U.S. Army Corps Eng. Beach Erosion Board Tech.*, Memo 63.

Iribarren, C. and Nogales, C. (1949). Protection des ports. In *17th Int. Nav. Congr.*, pages 31–80, Lisbon, Portugal.

Jackson, N., Masselink, G., and Nordstrom, K. (2004). The role of bore collapse and local shear stress on the spatial distribution of sediment load in the uprush of an intermediate-state beach. *Marine Geology*, 203:109–118.

Jensen, A., Pedersen, G., and wood, D. (2003). An experimental study of wave run-up at a steep beach. *J. Fluid Mechanics*, 486:161–188.

Johnson, D. (1919). *Shore Processes and Shoreline Development*. Wiley.

Kelly, D. M. (2009). *Bore-driven swash on a mobile beach*. PhD thesis, School of Civil Engineering, University of Nottingham, Nottingham, UK.

Kelly, D. M. and Dodd, N. (2009). Floating grid characteristics method for unsteady flow over a mobile bed. *Computers and Fluids*, 38:899–909.

Kelly, D. M. and Dodd, N. (2010). Beach-face evolution in the swash zone. *Journal of Fluid Meechanics*, 661:316–340.

King, C. (1972). *Beaches and Coasts*. Edward Arnold, London.

Kirby, J. and Dalrymple, R. (1982). Numerical modeling of the nearshore region. Res. Report CE-82-24, Dep. Civ. Eng. Univ. Delaware, Newark, Delaware.

Kobayashi, N. and Johnson, B. D. (2001). Sand suspension, storage, advection and settling in surf and swash zones. *J. Geophys. Res.*, 106(C5):9363–9376.

Komar, P. and Miller, M. (1975). On the comparison between the threshold of sediment motion under waves and unidirectional currents with a discussion of the practical evaluation of the threshold. *J. Sediemt. Petrol.*, 45:362–367.

Lanzoni, S. and Tubino, M. (1999). Grain sorting and bar instability. *J. Fluid Mech.*, 393:149–174.

Larson, M. and Krauss, N. (1989). Sbeach: Numerical model for simulating storm-induced beach beach change report 1: Theory and model foundation. Tech. Report CERC-89-9.

Liu, J. and Zarillo, G. (1989). Distribution of grain sizes across a transgressive shoreface. *Marine Geology*, 87:121–136.

Liu, J. and Zarillo, G. (1993). Simulation of grain-size abundances on a barred upper shoreface. *Marine Geology*, 109:237–251.

Madsen, O. (1976). Wave climate of the continental margin: elements of its mathematical description. In Swift, D. and Stanley, D., editors, *Marine Sediment Transport and Environmental Management*, pages 65–87, New York.

Madsen, O. (1989). Tracer theory. In Seymour, R., editor, *Nearshore Sediment Transport*. Plenum Press.

Masselink, G., Evans, D., Hughes, M. G., and Russell, P. (2005). Suspended sediment transport in the swash zone of a dissiaptive beach. *Mar. Geol.*, 216:169–189.

Masselink, G. and Hughes, M. (1998). Field investigation of sediment transport in the swash zone. *Cont. Shelf Res.*, 18:1179–1199.

Masselink, G. and Hughes, M. G. (2003). *Introduction to Coastal processes & Geomorphology*. Hodder Arnold, London, UK.

Masselink, G. and Puleo, J. A. (2006). Swash zone morphodynamics. *Cont. Shelf Res.*, 26:661–680.

Masselink, G., Russell, P., Blenkinsopp, C., and Turner, I. (2010). Swash zone sediment transport, step dynamics and morphological response on a gravel beach. *Marine Geology*, 274:50–68.

Mei, C. C. (1990). *The Applied Dynamics of Ocean Surface Waves*, volume 1 of *Advanced Series on Ocean Engineering*. World Scientific, Singapore, second edition.

Miller, I. and Warrick, J. (2012). Measuring sediment transport and bed disturbance with tracers on a mixed beach. *Marine Geology*, 299-302:1–17.

Miller, R. and Zeigler, J. (1958). A model relating dynamics and sediment pattern in equilibrium in the region of shoaling waves, breaker zone and foreshore. *J. Geology*, 66:417–441.

Miller, R. and Zeigler, J. (1964). A study of sediment distribution in the zone of shoaling waves over complicated botton topograpphy. *In: R.L. Miller (Editor) Papers in Marine Geology*, pages 133–153.

Murray, S. (1967). Control of grain dispersion by paricle size and wave state. *J. of Geol.*, 75:612–634.

Nielsen, P. (1982). Explicit formulae for prectical wave calculations. *Coastal Eng.*, 6:389–398.

Parker, G. (1990). Surface-based bedload transport relation for gravel rivers. *Journal of Hydraulic Research*, 28:417–436.

Parker, G. and Andrews, E. (1985). Sorting of bedload sediment by flow in meander bends. *Water Resources Research*, 21:1361–1373.

Parker, G. and Sutherland, A. (1990). Fluvial armor. *Int. J. of Hydr. Res.*, 28:529–544.

Peregrine, D. and Williams, S. M. (2001). Swash overtopping a truncated beach. *J. Fluid Mech.*, 440:391–399.

Pritchard, D. and Hogg, A. J. (2005). On the transport of suspended sediment by a swash event on a plane beach. *Coastal Eng.*, 52:1–23.

Ribberink, J. (1987). *Mathematical modelling of one-dimensional morphological changes in rivers with non uniform sediment*. PhD thesis, School of Civil Engineering, Delft University of Technology.

Roos, P., Hulscher, S., and Knaapen, M. (2004). The cross-sectional shape of tidal banks. *J. Geophys. Res.*, 109.

Roos, P. C., Suzanne, J., T.A.G.P., V. D., Wientjes, I., and Van den Berg, J. (2007). Grain size sorting over offshore sand waves: Observation and modelling. In *River, Coastal, and Estuarine Morphodynamics: RCEM 2007*, pages 649–656.

Seminara, G., Colombini, M., and Parker, G. (1996). Nearly pure sorting waves and formation of bedload sheets. *J. Fluid Mech.*, 312:253–278.

Shen, M. C. and Meyer, R. E. (1963a). Climb of a bore on a beach. Part 2. Non-uniform beach slope. *J. Fluid Mech.*, 16:108–112.

Shen, M. C. and Meyer, R. E. (1963b). Climb of a bore on a beach. Part 3. Run-up. *J. Fluid Mech.*, 16:113–125.

Sherman, D., Nordstrom, K., Jackson, N., and Allen, J. (1994). Sediment mixing-depths on a low-energy reflective beach. *Journal of Coastal Research*, 10:297–305.

Smith, G. (1978). *Numerical solution of partial differential equations: Finite difference methods*. Oxford, 2nd edition.

Soulsby, R. L. (1997). Dynamics of marine sands. a manual for practical applications. SR 466, Hydraulics Research Wallingford, Wallingford, England.

Steenhauer, K., Pokrajac, D., and O'Donoghue, T. (2012). Numerical model of swash motion and air entrapment within coarse-grained beaches. *Coastal Eng.*, 64:113–126.

Stoker, J. (1957). *Water Waves*. Interscience, New York, N.Y.

Sunamura, T., Bnado, K., and Horikawa, K. (1978). An experimental study of sand transport mechanics and transport rate over asymmetric sand ripples. In Horikawa, K., editor, *Proc. 25th Japan. Conf. Coastal Eng. (in japanese)*, pages 250–254, Japan.

Sunamura, T. and Krauss, N. (1985). Predicion of average mixing depth of the sediment in the surf zone. *Marine Geology*, 62:1–12.

Synolakis, C. (1987). The run-up of solitary waves. *J. Fluid Mech.*, 185:523–545.

Thornton, E. and Guza, R. (1982). Energy saturation and phase speeds measured on a natural beach. *J. Geophys. Res.*, 87:9499–9508.

Toro, E. F. (2001). *Shock-capturing methods for free-surface shallow flows*. Wiley, New York, NY.

Tritthart, M., Schober, B., and Habersack, H. (2011). Non-uniformity and layering in sediment transport modelling: Flume simulations. *Journal of Hydraulic Research*, 49:325–334.

Van den Berg, J. and Van Damme, R. (2005). Sand wave simulation on large domains. In Parker, G. and Garcia, M., editors, *River, Coastal, and Estuarine Morphodynamics: RCEM 2005*, pages 991–997, Urbana, Illinois.

Van Oyen, T. and Blondeaux, P. (2009). Grain sorting effects on the formation of tidal sand waves. *Journal of Fluid Mechanics*, 629:311–342.

Van Oyen, T., de Swart H., and Blondeaux, P. (2011). Formation of rhythmic sorted bed forms on the continental shelf: an idialised model. *Journal of Fluid Mechanics*, 684:475–508.

Van Rijn, L. (1985). Sediment transport part i: Bed load transport part ii: Suspended load transport part iii: Bed forms and alluvial roughness. Technical Report 334, Waterloopkundig Laboratorium.

Van Rijn, L. (1997). Cross-shore sand transport and bed composition. In *Proc. Coastal Dynamics*, pages 88–98, Plymouth,UK.

Van Rijn, L. (1998). The effect of sediment transpot in cross-shore bed profiles. In *Proc. Coastal Engineering*, pages 2495–2508, Copenhagen, Denmark.

Van Wellen, E., Chadwick, A. J., and Mason, T. (2000). A review and assessment of longshore sediment transport equations for coarse grained beaches. *Coastal Eng.*, 40:243–275.

Walgreen, M. (2003). *Dynamics of sand ridges in coastal seas, the effect of storms, tides and grain sorting*. PhD thesis, Utrech University, Utrech, The Nederlands.

Walgreen, M., De Swart, H. E., and Calvete, D. (2003). Effect of grain sorting on the formation of shoreface-connected ridges. *J. Geophys. Res.*, 108(C3):3063, doi:10.1029/2002JC001435.

Walgreen, M., Swart, H. E., and Calvete, D. (2004). A model for grain-size sorting over tidal sand ridges. *Ocean Dynamics*, 54:374–384.

Zenkovitch, V. (1946). Coastal dynamics and morphology, part 1, wave processes. *Moskoi Transport. (reference from Zenkovitch 1964)*.

Zhu, F. (2012). *1D Morphological Modelling of Swash Zone beachface evolution*. PhD thesis, School of Civil Engineering, University of Nottingham, Nottingham, UK.

Zhu, F., Dodd, N., and Briganti, R. (2012). Impact of a uniform bore on an erodible beach. *Coastal Engineering*, 60:326–333.